Multifunctional Microbubbles for Ultrasound Targeted Treatment of Solid Tumours

Keiran Logan BSc (Hons)

Faculty of Life and Health Sciences

Ulster University

Thesis submitted for the degree of

Doctor of Philosophy

September 2019

I confirm that the word count of this thesis is less than 100,000 words.

Declaration

I hereby declare that with effect from the date on which the thesis is deposited in Ulster University Doctoral College, I permit

1. The Librarian of the University to allow the thesis to be copied in whole or in part without reference to me on the understanding that such authority applies to the provision of single copies made for study purposes or for inclusion within the stock of another library.

2. The thesis to be made available through the Ulster Institutional Repository and/or EThOS under the terms of the Ulster eTheses Deposit Agreement which I have signed.

I declare that this thesis and the work presented in it are my own and have been generated by me as the result of my own original research, with the exception of the chemical synthesis of the biotinylated ligand described in chapter 4 which was performed by Dr Sukanta Kamila, the development of the magneto-acoustic device which was developed and characterized by Lester Barnsley and co-workers at the University of Oxford, in vitro characterization of magnetic microbubbles was performed by collaborators at the University of Oxford, and the analysis of blood samples which was performed by Carmichael Torrance Diagnostic Services.

Acknowledgements

Firstly, I would like to thank my primary supervisor Professor John Callan for giving me the opportunity to work in such a diverse research environment and for providing me with constant support along the way. I would also like to thank my secondary supervisor Professor Anthony McHale. Your insights over the past three years have been invaluable.

I would like to thank Dr Heather Nesbit for her generosity in giving her time to help me with animal experiments whenever it was needed. I would like to thank the rest of my colleagues: Dr Federica Foglietta, Dr David Costley, Dr Jordan Atchinson, Mr Simon Porter, Dr Jason Sheng, Miss Sian Farrell, Mr Jinhui Gao, Mr Thomas McKaig and Talat Nahid Khan for your consistent help and support. I would like to thank Dr Barry Hyland for his guidance throughout the thesis writing process. I would like to acknowledge our collaborators at the University of Oxford for their help in making the MAD experiments possible. I would also like to thank Dr Sukanta Kamila for his expertise and tutelage in the field of chemical synthesis.

Dr Dean Nicholas, our conversations have sometimes been scientific in nature and have promoted new ideas. You have provided endless support and guidance from day one and have inspired me to be a better scientist. Thank you for the friendship.

Finally, I would like to thank my family. To my Mum and Dad, you may not know the ins and outs of what I do every day in the lab but your love and support have been unwavering over the past three years. To my partner in crime, Ellen. You give me the drive to keep going every day when times are tough and push me to be a better person. For this I thank you.

List of Figures and Tables

v

Table of Contents

List of abbreviations

[drug]	Drug concentration
$^{1}O_2$	Singlet Oxygen
$^{3}O^{2}$	Triplet Oxygen
BCT	Breast Conservation Therapy
DBPC	1,2-dibehenoyl-sn-glycero-3-phosphocholine
dFdC	2',2'-difluorodeoxycytidine
dFdCDP	difluorodeoxycytidine diphosphate
dFdCTP	difluorodeoxycytidine triphosphate
dFdU	2',2'-difluorodeoxyuridine
DMEM	Dulbecco`s Modified Eagle Media
DMF	Dimethylformamide
DMSO	Dimethylsulfoxide
Dox	Doxorubicin
DSPC	1,2-distearoyl-sn-glycero-3-phosphocholine
ECOG	The Eastern Cooperative Oncology Group
EPR	Enhanced permeability and retention
ESI-MS	Electrospray Ionisation Mass Spectrometry
FBS	Fetal Bovine Serum
FDA	Food and Drug Administration
Gem	Gemcitabine
HIFU	High Intensity Focused Ultrasound
HPLC	High Performance/Pressure Liquid Chromatography

I.P	Intraperitoneal
ISC	Intersystem Crossing
I.V	Intraveneous
LRR	Locoregional Reccurance
MALDI-TOF	Matrix-Assisted Laser Desorption/Ionization Time Of Flight
MB(s)	Microbubble(s)
MeOH	Methanol
MHRA	Medicines and Healthcare products Regulatory Agency
MTT	3-(4,5-dimethylthiazol-2-yl)-2,5-diphenyltetrazolium bromide
nabPTX	Paclitaxel Albumin Nanparticles
NICE	National Institute for Health and Care Excellence
NMR	Nuclear Magnetic Resonance
P2P	Peak to Peak
PBS	Phosphate Buffered Saline
PDAC	Pancreatic Ductal Adenocarcinoma
PDT	Photodynamic Therapy
PEG	Polyethylene Glycol
PFB	Perflourobutane
PI	Propidium Iodide
PLGA	poly(lactic-co-glycolic acid)
PNP	Peak Negative Pressure
PPP	Peak Positive Pressure
PRP	Pulse Repetition Frequency

PTLC	Preparative Thin Layer Chromatography
PTX	Paclitaxel
RB	Rose Bengal
ROS	Reactive Oxygen Species
RPMI	Roswell Park Memorial Institute
SCID	Severe Combined Immunodeficient
SDT	Sonodynamic Therapy
SF_6	Sulfur Hexaflouride
S_N2	Bi-molecular Nucleophilic Substitution
SOSG	Singlet Oxygen Sensor Green
TEA	Triethylamine
US	Ultrasound
WHO	World Health Organisation
$\phi\Delta$	Singlet Oxygen Quantum Yield

Chapter 1

Introduction

1.1. Cancer

In developed countries, cancer is the second leading cause of death behind cardiovascular disease with an estimated 18.1 million people diagnosed each year and 9.6 million cancer related deaths reported in 2018. (1) Despite the introduction of new and improved chemotherapies over the past two decades, cancer deaths continue to rise due to a growing and aging population. Cancers of the lung and breast in both men and women have the highest incidence of new cases worldwide each year making up 23.2% of all new cancer cases followed by prostate and colorectal cancers. (1)

In simplistic terms, cancer can be characterised as a disease which arises when normal cell growth in the body is disrupted through alterations in the genes which control this process, resulting in the uncontrolled division of cells. These cells can subsequently invade surrounding tissues as well as other organs in a process known as metastasis. In addition to uncontrolled cell growth, cancers are characterised by the downregulation of antiapoptotic proteins which prevent programmed cell death. (2)

Significant progress has been made over the past few decades to identify the underlying mechanisms of the disease. These "hallmarks of cancer" were elegantly summarized in the seminal review by Hanahan & Weinberg and were categorised into ten groups: (i) the sustenance of proliferative signalling, (ii) evasion of growth suppressors through the down regulation of tumour suppressor gene expression, (iii) resistance to cell death, (iv) replicative immortality, (v) induction of angiogenesis, (vi) induction of invasion and metastasis, (vii) genomic instability and mutation, (viii) evasion of immune destruction, (ix) tumour inflammation and (x) downregulation of cellular energetics. (2)

Table 1.1. Treatment strategies for targeting specific cancer hallmarks

Hallmark	Treatment strategy	Examples	Reference
Sustaining proliferative signalling	EGRF inhibitors	Cetuximab, Erlotinib	(3), (4)
Evading growth suppressors	Cyclin-dependent kinase inhibitors	Palbociclib, Ribociclib	(5)
Avoiding immune destruction	Immune activating anti-CTLA4 mAb	Ipilimumab, Tremelimumab	(6)
Enabling replicative immortality	Telomerase inhibitors	Fomivirsen, Imetelstat	(7), (8)
Tumour-promoting inflammation	Selective anti-inflammatory drugs	Ibuprofen, Celecoxib	(9), (10)
Activating invasion & metastasis	Inhibitors of HGF/c-Met	Cabozantinib, Crizotinib	(11), (12)
Inducing angiogenesis	Inhibitors of VEGF signalling	Bevacizumab, Aflibercept	(13), (14)
Genome instability & mutation	PARP inhibitors	Olaparib, Talazoparib	(15), (16)
Resisting cell death	Proapoptotic BH3 mimetics	Venetoclax, Navitoclax	(17), (18)
Deregulating cellular energetics	Aerobic glycolysis inhibitors	2-deoxy-D-glucose, 3-Bromopyruvate	(19), (20)

Current chemotherapy drugs actively target specific molecular pathways involved in many of the hallmarks described above (Table 1.1.). This specific targeting of pathways was the cause of much excitement within the field as active targeting of a specific pathway meant that off-target side effects would be minimised whilst still maintaining a high therapeutic efficacy. However, current clinical results to date have demonstrated that due to the heterogeneity of tumour cells, sub-fractions of cancer cell populations survive initial treatment and are free to continue replicating. This adaptive resistance often leads to localised recurrence. Furthermore, resistance to certain treatments may be brought about through treatment induced secondary mutations. For example, patients can develop an acquired resistance upon exposure to certain endothelial growth

factor receptor (EGFR) inhibitors. (21) Indeed, cancer cells are capable of shifting their dependence on a particular hallmark capability, thereby becoming more dependent on another. (2) This often leads to a reduced response to targeted therapies. For this reason, there is now a growing trend within oncology in using combinations of chemotherapies to maximise treatment response.

1.2. Pancreatic cancer

1.2.1. Overview

Pancreatic cancer is one of the most lethal malignant neoplasms worldwide. A 2012 study estimated deaths from pancreatic cancer to be 331,000 per year, making it the seventh leading cause of cancer related deaths worldwide for both males and females. (22) Pancreatic ductal adenocarcinoma (PDAC) accounts for more than 90% of pancreatic cancer cases. The survival rate for this form of the disease is extremely poor with a 1-year survival of less than 18% which drops to less than 4% after 5 years. Due to the asymptomatic nature of the disease, early detection of pancreatic tumours is often challenging. As a consequence, many patients will present with inoperable tumours or distant metastases leading to increased rates of mortality. The 5-year survival rate for pancreatic cancer has only increased by 2% since 1975 (23), clearly demonstrating the deadliness of the disease and a need for improving the survival rates of those who are diagnosed with pancreatic cancer. National Institute for Health and Care Excellence (NICE) treatment guidelines for advanced pancreatic cancer recommend combination chemotherapy with FOLFRINOX or gemcitabine + Abraxane as the first line treatment in patients with an eastern cooperative performance status (ECOG) of 1 or 2. (24) However, these combination treatments are often poorly tolerated by an elderly patient population. Therefore, novel therapeutic alternatives are highly sought-after.

1.2.2. Anatomy of the Pancreas

The pancreas has a critical function within the human gastrointestinal tract. It is located in the retroperitoneum directly behind the stomach and is generally split into four main segments: (i) the head, (ii) neck, (iii) body and (iv) tail. The head of the pancreas is surrounded by the neighbouring duodenum while the tail lies near the hilium of the spleen. The body of the pancreas lies behind the distal portion of the stomach between the tail and neck while the neck of the pancreas lies in close proximity to the superior mesenteric artery and vein (Figure 1.1). (25)
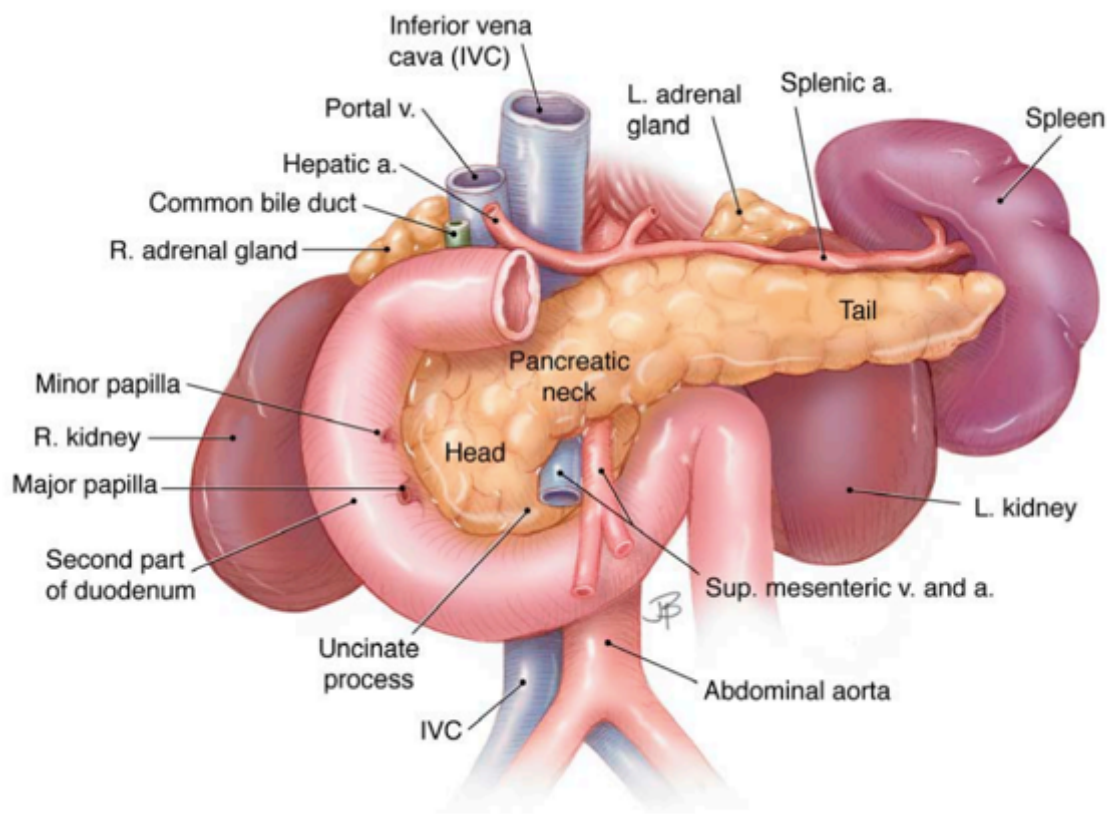
Figure 1.1. Illustration of the anatomy of the pancreas. (Taken from (25))

The pancreas serves two important functions within the human body. First, as an exocrine organ, secreting digestive enzymes such as pancreatic proteases, lipases and amylases from the bile duct in the head of the pancreas into the neighbouring duodenum. This role accounts for approximately 95% of the mass of the pancreas. The second function of the pancreas is as an endocrine organ made up of alpha, beta and acinar cells in the pancreatic islets of Langerhans. These cells serve to produce and secrete hormones such as insulin,

glucagon, somatostatin, and pancreatic polypeptide into the splenic artery. This role accounts for a relatively small portion of the mass of the pancreas (1-2%). (25)

The majority of pancreatic tumours are adenocarcinomas (PDAC) which affect the exocrine cells which line the pancreatic duct. Between 60-70 % of pancreatic cancers occur in the head of the pancreas, whereas 20-30% occur in the body and tail. (26) According to the location of the tumour within the pancreas, presentation of symptoms can often vary. Patients with tumours originating in the head of the pancreas often present with jaundice and hyperbilirubinemia as a result of obstruction of the common bile duct while tumours of the body or tail often present with middle-back pain and weight loss. There have been numerous studies which have suggested that the anatomical location of tumours within the pancreas is a significant prognostic factor for overall survival. (27–29). These findings were further corroborated by a recent meta-analysis which found that tumours located in the head of the pancreas coincided with a significantly improved survival. (30)

1.2.3. Incidence and mortality

Pancreatic cancer is the 11th most common cancer in the world with 458,918 new cases and 432,242 deaths (4.5% of all cancer deaths) reported in 2018 making it the 7th leading cause of cancer related death. (1) The disease is also expected to become the 2nd leading cause of cancer related death in the United States by 2030. (31) Pancreatic cancer is slightly more common in men than in women. For both men and women, the likelihood of developing the disease increases with age with most cases being diagnosed at 70 years old.

1.2.4. Risk factors

Risk factors for pancreatic cancer can be broadly separated into two categories: (i) controllable and (ii) uncontrollable. Uncontrollable risk factors include gender, race, age and genetic inheritance. As has been mentioned previously, the incidence of pancreatic cancer is elevated in both the male and elderly populations. Ethnicity is also a risk factor for pancreatic cancer with the black population being at higher risk of the disease than Caucasian populations. (32)

Family history is a significant risk factor in people with first degree relatives having had pancreatic cancer, with this group being at significantly higher risk of developing the disease when compared to the general population. (33,34) The main controllable risk factor for pancreatic cancer is smoking, with smokers being twice as likely to develop the disease than non-smokers. (35–37) There is also a correlation between body mass index (BMI) and pancreatic cancer, with a BMI ≥30 indicating people with an increased risk. (38) Other notable controllable risk factors include high alcohol consumption, consumption of processed meats, and occupational exposure to carcinogens. (39)

1.2.5. Molecular mechanisms of pancreatic cancer

The development of pancreatic tumours is as a result of multiple complex molecular alterations within pancreatic cells. The formation of tumours from precursor lesions (pancreatic intraepithelial neoplasia (PanIN)) through to carcinoma is a multistep process. (40) In addition to PanIN, pancreatic cancer can also arise as a result of other precursor lesions such as intraductal papillary mucinous neoplasms and mucinous cystic neoplasms. (41) Accordingly, most early detection and screening studies are aimed at finding these precursor lesions, as resection of these lesions at an early stage can halt the development of advanced disease. Generally PanIN can be further characterised into grades 1A, 1B, 2 and 3 which represent incremental increases in cytological atypia. (42) Following the progression from PanIN-1 to PanIN-3, many specific genetic changes such as loss/gain of tumour promoting/suppressing genes and microRNA overexpression, resulting in an invasive phenotype. (43)

Pancreatic cancer, as with most cancers, arises as a result of mutations in proto-oncogenes, tumour-suppressor genes, and genomic maintenance genes. Proto-oncogenes have an important role in the regulation of growth factors, signal transduction, transcription factor and apoptotic inhibitors. Oncogenes arise as a result of mutations in proto-oncogenes resulting in permanent overproduction of growth factors as well as permanent apoptotic inhibition, resulting in uncontrolled cell proliferation. This process is often likened to a car with the accelerator jammed on but with no brake pedal. (42)

Table 1.2. List of frequently mutated genes in pancreatic cancer. Reproduced from (42).

Gene name	Mutation frequency (%)	Type	Signalling or system
KRAS	70-95	Proto-oncogene	Ras/Raf/MAPK
TP53	20-70	Tumour-suppressor	Apoptosis Cell cycle control
CDKN2A	49-98	Tumour-suppressor	Cell cycle control
SMAD4 DPC4	19-50	Tumour-suppressor	TNFbeta/SMAD

The most commonly mutated gene in PDAC is the KRAS gene. This gene plays a key role in mediating downstream signalling by the activation of transcription factors, which has been involved in over 90% of pancreatic carcinogenesis. (44) Tumour suppressor genes are also commonly mutated in pancreatic cancer patients. The gene, TP53, is mutated in approximately 60% of pancreatic cancers. (45) The main function of tumour suppressor genes is to control cell proliferation. Mutations in these genes can result in uncontrolled cell proliferation.

1.2.6. Treatments for pancreatic cancer

Due to both the aggressive and asymptomatic nature of PDAC, approximately 50% of patients will present with a metastatic form of the cancer, meaning that the cancer has spread to other parts of the body (most commonly the liver, lungs or peritoneum). (46) Treatment options for this patient group are limited and are generally palliative involving chemotherapy regimens such as FOLFRINOX (leucovorin, fluorouracil, irinotecan, and oxaliplatin). Approximately 20% of patients will present with tumours which are deemed suitable for surgical resection. (47) For patients who are eligible for surgery and who obtain an R0 resection, the overall survival improves considerably with a mean survival of 20 - 24 months. (48) Approximately 30% of patients will present will locally-advanced of borderline-resectable tumours. Tumours under this classification

may still be confined to the pancreas but due to their size or anatomical position within the pancreas, are deemed unsuitable for R0 resection. Since it is generally understood that surgical resection with clear margins (R0) is an indicator for improved overall survival, there is a growing interest in the use of neo-adjuvant chemotherapy for the treatment of this sub-group.

The overall rationale for neo-adjuvant chemotherapy in PDAC is to: (49)

1. increase rates of patients eligible for curative R0 resection by reducing tumour bulk and involvement of nearby critical structures.
2. downstage disease.
3. ensure that all patients receive chemotherapy.
4. allow emergence of resistant, already present metastatic disease, if such exists to better inform future clinical decisions.
5. treat locally invasive disease before resection, as surgery may alter perfusion in the area leading to earlier onset of metastasis.
6. treat micro-metastatic disease earlier, at the time of diagnosis.

The significant benefit of neoadjuvant chemotherapy for patients with locally advanced or borderline-resectable pancreatic cancer was illustrated in a 2010 systematic metanalysis which revealed that approximately one third of patients staged with locally advanced/unresectable disease, could undergo successful resection following a regimen of neoadjuvant chemotherapy and could consequently achieve a median survival comparable with that of initially resectable tumour patients. (Figure 1.2). (48)
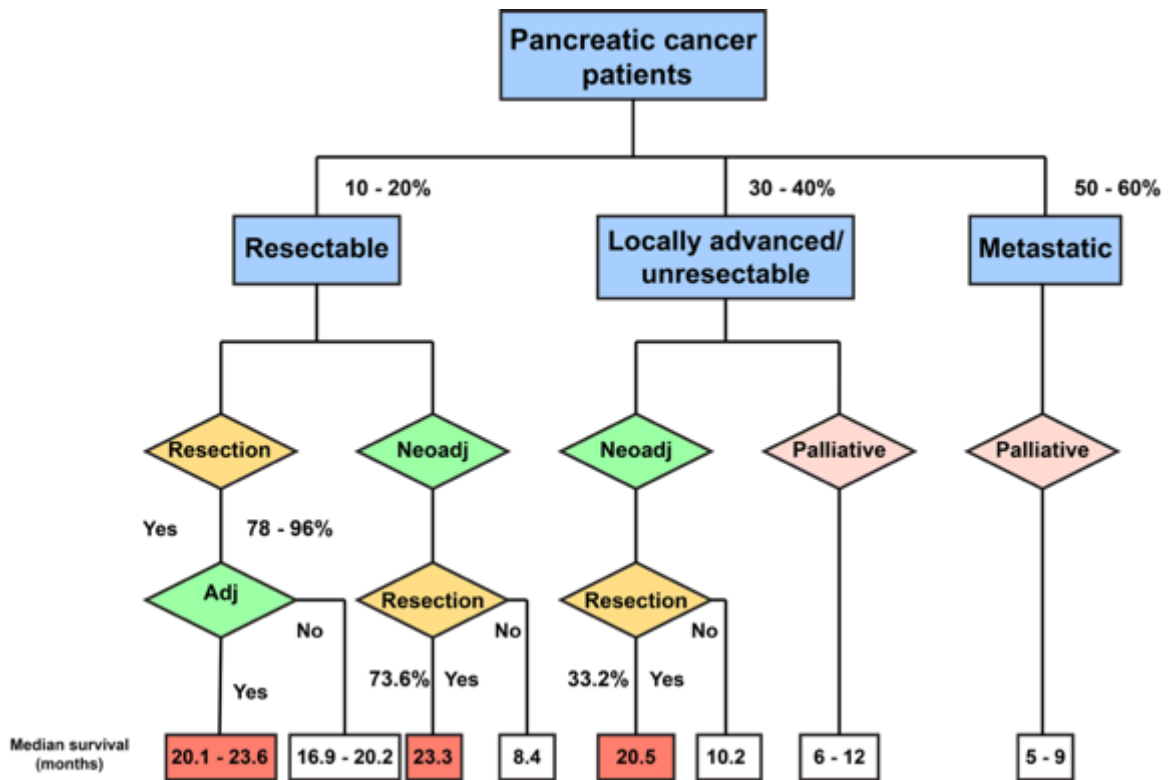
Figure 1.2. Diagram illustrating the effectiveness of neo-adjuvant chemotherapy compared with other treatment strategies. Reproduced from (48).

1.2.6.1. Chemotherapy

1.2.6.1.1. FOLFRINOX

Following the landmark PRODIGE 4/ACCORD 11 trial published in 2011, FOLFRINOX has become a gold standard treatment for patients with advanced or metastatic pancreatic cancer. FOLFRINOX is a combination infusion of 5-Flourouricil (5-FU) leucovorin, irinotecan and oxaliplatin. The antimetabolite 5-FU in combination with oxaliplatin and irinotecan was initially developed for the treatment of metastatic colorectal cancer. (50)

5-flourouracil (5-FU) is an antimetabolite drug which works by inhibiting critical biosynthetic processes within the cell through incorporation into DNA or RNA. 5-FU is based on the nucleobase uracil and is intracellularly metabolised into numerous active forms: fluorodeoxyuridine monophosphate (FdUMP), fluorodeoxyuridine triphosphate (FdUTP) and fluorouridine triphosphate (FUTP). (51,52) Lecouvorin or folinic acid is the reduced form of folic acid and has been shown to modulate the effect of 5-FU by enhancing the inhibition of thymidylate synthetase. (53,54)

a)   b)
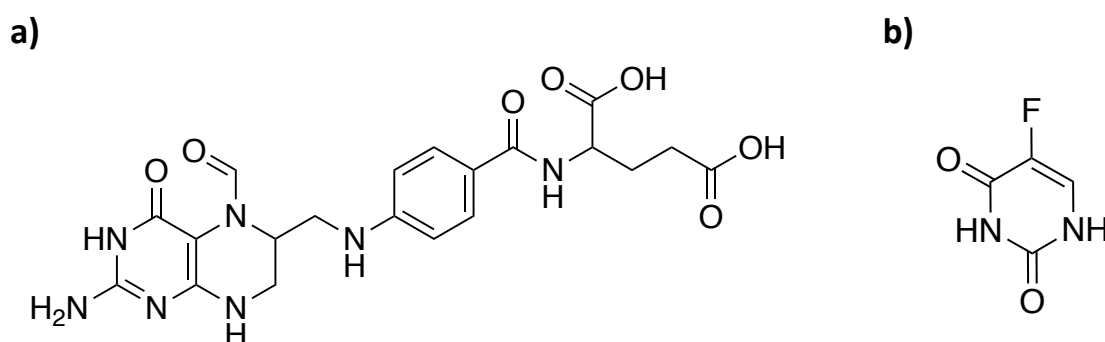
Figure 1.3. Chemical structures of a) Lecouvorin and b) 5-Flourouricil (5-FU).

Irinotecan is a water-soluble derivative of the natural product camptothecin. (55) Irinotecan is a prodrug which is metabolised intracellularly to 7-ethyl-10-hydroxycamptothecin (SN-38), which primarily acts as a topoisomerase 1 inhibitor and is approximately 1000 times more potent than irinotecan. (56) As well as being a part of FOLFRINOX, a nanoliposomal dosage form of irinotecan along with 5-FU is currently used as a second line treatment for advanced pancreatic cancer. (57)

a)   b)
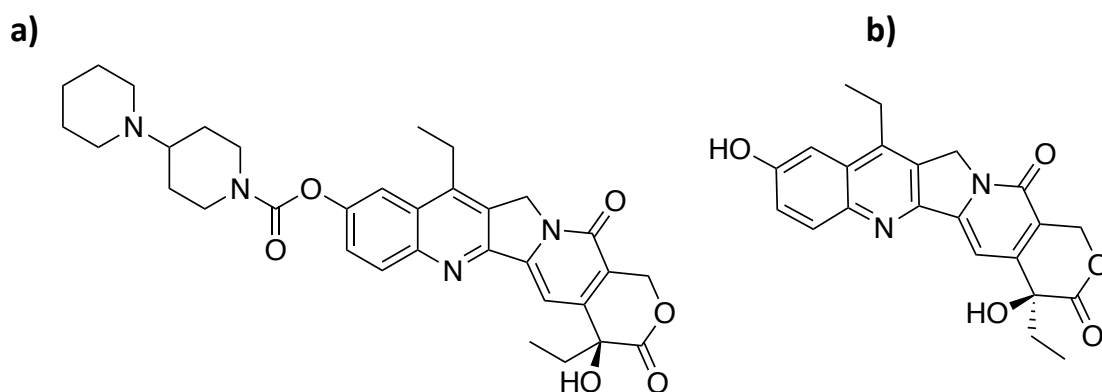
Figure 1.4. Chemical structures of a) irinotecan and b) SN-38.

Oxaliplatin is a platinum compound similar in structure to cisplatin. It has a characteristic bidentate oxalate leaving group which has been attributed in part to its activity. (58) The precise cytotoxic mechanisms of action of platinum-based drugs is still not fully understood, however these agents are generally thought to form crosslinks with DNA, which subsequently disrupts DNA replication, leading to apoptosis. (59–61)
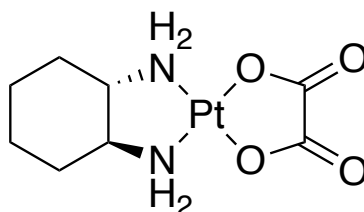
Figure 1.5. Chemical structure of oxaliplatin.

1.2.6.1.2. Gemcitabine

Gemcitabine (Gem) is a deoxycytidine nucleoside analogue first patented by Eli Lilly in 1983 as an antiviral medication and later approved for human use as an antineoplastic drug in 1995. (62) It has since been used clinically for a variety of solid tumours including breast, ovarian and lung cancers. (63,64) Structurally, Gem is composed of a cytidine ring fused to a di-fluorinated deoxyribose ring (Figure 1.6). (65)
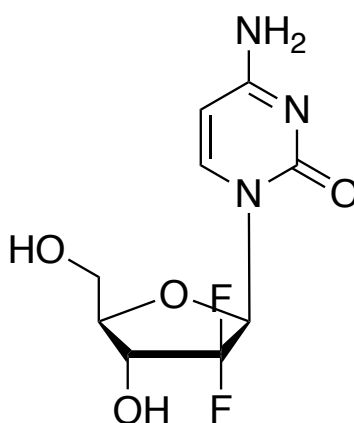
Figure 1.6. Chemical structure of gemcitabine (Gem).

Gem is a prodrug which must first be metabolised into the active triphosphate form (2',2'-difluoro-2'-deoxycytidine triphosphate). Once shuttled into the cell by nucleoside transporter proteins, Gem is mono-phosphorylated by deoxycytidine kinase enzymes. This species is then further phosphorylated by uridine monophosphate/cytidine monophosphate kinase (UMP-CMP kinase) to 2',2'-difluoro-2'-deoxycytidine diphosphate (dFdCDP) before a final phosphorylation step to 2',2'-difluoro-2'-deoxycytidine triphosphate (dFdCTP). (66) The anticancer activity of Gem is mediated by replacement of the nucleoside cytidine with the active dFdCTP thereby preventing DNA elongation, consequently leading to cell death (Figure 1.7). (67) Additionally, both dFdCDP and dFdCTP are involved in direct and indirect inhibition of enzymes responsible for metabolising deoxynucleotides thereby improving the chances of dFdCTP incorporation within DNA. (68)
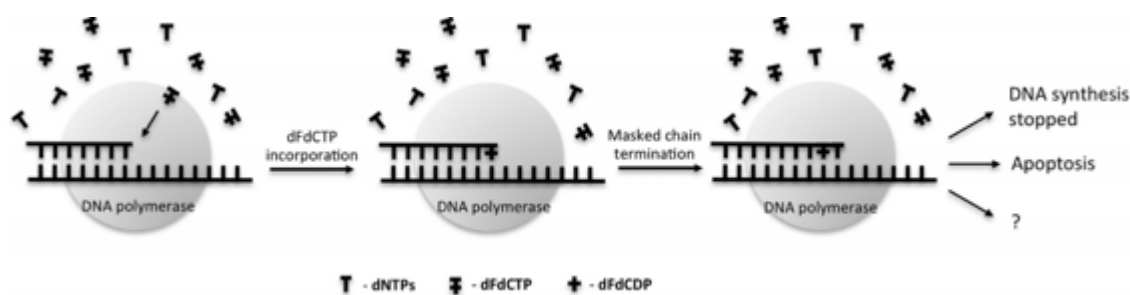
Figure 1.7. Diagram illustrating the masked chain termination. DNA polymerase incorporates dFdCTP into the DNA sequence during DNA synthesis. This is followed by the incorporation of another nucleotide triphosphate (dNTP). This disables the action of DNA polymerase resulting in the termination of chain elongation which can lead to apoptotic cell death. Taken from (68).

Despite the multiple mechanisms of action for Gem, there are also numerous pathways that generate resistance to this drug. These include deficiency of nucleoside transporter proteins, down-regulation of the rate-limiting enzyme deoxycytidine kinase, and up-regulation of Ribonucleoside Reductase M1/M2 (RRM1/RRM2) (responsible for the synthesis of deoxyribonucleotides from ribonucleotides), and deactivation to an inactive uridine derivative catalysed by cytidine deaminase enzymes. (69–72) Results from the ESPAC-3 trial showed that patients with low levels of nucleoside

transporter proteins had an overall poorer survival than those with higher levels of these proteins. (73)
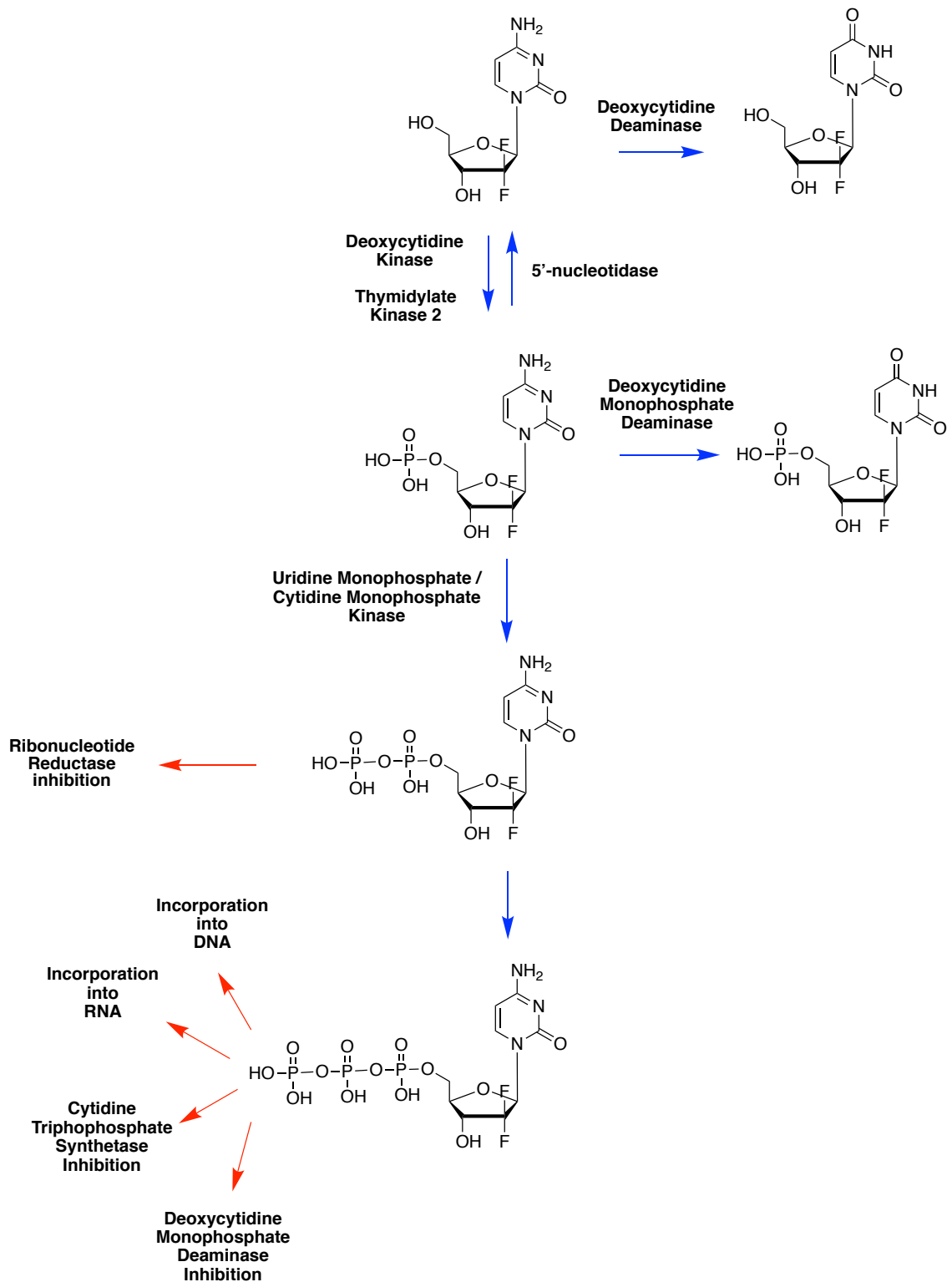
Figure 1.8. Scheme illustrating the metabolism and mechanism of action of Gem. Adapted from (74).

1.2.6.1.2.1. Gemcitabine prodrug development

As with most modern chemotherapeutics, nucleoside analogues such as Gem, 5-FU and cytarabine suffer from resistance by cancer cells. Resistance to chemotherapy is widely regarded as a key driver for poor survival and as a consequence much effort has been invested into developing prodrug strategies to overcome both innate and acquired resistance to chemotherapeutics. As was described in Section 1.2.6.1.2, there are three prominent mechanisms which underpin the resistance of cancer cells to Gem and other nucleoside analogues. These include: (i) reduced intracellular conversion of Gem to the active dFdCDP and dFdCTP forms through down-regulation of kinase-type enzymes which are responsible for the rate limiting first phosphorylation step (75), (ii) rapid conversion of Gem to inactive uridine derivatives through overexpression of cytidine deaminase (76), (iii) reduced uptake of Gem resulting from a deficiency of nucleoside transporter proteins. (77)

Accordingly, many prodrugs of Gem have been developed to improve its pharmacokinetic profile (by addition of PEG, valproate, squalene, linear acyl groups and phosphoramidate moieties). (78) Gem prodrugs with Gem attached to a phospholipid have also been developed to bypass multiple resistance pathways. Alexander et al developed a Gem-phospholipid prodrug, with Gem conjugated to the phospholipid at the 5′ position. It was found that, in contrast to the free drug, the highly lipophilic prodrug did not enter the cell via hENT1 transporter proteins but through passive diffusion. In addition, it was found that the prodrug was not rapidly removed from the cell by efflux pumps and wasn't reliant on activation through kinase mediated phosphorylation. (79) Gem has also been conjugated to fatty acids at the N-position with an amide bond. In addition to overcoming various resistance mechanisms, the addition of a lipophilic moiety to Gem also affords the opportunity to formulate the prodrug into a micro/nano-particulate formulation. Wang et al successfully synthesised an N-stearoyl derivative of Gem and formulated it into DSPE-PEG micelles. In BxPC-3 cells the deamination rate of Gem was significantly reduced. Furthermore, Gem-loaded micelles showed a significantly improved circulation time and subsequently a 3-fold improvement in intertumoral uptake when compared to free Gem in BxPC-3 ectopic xenografts. (80)

1.2.6.1.3. Paclitaxel

Paclitaxel (PTX) is a cytotoxic anticancer drug of the taxane class of compounds. It was first isolated from the bark of the pacific yew tree following reports from a British official in the Indian subcontinent that parts of the European yew, Taxus baccata, were being used in a clarified butter preparation for the treatment of cancer. (81) This resulted in a national cancer institute (NCI) lead expedition which resulted in the isolation of "taxol" in 1964. Following extensive pre-clinical studies, PTX was later approved for clinical use by the FDA in 1992 and has since become one of the most profitable anticancer agents on the market. (82)
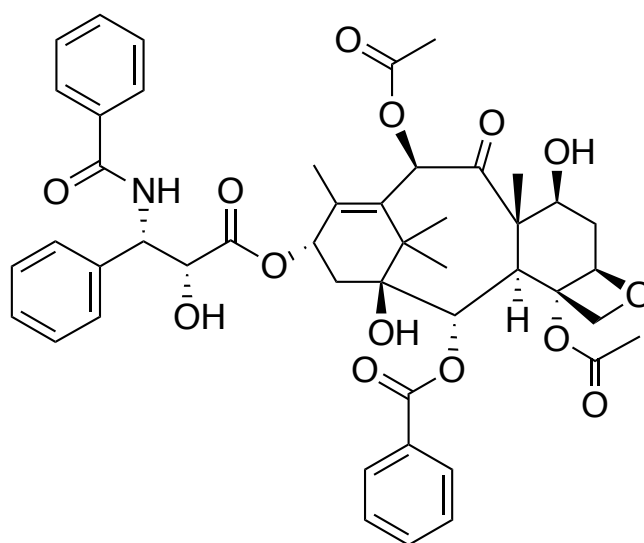
Figure 1.9. Chemical structure of paclitaxel (PTX).

The structure of PTX consists of a complex tetracyclic terpenoid with multiple functional sites essential to its activity including the C-13 side chain, C-2 benzoate functionality and the fused oxetane ring (Figure 1.9). (83–85) PTX induces cytotoxicity through the stabilization of tubulin polymers which prevents correct spindle formation and leads to inhibition of cell replication at the G2/M phase (cytostatic). (86)

Despite its potent activity in halting the growth of neoplastic cells, PTX suffers from extremely poor aqueous solubility (< 0.1 µg/mL) (87) which limits effective delivery of the drug. Attempts have been made to improve the solubility of PTX through the use of a formulation containing polyethoxylated castor oil and ethanol (Cremophor EL). (88) However, this formulation has been associated

with acute allergic reactions through activation of the immune protein - complement C3, followed by histamine release as well as severe anaphylaxis, hyperlipidemia, abnormal lipoprotein patterns, aggregation of erythrocytes, and prolonged, sometimes irreversible sensory neuropathy. (89–91)

As a result of Cremophor EL-induced toxicities, an effort was made to develop Cremophor EL-free delivery strategies. This culminated in the development of an albumin-bound PTX nanoparticulate formulation (nabPTX) which was developed by American BioScience and approved for human use in 2005 (Figure 1.10). (92)
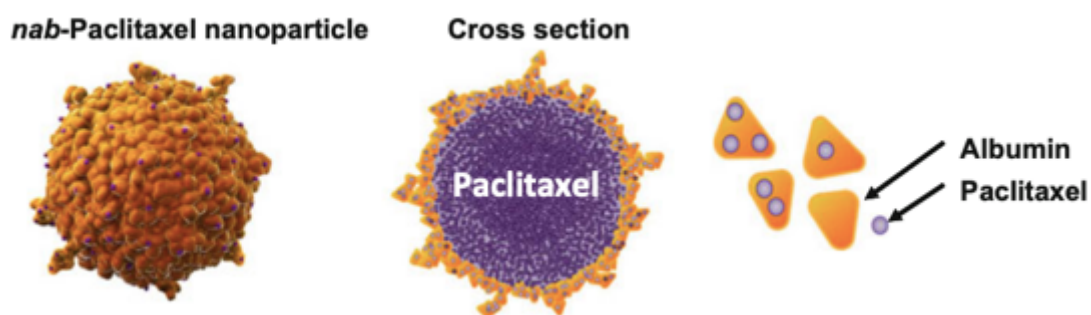
Figure 1.10. Schematic representation of albumin bound PTX nanoparticles. Taken from (93)

Following intravenous injection of nabPTX, the nanoparticles undergo dissolution and break down into smaller PTX-albumin complexes with a small fraction of unbound PTX. (94) Gardner et al demonstrated in a randomised crossover pharmacokinetic study (PK) that albumin-bound PTX accounted for ~94% of the drug following administration with the unbound fraction being ~6% which was significantly higher than the Cremophor EL control group (2.4%, $p < 0.001$). (95)

Following administration, it has been shown that nabPTX shows high accumulation within tumours. The enhanced permeation and retention effect (EPR) has been proposed as a possible mechanism for tumour accumulation. (94) The EPR effect is based on the premise that the vasculature within tumours displays a "leaky" architecture which allows particles of a certain size (< 200 nm) to escape the circulation through small pores in the vessel walls. (96) In addition, as the lymphatic drainage in these vessels is often damaged or compromised, the end result is a net accumulation of molecules (i.e. albumin) within the tumour

microenvironment. (97,98) However due to the heterogeneous blood supply, elevated interstitial fluid pressure (IFP), and large transport distances in the tumour interstitium, which hinder drug delivery in human subjects, the overall effect of the EPR effect in humans is thought to be limited. (93)

An alternative proposed mechanism for nabPTX tumour accumulation is the prevalence of secreted protein acidic and rich in cysteine (SPARC) proteins. These proteins have a high affinity for albumin and are observed in abundance within tumour interstitium. Despite the positive correlation between SPARC levels and disease progression (99,100), many studies have shown that there is also a positive correlation between SPARC levels and treatment efficacy of nabPTX. (101–103)

1.2.6.1.4. Combination chemotherapy with Gem + nabPTX

The use of combinations of chemotherapy drugs has gained traction in recent years as this permits the targeting of two separate biochemical pathways and reduces the likelihood of chemoresistance. The combination of Gem and nabPTX showed early promise as a combination therapy in preclinical murine models. Von Hof et al demonstrated that mice treated with nabPTX display a significantly depleted desmoplastic stroma when compared to mice treated with Gem alone. In addition, mice treated with nabPTX were also observed to have dilated vessels within the tumour milieu. Mice treated with the combination therapy showed a marked improved response (55%) when compared to Gem alone (24%) and nabPTX alone (36%) which was the authors attributed to a decrease in stromal content and improved tumour vascularisation. Furthermore, mice treated with the combination therapy showed a 2.8-fold increase in intertumoral Gem concentration compared with the Gem only group. (101) Subsequent preclinical results from Frese and co-workers described how mice treated with nabPTX in combination with Gem, not only increased the ratio of dFdC to dFdU, but also increased intratumoural levels of the active dFdCTP suggesting that PTX directly affects the metabolism of Gem. Additional work also revealed a decrease in CDA protein levels – the primary catabolic enzyme for Gem, in mice treated with the nabPTX. (104)

These encouraging preclinical findings were corroborated in human clinical studies. The MPACT phase 3 trial evaluated the efficacy of the combination in patients with metastatic pancreatic cancer and found a significant improvement in overall survival for patients treated with the combination (8.5 months) compared with Gem alone (6.7 months). (105) Results recently published from the LAPACT trial in patients with previously untreated locally advanced pancreatic cancer showed a progression free survival of 10.2 months. (106)

The current clinical evidence available on combination chemotherapy in pancreatic cancer has informed the choice of FOLFRINOX and Gem + nabPTX as first line treatments for the disease. (105,107) However, in spite of the improved efficacy in comparison to traditional monotherapy, combination therapy is typically accompanied by significantly enhanced side effects, such as neutropenia, febrile neutropenia, thrombocytopenia, diarrhoea, sensory neuropathy, alopecia and nausea which ultimately diminishes the quality of life for the patient, given the relatively small improvement in overall survival. (105,107)

1.3. Breast cancer

Breast cancer is the second most common form of cancer globally with almost 2.1 million new cases reported in 2018. (1) It is estimated that 627,000 women died from breast cancer in 2018 alone, representing 15% of all cancer deaths among women, making breast cancer the deadliest cancer in women. (1) Approximately 80% of invasive breast cancers arise from the ducts of the breast with the remaining cases evolving from the terminal duct-lobular apparatus, which has a 12-fold increased risk of developing into invasive breast cancer. (108)

1.3.1. Risk factors

Genetic and inherited risk factors make up only a small fraction of cases (5 - 10%). These include a family history of breast and ovarian cancer as well as inheritance of mutated gene such as BRCA1 and BRCA2. (1) The main drivers for breast cancer incidence are generally non-hereditary. Age has been highlighted as an

uncontrollable risk factor with incidences beginning to increase after 20 years of age. There has been an association made between breast cancer incidence and the age of menarche (inverse) and age of menopause (direct) with a 2012 study finding that breast cancer risk increased by a factor of 1.05 and 1.03 for every year younger at menarche and every year older at menopause, respectively. (109) Exogenous use of hormones has also been linked with increased incidence of the disease with a 24% increase risk with hormonal birth control and 40% increased risk for menopausal hormone therapy. (110)(111) Other risk factors include obesity, height (higher incidence in taller women) and smoking. (112)

1.3.2. Breast cancer disease classification

The World Health Organisation (WHO) has listed 21 distinct histological types of breast cancer based on morphology, growth and architecture patterns highlighting the heterogeneity of the disease. (113) The vast majority of cancers in the breast are adenocarcinomas which arise from epithelial tissues in the terminal duct lobular units and often spread throughout the extensive surrounding stroma. A large subgroup of this group is classified as "invasive carcinoma of no special type" or NST. The remaining so called "special" types can be further subcategorised into lobular, medullary, mucinous and tubular cancers among others. (113)
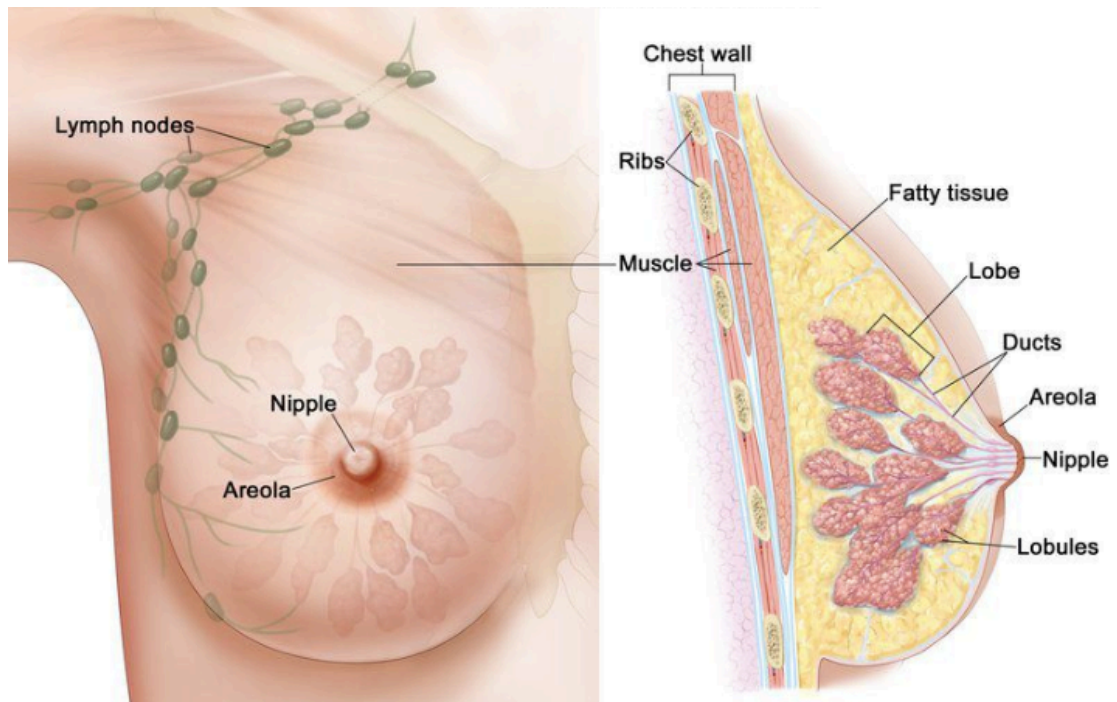
Figure 1.11. Diagram showing the anatomy of the breast and chest wall. Taken from (114)**.**

Due to the heterogeneity of the NST class of breast tumours, molecular classification is essential in discriminating between various subgroups. Breast cancers can be classified using immunohistological staining techniques for the presence of estrogen and progesterone receptors. The presence or absence of both of these receptors are defined as hormone receptor (HR) positive/negative respectively. (115) Approximately 70% of breast cancer patients have tumours cells which stain positive for estrogen receptor or progesterone receptor proteins and these patients respond well to endocrine therapies such as tamoxifen, letrozole, anastrozole, or exemestane. (116) Besides ER and PR status, the human epidermal growth factor receptor-2 (HER2) is also a promising molecular target. Part of the epidermal growth factor receptor family, HER2 is amplified or overexpressed in 20 - 30% of breast cancers and is associated with a poor prognosis. (117) This subset of tumours are often treated with the monoclonal antibody, trastuzumab (Herceptin). (117)

1.3.3. Treatments

The primary objectives for treatment of non-metastatic breast cancer is to remove the cancerous tissue from the breast and surrounding lymph nodes. This is often achieved firstly through surgical resection of the primary tumour or removal of the auxiliary lymph nodes followed by radiotherapy. (116) Systemic therapy may be in the form of neo-adjuvant therapy (before surgery) in an effort to reduce tumour burden prior to surgery to improve surgical margins, or adjuvant therapy which is aimed at removing any cancerous cells which were left behind following resection.

The benefit of neoadjuvant systemic chemotherapy has been demonstrated in multiple clinical studies (118–121), and has distinguished a clear correlation between complete pathological response / breast conservation and improved survival odds. (122,123) As outlined previously, patients with HR+ cancers will generally be given a regimen of endocrine therapy and patients with HER2+ cancers will be given Herceptin. However, for the subgroup of patients whose tumours are negative for both HR and HER2, so called triple negative breast cancer, chemotherapy alone is currently the only systemic therapy on offer. (116) In the neoadjuvant setting, triple negative breast cancers are often treated with a combination of an anthracycline drug such as doxorubicin in combination with a platinum-containing chemotherapy (see above for oxaliplatin). Systemic chemotherapy in the adjuvant setting usually involves anthracyclines in combination with other agents. These combinations include Fluorouracil, Doxorubicin and Cyclophosphamide (FAC) or Fluorouracil, Epirubicin and Cyclophosphamide (FEC). More recently, taxane based chemotherapeutics, such as PTX and the structurally similar docetaxel, have been used in combination with anthracyclines to reduce the chance of axillary metastases. A meta-analysis of 13 randomized clinical studies containing 22,903 patients concluded that the addition of a taxane to an anthracycline-based regimen improves the disease-free survival (DFS) and overall survival (OS) of high-risk early breast cancer patients. (124)

1.3.3.1. Doxorubicin

Doxorubicin (Dox) is an anticancer drug of the anthracycline class of compounds first extracted from *Streptomyces peucetius var. caesius* in the 1970's. (125)
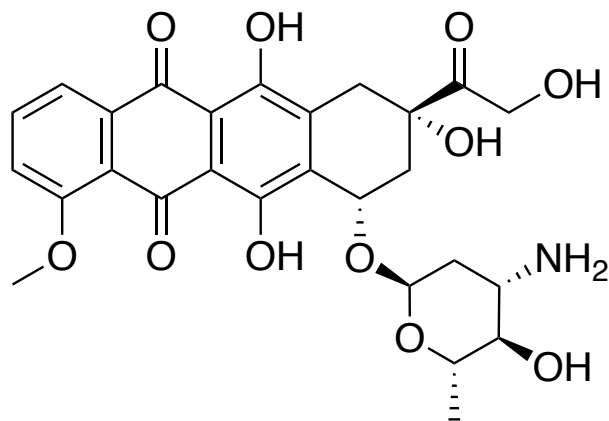
Figure 1.12. Chemical structure of doxorubicin (Dox).

Structurally, Dox consists of a tetracyclic quinoid aglycone adriamycinone (14-hydroxydaunomycinone) linked to the aminosugar daunosamine. (126) There are two primary mechanisms by which Dox kills cancer cells. Firstly, Dox is capable of intercalating base pairs within DNA molecules. It also binds to topoisomerase l and ll which are essential for DNA damage repair mechanisms. Following failure to repair DNA damage and growth inhibition in the G1 and G2 phases of the cell cycle, the apoptosis pathway is triggered. (127) Additionally, Dox can be intracellularly oxidised to Dox-semiquinone which upon reduction back to Dox, facilitates generation of reactive oxygen species (ROS) which can lead to lipid peroxidation (resulting in membrane damage), DNA damage, oxidative stress and apoptosis. (128)
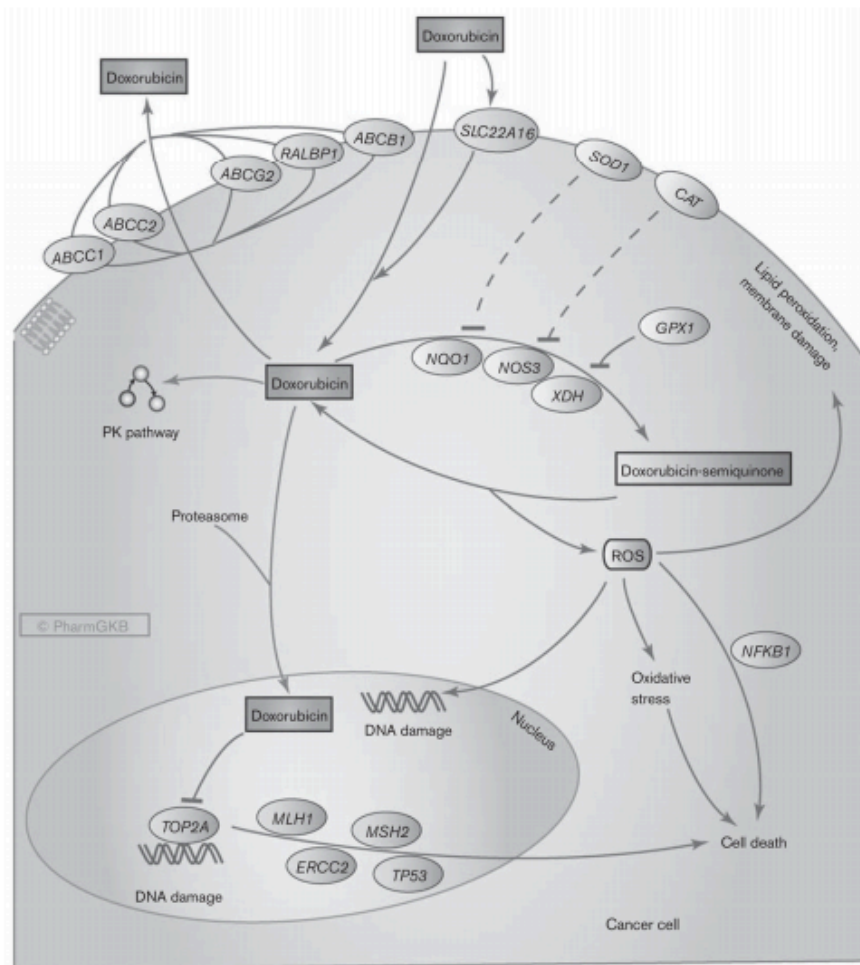
Figure 1.13. Illustration of the cellular pharmacodynamic mechanisms of Dox. Taken from (125).

Despite being highly efficient at killing cancer cells, Dox has been shown to be particularly cardiotoxic. (129) A 2013 meta-analysis of 18 studies containing 22,815 patients treated with anthracyclines found that 6% of patients displayed overt cardiotoxicity with 18% developing subclinical cardiotoxicity. (130) There is yet to be a consensus on the exact mechanism of Dox-induced damage to cardiomyocytes. However, it is thought to be as a result of modification/depletion of cardiolipin which induces the release of cytochrome C into the cytosol leading to apoptosis in addition to activating p38 MAPK. These events are triggered by the production of reactive oxygen species (ROS) produced during the metabolism of Dox. The enhanced effect to cardiac myocytes is likely due to their comparatively high concentration of mitochondria and subsequent reliance on oxygen-mediated phosphorylation as a means of

energy production in comparison to tumour cells which rely mainly on glycolysis for energy production even in aerobic conditions. (131,132)

1.3.4. Locally recurrent breast cancer

As mentioned in section 1.3.3., surgical resection in the form of a mastectomy is the first line treatment for patients with anatomically accessible breast tumours. Unfortunately, approximately 10 to 13% of patients who receive breast conservation therapy (BCT) develop locoregional recurrence (LRR) within 10 years of their initial treatment, and 3 to 8% of patients who receive a standard mastectomy in combination with adjuvant radiotherapy will also develop LRR, which in many cases is an indicator for distant metastatic disease. (133,134) A review by Wapnir and co-workers suggested 5-year survival probabilities ranging between 45% and 80% after LRR. (135) In addition, full-thickness chest wall resection is generally perceived as a high-risk and highly skilled operation causing significant disfiguration to the patient along with a poor prognosis. As a consequence, the application and utility of surgery is limited in this patient group. (136) There are few studies in the published literature which allude to the benefit of systemic chemotherapy for patients with LRR. A 2014 randomized controlled trial (COLOR) with 85 patients with LRR randomly assigned to receive chemotherapy and 77 assigned to receive no chemotherapy, showed that 28% of patients who received chemotherapy had disease-free survival events (defined as any recurrent disease, second primary tumour, or death from any cause) compared with 44% in patients receiving no chemotherapy at follow up (4.9 years). The study also found that 15% of patients receiving chemotherapy suffered from serious adverse events such as neutropenia, febrile neutropenia, intestinal infection, abdominal pain, respiratory and pulmonary infection among other. (137) This study clearly highlights the potential benefit in the use of systemic chemotherapy for the treatment of patients with LRR but also highlights an opportunity for the targeted delivery of chemotherapeutics to reduce systemic side effects.

1.4. Targeted cancer treatments

Systemic chemotherapy has been a mainstay in cancer treatment and prevention for more than 60 years. However, as has been discussed in previous sections, the utility of conventional chemotherapy is limited by the, often severe, side effects associated with systemic delivery of these agents. Often, large doses of these drugs are delivered, with only a very small fraction reaching the target tumour site. (138) As a result, substantial quantities of these agents are required to establish an adequate therapeutic response. There is therefore a growing need for a more targeted approach to the delivery of these drugs which will ultimately improve the efficacy of the treatments but also the quality of life for the patient.

1.4.1. Photodynamic therapy

Photodynamic therapy (PDT) is a targeted cancer treatment that been used predominantly for superficial neoplasms. PDT involves the irradiation of a light-sensitive drug (photosensitiser) in the target tissue with light of an appropriate wavelength, triggering the localised release of cytotoxic ROS in the target tissue. The use of PDT as a cancer therapy is particularly attractive due to its targeting ability with release of cytotoxic ROS controlled by the precise positioning of the light source. For this reason, PDT is an attractive alternative to traditional systemic chemotherapy.

PDT requires the combination of three distinct components: (i) sufficient concentration of a photosensitiser, (ii) presence of molecular oxygen (O_2), and (iii) light of appropriate wavelength. The photosensitiser alone has negligible toxicity. However, upon radiation with light at an appropriate wavelength, an electron in the photosensitiser is excited from its singlet ground state (^1PS) to the relatively short-lived first excited singlet–state ($^1PS^*$). The excited electron can then either return to the singlet ground state, emitting a photon of light in the process, known as fluorescence emission, or it can flip its spin state and engage in a process known as inter-system crossing (ISC), converting to the first excited triplet state ($^3PS^*$). The triplet state electron can either return to the ground state releasing a photon, known as phosphorescence or alternatively transfer the excited state energy to a neighbouring molecule such as O_2 resulting in the production ROS (Figure 1.11).
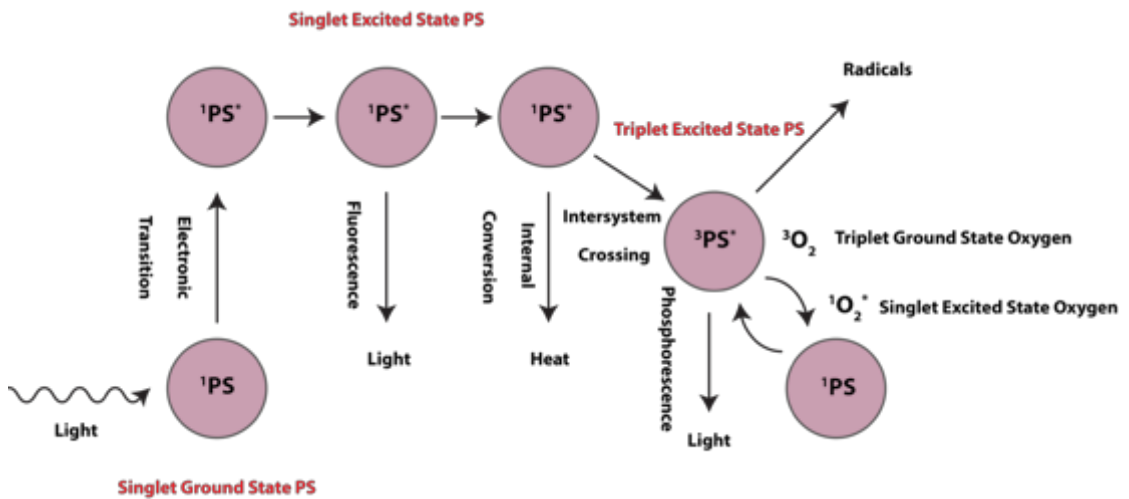
Figure 1.14. Diagram illustrating the electronic transitions underpinning photodynamic therapy.

Two types of photochemical reactions of electrons in the T_1 state have been postulated (Figure 1.14). The first involves redox reactions between the T_1 state of the sensitizer and a neighbouring substrate, such as another nearby sensitiser molecule, to yield free radicals. These radicals are capable of interacting with O_2 to produce superoxide (O_2^-) ions and the highly reactive hydroxyl ions (OH^-). (139) Due to its characteristic triplet ground state, molecular oxygen is able to interact with the excited triplet sate of the photosensitiser. This interaction yields singlet oxygen ($^1O_2$) which can induce severe oxidative damage to biological substrates and can eventually lead to cell death. While it is generally accepted that singlet oxygen resulting from type 2 reactions is the major cause of cell death in PDT, type 1 reactions are thought to predominate in hypoxic conditions. (140,141)

Type 1

$$^3PS^* + S \longrightarrow PS^- + S^+$$

$$PS^- + O_2 \longrightarrow PS + O_2^-$$

$$Light + {}^1PS \longrightarrow {}^3PS^* \longrightarrow {}^3PS^* + O_2^* \longrightarrow PS^+ + O_2^-$$

Type 2

$$^3PS^* + {}^3O_2 \longrightarrow {}^1PS + {}^1O_2$$

$$^1O_2 + S \longrightarrow S_{add}$$
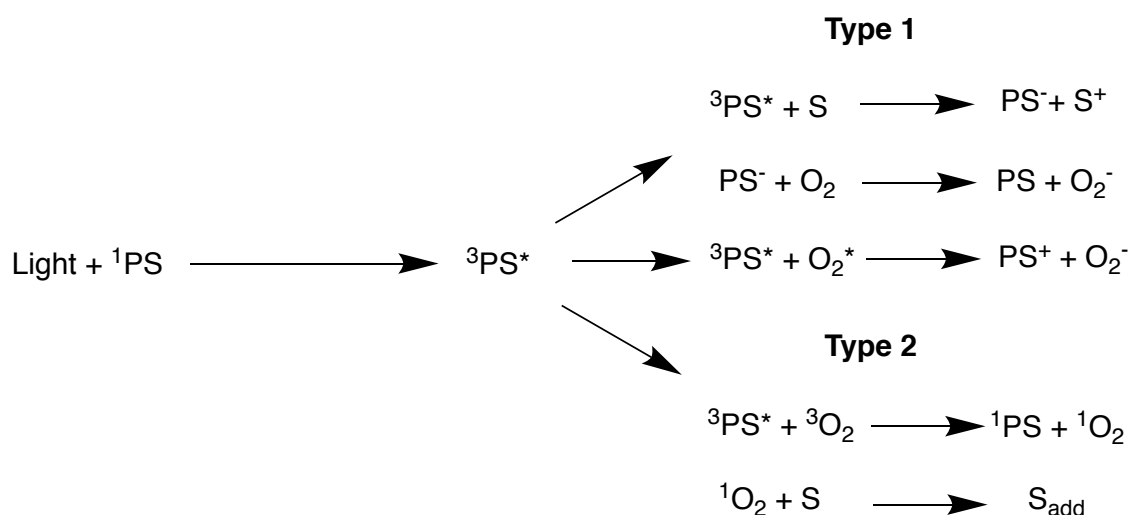
Figure 1.15. Type-I and Type-II photoreactions. Reproduced from (139).

It is generally understood that photoinduced cell death is primarily as a result of oxidative stress causing damage to proteins, fats and other biomolecules leading to either apoptosis, necrosis or autophagy - with damage to mitochondria resulting in apoptosis, significant damage to cellular membranes resulting in necrosis, and damage to lysosomes or endoplasmic reticulum resulting in autophagy. (142) In addition, treatment of tumours with PDT has been associated with a systemic immune response. This can manifest in the form of a strong inflammatory response with large numbers of monocytes or macrophages, neutrophils and dendritic cells infiltrating the treated site to attack damaged tumour cells. (143)

1.3.1.1. Photosensitisers

Photosensitisers are compounds which are capable of absorbing light at a specific wavelength range and converting that energy into cytotoxic ROS. An ideal photosensitiser should be capable of producing ROS in an efficient and controlled manner while reducing any potential side effects. An efficient photosensitiser should be capable of producing ROS in sufficiently high concentrations as a result of a high triplet state quantum yield. (144,145) To date several photosensitisers have been clinically approved for the treatment of various cancers and these have been summarised in Table 1.3.

Table 1.3. Overview of clinically approved photosensitisers. Adapted from (146)

Generation	Name	Excitation wavelength (nm)	Manufacturer	Indication
1	Photofrin®	630	Axcan Pharma, Canada	Esophageal cancer, Lung adenocarcinoma, Endobronchial cancer
2	Metvix®/Metvixia®	570–670	Galderma, UK	Basal cell carcinoma
2	Foscan®	652	Biolitec, Germany	Advanced Head and neck cancer
2	Laserphyrin®	664	Meiji Seika, Japan	Early centrally located lung cancer
2	Redaporfin®	749	Luzitin, Portugal	Biliary tract cancer

1.4.1.1.1. Rose Bengal

Rose Bengal (RB) is a synthetic halide derivative of fluorescein from the xanthene class of dyes and is currently clinically approved as a dye for ophthalmic defects. (147) Structurally, RB consists of a tetra-iodinated xanthene ring system bonded to a tetra-chlorinated benzoic acid moiety (Figure 1.16). RB is sold commercially as the disodium salt which dramatically improves its aqueous solubility.
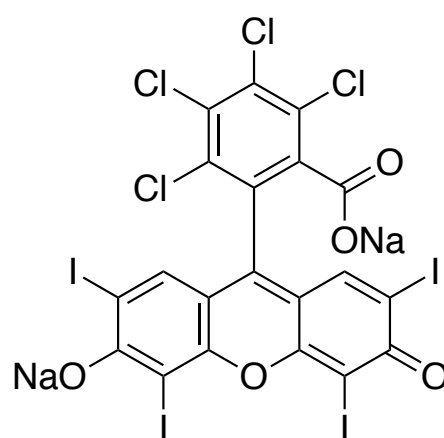
Figure 1.16. Chemical structure of rose bengal.

RB absorbs visible light efficiently at around 550 nm and has a resultant singlet oxygen quantum yield of 0.76 (MeOH) (148,149) The quantity of singlet oxygen generated by a photosensitizer is a function of the efficiency of a spin-forbidden electronic transition from a singlet to a triplet state (ISC). The introduction of "heavy atoms" into a molecule is known to have an influence over the rate of ISC. (150) The near 8-fold higher singlet oxygen quantum yield of RB in comparison to its parent compound fluorescein ($\phi_\Delta = 0.1$), is an example of such an effect and is the result of the iodine atoms present on the molecule. (148) In addition, RB has a relatively broad excitation band in the green region of visible region of the spectrum (480-550 nm) and possesses a high extinction co-efficient (εmax = 99,800 M^{-1} cm^{-1} at 532 nm). (151) RB has also been shown in in vivo models to undergo rapid clearance from the systemic circulation. Accordingly, RB is regarded as a highly efficient photosensitiser and has been used as model drug for various applications such as anti-microbial and anti-cancer therapies which will be discussed in more detail in later sections. (152,153)

1.4.1.2. Limitations of PDT

In spite of the excellent anti-cancer effects of PDT, the utility of this approach in oncology has so far been limited to superficial lesions such as cancers of the skin. This is as a result of three important shortcomings of PDT: (i) PDT induced cell damage is hindered by heterogeneous distribution of the photosensitiser within the tumour, (ii) even photons with a wavelength in the near infrared region of the spectrum can only penetrate through skin to a depth of less than 1 cm which means that during the treatment of deeper-seated tumours, invasive positioning of the light source is required to get maximum benefit from the treatment, (154) (iii) the efficacy of PDT is severely limited in the hypoxic cores of deeply seated tumours as there is less available oxygen present for the excited triplet state of the sensitiser to interact with.

1.4.2. Sonodynamic therapy

Sonodynamic therapy (SDT) is in principle very similar to PDT with the exception that light is replaced by low intensity ultrasound (US). SDT has been proposed to overcome the limitation of light penetration through human tissue. Much like PDT, SDT relies on three key components: (i) a sensitiser (sonosensitiser), (ii) molecular oxygen (O_2) and (iii) a source of US (Figure 1.17).
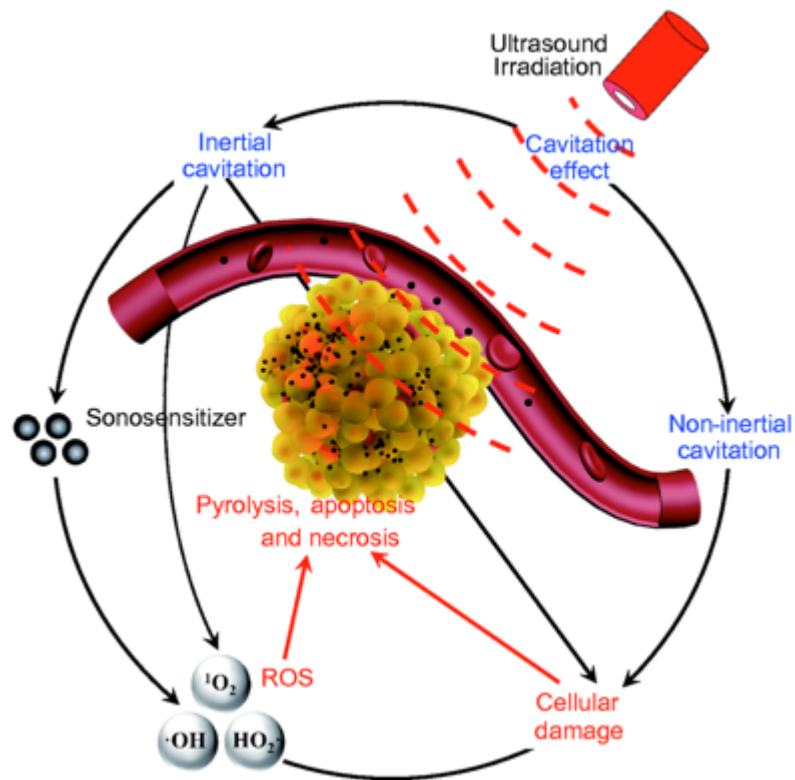
Figure 1.17. Schematic of sonodynamic therapy in a stylized cancer cell. Taken from (155)

The main advantage of SDT over PDT is increased tissue penetration depth as effective doses of ultrasound can be delivered tens of centimetres through soft tissue and bone. US is a safe, clinically approved imaging modality which has been used for many years in the detection of tumours, blood flow analysis, and obstetrics. (156–158)

1.4.2.1. Physical principles of US

Sound is a wave which propagates through a medium transferring its mechanical energy. The sound wave is made up of high (compression) and low (rarefaction) pressure regions (Figure 1.18). Ultrasound is the term applied to sound waves with frequencies greater than 20 kHz and is undetectable by the human ear. Instruments used for diagnostic US employ frequencies in the range of 5 – 10 MHz. (159) US attenuation is the reduction in energy of the US wave as it propagates through tissue. This loss in energy is amplified as the frequency of the wave increases. In tissue, attenuation increases almost linearly with frequency (Table 1.4).
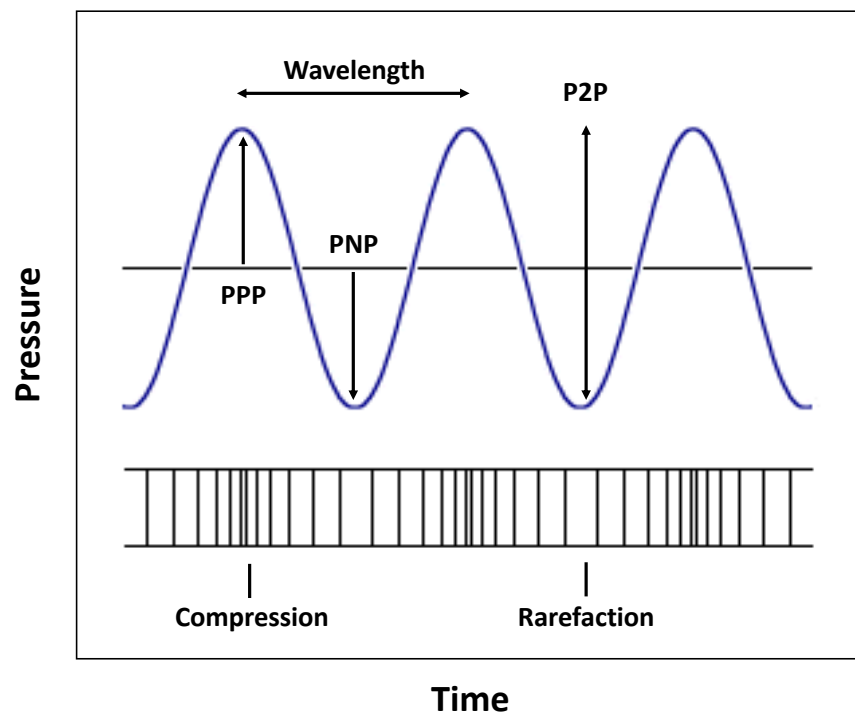
Figure 1.18. Illustration of a longitudinal sound wave (top) and a transverse sound wave (bottom). (PPP - peak positive pressure, PNP - peak negative pressure, P2P - peak to peak pressure).

US frequencies typically adopted for use in SDT range from between 0.4 and 3 MHz which makes it ideally suited for treating deeply seated tumours due to the inverse relationship between US frequency and attenuation in tissue. (160)

Table 1.4. Attenuation coefficients of various tissues. Adapted from (159)**.**

Tissue	Attenuation (dB/MHz-cm)	Reference
Aqueous humor (human)	0.10	(161)
Blood (human, heparinized)	0.22	(162)
Bone (human, femur)	25.6	(162)
Breast (human)	0.28–0.63	(162)
Breast (human)	1.7	(163)
Choroidal melanoma (human)	0.90	(162)
Fat (human, subcutaneous, ex vivo)	0.64	(162)
Liver (human, ex vivo)	0.64	(162)
Ocular lens (human)	2.0	(161)
Uterus (human)	0.22–0.44	(162)
Vitreous humor (human)	0.10	(161)

US power density or intensity is a measure of the power applied to a defined area (W/cm^2). The loss of energy of the US wave though attenuation is converted to heat energy which increases the temperature of the treated tissue (Table 1.4). This effect has been used as an advantage by clinicians involved with high intensity focused ultrasound (HIFU), where thermal ablation is used to selectively increase the temperature of tumour tissue ($56 – 100^oC$) resulting in rapid cell necrosis within the focal region. (164,165) Using the US parameters typically adapted for diagnostic applications, thermal effects are an undesirable side effect. The extent of temperature increases within the focal volume can be tempered through the use of pulsed wave US (PW) as opposed to continuous wave (CW) (Figure 1.16). The PW application of US is characterised by the term - duty cycle, which is defined as the pulse duration over a given pulse repetition period. (158)

a)

b)
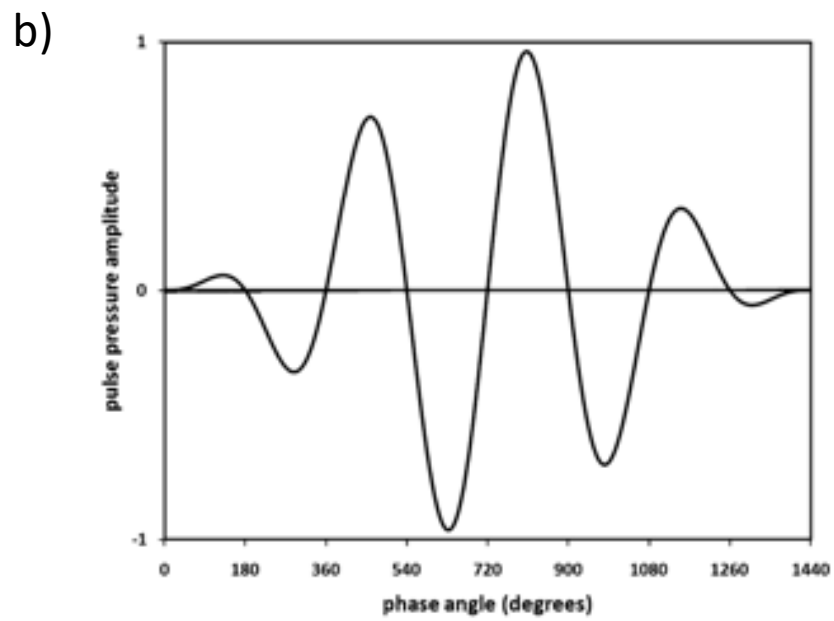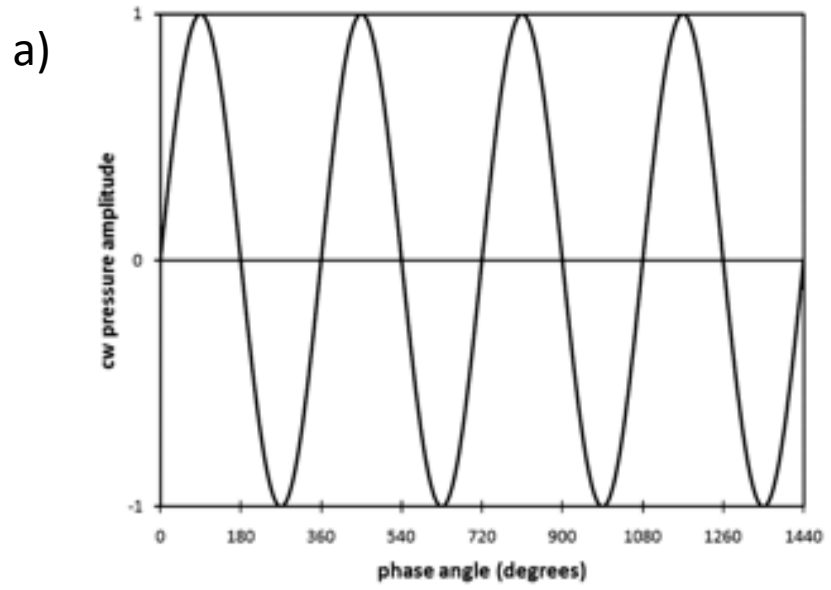
Figure 1.19. Diagram of a) a continuous wave (CW) and b) a pulsed wave (PW). Adapted from (159)**.**

1.4.2.2. Proposed mechanisms of SDT

While the underlying mechanisms of PDT are extremely well understood, no consensus currently exists regarding the precise mechanism for SDT. As mentioned previously, SDT relies on activation by a sound wave propagating through tissue. Under the correct parameters, this process can lead to the formation of nucleation sites whereby dissolved gasses in tissue come out of solution forming small gas filled bubbles. These bubbles can oscillate in an US wave, and under the correct conditions, can collapse. (166) As a result of the rapid compression of the bubble during this collapsing event, extremely high temperatures and pressures can be generated. This event is known as inertial cavitation and is widely regarded to be the source of US-induced activation of sonosensitisers through two primary mechanisms: (i) pyrolysis and (ii) sonoluminescence. (167–169)

1.4.2.2.1. Pyrolysis

Following the collapse of a cavitating bubble, a significant increase in localised temperature and pressure may occur which can reach up to 10,000 K and 81 MPa. As the heat generated by the collapsing bubble is highly focussed and cannot be efficiently dispersed through thermal diffusion, this leads to localised hot spots. Assuming that these localised areas of high temperature are in close proximity to a sensitiser molecule, this can lead to the break-down of the sensitiser into radicals which can induce a cytotoxic effect in cells. (167) It has also been proposed that through the direct pyrolysis of water vapour, the short-lived H and OH radicals may interact with the sensitiser to produce longer lived radicals. (170) It should be noted that investigations into pyrolysis as a potential mechanism for US-induced cytotoxicity, adopted US frequencies far below that used for SDT (1-3 MHz). There is therefore little evidence to support this theory in the context of the US frequencies used in SDT.

1.4.2.2.2. Sonoluminescence

Sonoluminescence is a theory first reported in 1933 by Marinesco and Trillat is the generation of light following US irradiation of a solution. (171) Like before, this is as a result of the extreme localised temperatures and pressure produced

as a result of inertial cavitation. While there has been no consensus on the precise mechanism of this light production, it is thought to result from black-body radiation, bremsstrahlung radiation or a combination thereof. (172) However, the precise mechanism is believed to be of thermal origin resulting from the compression phase of bubble collapse. (173) Studies conducted by Umemura et al found that light could be generated from air saturated saline solutions insonated with US at frequencies relevant to SDT (1.93 MHz) in the wavelength range of 250 – 650 nm with a peak intensity at 400 – 450 nm. Under these conditions the investigators found that the sensitiser, hematoporphyrin, was capable of absorbing the emissions produced in this spectral region. Provided that the sonosensitiser is in close proximity to the cavitating bubble, these finding provide an explanation for the generation of singlet oxygen as the light generated from sonoluminescence could activate the sensitiser via the same mechanisms described above for PDT. (160,168) A 2019 study by Beguin et al provided further support towards the theory of sonoluminescence. Using sophisticated photo-acoustic instrumentation, they demonstrated for the first time that upon insonation of RB in the presence of gas filled microbubbles, significant quantities of photons could be generated. Indeed, the light produced was in the wavelength range required to activate RB. (174)

1.4.2.3. Sonodynamic therapy for the treatment of cancer

The first application of SDT to treat cancer was studied by Yumita and Umemura. In these studies, the sensitiser hematoporphyrin was used to treat the rat hepatoma cell line - AH-130, and the mouse sarcoma - sarcoma 180, derived from the ascites fluid of rats and mice respectively. The cells were suspended in air saturated aqueous medium and insonated at a frequency of 1.92 MHz. In all cases, cells treated with the sensitiser alone showed no signs of cell damage. However, when insonated with US, significant cell lysis was observed. Interestingly, cells treated with US alone also showed signs of cell damage which may have been a result of cavitation effects within the air saturated medium. (175,176) Later, in vivo studies conducted by the same group in an ectopic colon adenocarcinoma murine model treated with an intravenous injection the gallium-porphyrin complex (ATX-70) followed by US treatment (2 MHz, 3 W/cm²) showed a 50% decrease in tumour volume after 3 days. (177) A later study by Yumita and co-

workers investigated the use of ATX-70 to treat breast tumours. Mammary tumours were induced following gavage of the potent carcinogen 7,12-dimethylanthracene (DMBA). Rats were then treated with ATX-70 at 2.5 mg/Kg and US at 3 W/cm². The results showed a marked synergistic effect between ATX-70 and US treatment with significant reductions in tumour volumes and no regrowth occurring following treatment. (177)

The studies discussed thus far utilised US intensities between 1 and 3 W/cm². Studies have also been undertaken using much higher US intensities. For example, Ohmura and co-workers found that treatment of rat intracranial glioma using 5-aminolevulinic acid (5-ALA) and US at 10 W/cm² showed significant reduction in tumour volume with no damage to surrounding brain tissue. However significant necrotic lesions were observed upon increasing the intensity above 20 W/cm². (178) In addition to the studies discussed in this section, the utility of SDT for anticancer application has been extensively studied in numerous in vitro and in vivo models and has been the subject of multiple comprehensive reviews. (160,179,180)

1.4.2.4. Limitations of sonodynamic therapy

As has been discussed throughout this section, the main advantage of SDT over PDT is the enhanced tissue penetration capabilities enabling the activation of the sensitiser in deep seated tumours like those of the breast or the pancreas. However, despite this, SDT also suffers from some of the same shortcomings as PDT. The first shortcoming is the inherent hypoxic nature of many solid tumours. While the average oxygen partial pressure in normal tissue is approximately 30–50 mmHg (181) this drops to approximately 28 mmHg for breast tumours (182) and further to approximately 2 mmHg for PDAC. (183,184) This severely limits the effectiveness of SDT for the treatment of solid tumours, as the primary mechanisms of action of SDT involves the production of ROS, which is significantly diminished in hypoxic environments. Much like PDT, SDT requires the systemic administration of a photosensitiser into the body. Therefore, the same common side effects associated with PDT will also be true for SDT. These side effects can be surprisingly unpleasant given the targeted nature of the treatment and include hypersensitivity to light. For example, a phase 1 study

investigating the effect of endoscopic US guided PDT for locally advanced pancreatic cancer noted adverse events including sun burn to the hands and skin hyperpigmentation. (185) Granted, these adverse events are significantly less severe than those associated with traditional systemic chemotherapy. However, through targeting the delivery of the sonosensitiser to the tumour site, administration of a lower dose may be possible, which would mitigate any adverse off-target side effects.

1.4.3. Ultrasound for targeted drug delivery in cancer treatment

US mediated drug delivery relies on the presence of a biocompatible drug carrier which responds to an US stimulus causing the active release of the payload at the target site. (186) The extent to which the drug carrier releases the drug is dependent upon two variables: (i) the type of US used and (ii) the responsiveness of the drug carrier. Depending on the type of US used for this application, the drug release from the carrier can be through either a thermal or mechanical process. The absorbance of US into tumour tissue can result in localised hyperthermia which can be used for thermal ablation surgery (187,188) or to trigger the release of drugs from thermally responsive liposomes. (189) Thermally responsive liposomes have been the subject of recent clinical attention following the development of ThermoDox – a liposomal formulation of Dox which has been shown to release $80 – 100\%$ of its drug load within 20-40 seconds upon mild US induced hyperthermia ($41.3^{\circ}C$). (190) In addition to thermal mechanisms, enhancement of drug delivery through a mechanical mechanism has also been explored. Wang et al demonstrated that intratumoral delivery of the anticancer immunoglobulin drug trastuzumab could be enhanced through application of US (1 MHz, 8.95 MPa) prior to administration of the drug. (191) However drug delivery can also be mediated using much lower pressures (i.e. 1-2 MPa) than those adopted in this study. This can be achieved through the use of cavitation nuclei which result from dissolved gases being removed from tissue or from the administration of US responsive gas filled particles. (192)

1.4.3.1. Microbubbles

Microbubbles (MBs) are gas-filled microparticles with a stabilised coating which can be made of a variety of materials such as phospholipids (193), polymers (194) or proteins (195). MBs currently have regulatory approval as diagnostic contrast agents (Table 1.5). As there is minimal difference in the acoustic impedance of the blood relative to other soft tissue, it is difficult to visualise critical vasculature including valves of the heart using traditional US techniques. Upon insonation, the high compressibility of the MBs gas core allows them to contract in the positive pressure phase and expand in the negative pressure phase of the US wave. (196,197) The non-linear oscillations of MBs exposed to low acoustic pressures, facilitates the production of acoustic radiation over a wide frequency range which can easily be detected by diagnostic hydrophones allowing the sonographer to distinguish between critical vasculature and the surrounding tissue. (198)

Table 1.5. Overview of clinically approved microbubble contrast agents. Adapted from (199).

Name	Shell type	Core gas	Diameter (μm)	Concentration (MBs/mL)
SonoVue®	Phospholipid	SF_6	1.5 -2.5	$1.5\text{-}5.6 \times 10^8$
	DSPC: 0.038 mg/mL DPPG: 0.038 mg/mL DPPA: 0.008 mg/mL			
Definity®	Phospholipid	C_3F_8	$1.1 - 3.3$	1.2×10^{10}
	DPPC: 0.401 mg/mL DPPA: 0.045 mg/mL DPPE-mPEG5000: 0.304 mg/mL			
Optison®	Protein	C_3F_8	$3.0 - 4.5$	$5.0\text{-}8.0 \times 10^8$
	Human serum albumin			

Despite the wide variety of MB shell materials available (Figure 1.20), phospholipids remain the most popular. Phospholipid shells offer several advantages over protein or polymer shelled MBs. Given the amphiphilic nature of phospholipids, they self-assemble into highly ordered monolayers with the hydrophilic head group pointing out towards the aqueous medium and the

hydrophobic acyl chains pointing in towards the carrier gas. The inherent curved surface of MBs induces a Laplace overpressure across the gas–liquid interface. In the case of uncoated MBs, this can lead to destabilisation of the MB through Ostwald ripening. (197) Phospholipids with saturated acyl chains are capable of forming tightly packed monolayers which decreases surface tension, stabilising the MBs against dissolution. As a result of their stability, phospholipid MBs are amenable to a wide variety of fabrication techniques including sonication, high-shear emulsification, membrane emulsification, ink-jet printing, coaxial electrohydrodynamic atomisation and microfluidics. (193)
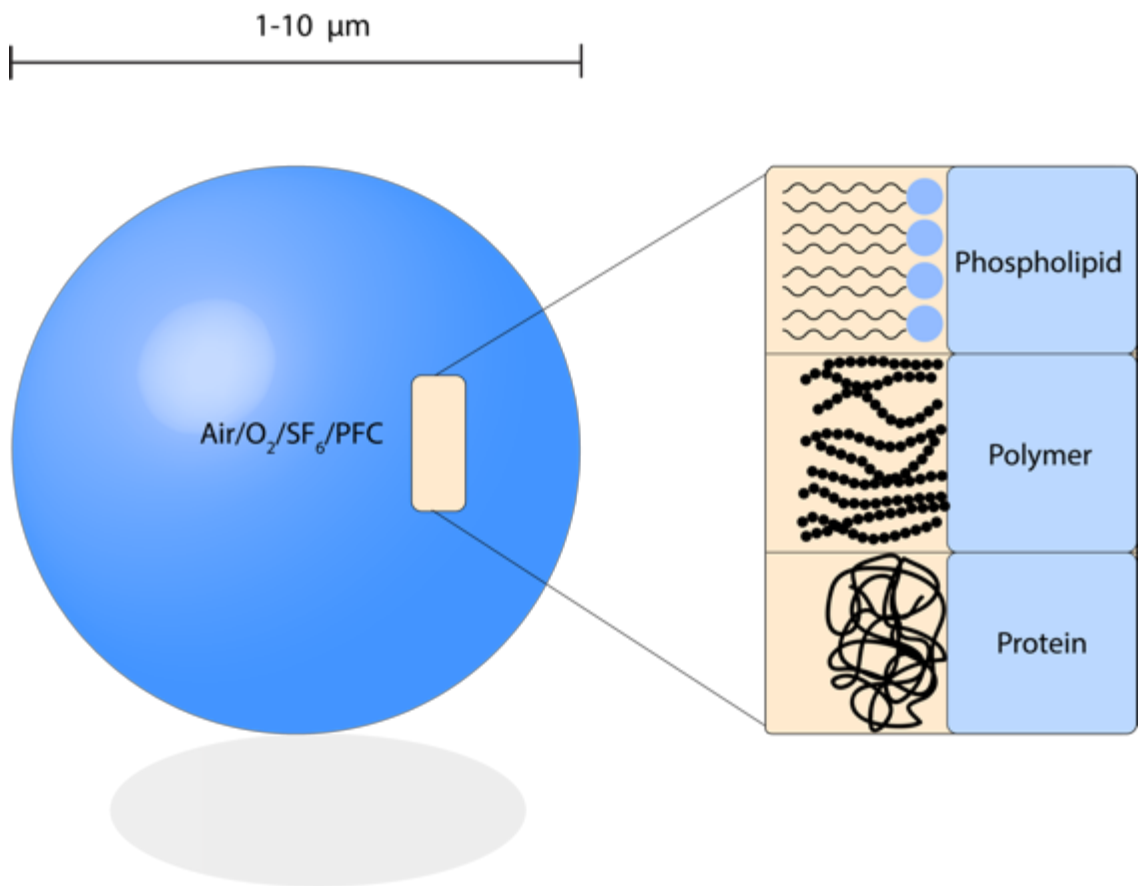
Figure 1.20. Illustration showing the structure of a typical MB with different shell compositions including, but not limited to, phospholipids, polymers and proteins. Adapted from (200)**.**

By far the most common method for MB fabrication is sonication which involves the rapid dispersion of gas within a medium containing the phospholipids using high frequency US. (193) The mechanism of MB formation using sonication is believed to proceed via two steps. The first involves the entrapment of gas within the aqueous medium. The phospholipids then subsequently self-assemble so to coat the gas bubble. The second step involves the break-up of the coated bubble into smaller bubbles as shown in Figure 1.21.
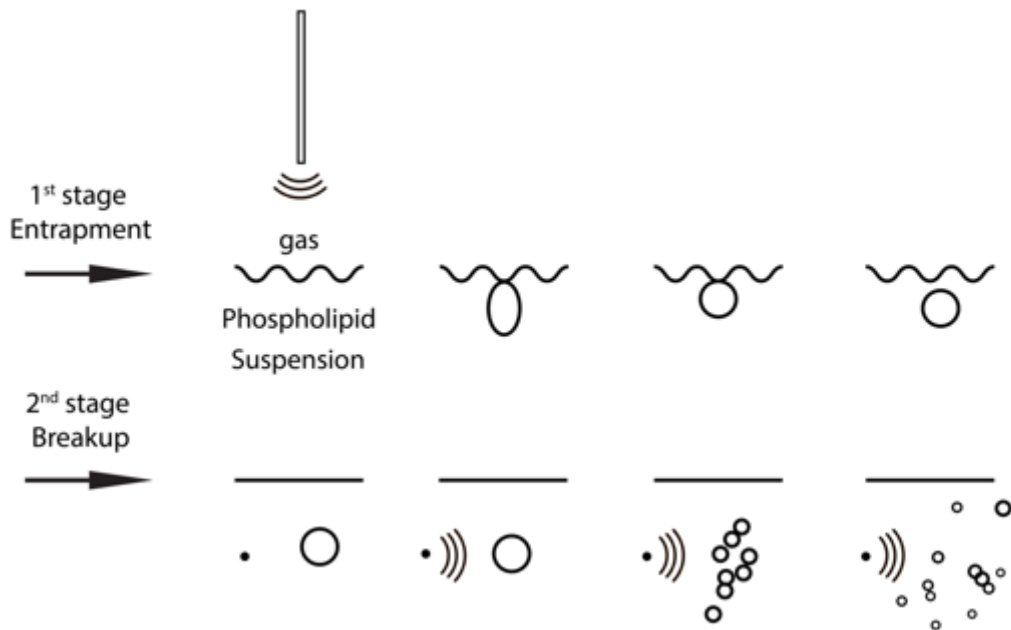
Figure 1.21. Diagram illustrating the proposed mechanism of microbubble formation using sonication. The first step in the mechanism involves the entrapment of gas within the aqueous medium to form large bubbles. This is followed by subsequent breaking up of these large bubble into smaller bubbles. Adapted from (201)**.**

1.4.3.1.1. Interaction of MBs with US

When exposed to an US wave, the compressibility of MBs allow them to compress in the high-pressure region of the wave and expand in the rarefaction region of the wave. (202) When insonated with relatively low acoustic pressures (<50 kPa), MB oscillations are described as being symmetrical or linear. When oscillating linearly, MBs are compressed in the in the rarefaction portion of the wave and expand in the positive portion of the wave, both to the same degree. When acoustic pressures are further increased (50-200 kPa), MBs become more resistant to compression than to expansion which leads to non-linear

oscillations.(203) The signals produced from these oscillations contain frequencies corresponding to the insonation frequency (fundamental) as well as other harmonic frequencies. When the acoustic pressure is further increased (>200 kPa), destruction of MBs can occur which typically results in broadband emissions. (203) These various MB emissions can be observed experimentally using passive cavitation detection (PCD).

1.4.3.1.2. Factors affecting MB stability and dissolution

MB stability is a critical consideration for formulation design. For a bubble in solution there exists a pressure differential between the inside and the outside of the curved bubble surface that forms at the gas-liquid interface. This pressure, known as the Laplace pressure, is determined using the Young–Laplace equation, expressed as $\Delta P = 2\sigma/R$, where σ is the surface tension and R is the radius of the bubble. (199) This can then be used along with Epstein and Plesset's model, to determine the dissolution rate for an uncoated MB. (204) Despite the dependence of this model on the assumptions of constant hydrostatic pressure and temperature on an uncoated bubble, the model demonstrates how the core gas properties of a MB are critical in the determination of MB stability. The Epstein-Plesset model predicts that an uncoated bubble will rapidly dissolve in unsaturated media. Measure can and have been taken to improve the stability of MBs against dissolution. These include the use of hydrophobic core gases such as perfluorocarbons which have aqueous solubilities which are orders of magnitude lower than air. The MB coating is also an important factor with an increase in shell packing or thickness decreasing the gas diffusion rate which strengthens MBs against the Laplace pressure. (204)

1.4.3.1.1. MBs as drug delivery vehicles

The use of MBs as drug carriers provides the unique opportunity to simultaneously deliver both drug molecules and gas to the target site. The first report of drug loaded MBs was published in 1998 by Unger et al who described the preparation of acoustically active lipospheres (AALs) loaded with PTX. In this instance the drug was dispersed in soybean oil. This mixture was then added to a vial containing an aqueous suspension of phospholipids with a headspace of perflourobutane gas (PFB). The vial was mechanically agitated in a Vialmix® device to produce gas filled microparticles with an average size of 2.9 μm.

Despite the excellent drug loading capabilities of the AALs reported in this study (15 mg/mL), the thick oil layer provided rigid stability to the MBs meaning that high mechanical indices were required to initiate drug release. (205) PTX, among other hydrophobic drugs, has also been successfully loaded into MBs without the use of a thick oil layer. Xing et al reported the preparation of PTX loaded MB with PTX hydrophobically incorporated into the acyl chain layer of the MB shell. In a murine model of ovarian cancer these MBs proved to be effective, with mice treated with PTX-MB showing significantly greater tumour growth inhibition than mice treated with free PTX at the same dose. (206)

Other studies have investigated the use of MBs with a net positive surface charge for gene delivery through the addition of cationic lipids into the MB shell. (207,208) Wang et al compared the loading capabilities of cationic versus neutral shelled MBs for gene delivery. Cationic MBs were prepared using 1,2-stearoyl-3-trimethylammonium-propane (DSTAP) as a component of the lipid shell to create a positively charged surface with a zeta potential of +15.8 mV compared to – 0.3 mV for the neutrally charged MBs. Results revealed a loading of 14.9 μg/5x10^8 MBs for cationic MBs compared to 0.27 μg/5x10^8 MBs for neutral MBs which subsequently resulted in a 2.4–3.2-fold higher mean drug delivery in vivo. (207) The utility of charged surface MBs has remained limited to the delivery of large biological molecules such as DNA or charge proteins.

An alternative drug loading strategy for small molecule drug delivery is to load drugs to the surface of the MBs using covalent or non-covalent conjugation strategies. Nomikou et al reported the covalent attachment of RB to the surface of a phospholipid MB (RB-MB) using carbodiimide chemistry. In this study they reported an improved cytotoxicity profile for RB-MB conjugate

compared to RB alone which the authors attributed to cavitation induced energy transfer to the sensitiser. (209) Alternatively, drugs have been successfully attached the surface of MBs using a non-covalent avidin-biotin bridge, through the use of a biotin-functionalised phospholipid. The high biotin affinity of avidin/streptavidin enables rapid and facile binding to the terminal end of the phospholipid. Using this strategy biotinylated ligands can be loaded onto the surface of avidin-functionalised MBs. This strategy has also been used to load biotinylated liposomes onto the surface of biotin functionalised MBs. (210) Given the high drug loading capacity of liposomes and that one mole of MB-bound avidin is capable of binding to three additional moles of biotinylated payload means that large quantities of drug can be loaded onto MB using this strategy. Furthermore, liposomes are capable of encapsulating a variety of hydrophobic, hydrophilic and amphiphilic drugs. This strategy has proved effective in small preclinical investigations. However, the complexity of the manufacturing process has provided the greatest challenge towards clinical translation. (211–213)
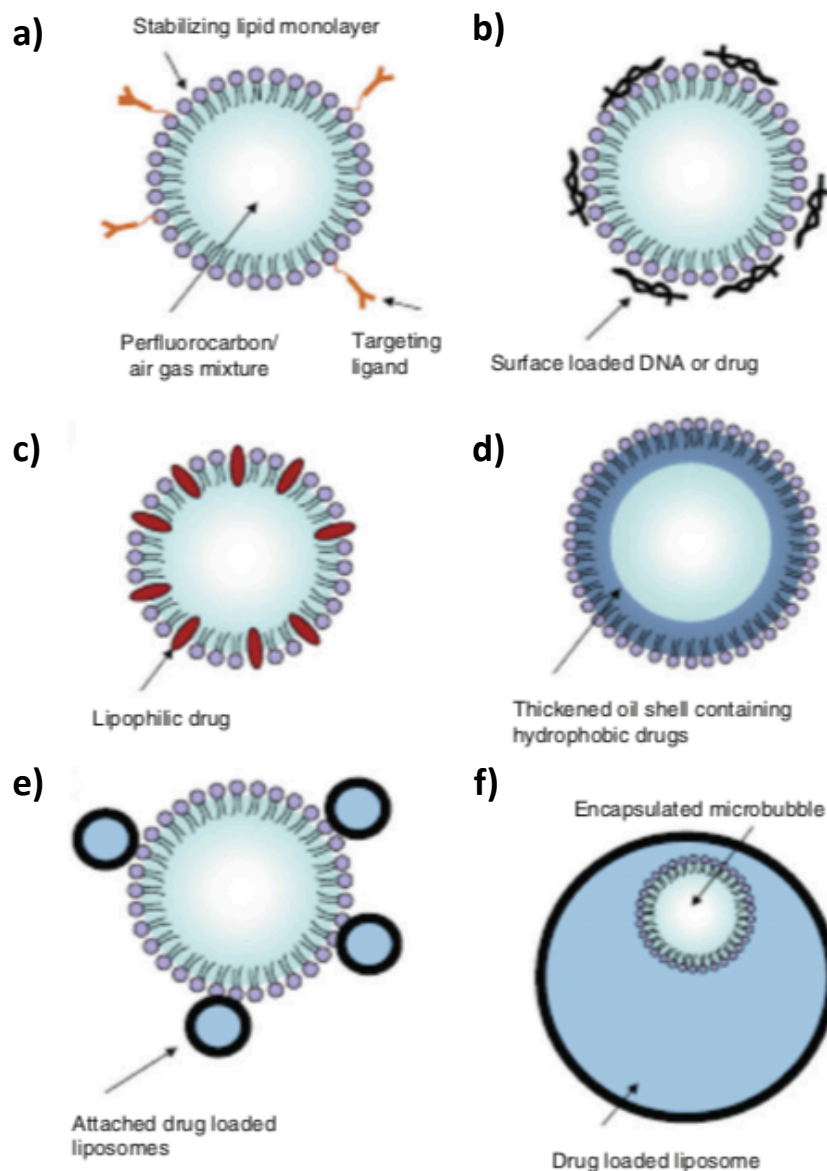
Figure 1.22. Diagram showing different drug loading strategies for MBs. a) drugs can be covalently/non-covalently bound to the surface of the MB using a linker (e.g. avidin-biotin) (214) **b) charged molecules (e.g. DNA) can be bound to the surface of charged MBs through electrostatic attraction** (207) **c) highly lipophilic molecules (e.g. PTX) can be loaded within the acyl chains of the phospholipid monolayer through hydrophobic interactions** (215) **d) lipophilic molecules can be dissolved/dispersed in an oil (e.g. corn oil, soy bean oil) surrounding a gas core and coated with phospholipids (e.g. AALs)** (205) **e) Nanoparticles (e.g. liposomes) can be bound to the surface of MBs using covalent/non-covalent binding (e.g. avidin-biotin)** (216) **f) MBs can be nested within nanoparticles (e.g. liposomes), along with a drug. Upon insonation, the MB can rupture the outer liposome, releasing the drug** (217). **Taken from** (210).

1.4.3.1.2. Sonoporation enhanced drug delivery

Currently, the clinical use of MBs for drug delivery has been limited to the co-administration of an already approved US contrast agent alongside a systemic dose of an approved chemotherapy agent. (218) The primary objective of these clinical studies is to improve the uptake of these drugs into tumours through a process known as sonoporation. As described earlier, during the rarefaction and compression cycles generated by an US field, MBs repeatedly expand and contract due to the change in acoustic pressure. Under a low acoustic pressure US beam, MBs oscillate with a relatively low amplitude about their equilibrium volume at the frequency of the US exposure in a process known as stable cavitation. When a MB is in close proximity to a cell, the expansion and contraction cycles can induce small openings in the cell membrane. (219) Additionally, MBs adjacent to a solid structure such as a cell are capable of generating high velocity fluid flow known as microstreaming. (220) The shear stresses, resulting from microstreaming, being exerted on the cells can be sufficient in some cases to cause sonoporation. A theoretical analysis by Wu et al found that when Optison MBs (3 μm) were insonated at 2 MHz and 0.4 MPa with an acoustic pressure of 0.4 MPa, the shear stress generated was calculated to be 1.1 kPa. (221)

Above a defined pressure threshold, MBs undergo rapid expansion and subsequent collapse, known as inertial cavitation. As a result of this violent collapse, extremely high localised temperatures and pressures are generated which are often accompanied by shock waves and high-speed fluid microjets. The resultant shock waves and high-speed microjetting can cause pitting of cell membranes, facilitating the uptake of drugs. (222) Indeed MB inertial cavitation has also been shown to rupture to capillary walls thereby reducing the high interstitial fluid pressure which is a characteristic drug delivery barrier within tumours, thereby allowing drugs or resultant particles to extravasate into the surrounding tissue. (223,224)
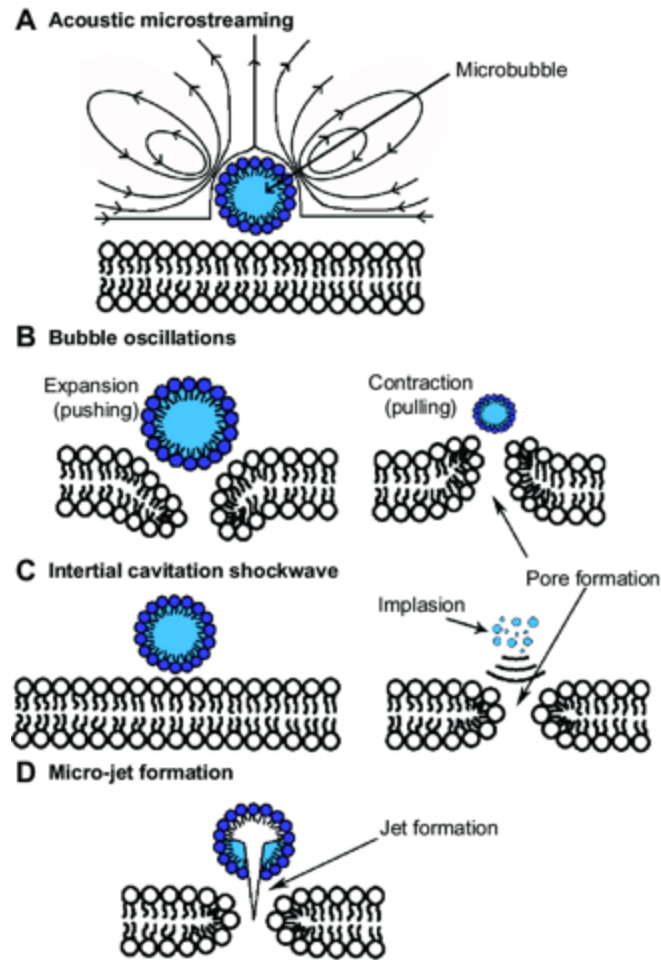
Figure 1.23. Mechanisms of microbubble mediated sonoporation including acoustic microstreaming, oscillatory pulling and pushing, shockwave and micro-jet induced pore formation. Taken from (225).

Kotopoulis and co-workers have exploited the biophysical effects of MB cavitation to aid in the delivery of chemotherapy to pancreatic tumours. Initial pre-clinical findings in orthotopic MIA-PaCa-2 xenografts treated with SonoVue MBs, co-administered with Gem (125 mg/kg) and insonated with US (1 MHz, 0.688 W/cm², PNP - 0.20 MPa) showed significantly lower primary tumour volumes when compared to mice treated with Gem alone. (226) These promising pre-clinical results inspired a recent phase 1 clinical trial in PDAC patients, combining SonoVue MBs and Gem, using a clinical diagnostic platform for delivery of the US stimulus. The results from this study showed a near doubling in median survival for patients treated with US, MBs and Gem compared to patients treated with Gem alone. (227) However, the treatment protocol still

involved administering a clinical dose of Gem. As a consequence, these studies have done little to mitigate the severe side effects associated with systemic chemotherapy.

1.4.3.1.3. Targeted microbubbles for cancer therapy

A number of different active targeting strategies have been adopted in an effort to improve the retention of MBs within the tumour vasculature. This often involves incorporation of targeting ligands including antibodies, peptides, and small molecules into/onto the shell of the MB during or after MB fabrication through covalent or non-covalent conjugation. (228) Recently Bracco developed a MB contrast agent comprised of phospholipids covalently bound to a 5.5 kDa heterodimeric peptide which has a high binding affinity for kinase domain receptor (KDR) - an angiogenic marker overexpressed in many cancers. (229–233) Although this MB was designed for diagnostic purposes, the underlying targeting technology has vast potential for use in targeted drug delivery to many forms of solid tumour. In another study, Villanueva and co-workers developed a phospholipid MB with an antibody (anti-ICAM-1) incorporated into the MB shell. The MB conjugate showed a 40-fold increase in targeting to interleukin-1B–activated endothelial cells compared to non-targeted MBs in an in vitro model. (234)

An alternative strategy developed by Stride et al involved the incorporation superparamagnetic nanoparticles (SPIONs) into phospholipid MBs. Making the MBs magnetically responsive means it is possible to enhance their retention at a target site using a magnetic field prior to US mediated MB destruction. In a study by Stride et al, a number of different magnetic MB formulations were prepared, and their transfection efficiency determined using bioluminescence imaging. The results demonstrated that plain MBs mixed with a magnetic micelle or MBs prepared with magnetic material loaded directly into the shell proved much more effective than either the magnetic micelles or plain MBs alone. (235) In an in vivo study later conducted by the same group, animals were again injected with the magnetically responsive MBs along with the luciferin expressing plasmid, pGL4.13, and a small magnet was placed above the animal's right lung. The results demonstrated that the bioluminescence signal

was confined to the right lung only, when the animal was exposed to both magnetic and US fields. (236) Despite the promising preclinical results for US/magnetically responsive MBs, current treatment strategies are hindered through the simultaneous application of magnetic and US fields which can be especially cumbersome and inaccurate in small animal models.

1.4.3.1.4. MBs and SDT for cancer therapy

As described in Section 1.4.2.4, the full potential of SDT as a clinical technique has two main limitations. The first is due to the need for systemic, untargeted administration of the sonosensitiser which can lead poor tumour uptake and unpleasant side effects caused by light sensitivity. The second limitation is due to the inherent hypoxic nature of most solid tumours. As SDT relies on the formation of cytotoxic ROS, the lack of available oxygen poses a therapeutic barrier towards an effective tumour response. In an attempt to overcome the first shortcoming, Nomikou et al covalently attached the sonosensitiser RB to the surface of a phospholipid MB through the use of carbodiimide chemistry. An in vitro DPBF (1,3-diphenylisobenzofuran) assay aimed at measuring ROS generation, revealed that the MB conjugate produced significantly more singlet oxygen than RB alone at the same concentration following US activation. The authors postulated that the enhanced singlet oxygen production was as a result of inertial cavitation of the MB resulting in sonoluminescence-mediated sensitiser activation. This translated into a significant decrease in tumour volume of 18% in a murine model of prostate cancer when compared to an increase in tumour volume of 50% observed in control mice treated with the same MB conjugate without US stimulation. In spite of this promising finding, the utility of this MB conjugate was limited by poor stability. (209) Further work by McEwan et al attempted to remedy this through the use of polymer shelled MBs. The polymer – poly(lactic-co-glycolic acid) (PLGA), was chosen as the shell material in this case, in light of its biocompatibility and widespread use in many formulations. In addition, it has also been suggested that polymeric coatings provide a greater degree of control over the MB destruction threshold. (193) As before, RB was covalently bound to the terminal end of the PLGA molecule using carbodiimide chemistry. For comparative purposes, phospholipid MBs were also prepared as described before. The study revealed a significantly enhanced

stability for PLGA MBs when compared to phospholipid MBs. Furthermore, in vivo studies revealed a significant decrease in tumour growth for PLGA RB-MBs in the presence of US when compared to the same in the absence of US. However, the overall drug loading ability of the polymeric MBs was approximately 34% lower than that of the phospholipid MB. (237) Despite significant progress being made to facilitate the delivery of sonosensitisers to the tumour site, the potential of SDT was still restricted through hypoxic conditions within solid tumours.   A 2015 study by McEwan et al reported the development of oxygen carrying lipid MBs (O_2MBs) with RB non-covalently bound to the surface using an avidin-biotin interaction. This was facilitated through the synthesis of a biotinylated derivative of RB which was bound to the surface of an avidin functionalised MB shell. When compared to MBs prepared with SF_6 in the MB core, the O_2MB generated significantly more singlet oxygen in degassed buffer. Furthermore, when the human pancreatic cancer cell line BxPC-3 was cultured in a hypoxic chamber and treated with O_2MB-RB or SF_6 loaded MB-RB plus US, a significantly lower cell viability was observed for the O_2MB-RB formulation. A similar trend was also observed in vivo in mice bearing ectopic BxPC-3 xenografts, with O_2MB-RB showing a 45% reduction in tumour volume 5 days following the initial treatment. The authors suggested that the in vivo effect was directly attributable to the presence of O_2MB supplying additional oxygen as a substrate for SDT mediated ROS production. (214)

The concept of oxygen carrying MBs for the delivery of sonosensitisers was taken a step further in 2016 when McEwan et al successfully prepared O_2MB bearing the antimetabolite drug 5-FU, in addition to O_2MB bearing RB. A similar approach was adopted in this study with regards to drug conjugation, with both drugs being attached to the MB shell through avidin-biotin linkages. In contrast to their previous publications, a phospholipid with a longer acyl chain (PC 22:0) was used as the main lipid component of the MB formulation. (238) This was based on the finding by Borden et al, that increasing the acyl chain length can have a significant effect on the physiochemical characteristics of MBs and can prolong the dissolution time of MBs in a degassed medium. (239) Rather unsurprisingly, McEwan et al found that the MBs were more stable with respect to oxygen retention when compared to their earlier MB formulation (PC 18:0). Additionally, it was found that combined SDT and antimetabolite therapy using the O_2MB showed an enhanced cytotoxicity profile in three different pancreatic

cancer cell lines cultured in an anaerobic cabinet when compared with either SDT or 5-FU treatments alone. In addition, when mice bearing ectopic BxPC-3 tumours were treated with the combined therapy, a statistically significant reduction in tumour volume was observed when compared to the control mice. (238) A similar approach was also adopted by the same group but used Gem in place of 5-FU, as Gem has since superseded 5-FU as the antimetabolite of choice in clinical practice. (240) One shortcoming of the latter two studies was that two separate MB formulations were prepared: one bearing RB and the other bearing the antimetabolite derivative. These then had to be mixed in a 1:1 volume ratio which means that the effective dose of each active agent was reduced by 50%. This is especially significant when considering that the dose of antimetabolites administered using the MBs is orders of magnitude lower than their typical clinical dose. (241)

1.4. Overall aim and specific chapter objectives

The overall aim of the work conducted in this thesis was to develop novel MB based formulations to enable targeted chemo-SDT treatment of breast / pancreatic cancer models. An overview of the aims for each chapter is provided below. More specifically to develop MB formulations capable of delivering multiple payload drugs on a single MB. A secondary aim is to improve the targeting potential of these MB formulations though the incorporation of magnetically responsive nanoparticles into the MB coating. A further aim is to develop MB formulations which are amenable to clinical translation through optimisation of MB fabrication protocols which do not involve post-production manipulation of MBs.

1.4.1. Chapter 3 - Treatment of MCF-7 Breast Cancer Using Ultrasound Responsive Microbubbles Loaded with Paclitaxel, Doxorubicin and Rose Bengal.

This chapter investigated the development of MBs carrying either PTX and RB or PTX and Dox. In both cases, PTX was loaded hydrophobically into the lipid shell of the MBs and RB / Dox was attached to the surface using the avidin-biotin interaction. By using a combination of the two MB formulations, the effect of targeted PTX / Dox / SDT treatment was established in an MCF-7 murine model of breast cancer. The results from this chapter have been published in (242).

1.4.2. Chapter 4 - Targeted Delivery of Paclitaxel, Gemcitabine and Rose Bengal to Pancreatic Tumours Using a Multifunctional Microbubble Delivery Platform.

Gem-Abraxane is a first line chemotherapy combination for pancreatic cancer. Previous work has also demonstrated the benefit of combining Gem with SDT in pre-clinical pancreatic cancer models. The aim of the work undertaken in this chapter was to develop a single MB formulation capable of carrying PTX /Gem /RB and determine how effective targeted chemo-sonodynamic therapy using this formulation was in a pre-clinical murine model of pancreatic cancer.

1.4.3. Chapter 5 - Magnetic Microbubble Mediated Chemo-Sonodynamic Therapy using a Combined Magnetic-Acoustic Device

Previously published work has indicated that magnetically responsive Gem / RB loaded MBs enhanced the chemo-sonodynamic therapy treatment of murine pancreatic tumours that were exposed to both magnetic / US fields during treatment, compared to an US field alone. In this chapter, two shortcomings of this work were addressed by preparing a single MB formulation carrying both Gem / RB and using a single co-aligned probe to deliver the combined magnetic / US fields. The efficacy of this approach was determined in a murine model of pancreatic cancer.

1.4.4. Chapter 6 - Microbubble Mediated Delivery of Novel Gemcitabine Phospholipid-Pro-drug and Paclitaxel

When considering potential clinical translation of the work undertaken in Chapters 3-5, it became apparent that significant manipulation would be required at the treatment site to first generate the MB formulation and then attach any biotinylated payloads. To minimise the need for any post-MB manipulation, this chapter investigated the potential to generate MBs carrying both the hydrophobic PTX and the hydrophilic Gem without any post-MB manipulation. This involved the synthesis of a lipid functionalised with Gem and its assembly into MBs with PTX non-covalently incorporated in the lipid shell. Efficacy of the Gem/PTX MBs following UTMD mediated release was determined in a murine model of pancreatic cancer.

1.5. Statement of collaboration

The synthesis of compound 12, discussed in chapter 4 and 5, was carried out by Dr Sukanta Kamila. The design and fabrication of the MAD device, discussed in chapter 5, was conducted by Dr Lester Barnsley and Dr Michael Gray. In vitro characterisation of the magnetic MBs, discussed in chapter 5, including drug delivery in agar phantoms and singlet oxygen generation, was performed by Dr Estelle Beguin.

Chapter 2

Methodology

2.1. Materials and reagents

Reagents and solvents were purchased from commercial sources at the highest possible grade. Panc-1, BxPC-3 and Mia Paca-2 cells were obtained from the American Type Culture Collection (ATCC) (Manassas, VA, USA) and Matrigel from BD Biosciences (San Jose, CA, USA). SCID mice (C.B-17/IcrHanHsd-PrkdcSCID) were bred in house. All phospholipids were purchased from Avanti Polar Lipids (Alabaster, AL, USA). Rose bengal and biotin were purchased from Sigma Aldrich (St. Louis, MO, USA). Doxorubicin, gemcitabine and paclitaxel were purchased from XABC (Shaanxi, China). Avidin from egg white was purchased from Thermo Fisher (Waltham, MA, USA). Iron oxide nanoparticles (IONPs) (50 nm hydrodynamic diameter) were custom conjugated by Ocean NanoTech (San Diego, CA, USA). MBs were formed using a Microson ultrasonic cell disruptor, 100 W, 22.5 kHz, from Misonix Inc. (Farmingdale, NY, USA). Optical microscope images were obtained using a Leica DM500 optical microscope (Wetzlar, Germany). Analysis of MB size and concentration was determined using a bespoke MATLAB algorithm (2010B, MathWorks, Natick, MA, USA). UV-Vis spectra were recorded with a Varian Cary spectrophotometer (Palo Alto, CA, USA), using quartz cells (path length = 1 cm). UV absorbance of MTT was analysed using a Fluostar Omega plate reader (BMG Labtech, Ortenberg, Germany). NMR spectra were obtained on Varian 500 MHz instrument at 25.0 ± 1 °C (Palo Alto, CA, USA) and processed using TopSpin software (Bruker, Billerica, MA, USA). ESI-MS were obtained using a Finnegan LCQ-MS instrument (San Jose, CA, USA). HPLC analysis was carried out on a Shimadzu LC-8 preparative pump system (Shimadzu Corp., Kyoto, Japan). Statistical error in data was expressed as standard error of the mean (SEM), while statistical analysis was undertaken using either a 2-tailed Students t-test or a one-way ANOVA followed by Tukey's post hoc test.

2.2. Synthesis of biotinylated doxorubicin (5)

Biotin-N-hydroxysuccinimide ester (**3**) was prepared by the reaction of biotin (**1**) and N,N-disuccinimidyl carbonate (**2**) following a literature procedure. (243) To an ice-cold solution of **3**, (0.14 g, 0.41 mmol) in DMF (10 ml) was added doxorubicin hydrochloride (**4**, 0.3 g, 0.41 mmol) under a nitrogen atmosphere. After stirring for 30 min, triethylamine (0.5 ml, 2 mmol) was added to the reaction mixture and the contents stirred for 12 hrs at room temperature. The reaction was monitored by thin layer chromatography (TLC) (Merck Silica 60, HF 254, methanol-dichloromethane, 1:4). After completion of the reaction, excess diethyl ether (100 ml) was added to the reaction mixture. The resultant red precipitate was filtered and washed three times with diethyl ether (50 ml x 3). The solid was then subjected to preparative thin layer chromatography (PTLC) purification (methanol:dichloromethane, 1:4) to obtain 0.25 g (yield = 78%) of **5**. ^{1}H NMR (DMSO-d$_6$) δ :7.84 (*d*, J = 7.5 Hz, 2H, aromatic), 7.58 (*d*, J = 7.5 Hz, 1H, aromatic), 6.36 (*s*, 1H, NH), 6.29 (*s*, 1H, NH), 5.37 (*brs*, 1H, OH), 5.22 (*brs*, 1H, OH), 4.87 (*s*, 2H, -CH2-OH), 4.51 (*brs*, 2H, OH X 2), 4.36-4.33 (*m*, 1H, CH), 4.25-4.22 (*m*, 1H, CH), 4.16-4.13 (*m*, 1H, CH), 3.99 (*s*, 3H, OC*H$_3$*), 3.60-3.58 (*m*, 1H, C*H*), 3.55 (*brs*, 2H, O*H* X2), 3.10-3.00 (*m*, 4H, C*H2* X1, C*H* X 2), 2.88-2.54 (*m*, 3H, C*H2* X 1, C*H*), 2.20-2.00 (*m*, 1H, C*H*), 1.63-1.50 (*m*, 4H, C*H2* X 2), 1.42- 1.22 (*m*, 11 H, C*H3* X 1, C*H2* X 4). ^{13}C NMR (DMSO-d$_6$): 177.6, 176.9, 174.8, 166.4, 163.0, 161.2, 153.7, 152.7, 137.4, 132.4, 120.4, 119.4, 99.5, 97.8, 80.15, 75.1, 72.7, 66.4, 61.4, 59.5, 55.7, 47.8, 33.8, 31.9, 28.9, 28.8, 28.5, 28.4, 24.9, 19.8, 17.6, 17.1. Negative mode ESI-MS: [M-H]: calculated for $C_{37}H_{43}I_2N_3O_{13}S$ = 769 Da, found = 768 Da.

2.3. Synthesis of biotin rose bengal (8)

2.3.1. Synthesis of rose bengal amine (7) 2-Aminoethyl 2,3,4,5-tetrachloro-6-(6-hydroxy-2,4,5,7-tetraiodo-3-oxo-3H-xanthen-9-yl)benzoate:

To a solution of rose bengal disodium (**5**, 1.0 g, 1.0 mmol) in anhydrous DMF (10 mL) was added 2-bromoethylamine (0.32 g, 1.5 mmol) and the mixture was stirred at 80°C for 7 hrs. The DMF was then removed under reduced pressure and the residue stirred for 18 hrs in diethyl ether (200 mL). The solution was filtered and the resulting solid stirred in water (200 mL) for 18 hrs. The suspension was filtered and the solid was recrystallised from methanol to yield

the product as a dark red solid. ^{1}H NMR (500 MHz, DMSO-d$_6$): 2.42 (*t*, C*H2*, 2H), 3.80 (*t*, OC*H2*, 2H), 7.26 (*s*, Ar*H*, 2H), 7.60 (*s*, N*H2*, 2H). ^{13}C NMR (500 MHz, DMSO-d$_6$): 19.0, 37.5, 49.3, 56.5, 62.7, 76.6, 97.9, 129.6 130.6, 132.4, 133.4, 10.6, 110.9, 134.7, 135.7, 136.4, 137.0, 139.6, 157.5, 163.2, 172.3. ESI-MS: calculated for $C_{22}H_9Cl_4I_4NO_2$ = 1016.53, found 1016.13

2.3.2. Synthesis of biotin rose bengal (8) 2-(5-(2-Oxohexahydro-1H-thieno[3,4-d]imidazol-4-yl)pentanamido)ethyl2,3,4,5-tetrachloro-6-(6-hydroxy-2,4,5,7-tetraiodo-3-oxo-3H-xanthen-9-yl)benzoate:

To a solution of rose bengal amine (74 mg, 74 µmol) in 2 mL DMF, 3 (25 mg, 74 µmol) dissolved in DMF (2 mL) was added. Triethylamine (TEA, 10 µl, 0.71 µmol) was added to the mixture which was then stirred at room temperature for 12 hrs. The resulting solution was placed in a solution of hexane: chloroform (200 ml, 4:1) and stirred for 24 hrs at room temperature. The solution filtered and the filtrate retained. The filtrate was washed three times with diethyl ether and dried in a vacuum oven to yield **8** as a red powder (14 mg, 10%). ^{1}H NMR (500 MHz, DMSO-*d$_6$*): 1.28 (*m*, C*H2*, 2H), 1.45 (*m*, C*H2*, C*H*, 3H), 1.57 (*m*, C*H*, 1H), 1.60 (*t*, C*H2*, 2H), 2.52 (*q*, C*H*, 1H), 2.58 (*m*, C*H*, 1H), 2.79 (*q*, C*H*, 1H), 2.97 (*t*, C*H2*, 2H), 3.10 (*m*, SC*H*, 1H), 3.85 (*t*, OC*H2*, 2H), 4.09 (*t*, C*H*, 1H), 4.28 (*t*, C*H*, 1H), 6.34 (*s*, N*H*, 1H), 6.41 (s, N*H*, 1H), 7.46 (*s*, Ar*H*, 2H), 7.56 (*brs*, N*H*, 1H). ^{13}C NMR (125 MHz, DMSO-*d$_6$*): 8.98, 9.03, 25.52, 28.57, 29.45, 31.72, 35.52, 37.34, 46.07, 53.13, 55.86, 59.66, 61.48, 64.65, 76.50, 97.69, 110.56, 124.271, 129.37, 130.48, 132.34, 134.79, 135.50, 136.41, 139.79, 157.42, 163.13, 163.57, 172.23, 172.68, 228.31, 230.86. ESI-MS: calculated for $C_{32}H_{23}Cl_4I_4N_3O_7S$ = 1243.0 found = 1241.

2.4. Synthesis of biotin-Gem-RB (12)

2.4.1. Synthesis of N-(2-(bis(2-aminoethyl)amino)ethyl)-5-(2-oxohexahydro-1H-thieno[3,4-d]imidazol-4-yl)pentanamide (10)

To a stirred solution of tris(2-aminoethyl)amine (**9**) (0.22 g, 1.5 mmol) and trimethylamine (TEA) (catalytic amount) in anhydrous dimethylformamide (DMF) (5 mL), **3** (0.5 g, 1.5 mmol) was added and the reaction mixture was stirred at 0°C under a nitrogen atmosphere for 30 min. The solvent was removed under reduced pressure and the residue was triturated with diethyl ether. The crude product was purified by column chromatography on basic (TEA) silica gel (methanol: dichloromethane 1:9 to 3:7) to give **10** (0.33 g, 61% yield) as a white

semi solid. ^{1}H NMR (DMSO-d_6): δ 7.94 (*brs*, 1H, N*H*), 6.42 (*brs*, 1H, N*H*), 6.35 (*brs*, 1H, N*H*), 4.49 (*brs*, 4H, N*H$_2$* X 2), 4.29 (*s*, 1H, C*H*), 4.12 (*s*, 1H, C*H*), 3.07-3.02 (*m*, 6H, C*H$_2$* X 3), 2.88-2.82 (*m*, 1H, C*H*), 2.44-2.06 (*m*, 10H, C*H$_2$* X 5), 1.59-1.48 (*m*, 4H, C*H$_2$* X 2), 1.47-1.29 (*m*, 2H, C*H$_2$*). ESI-MS: calculated for $C_{16}H_{32}N_6O_2S$, 372.23; found 373.31 (M + H)$^+$.

2.4.2. Synthesis of bis(2,5-dioxopyrrolidin-1-yl) 8,8'-((((2-(5-(2-oxohexahydro-1H-thieno[3,4-d]imidazol-4-yl)pentanamido)ethyl)azanediyl)bis(ethane-2,1-diyl))bis(azanediyl))bis(8-oxooctanoate) (11)

To a stirred solution of compound **10** (0.5 g, 1.3 mmol) and TEA (catalytic amount) in 10 mL anhydrous DMF was added disuccinimidyl suberate (1 g, 2.7 mmol) and the reaction mixture stirred at room temperature for 6 hrs under a nitrogen atmosphere. After completion of the reaction, excess diethyl ether (200 mL) was added to the reaction mixture. The white precipitate thus obtained was filtered and washed 3 times with diethyl ether (50 mL x 3). The crude product was purified by column chromatography on basic (TEA) silica gel (methanol:chloroform 1:4 to 1:1) to give 11 (0.83 g, 71% yield) as a white solid. ^{1}H NMR (DMSO-d_6): δ 7.94 (*brs*, 2H, N*H* X 2), 7.67 (brs, 1H, N*H*), 6.41 (*brs*, 1H, N*H*), 6.34 (*brs*, 1H, N*H*), 4.29 (*s*, 1H, C*H*), 4.12 (*s*, 1H, C*H*), 3.06-3.04 (*m*, 3H, C*H* and C*H$_2$*), 2.88-2.72 (*m*, 6H, C*H$_2$* X 3), 2.71-2.63 (*m*, 8H, C*H$_2$* X 4), 2.45-2.34 (m, 6H, C*H$_2$* X 3), 2.20-2.06 (*m*, 10H, C*H$_2$* X 5), 1.60-1.21 (*m*, 22H, C*H$_2$* X 11). ^{13}C NMR (DMSO-d_6): 172.5, 170.7, 163.1, 162.7, 61.4, 59.6, 55.8, 53.9, 39.9, 39.8, 39.6, 37.3, 36.2, 35.6, 31.2, 28.7, 28.5, 25.8, 25.7, 25.6. ESI-MS: calculated for $C_{40}H_{62}N_8O_{12}S$, 878.4; found 901.3 (M +Na)$^+$.

2.4.3. Synthesis of ((2R,3R,5R)-5-(4-amino-2-oxopyrimidin-1(2H)-yl)-4,4-difluoro-3-hydroxytetrahydrofuran-2-yl)methyl 4,11,19-trioxo-15-(2-(5-(2-oxohexahydro-1H-thieno[3,4-d]imidazol-4-yl)pentanamido)ethyl)-1-((2,3,4,5-tetrachloro-6-(6-hydroxy-2,4,5,7-tetraiodo-3-oxo-3H-xanthen-9-yl)benzoyl)oxy)-3,12,15,18-tetraazahexacosan-26-oate (12)

To a stirred solution of **11** (0.4 g, 0.45 mmol) in anhydrous DMF (5 mL) was added gemcitabine hydrochloride (0.136 g, 0.45 mmol) and TEA (0.5 mL) and the reaction was stirred at 22°C for 24 hrs under a nitrogen atmosphere. After

completion of the reaction, **7** (prepared separately as described in Section 2.3.1) (0.43 g, 0.45 mmol) in anhydrous DMF (5 mL) and TEA (0.5 mL) were added to the reaction mixture and continued to stir for 24 hrs. Once the reaction was complete, excess diethyl ether (200 mL) was added to the solution and stirred for 30 min. The pink red precipitate thus obtained was triturated with diethyl ether (100 mL), ethyl acetate (100 mL), acetone-water mixture (1:9, 100 mL) and finally with ethyl acetate-hexane mixture (1:1, 100 mL) respectively to afford a pink powder of compound **12** (0.26 g, 30% yield). ^{1}H NMR (DMSO-d_6): δ 7.95 (*brs*, 2H, N*H*$_2$), 7.69 (*s*, 1H, C*H*, aromatic proton), 7.68 (*s*, 1H, C*H*, aromatic proton), 7.37(s, 1H, C*H*), 7.32 (*brs*, 4H, N*H* X 4), 6.89 (*s*, 1H, C*H*), 6.42 (*brs*, 1H, N*H*), 6.35 (*brs*, 1H, N*H*), 6.22 (*d*, 1H, C*H*), 6.13 (*brs*, 1H, N*H*), 5. 78-5.77 (*m*, 1H, C*H*), 5.19 (*s*, 1H, C*H* X 2), 4.9 (*brs*, 1H, O*H*), 4.30 (*s*, 2H, -OC*H*$_2$), 4.13 (*s*, 2H, -OC*H*$_2$), 3.79-3.60 (*m*, 3H, C*H*, C*H*$_2$), 3.39-3.32 (*m*, 2H, C*H*$_2$), 3.07 (*brs*, 6H, N-N*H*C*H*$_2$ X 3), 2.94-2.84 (*m*, 6H, NC*H*$_2$ X 3), 2.81 (*brs*, 1H, O*H*), 2.45-2.46 (*m*, 3H, C*H*, C*H*$_2$), 2.17-2.06 (*m*, 10H, C*H*$_2$ X 5), 1.60- 1.10 (*m*, 22H, C*H*$_2$ X 11). ^{13}C NMR (DMSO-d_6): 171.8, 165.98, 163.2, 162.7, 159.3, 155.0, 150.5, 145.8, 141.2, 131.0, 128.7, 123.5, 116.2, 95.0, 80.9, 69.3, 61.5, 59.6, 59.4, 55.8, 51.7, 45.8, 40.2, 37.3, 37.05, 36.2, 35.5, 31.0, 28.7, 28.5, 28.2, 25.6. ESI-MS: calculated for $C_{63}H_{72}Cl_4F_2I_4 N_{10}O_{15}S$, 1925.98; found 1925.90 (M - H)$^-$.

2.5. Synthesis of LipidGem (15)

A chloroform solution (20 mL) of 1,2-dibehenoyl-sn-glycero-3-phosphocholine (500 mg, 480 μmol) was added to a stirred solution of gemcitabine hydrochloride (400 mg, 1.5 mmol) and phospholipase D from Streptomyces *sp* (3 mg, 900 units) in sodium acetate buffer (200 mM, pH 4.5, 5 mL) containing calcium chloride (200 mM). The mixture was stirred vigorously at 45°C for 6 hrs after which a solution containing chloroform (10 mL) and methanol (15 mL) was added. The organic layer was separated, and the aqueous layer washed twice with a chloroform/methanol mixture (2:1). The organic extracts were combined, dried using anhydrous sodium sulphate, filtered and concentrated in vacuo to yield a waxy, off-white solid. The crude product was purified using preparative thin layer chromatography (chloroform: methanol: ammonium hydroxide (7N), 65:25:4, Rf – 0.41) to give Lipid-Gem (25% yield).

2.6. Clonogenic assay in MCF-7 cells treated with Dox, PTX, SDT and combinations thereof

The human breast adenocarcinoma cell line (MCF-7) was cultured in DMEM supplemented with 10% FBS, 100 μg/ml streptomycin and maintained in a humidified, 5% CO_2 atmosphere at 37°C. MCF-7 cells were seeded (5 x10^3) into each well of a 96 well plate and 24 hrs later cells were treated with PTX (1 nM), Dox (10 nM), RB (10 nM) or combinations thereof for 3 h, followed by replacement of the media. Selected wells were treated with US for 30 s delivered using a Sonidel SP100 sonoporator (frequency - 1 MHz, power density - 3.0 W/cm^2, duty cycle - 50% PRF - 100 Hz). After 18 hrs, cells were pooled from 2 wells and seeded in a 6 well plate containing 5 ml of complete media. Plates were placed in an incubator for 7 days. Medium was removed from wells and fixation/staining solution (1 mL) [consisting of crystal violet (0.05% w/v), formaldehyde (2.7% v/v), PBS (10% v/v), methanol (1% v/v) and distilled water (86.3% v/v)] was added to each well at room temperature for 20 min. The solution was removed, and wells were washed with water. Digital photographs were taken using a Canon EOS100D DSLR and colony formation was analysed using Image J software.

2.7. *In vitro* treatment of BxPC-3 and Mia-PaCa-2 cells with Gem, 8 and 12.

The human primary pancreatic adenocarcinoma cell line BxPC-3 was maintained in RPMI 1640 medium which was supplemented with 100 U/mL penicillin, 100 mg/mL streptomycin, and 10% fetal bovine serum (FBS) in a humidified 5% CO_2 atmosphere at 37°C. The Mia-PaCa-2 cell line was maintained using Dulbecco's Modified Eagle's Medium (DMEM) containing 1 g/L glucose and supplemented with 100 U/mL penicillin, 100 mg/mL streptomycin, and 10% fetal bovine serum (FBS) in a humidified 5% CO_2 atmosphere at 37°C. These cells were seeded into 96-well plates at a density of 5000 cells per well. The plates were then incubated for 24 hrs followed by the addition of 100 μL of media spiked with Gem, **8** or **12** at concentrations ranging from 0.001-1000 μM. The cells were then further incubated for 48 hrs before the cell viability was determined by an MTT assay.

2.8. Preparation of drug loaded MBs

For the preparation of MBs containing PTX in the shell, first 1,2-dibehenoyl-sn-glycero-3-phosphocholine (DBPC) (4.0 mg, 4.44 μmol), 1,2-distearoyl-sn-glycero-3-phosphoethanolamine-N- [methoxy(polyethylene glycol) -2000] (DSPE-

PEG(2000)) (1.35 mg, 0.481 μmol) and 1,2- distearoyl-sn-glycero-3-phosphoethanolamine-N-[biotinyl(polyethylene glycol)-2000] (ammonium salt) (DSPE-PEG (2000)-biotin) (1.45 mg, 0.481 μmol) were dissolved in chloroform in a glass vial at a molar ratio of 82:9:9. To this solution was added PTX (5 mg, 5.86 μmol) dissolved in chloroform (100 μL). The solvent was removed under vacuum at room temperature yielding a translucent film. For MBs prepared using **15**, the film was prepared as described above with the exception that **15** (5 mg, 4.71 μmol), 1,2-distearoyl-sn-glycero-3-phosphoethanolamine-N-[methoxy(polyethylene glycol)-2000] (1.43 mg, 0.51 μmol) and PTX (2.5 mg, 2.93 μmol) were used. For MBs not containing PTX, the same procedure for thin film formation described above was used, with the exception that no PTX was added. The film was then reconstituted in 2 mL of a solution containing PBS (pH 7.4 $\pm$ 0.1), glycerol and proplyene glycol (8:1:1 volume ratio) and heated in a water bath at 80°C for 30 min. The cloudy colloidal suspension was sonicated using a Microson ultrasonic cell disrupter at an amplitude of 22% for 1 min and then at an amplitude of 90% in a perflourobutane (PFB) atmosphere for 30 sec. The MBs were then cooled on ice for 10 min followed by centrifugation (100 RCF) for 3 min and the liquid laying below the surface of the MB cake (infranatant) was removed. The MB-PTX cake was then washed a further 2 times with PBS (pH 7.4 $\pm$ 0.1). These MB were either used straight away (plain MB or MB-PTX) or avidin functionalisation was carried out through the addition of an aqueous solution of avidin (10 mg/mL). The MB suspension was then mixed using an orbital shaker for 10 min in an ice bath to allow for the reaction to take place. The MBs were then centrifuged (100 RCF) for 3 min, the infranatant removed and the MB cake washed with PBS solution (2 mL, pH 7.4 $\pm$ 0.1) which was again removed following centrifugation. The MB cake was again reconstituted in PBS solution (2 mL, pH 7.4 $\pm$ 0.1), mixed with an aqueous solution containing one of: (i) **5**, (ii) **8** or (iii) **12** (1 mL, 5 mg/mL) for 5 min. The drug loaded MBs were then centrifuged (100 RCF) for 3 min. Following removal of the infranatant, the MB cake was then washed with PBS (2 mL, pH = 7.4 $\pm$ 0.1), centrifuged, and the MB cake isolated. This washing / centrifugation procedure was repeated twice further with the final MB cake reconstituted in 2 mL of PBS. Drug loaded MagMBs were prepared following the protocol described above with the exception that 2-dibehenoyl-sn-glycero-3-phosphocholine coated IONPs (150 μL, 3.75 mg iron) were added to the colloidal lipid suspension prior to MB formation.

In vitro, MagMB characterisation was completed using **8** to prevent wastage of the more difficult to synthesise **12**. Drug-loaded MBs bearing **5, 8** or **12** were kept in reduced light conditions and on ice prior to use. When oxygenated MB were required, MBs were sparged with oxygen gas for a total of 2 mins to allow gas exchange to occur and these are referred to with the prefix O$_2$MB- (e.g. O$_2$MB-RB) (Figure A7). Otherwise, they are referred to with the prefix MB- (e.g. MB-RB).

2.9. Determination of size distribution and concentration of MBs.

An appropriate aliquot of freshly prepared MB suspension was diluted in PBS solution (2 mL, pH 7.4 ± 0.1). A 10 µL sample was then loaded into a haemocytometer and viewed under a microscope (x40 objective). Images (n=20) were taken of the MB suspension and saved as high resolution TIFF files. These images were then analysed using a bespoke MATLAB algorithm as described in (244). Based on the known area per pixel and known frame volume, the distribution of MB diameters and mean MB concentration could be determined. For calibration purposes, commercial MBs (SonoVue) were also analysed and compared to values provided by the manufacture (*data not shown*).

2.10. Determination of PTX loading

An appropriate volume of MB-PTX was removed and diluted in a mixture of acetonitrile and water (1:1 v/v). This sample was then sonicated to fully solubilise the MBs and the sample was then placed in a 2 mL HPLC vial. The drug loading for PTX was then determined using reverse phase HPLC. A volume of 50 µL was injected onto a Phenomenex C$_{18}$ column (250 × 4.6 mm, 5 µm) and the sample was eluted using a mobile phase consisting of acetonitrile and water (1:1), a flow rate of 1.5 mL/min and a detection wavelength of 227 nm. The loading of PTX was calculated by the following equation:

Equation 1.

$$Drug\ loading\ = \frac{Mass\ of\ PTX\ in\ film}{Mass\ of\ lipid\ material\ in\ film} * 100$$

2.11. Determination of drug loading of 5, 8, 12 and 15

Using 1 mM stock solutions prepared in PBS solution (5% DMSO, 2 mL, pH 7.4 ± 0.1) for **5**, **8** and **12** and a solution of methanol and chloroform (20:1) for **15**, appropriate calibration standards were prepared. These standards were loaded into a quartz cuvette and the UV absorbances were read between 200 and 800 nm. Calibration curves for **5**, **8, 12 and 15** were then constructed using the absorbance at the λmax. Samples were prepared from freshly synthesised MBs by taking an appropriate aliquot of the MB suspension and diluting in PBS solution (2 mL, pH 7.4 ± 0.1). This suspension was then sonicated for 1 min to fully destroy MBs and solubilise **5**, **8** or **12**. This sample was then placed in a quartz cuvette and the absorbance was read at 480 nm, 560 nm and 280 nm for **5**, **8/12** and **15** respectively.

2.12. Characterisation of MB iron loading

As DBPC-IONPs were incorporated within the MB coating, the functionalisation of MBs with drug products on its outer surface is unlikely to affect the iron loading of the MBs. The iron content of MagMBs was detected using inductively coupled plasma optical emission spectroscopy (ICP-OES, Perkin Elmer, Optima 8000). Iron measurements were performed at a wavelength of 238 nm and a calibration curve was constructed for iron in 2% nitric acid solution (0-1 mg/L) with a R^2 value of 0.9999 prior to sample measurements.

2.13. Determination of MB stability

MBs were prepared as described in Section 2.8. Immediately following synthesis, MBs were characterised in terms of MB concentration according to Section 2.9. Batches of MBs were then placed in a water bath in an incubator at 37°C and the MB concentration was determined at t = 10, t = 60, t = 120 and t =180 min.

2.14. Production of singlet oxygen from MagO₂MB-RB exposed to US

The production of singlet oxygen ($^1O_2$) from activated RB exposed to US was determined using SOSG. A sample of 9 mL degassed PBS, ± 5x10⁷ MB/mL, ± 541 μM biotin-RB, and 1.25 μM SOSG was exposed to 1.17 MHz, 0.70 MPa peak

negative pressure, 30% duty cycle (DC), 100 Hz pulse repetition frequency (PRF) US for 3.5 minutes. Sample exposure was undertaken using a custom-made tank with the built-in transducer driven at 1.17 MHz. The sample was injected into a holder placed in the pre-focal region of the transducer to ensure a uniform pressure field at the top of the sample chamber. The fluorescence intensity of SOSG (Ex: 490 nm / Em: 520 nm) was measured for each sample with and without US exposure. To minimise the scattering from MBs in the sample without US exposure, increased hydrostatic pressure was applied to the sample using a sealed syringe to destroy the bubbles prior to fluorescence measurement. The generation of $^1O_2$ was then calculated as a percent change in SOSG fluorescence intensity at 520 nm for a sample exposed to US compared to a control sample for each experimental run. In addition to measuring $^1O_2$ generation, the characterisation of MB acoustic emissions during US exposure were recorded using PCD focused on the top of the sample chamber. A 2 MHz analog high-pass filter was used to remove the drive frequency from the recorded signal before pre-amplification, digitization, and storage onto a computer drive. The power spectral density was calculated for each PCD signal acquisition. These results were used to quantify cavitation activity during each experiment (3.5 minutes exposure) by determining the cumulative energy at ultraharmonic frequencies ($f_0*(n+0.5)$, with $f_0 = 1.17$ MHz and $n = 2,3...9$), which are indicative of nonlinear bubble oscillations.

2.15. Magnetic-Acoustic-Device (MAD) and control device

The MAD was designed as described by Barnsley *et al*. (245) Briefly, the magnetic body consisted of N52 grade NdFeB permanent magnet material whose geometry was optimized to have a maximum magnetic field of 0.2 T at a distance of 10 mm from the body's leading edge. An integrated ultrasonic element with a focal distance also of 10 mm provided a pressure field that spatially overlapped with the magnetic field peak, with sufficient amplitude to cause inertial cavitation of MBs used in this study. An aluminium-bodied copy of the MAD (hereafter referred to as "aMAD") was produced to provide an US-only control for *in vitro* and *in vivo* experimentation. In order to span the gap between the US element and the delivery site of interest in the present work, a coupling cone was cast from paraffin wax and secured with US gel. The cone material was chosen

for its ease of casting and minimal transmission loss in the 1 MHz frequency range as determined by through-transmission measurements. Since the acoustic boundary conditions for this configuration were different from those used in the initial characterization, both the MAD and the aluminium copy were recalibrated.

2.16. Drug delivery comparison in agar between devices

Drug delivery was quantified in vitro by flowing MagO$_2$MB-RB ($1.7 \times 10^8 \pm 0.6 \times 10^8$ MB/mL, [RB] = 500 ± 50 μM) through a tissue mimicking agar phantom. The phantom body was formed within a Delrin frame filled with 1.25% agar gel. The cured agar phantom was 7 mm thick and covered in clear and acoustically transparent Mylar films on each side. Each phantom contained at least one straight channel of 1.2 mm diameter, with fittings on the frame for connection to a syringe pump and drain tubing. A tube size of 1.2 mm diameter was chosen as this was consistent with the vasculature which surrounds pancreatic tumour lesions. (246) During testing, the phantom was partially immersed in a water bath heated to $36 \pm 1°C$, with the upper phantom surface in air so that acoustic boundary conditions would be similar to those in the *in vivo* experiments. The phantom assembly was free of ferrous metal parts in order to minimize the likelihood of secondary magnetic fields influencing the results. For acoustic treatments (MAD or aMAD), the device was held in place with a lab clamp, and the cone tip was coupled to the phantom face with water. Acoustic drive pulses (3000 cycles of 1.17 MHz, 30% duty cycle) were provided so that the peak negative pressure 10 mm in front of the device would be 0.7 MPa. This level matched the spatial peak value from a separate device that had been used in previous SDT experiments. (214,247) Ultrasonic emissions from the channel were recorded using a single PCD. Initial positioning of the agar flow channel and the acoustic instrumentation was guided by a crosshair laser to ensure proper alignment. The MAD was used for: (i) its co-aligned magnetic and acoustic fields (group: "MAD") (ii) its magnetic field only (US off) (group: "Mag"), and (iii) its magnetic field (MAD US off) with the acoustic field of the (aMAD) to study the non-coaligned fields (group: "US + Mag"). The aMAD was also used on its own for the US only control (group: "US"). For all treatment groups, MagMB-RB were injected at a flow rate of 0.2 mL/min which. This flow rate produced a Reynolds number of 2.65 which is physiologically relevant. US was applied for 3.5 minutes,

after which the treated channel was rinsed with 1 mL deionised water. The agar channel was immediately cut out (0.7 mL volume) and reserved for analysis after the experiment. After all groups were completed in a single test day, the reserved cut out agar channels were melted, sampled onto a pre-heated 96-well plate and left to equilibrate at 45°C for 15 minutes. Absorbance spectra were acquired at that temperature using a plate reader to measure the amount of RB delivered in the agar volume. Spectra were normalised to no-treatment controls and the samples' absorption intensities at 559 nm were compared to a standard curve for biotin-RB in melted 1.25% agar at 45°C ($R^2 = 0.9991$).

2.17. Culture of MCF-7 spheroids

MCF-7 cells were maintained using Dulbecco's Modified Eagle's Medium (DMEM) containing 1 g/L glucose and supplemented with 100 U/mL penicillin, 100 mg/mL streptomycin, and 10% fetal bovine serum (FBS) in a humidified 5% CO_2 atmosphere at 37°C. Spheroids were generated by growing MCF-7 cells in 96 well Carrier Plates (ULA) from PerkinElmer. Cells were seeded (8 x10^3, 100 μL) in selected wells. After 24 hrs, 100 μL of media was added to each well and plates were incubated at 37°C in a humidified 5% CO_2 atmosphere for a further 3 days to allow the cells to aggregate. Media was replenished every 3 days by removing 100 μL of old media and replacing it with 100 μL of fresh media.

2.18. Culture of Panc-1 spheroids

The human primary pancreatic carcinoma cell line PANC-1 was maintained in Dulbecco's Modified Eagle's Medium (DMEM) containing 1 g/L glucose and supplemented with 100 U/mL penicillin, 100 mg/mL streptomycin, and 10% fetal bovine serum (FBS). Cells were incubated at 37°C in a humidified atmosphere with 5% CO_2. Spheroids were prepared by seeding 2000 cells (200 uL) into a pre-coated 96-well plate (60 uL 1.5% agarose per well) for 4 days.

2.19. In vitro cytotoxicity in MCF-7 Spheroids

After 3 days of incubation following seeding, spheroids were allocated to groups and treated according to the following conditions: untreated (drug-free

medium), MB (no drugs), PTX/Dox only ([PTX] = 0.34 μM, [Dox] = 1 μM), and MB-PTX-Dox / MB-PTX-RB ([Dox] = 1 μM, [RB] = 10 μM). Where required, individual wells were then placed in direct contact with the emitting surface of a Sonidel SP100 sonoporator with US gel used to mediate contact. Each well was treated with US for 30 seconds (frequency - 1 MHz, power density - 3.0 W/cm^2, duty cycle - 50%, PRF = 100 Hz). Plates were incubated in a humidified 5% CO_2 atmosphere at 37°C for 3 hrs and then wells were washed 3 times with PBS before fresh medium was added. 48 hrs after treatment, 5 spheroids per replicate from each condition were collected in an Eppendorf tube, washed with PBS and then incubated with trypsin/EDTA for 15 min at 37°C. The resultant cellular suspension was then incubated for 3 hrs with MTT [10 μL (5 mg/mL) in 100 μL of medium). The absorbance was then measured at 570 nm using FLUOstar Omega microplate reader. Data were expressed as % cell viability by comparison with untreated controls. In addition to MTT analysis, propidium iodide (P.I.) staining was also performed to determine cellular damage to the spheroid corona. Following treatment, spheroids were washed 4 times with PBS to remove excess medium and then incubated with a solution of P.I. in PBS (100 μg/mL). Spheroids were then incubated in the dark at room temperature for 40 min and then washed 3 times with PBS to remove excess P.I. Micrographic images were recorded using a NIKON Eclipse E400 Phase contrast microscope in bright field and fluorescence modes (540 nm band pass excitation and 570 nm long pass emission filter). Image J software was used to quantify P.I. fluorescence and it was expressed as a % of P.I. fluorescence intensity/μm^2, i.e. the P.I. fluorescence was normalized according to the area of the spheroid.

2.20. In vitro cytotoxicity in Panc-1 Spheroids

Panc-1 spheroids were cultured as described above. The media in each well was replaced with either fresh drug-free media, MB-PTX ([5 μM]), MB-Gem-RB ([6.8 μM]) and MB-PTX-Gem-RB ([PTX] – 5 μM, [Gem/RB] – 6.8 μM), MB-LipidGem ([LipidGem] = 10 μM) or MB-LipidGem-PTX ([Lipid-Gem] = 10 μM, [PTX] = 6.2 μM). Wells were then treated individually with US for 30 seconds (frequency - 1 MHz, power density - 3.0 W/cm^2, duty cycle - 50%, PRF – 100 KHz). Two days after initial treatment, Panc-1 spheroids were washed four times with PBS to remove excess drug and then incubated with a solution P.I. in PBS (100 μg/mL).

Spheroids were then incubated in the dark at room temperature for 40 min and then washed 3 times with PBS to remove excess P.I. Micrographic images were recorded using a NIKON Eclipse E400 Phase contrast microscope in bright field and fluorescence modes (540 nm band pass excitation and 570 nm long pass emission filters). Image J software was used to quantify P.I. fluorescence and it was expressed as a % of P.I. fluorescence intensity/μm^2, i.e. the P.I. fluorescence was normalized according to the area of the spheroid. Additionally, total cell viability within the spheroid structure was determined suing an MTT assay. After 48 hrs following treatment, 5 spheroids per replicate from each condition were collected in an Eppendorf tube, washed with PBS and then incubated with trypsin/EDTA for 15 min at 37°C. The resultant cellular suspension was then incubated for 3 hrs with MTT [10 μL (5 mg/mL) in 100 μL of medium). The absorbance was then measured at 570 nm using FLUOstar Omega microplate reader. Data were expressed as % cell viability by comparison with untreated controls.

2.21. In vivo cytotoxicity in MCF-7 xenografts treated with O$_2$MB-PTX-Dox and/or O$_2$MB-PTX-RB ± US

All animals employed in this study were treated humanely and in accordance with licenced procedures under the UK Animals (Scientific Procedures) Act 1986. MCF-7 cells were maintained using Dulbecco's Modified Eagle's Medium (DMEM) containing 1 g/L glucose and supplemented with 100 U/mL penicillin, 100 mg/mL streptomycin, and 10% fetal bovine serum (FBS) in a humidified 5% CO$_2$ atmosphere at 37°C. MCF-7 cells (5 x10^6) in 100 μL Matrigel were sub-cutaneously implanted into the rear dorsum of 8-week old female SCID (C.B-17/IcrHan®Hsd-Prkdcscid) mice. Palpable tumours appeared approximately 1-2 weeks after cell implantation. Once tumours became palpable, dimensions were measured using Vernier callipers. Tumour volume was calculated using the equation:

Equation 2.

$$Tumour\ volume = \frac{length * width * height}{2}$$

Once tumours reached approximately 65 mm^3 animals were separated into the following groups: Group 1 remained untreated, groups 2 and 3 received an intravenous (IV) injection (50 μL) of a mixed suspension of O^{2}MB-PTX-RB and O$_2$MB-PTX-Dox (6.18 x10^7 MB, [PTX] = 1.13 $\pm$ 0.16 mg/kg, [RB] = 2.63 $\pm$ 0.35 mg/kg, [Dox] = 0.97 $\pm$ 0.15 mg/kg with (group 2) or without (group 3) US exposure. Group 4 received an I.V injection (100 μL) of a Cremophor suspension containing PTX (4.7 mg/kg) and Dox (2.5 mg/kg). US was administered directly to the tumour site using a Sonidel SP100 sonoporator (3.5 W/cm^2, 1 MHz, 30% duty cycle, and PRF = 100 Hz; PNP = 0.48 MPa; M.I. = 0.48) during, and 30 min after I.V administration (for a total of 7.0 min) using US gel to mediate contact. Animals were treated on days 0, 7 and 21 and both the tumour volume and body weight measurements recorded at the indicated times.

2.22. In vivo cytotoxicity experiments in BxPC-3 xenografts

BxPC-3 cells were maintained in RPMI 1640 both supplemented with 100 U/mL penicillin, 100 mg/mL streptomycin, and 10% fetal bovine serum (FBS) in a humidified 5% CO$_2$ atmosphere at 37°C. BxPC-3 cells (5 x10^6) in 100 μL Matrigel were sub-cutaneously implanted into the rear dorsum of 8-week old female SCID (C.B-17/IcrHan®Hsd-Prkdcscid) mice. Palpable tumours appeared approximately 1-2 weeks after cell implantation. Once tumours became palpable, dimensions were measured using Vernier callipers. Tumour volume was calculated using the equation outlined in Section 2.21. For experiments discussed in chapter 4 animals were treated with either an intravenous (IV) injection (100 μL) of a suspension of O^{2}MB-PTX-Gem-RB (6.86 x10^7 $\pm$ 1.99 x 10^6 MB) ([PTX] – 2.44 $\pm$ 0.37 mg/kg, [Gem] - 0.5 $\pm$ 0.04 mg/kg, [RB]- 1.85 $\pm$ 0.14 mg/kg) or an I.P injection (100 μL) of gemcitabine hydrochloride in sterile PBS (120 mg/kg) or remained untreated. For experiments discussed in chapter 5 animals were treated with either an intravenous (IV) injection (100 μL) of a suspension of MagO$_2$MB-RB-Gem ([MB] = (1.25$\pm$0.41) x 10^9 MB/mL, [RB] – 2.54 $\pm$ 0.39 mg/kg, [Gem] - 0.69 $\pm$ 0.11 mg/kg) or an I.P injection (100 μL) of gemcitabine hydrochloride in sterile PBS (120 mg/kg). For experiments described in chapter 6 animals were treated with either an intravenous (IV) injection (100 μL) of a suspension MB-LipidGem (9.97 x10^8 MB/mL, 2.77 mg/kg), MB-LipidGem-PTX – 8.6 x10^8 MB/ mL, [LipidGem] = 3.15 mg/kg, [PTX] = 1.98 mg/kg) or an I.P injection (100 μL) of

gemcitabine hydrochloride in sterile PBS (120 mg/kg) For experiments discussed in chapter 6, US was administered directly to the tumour site using a Sonidel SP100 sonoporator (3.5 W/cm^2, 1 MHz, 30% duty cycle, and PRF = 100 Hz; PNP = 0.48 MPa; M.I. = 0.48) during I.V/I.P injection. For experiments described in chapter 4, US was applied as described above with the addition of a second US treatment applied 30 min after I.V administration (for a total of 7.0 min). For experiments described in chapter 5, US was applied using the MAD/aMAD devices. The drive instrumentation and settings were the same as those used for the *in vitro* drug delivery experiments described in Section 2.16. The cone of the MAD (or aMAD) was coupled to the skin of the subject using US gel. In order to minimize acoustic field uncertainties and tissue damage risk, the subjects were treated lying prone over a mat of US absorbing material (Aptflex F28, Precision Acoustics, Dorset, UK). To improve free transmission of sound into the absorber, the abdominal hair was removed from the subjects, and their skin coupled to the mat with US gel. For experiments discussed in chapters 4 and 6, tumour volume was measured using callipers as described in Section 2.21 and for chapter 5, tumour volume was measured using the Peira TM900 tumour measuring device (Beerse, Belgium). The TM900 platform includes measurement software allowing visualisation of the tumour topography, allowing tumour dimensions (weight, length and height) to be automatically measured. For all in vivo experiments, subject weight was monitored closely for the entirety of the investigation.

2.23. In vivo cytotoxicity experiments in MIA-PaCa-2 xenografts

MIA-PaCa-2 cells were maintained in DMEM medium supplemented with 100 U/mL penicillin, 100 mg/mL streptomycin, and 10% fetal bovine serum (FBS) in a humidified 5% CO_2 atmosphere at 37°C. MIA-PaCa-2 cells (5 x10^6) in 100 µL Matrigel were sub-cutaneously implanted into the rear dorsum of 8-week old female SCID (C.B-17/IcrHan®Hsd-Prkdcscid) mice. Palpable tumours appeared approximately 1-2 weeks after cell implantation. Once tumours became palpable, dimensions were measured using Vernier callipers. Tumour volume was calculated using the equation outlined in Section 2.21. Group 1 remained untreated, group 2 received an I.V injection (100 μL) of a suspension of O^{2}MB-PTX-Gem-RB (6.47 x 10^7 ± 1.86 x10^6 MBs) ([PTX] - 3.38 ± 0.21 mg/kg, [Gem] – 0.82

± 0.06 mg/kg, [RB] – 3.02 ± 0.24 mg/kg). Group 3 received an intravenous (IV) injection (100 μL) of a suspension of O$_2$MB-PTX (7.01 x 107 ± 1.5 x 10^6 MBs) ([PTX] - 4.69 ± 0.75 mg/kg). Group 4 received an I.P injection (100 μL) of gemcitabine hydrochloride in sterile PBS (120 mg/kg) and an I.V injection of a Cremophor solution containing PTX (4.7 mg/kg). US was administered directly to the tumour site using a Sonidel SP100 sonoporator (3.5 W/cm^2, 1 MHz, 30% duty cycle, PRF = 100 Hz, PNP = 0.48 MPa, M.I. = 0.48) during, and 30 min after I.V administration (for a total of 7.0 min) using US gel to mediate contact. Animals were treated on days twice weekly and both the tumour volume and body weight measurements recorded at the indicated times.

2.24. In vivo safety determination and blood analysis in healthy non tumour bearing mice

Healthy non-tumour bearing mice were separated into groups and treated with either US treatment only (Frequency = 1 MHz, power density = 3.5 W/cm2, duty cycle = 30%, PNP 0.4 MPa, duration 3.5 min) directed to the pancreas as would be the case in orthotopic tumour treatment, an intravenous (IV) injection (100 μL) of a suspension of O$_2$MB-PTX-Gem-RB (6.58 x10^7 ± 1.25 x10^6 MB, [PTX] = 2.03 ± 0.19 mg/kg [Gem] = 0.72 ± 0.07 mg/kg, [RB] = 2.66 ± 0.27 mg/kg), an intravenous (IV) injection (100 μL) of Gem, PTX and RB. PTX and RB were delivered by I.V injection with PTX pre-formulated in a cremaphor EL vehicle while Gem was administered by I.P injection ([Gem] = 120 mg/kg, [PTX] = 15 mg/kg, [RB] = 6 mg/kg) or remained untreated. The body weights of the animals in each group were recorded daily and 14 days following treatment, blood samples were removed and analysed for several key biochemical and haematological markers in both whole blood and serum. These markers included urea and alanine aminotransferase (ALT) which are markers for kidney and liver function respectively.

2.25. Ultrasound Parameters

The US source used in chapters 3,4 and 6 was the Sonidel SP100 was used as the US source. The specific US parameters used in chapters 3-6 were consistent with previous publications. (238)(240)(214)(247)(237)

Chapter 3

Treatment of MCF-7 Breast Cancer
Using Ultrasound Responsive
Microbubbles Loaded with
Paclitaxel, Doxorubicin and Rose
Bengal.

Chapter 3 - Treatment of MCF-7 Breast Cancer Using Ultrasound Responsive Microbubbles Loaded with Paclitaxel, Doxorubicin and Rose Bengal

3.0. Introduction

Breast cancer is the most prevalent form of cancer worldwide with 55,200 new cases reported in the UK alone in 2015. (248) Mastectomy is a common treatment for breast cancer with approximately 19,000 mastectomy surgeries performed in the UK each year. (249) As the physical and psychological effects of this treatment can be considerable, there is a growing need for more effective non-surgical treatments to reduce the overall mastectomy rate. Approximately 15% of patients will present with triple negative breast cancer. This type of cancer is characterised by the lack of lack of expression of the estrogen receptor (ER), progesterone receptor (PR), and human epidermal growth factor receptor 2 (HER2). (250) Although this subtype of patient is not eligible for hormone drugs, they are more likely to respond to neo-adjuvant chemotherapy. Neoadjuvant chemotherapy involves treatment with chemotherapy prior to surgical resection. There are four main rationales for this type of therapy. Firstly, it is expected to shrink the size of the primary tumour making an otherwise inoperable tumour, operable. Secondly, by reducing the size of the tumour, this should allow for the patient to undergo the less invasive and life altering breast conservation surgery (BCS). Thirdly, patients with locally advanced disease, who are at higher risk of developing metastases, could benefit from early, pre-operative chemotherapy. Finally, neoadjuvant chemotherapy gives provides the opportunity to observe potential tumour shrinkage, serving as a useful prognostic tool. (251,252) Neo-adjuvant chemotherapy has been used successfully to downstage tumours in advance of surgery and enable their removal by less invasive lumpectomy procedures. (253,254). This approach has proven effective in increasing the number of patients eligible for BCS without posing a risk to the overall or progression-free survival rate. (255) However, the chemotherapies used in these regimens are non-targeted to tumour tissue hence large quantities are administered to achieve a therapeutic response which often leads to undesirable side effects for the patient. (256)

Despite the success of surgical resection in improving the overall progression free survival of patients suffering with breast cancer, localised recurrence of the cancer into the chest wall following operable breast cancer has a reported 10-year incidence rate of 4–10% for patients that have underwent a full mastectomy and 10–16% for patients who have underwent BCS followed by adjuvant radiation therapy. (257–259) Unfortunately for this group of patients, the treatment options are limited with further surgical resection proving ineffective in many cases. Additional treatment with chemotherapy has shown signs of promise however the effect on the quality of life for these patients is reported to be considerable. There is therefore a need for more targeted treatments which can enable the effective treatment of these cancers without considerably affecting the quality of life for the patient.

As mentioned in Section 1.4.3.1.3, UTMD has been used previously in pre-clinical experiments to deliver the sonosensitiser Rose Bengal (RB) in combination with the antimetabolite drugs 5-flourouracil (5-FU) or Gemcitabine. (238,240,247) This strategy proved effective in treating pancreatic adenocarcinoma (PDAC) in *in vitro* and *in vivo* models of the disease and was able show significant control of tumour growth. Furthermore, a significantly lower dose was required to achieve a better therapeutic outcome than the clinical standard control groups treated with free drugs (i.e. non-MB bound). However, these works were limited in that the co-delivery of both the chemotherapy and the sonosensitiser was achieved through mixing of two separately produced batches. This work was very much focussed on pancreatic cancer and therefore utilised drugs indicated for this disease as part of the MB platform. To broaden the scope of UTMD mediated chemo-SDT to other cancers, methods for incorporating different chemotherapy drugs within the MB platform are required. To this end, the ability to incorporate two or more payloads within a single MB formulation would be hugely beneficial.

Paclitaxel (PTX) and Doxorubicin (Dox) are two chemotherapies commonly used in the management of breast cancer. PTX is an anti-cancer drug from the taxane class. It was originally extracted from samples from the bark of the Pacific yew tree. PTX primarily acts upon microtubules which are polymers made up of α and β- heterodimers. It stabilizes them against depolymerization and inhibits cell replication. (260) It has also been shown to bind to the

antiapoptotic gene Bcl-2, thus inducing apoptosis. (261) Given the likelihood of resistance to chemotherapeutic agents, it is commonplace to administer combinations of anti-cancer drugs so that separate cellular mechanisms can be targeted and exploited. Dox has been shown to be remarkably effective when administered in combination with PTX. Dox is a member of the anthracycline class of anti-cancer drugs. The mode of action of Dox is still a matter of debate however the leading hypothesis is that it inhibits DNA synthesis through obstruction and inhibition of topoisomerase II. (125) Given that previous studies have demonstrated the benefit of combining chemotherapy and SDT in pancreatic cancer, it was of interest to determine the effect of UTMD mediated chemo-SDT in the treatment of breast cancer, using PTX and Dox as chemotherapies and Rose Bengal as the SDT sensitiser. For practical reasons, it is desirable to the minimise the number of separate MBs required to deliver these three payloads. While it was not possible to design a single MB formulation carrying all three payloads at this stage, it was possible to use two separate MB formulations instead of three. To this end, the hydrophobic oil layer of the MB shell was utilised to encapsulate PTX, while Dox or RB was attached to the MB surface using the biotin-avidin interaction. PTX is a notoriously hydrophobic drug (cLogP = 4.73) and is an ideal candidate for incorporation within the oil layer. In contrast, the hydrophilic nature of Dox (cLogP = -0.78) and RB (cLogP = 3.46), meant they were not suitable for encapsulation in the MB oil layer and required derivatisation with biotin to enable attachment to the MB shell.

In this chapter, the preparation of these two MB formulations is discussed, one carrying PTX in the MB oil layer and Dox attached to the surface (MB-PTX-Dox) while the second also carried PTX in the oil layer but RB attached to the MB surface (MB-PTX-RB). Each formulation was characterised in terms of MB yield, stability and drug loading, while the efficacy of MB mediated chemo-sonodynamic therapy was determined in a three-dimensional (3D) spheroid model of human breast cancer and in a murine model of the disease bearing subcutaneous MCF-7 tumours.

3.1. Hypothesis and specific objectives

The main aim of this study was to determine whether O_2MB with PTX incorporated into the lipid shell and with Dox or RB attached to the MB surface perform significantly better than either Dox/PTX or SDT treatment alone in *in vitro* and *in vivo* models of MCF-7 breast cancer. The specific objectives were to:

1. determine the benefit of combining Dox / PTX with SDT in a MCF-7 breast cancer cell line.

2. prepare and characterise MB with PTX hydrophobically incorporated into the phospholipid shell (MB-PTX).

3. synthesise and characterise biotin functionalised Dox (biotin-Dox) and RB derivatives (biotin-RB).

4. prepare and characterise MB-PTX with either biotin-Dox (MB-PTX-Dox) or biotin-RB attached (MB-PTX-RB) to the MB surface.

5. determine the effectiveness of chemo-SDT using MB-PTX-Dox and MB-PTX-RB in a 3D MCF-7 spheroid model of breast cancer.

6. determine the effectiveness of chemo-SDT using O_2MB-PTX-Dox and O_2MB-PTX-RB in SCID mice bearing ectopic MCF-7 tumours.

3.2. Results and discussion

3.2.1. Effect of combining PTX, RB and Dox on MCF-7 cell colony forming ability

In advance of preparing and testing the MB-PTX-Dox and MB-PTX-RB formulations, the effectiveness of combining PTX, Dox and SDT treatments on the viability of MCF-7 cells was investigated. In this experiment, the concentration of each individual drug used was intentionally sub-lethal (i.e. drug concentration $< LD_{50}$), so that any benefit obtained by the combination treatment could easily be identified. In addition, as the action of US can influence the cellular uptake of drugs due to sonoporation, cells treated with Dox or PTX were also exposed to US, to control for any potential effects as a result of US exposure during SDT treatment. (227) Following treatment, the ability of cells in each treatment group to form colonies was investigated by performing a clonogenic assay. Cells from treated groups were seeded in 6 well plates and incubated for 8 days after which they were fixed and stained with crystal violet solution. Images were then captured of each well and colony numbers were subsequently analysed using ImageJ image analysis software.

The results are shown in Figure 3.4 and reveal no reduction in colony number for cells treated with a combination of PTX, Dox and RB in the absence of US compared to untreated cells. Treatment of cells with PTX + US, RB + US (i.e. SDT) or Dox + US reduced colony number by 7.3, 18.8 and 29.3% respectively compared to untreated cells, while cells treated with combined PTX, Dox and RB + US reduced the colony number by 44.0%. The lack of efficacy for the combined drug group in the absence of US was not surprising as sub-lethal doses of the drugs were used. However, the significant improvement in efficacy following exposure to US may result from a sonoporative effect that improves the uptake of these drugs. The fact that the greatest reduction in colony number was observed for the combined PTX, Dox and SDT treatment group suggests that these three treatments complement each other and improve the overall cytotoxic effect observed.
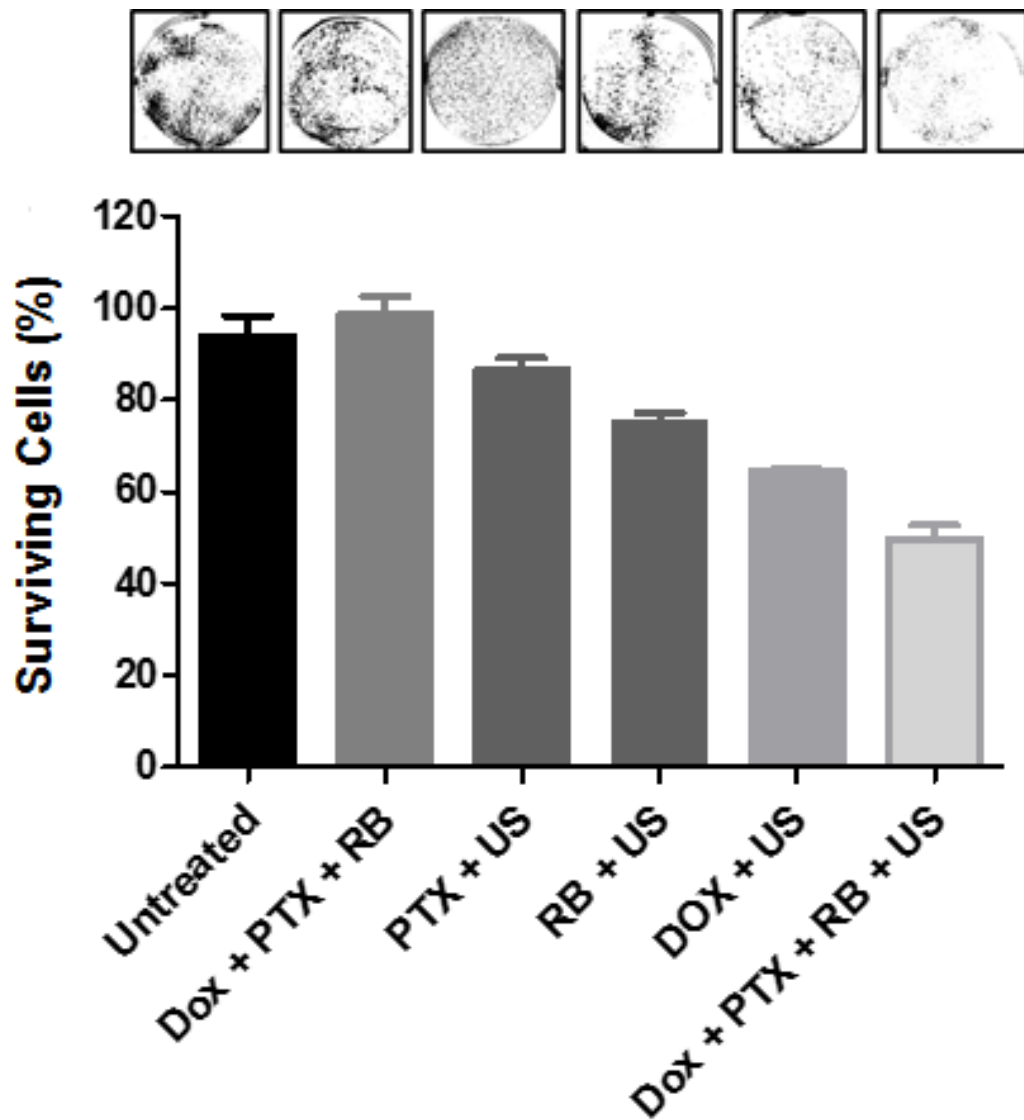
Figure 3.4. Plot showing percentage of surviving MCF-7 cells for each of the treatment groups.
Cells were treated with PTX +US (1 nM), Dox +US (10 nM), RB +US (10 nM) and PTX + Dox +
RB +US ([PTX] = 1 nM, [Dox] = 10 nM, [RB] = 10 nM). Crystal violet staining of representative
images are shown in the panel above each data bar. Error bars represent ± the standard error
(n = 3).

3.2.2. Preparation and characterisation of MB with PTX hydrophobically incorporated into the phospholipid shell (MB-PTX).

Encouraged by these results, the next step was to incorporate PTX, Dox and RB into the MB delivery vehicle as described in Section 2.8. Schematic representations of the MB-PTX-Dox and MB-PTX-RB formulations are shown in Figure 3.5 and illustrate the incorporation of PTX in the hydrophobic acyl layer of the MB shell with either biotin-Dox or biotin-RB attached to the MB surface using the biotin-avidin linkage.
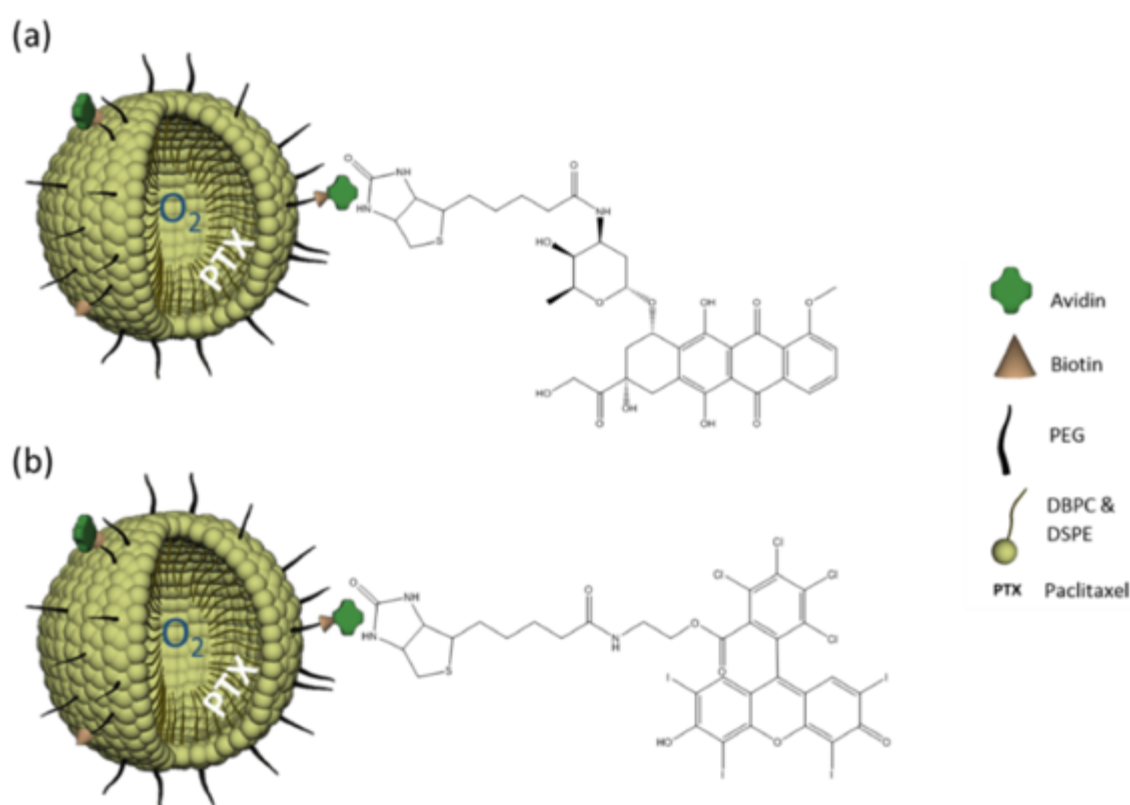
Figure 3.5. Schematic representation of (a) O₂MB-PTX-DOX and (b) O₂MB-PTX-RB

3.2.2.1. Preparation of MB-PTX

As described in Section 1.3.3.1, there are a variety of different protocols for synthesising lipid coated MBs. The first step in most cases involves the formation of a liposomal suspension through the hydration of a thin, dry phospholipid film in aqueous media, maintained above the lipid phase transition temperature. There are also several literature examples describing the synthesis of lipid-based

micro/nano-particles containing PTX. (262–267) In the majority of cases, PTX is either directly embedded into the MB shell or incorporated into liposomes which are subsequently conjugated to the MB surface. It was therefore hypothesised that PTX, being a highly hydrophobic drug, with a logP of approximately 3.96 and an aqueous solubility of less than 0.01 mg/mL (~10 μM) (268), should become embedded within the hydrophobic acyl chains of the amphiphilic phospholipids which coat the MB, providing the potential to load a second drug onto the surface of the MB.

The first step in the synthesis of MB-PTX was to form a phospholipid suspension containing PTX using the thin film hydration technique discussed previously. This was achieved by dissolving DBPC, DSPE-PEG (2000), DSPE-PEG (2000)-biotin and PTX in chloroform. After evaporation of the solvent the dried film was re-hydrated in a mixture of PBS, glycerol and propylene glycol and heated at 80°C to enable vesicle formation. The contents were then sonicated using a probe sonicator at low amplitude (22%) to enhance dispersion of the PTX within the particle suspension. To form the MBs, the PTX-lipid suspension was sonicated at a higher amplitude (89%) under an atmosphere of PFB gas. The solubility of PFB gas in aqueous media is relatively low and so helps to provide stability to the MB suspension prior to oxygenation. The newly formed MB-PTX suspension was then isolated by low-speed centrifugation and the infranatant (liquid below the MB cake) discarded to ensure non-incorporated PTX or lipids were removed. The MB-PTX were washed by mixing with PBS and again isolated by centrifugation.

3.2.2.2. Characterisation of MB-PTX

After each batch of MB-PTX were prepared, a sample was removed and the concentration and size of the MBs were analysed. This was achieved by loading a small diluted sample of the MB suspension into a haemocytometer chamber and capturing images using an optical microscope. The images were then analysed using a bespoke MATLAB image analysis algorithm as described in Section 2.9. A representative analysis is given in Figure 3.6 and reveals that PFB-MB-PTX have a mean diameter of 1.14 ± 0.73 μm and a mean concentration of $1.72 \times 10^9 \pm 2.91 \times 10^8$ MB/mL. These results were consistent with previous studies

where drug loaded MBs were synthesised suggesting that the addition of PTX has little effect on the MB concentration or morphology. (267,269)
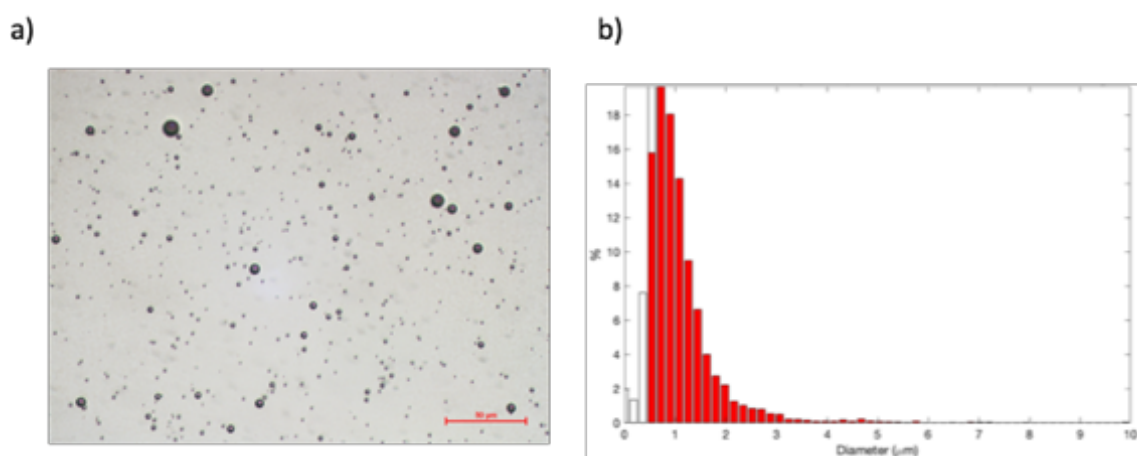
Figure 3.6. a) representative image of MB-PTX taken with 40x objective lens (1:25 dilution in PBS); b) corresponding size distribution analysis produced using a custom MATLAB algorithm (n=20 images). Scale bar represents 50 μm.

At this stage in the development process it was desirable to identify the amount of PTX that could be loaded into the MBs. To this end, three batches of MB-PTX were prepared with 0, 2.5 or 5 mg of PTX loaded into the lipid film prior to MB formation. A sample was taken from each batch and the MBs dissolved through the addition of acetonitrile. This sample was then diluted and was analysed using reverse phase HPLC. A calibration curve for PTX (Figure 3.7b) was constructed following the methods described in Section 2.10 using known concentrations PTX. Good linearity was observed between 0 and 0.6 mg/mL with an R^2 value of 0.9997. The equation of the line along with the peak area of the unknown sample was used to determine the amount of PTX within each of the batches.
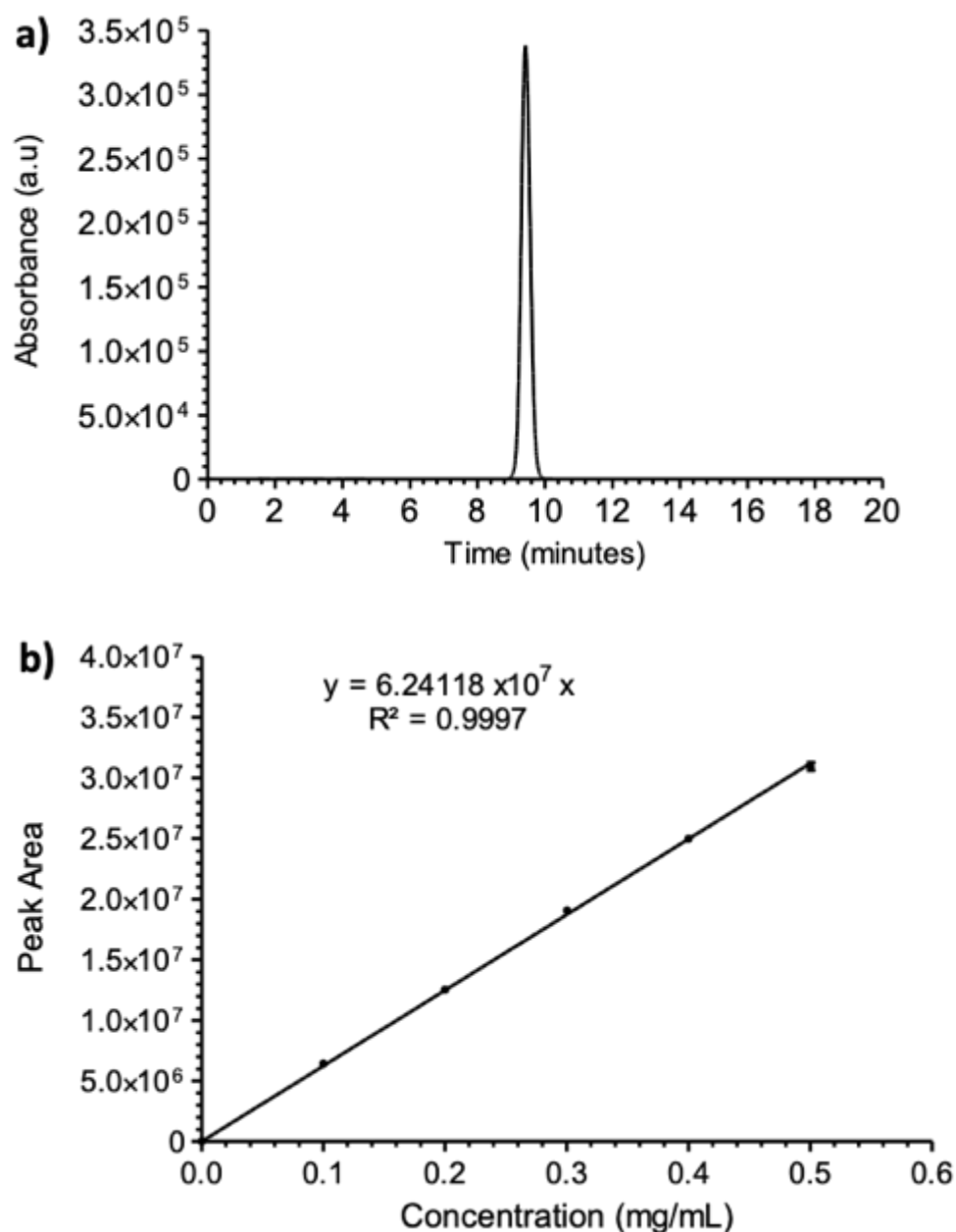
Figure 3.7. (a) Representative RP-HPLC-UV chromatogram of PTX and (b) Plot of peak area at 227 nm against concentration for PTX (n=3).

The loading of each batch of MB was normalised to MB concentration (i.e. µg / 10^8 MB). The mean PTX loading for the 2.5 mg loaded batches was 24.85 ± 5.78 µg/10^8 MB while for the 5 mg loaded batch PTX it was 62.75 ± 10.86 µg/10^8 MB (Figure 3.8). While no higher loadings were attempted, there may be capacity to further increase the loading of PTX in the MB shell by increasing the amount of the drug added during the film formation step. Loadings of higher than 5 mg have not been reported in the literature. In addition, 5 mg of PTX equates to

approximately the same total moles of phospholipid in the formulation. It is therefore likely that increasing this molar ratio further will have a minimal effect on drug loading.
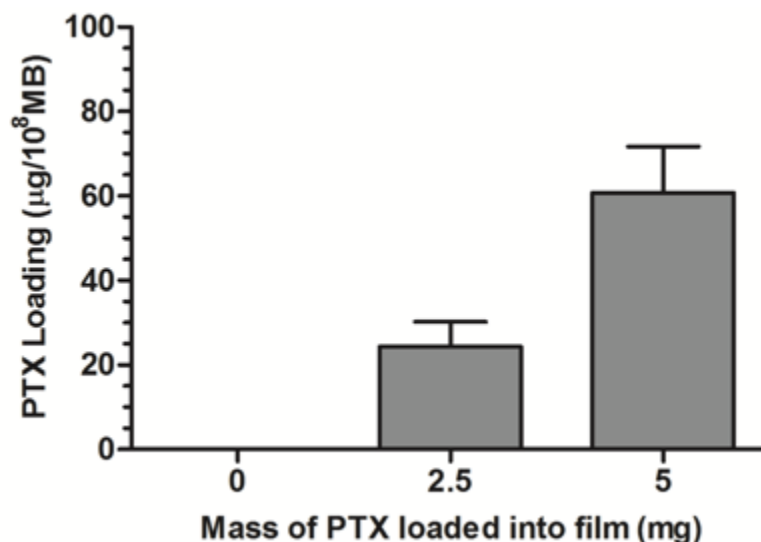
Figure 3.8. Graph showing the normalised loading of PTX in MB as the amount of PTX added to the lipid film increases from 2.5 to 5 mg (n=3). (2.5 mg batch: [PTX] = 24.85 ± 5.78 µg/10^8 MB, MB No = 8.69 x10^8 ± 2.77x10^7 MB and 5 mg batch: [PTX] = 62.75 ± 10.86 µg/10^8 MB, MB No = 9.79x10^8 ± 4.39 x10^7 MB).

3.2.2.3. Investigating the effect of PTX on MB stability at 37°C

The circulation half-life of commercial phospholipid contrast agents is typically less than 5 mins (270) so it is important that the MB concentration does not drop significantly over this time. It is also advantageous to ensure that if MB are prepared for clinical use (i.e. at the bedside), they have sufficient stability should any delay occur between preparation and use. Therefore, to identify if the addition of PTX into the phospholipid shell would reduce particle stability, a study was undertaken where normal MBs (i.e. prepared without PTX in the film) and O_2MB-PTX (prepared with 5 mg PTX in the film) were counted at various time-points following incubation at 37°C. The results are shown in Figure 3.9 and reveal a small but non-significant decrease in MB number for PTX-containing MB when compared to plain MB without PTX. However, more than 85% of the total MB population remained after 10 minutes incubation. This suggests that the

addition of PTX within the lipid monolayer does not significantly compromise MB stability.
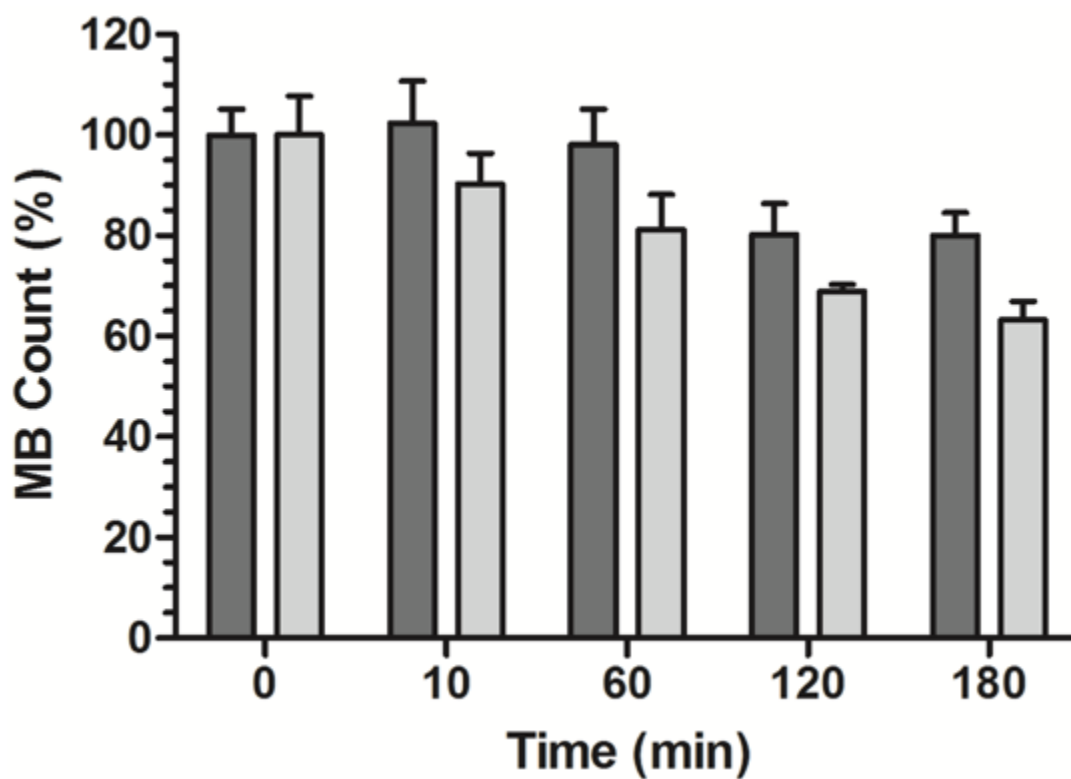
Figure 3.9. Plot showing % MB count of MBs containing no PTX (dark bars) or 5 mg of PTX (light bars) within the lipid film. (5 mg batch: [PTX] = 54.87 ± 10.28 µg/10^8 MB, MB No = 8.41x10^8 ± 2.78 x10^8 MB).

3.2.3. Synthesis of biotin-Dox and biotin-RB

To facilitate the attachment of Dox and RB to the surface of the microbubble, the biotin-avidin interaction was utilised as this has proven effective in previous studies.(238,240) It was therefore necessary to synthesise both biotin-Dox and biotin-RB to allow their attachment to the MB surface.

3.2.3.1. Synthesis and characterisation of biotin-Dox (5).

Biotin-Dox was synthesised according to the protocol outlined in Figure 3.10 and detailed in Section 2.2.
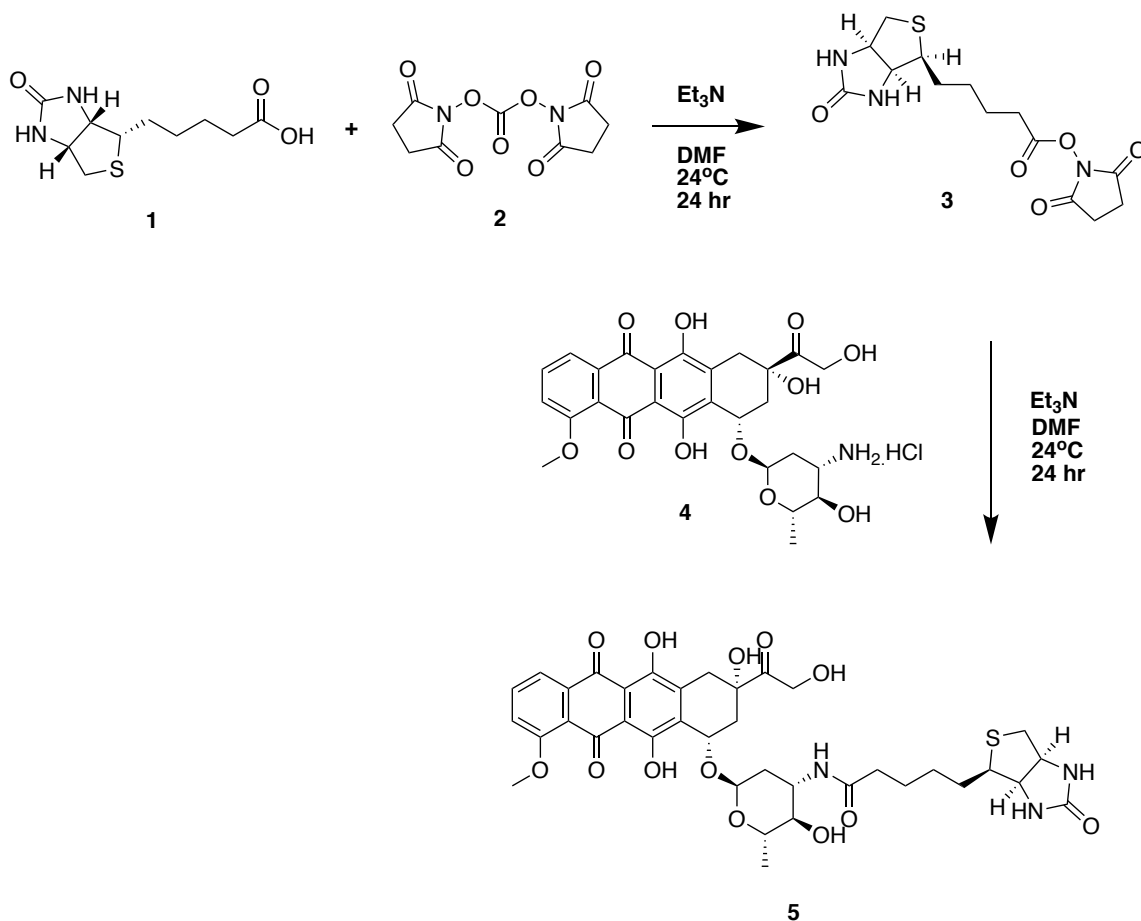
Figure 3.10. Synthetic procedure for the synthesis of biotin-Dox (5).

The first step of the reaction involved preparing the *N*-succinimidyl ester of biotin (**3**) (271) by reacting biotin (**1**) with *N,N′*-succinimidyl carbonate (**2**) in the presence of triethylamine (Et$_3$N) as a catalytic base. The activated ester of biotin was then reacted with the Dox daunosamine moiety (**4**) to form a

hydrolysable amide bond. The crude material was then purified using preparative thin layer chromatography (PTLC) to produce **5** in 70% yield.

The structure of biotin-Dox was confirmed using ESI-MS, ^{1}H-NMR and ^{13}C-NMR which are shown in Figures 3.11 – 3.14. The ^{1}H NMR spectrum is shown in Figure 3.11 and reveals a group of resonances between 1.27 and 1.56 ppm that represent the six methylene protons that are closest to the core biotin ring structure with the characteristic carbamide protons appearing as two sharp doublets between 6.29 and 6.36 ppm. The remaining two methylene protons appeared further downfield at 2.05 ppm due to their proximity to the amide bond. The 3 aromatic protons, corresponding to the anthraquinone unit, appeared on resonances centred at 7.59 and 7.84 ppm with the newly formed amide proton at appearing at 7.49 ppm. The stacked spectra shown in Figure 3.12 clearly shows the disappearance of the acidic proton from biotin (top spectrum, 12 ppm) and the appearance of the newly formed amide proton (bottom spectrum, 7.49 ppm). The ^{13}C NMR spectrum is shown in Figure 3.13 and reveals a resonance at 172 ppm corresponding to the newly formed amide carbonyl carbon. The remaining resonances in both the ^{1}H NMR and ^{13}C NMR spectra were assigned as indicated on the labelled structures accompanying each spectrum and this was facilitated by reference to the spectra of biotin and doxorubicin. The molecular weight of **5** was confirmed using ESI-MS. The ESI-MS spectrum is shown in Figure 3.14 and reveals a base peak of 792.2 Da corresponding to the $[M+Na]^+$ ion. These combined spectroscopic techniques confirmed the formation of **5**.
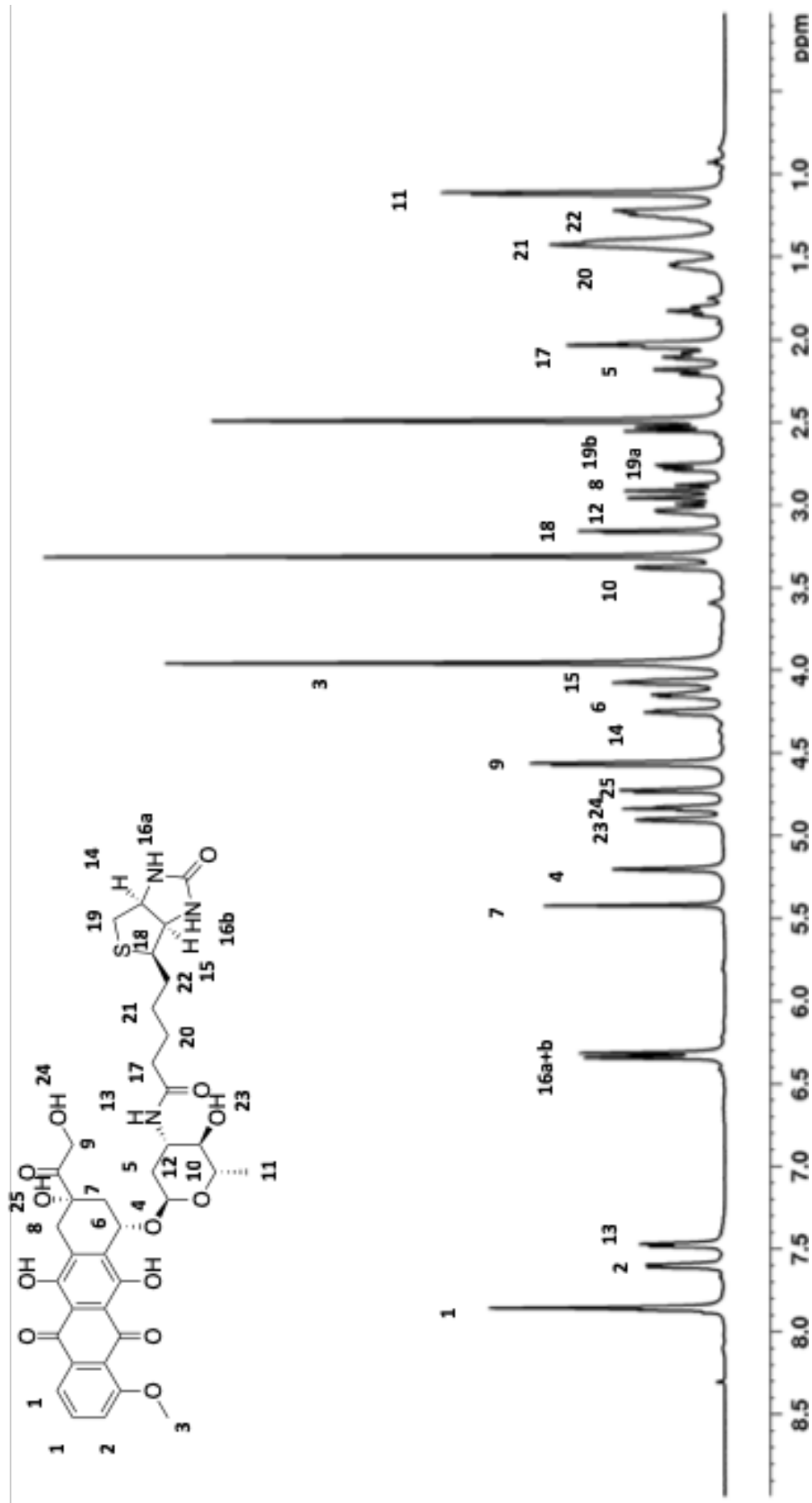
Figure 3.11. ^{1}H NMR spectrum of 5 recorded in DMSO-d6.

87
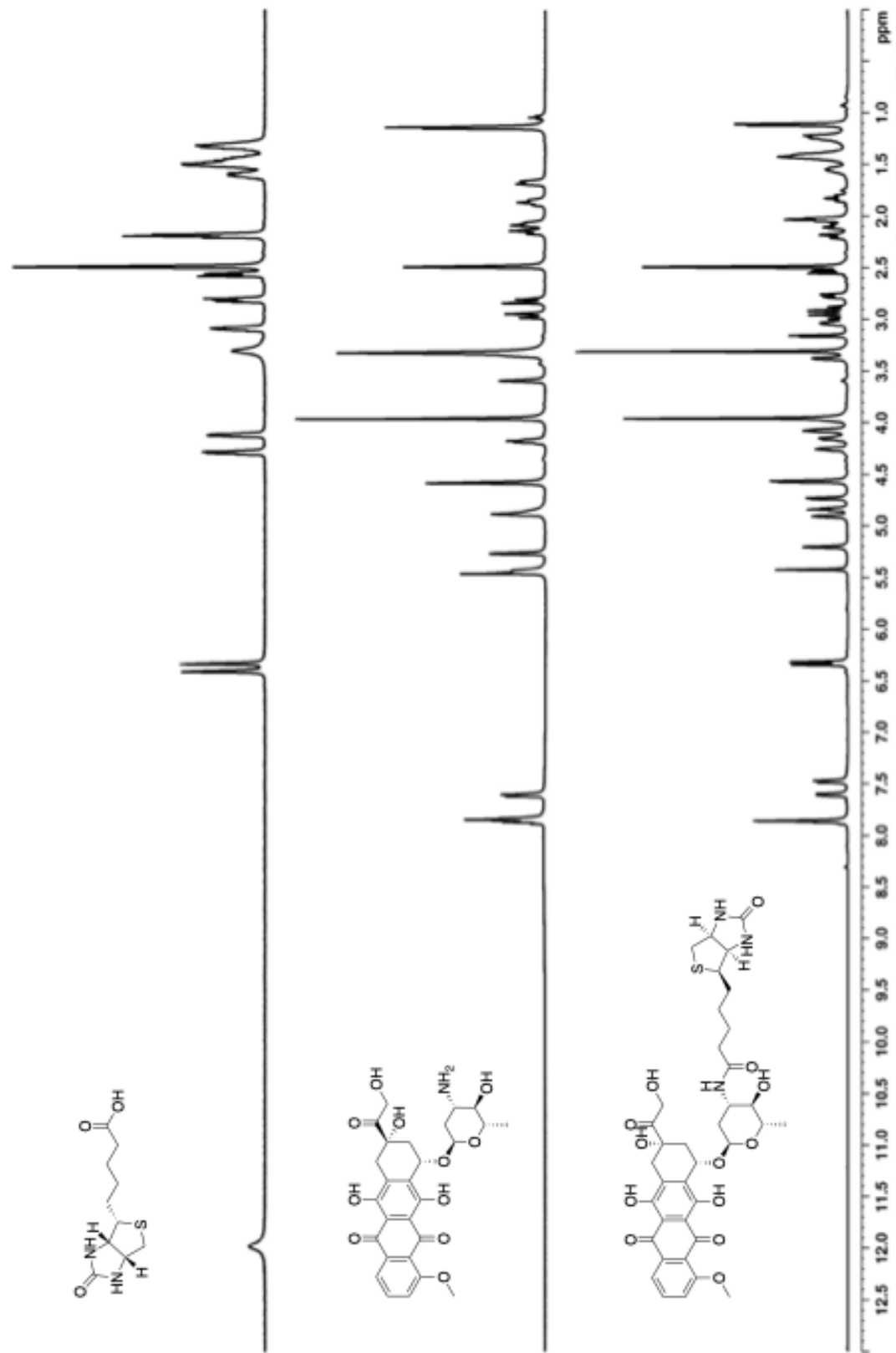
Figure 3.12. Stacked ^{1}H NMR spectra of 1 (top), 4 (middle) and 5 (bottom) recorded in DMSO-$d6$

88
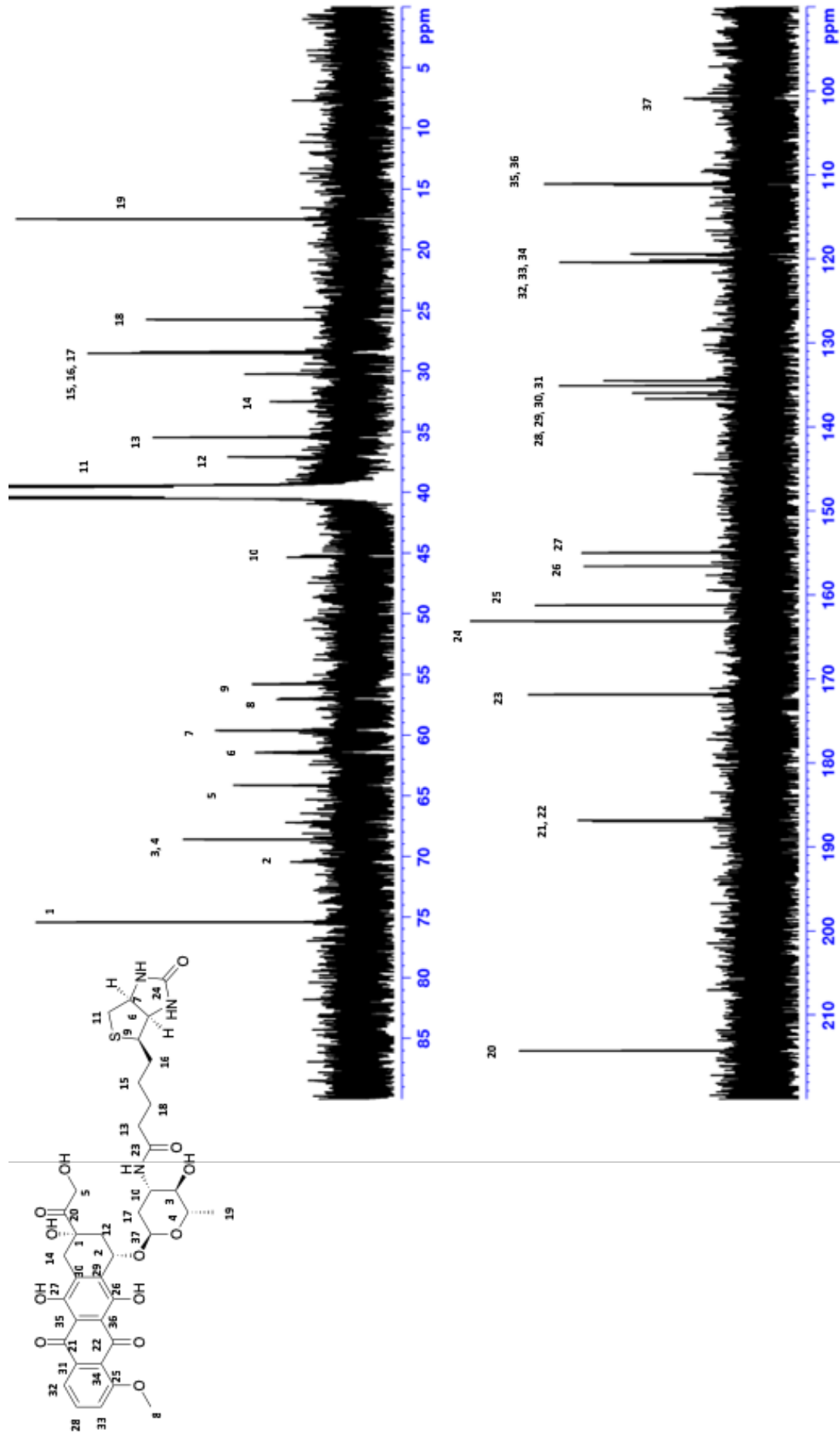
Figure 3.13. ^{13}C NMR spectrum of 5 recorded in DMSO-d6

89

Chemical Formula: C$_{37}$H$_{43}$N$_3$O$_{13}$S
Exact Mass: 769.2517
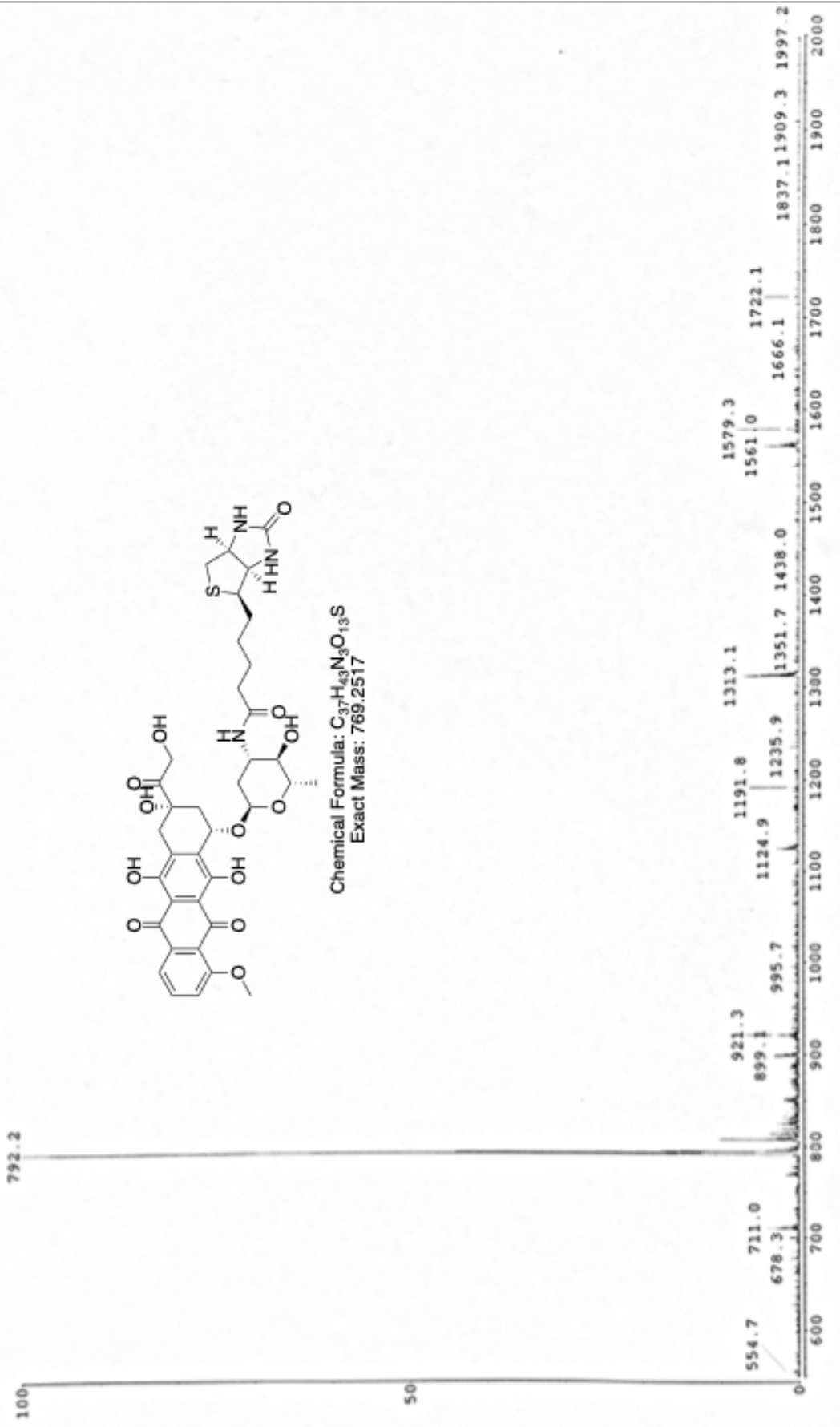
Figure 3.14. ESI-MS spectrum (positive mode) of 5 recorded in methanol.

90

3.2.3.2. Synthesis and characterisation of biotin-RB (8)

Biotin-RB was synthesised according to a literature procedure (214) as shown in Figure 3.15.
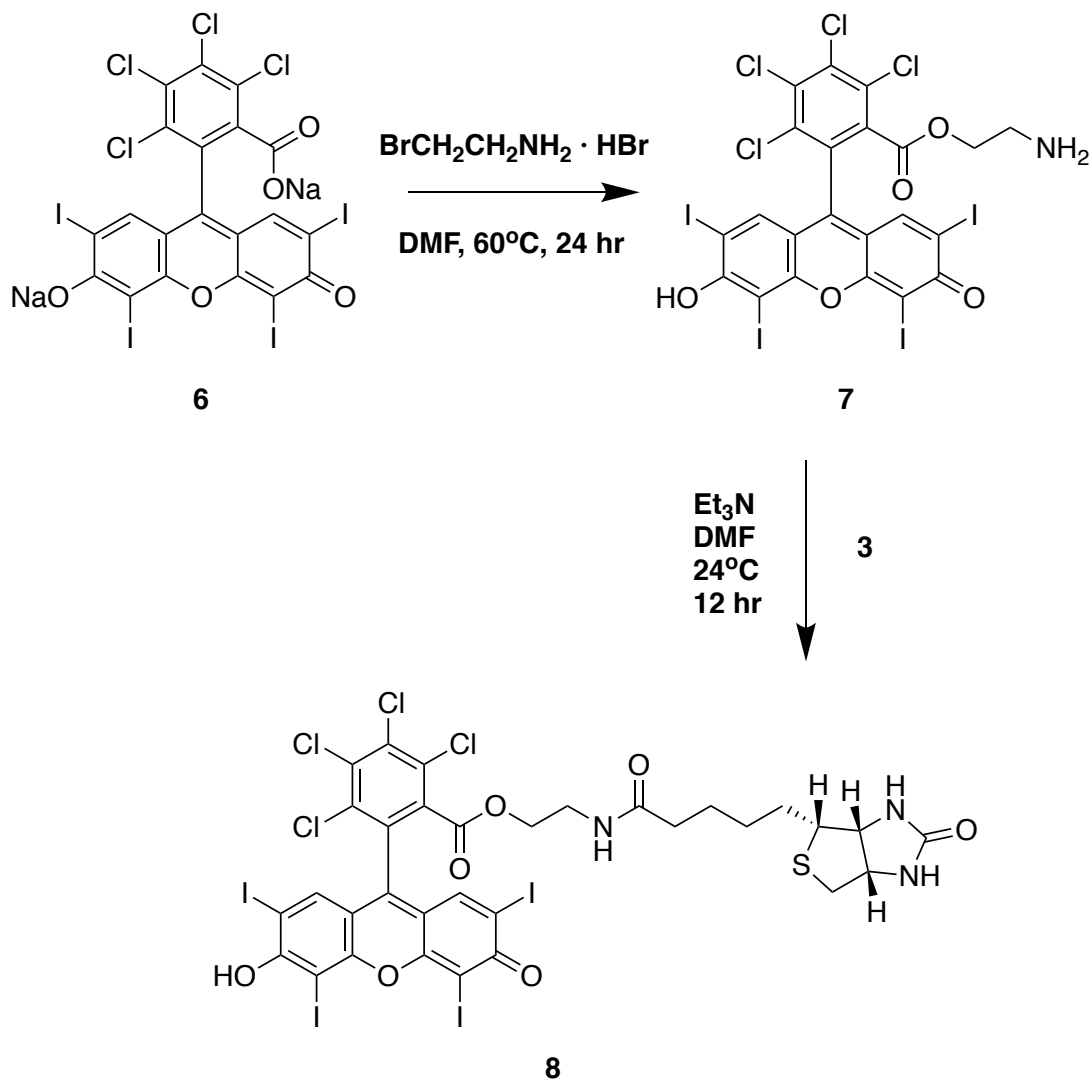
Figure 3.15. Synthetic procedure for the synthesis of biotin-RB (8).

The first step involved the formation of an ester bond between **6** and 2-Bromoethylamine hydrobromide through an S_N2 type reaction to yield **7**. This was then directly coupled with **3,** through an amidation reaction to produce the target compound **8**.

The structure of **8** was again confirmed using ESI-MS, ^{1}H-NMR and ^{13}C-NMR which are shown in Figures 3.16 – 3.19. The ^{1}H NMR is shown in Figure 3.16 and reveals the two characteristic aromatic ring protons from RB appearing

as a sharp singlet at 7.30 ppm with the four methylene protons closest to the RB ring appearing at 2.79 and 3.85 ppm. The characteristic carbamide protons from biotin appeared at 6.30 and 6.40 ppm while the 6 methylene protons closest to the biotin core were centred on resonances between 1.30 and 1.80 ppm. The remaining two methylene protons adjacent to the amide carbonyl group were observed as a resonance centred at 1.95 ppm. The stacked spectra shown in Figure 3.17 shows the disappearance of the amino protons of **7** (top spectrum, 7.7 ppm) and the new amide proton at 7.6 ppm indicating the formation of an amide bond between the amino group and the carboxyl group of biotin (middle spectrum). The ^{13}C NMR spectrum is shown in Figure 3.18 and reveals resonances in the upfield region between 20 and 70 ppm corresponding to the aliphatic carbons of biotin and the methylene carbons of the linker between RB and biotin. Resonances further upfield between 70 and 200 ppm were assigned to carbonyl carbons and the aromatic carbons of **6**. The remaining protons and carbons were assigned as annotated on the structure accompanying each spectrum. The molecular weight of **8** was confirmed using ESI-MS. The ESI-MS spectrum is shown in Figure 3.19 and reveals a base peak of 1241.4 Da corresponding to the [M+H]$^+$ ion. These analytical data were consistent with data from previous publications and confirm the formation of **8**.
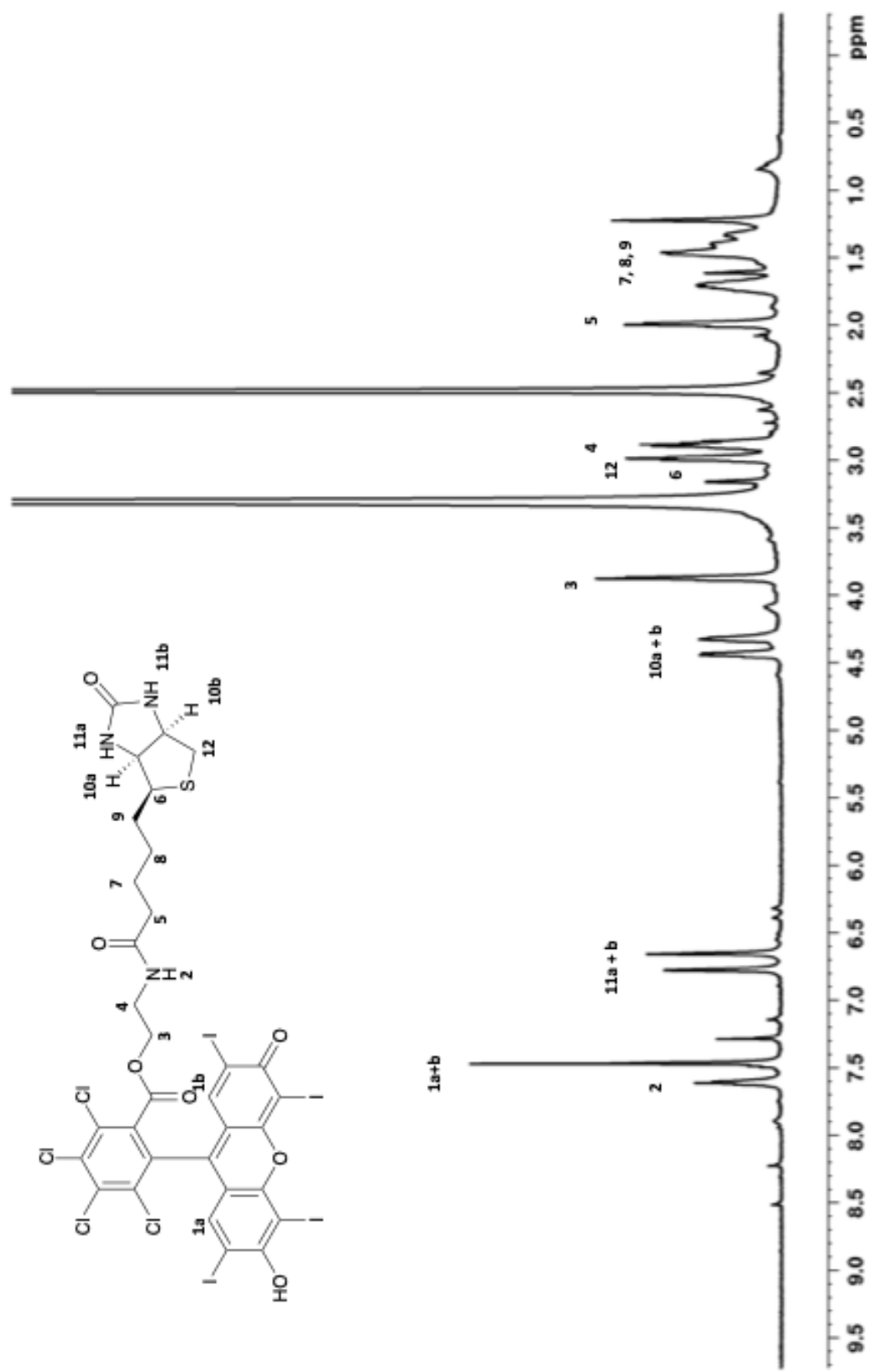
Figure 3.16. ^{1}H NMR spectrum of 8 recorded in DMSO-d6

93
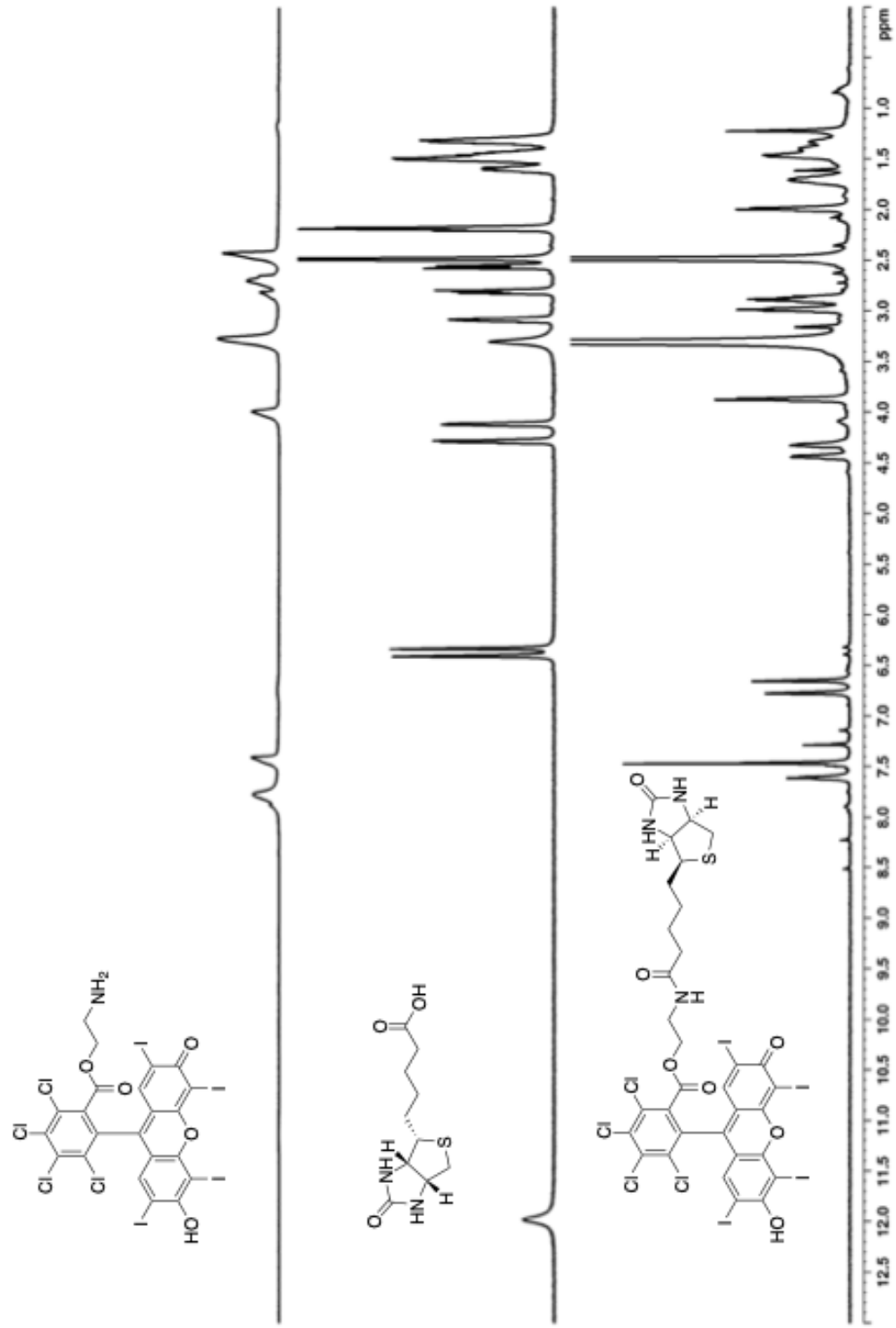
Figure 3.17. Stacked ¹H NMR spectra of 7 (top), 1 (middle) and 8 (bottom) recorded in DMSO-d6

94
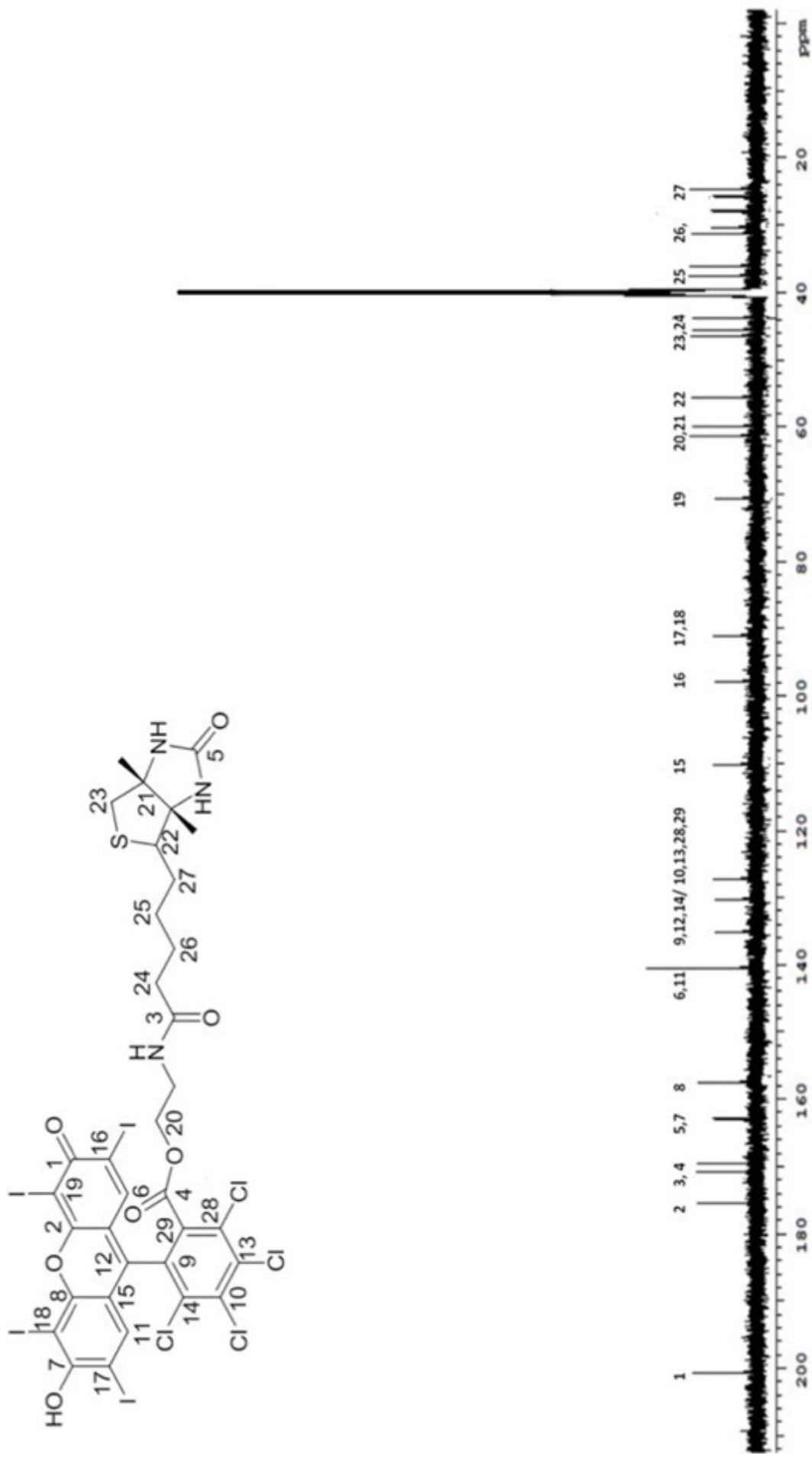
Figure 3.18. ¹³C NMR spectrum of 8 recorded in DMSO-d6.
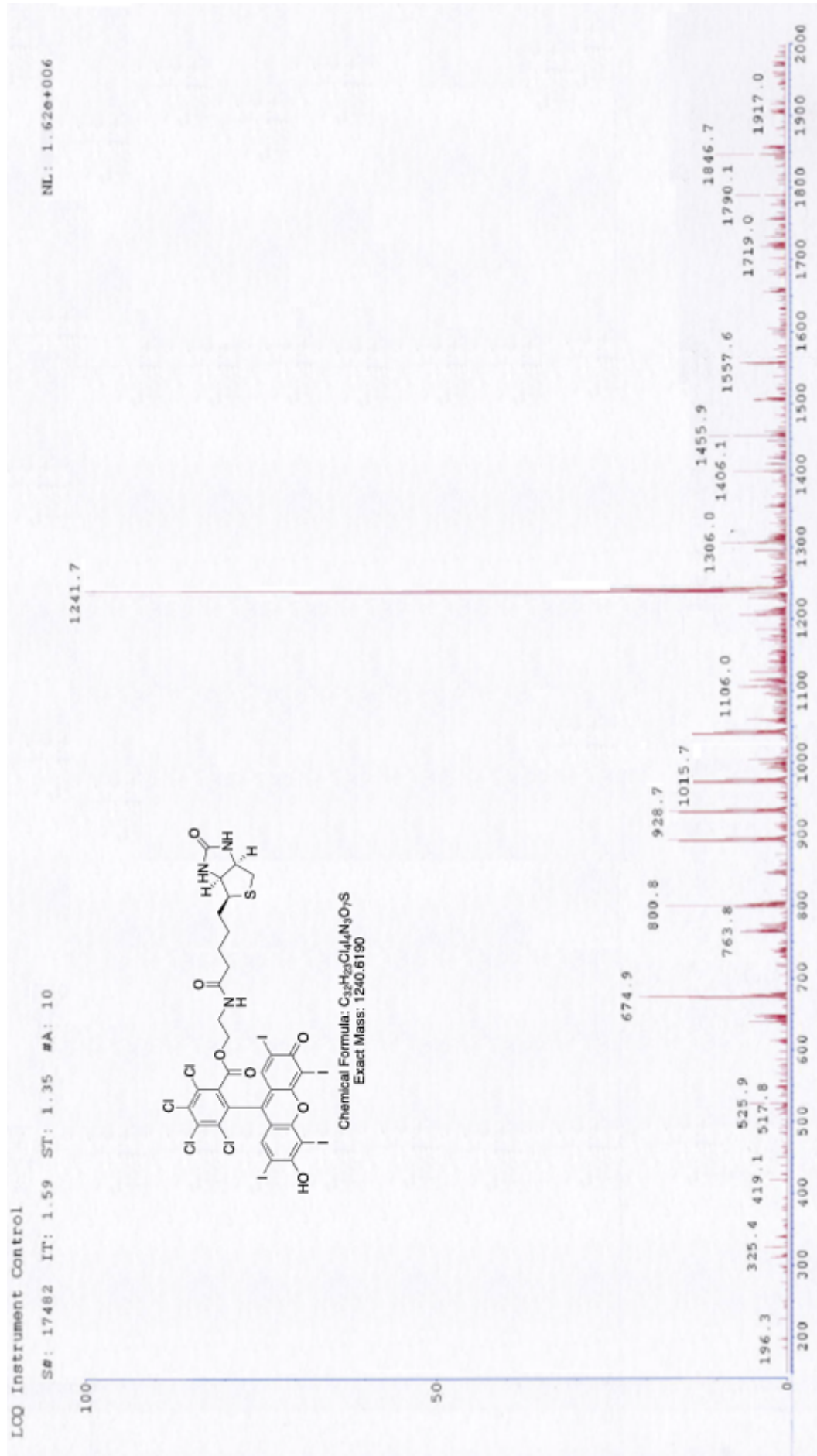
Figure 3.19. ESI-MS spectrum (positive mode) of 8 recorded in methanol.

96

3.2.4. Preparation of MB-PTX-RB and MB-PTX-Dox

Having confirmed the loading and stability of the MB-PTX, the next step was to add the biotinylated payloads to the MB surface. This was facilitated by first adding a solution of avidin to the PTX-MB that binds to the biotin of the DBPC-PEG-biotin lipid that comprises the MB lipid shell. As this lipid is functionalised with a PEG unit to which the biotin is attached, the biotin will be positioned on the exterior of the MB shell during the self-assembly process ensuring the MB surface can bind avidin. The interaction between biotin and avidin is one of the strongest non-covalent interactions known in nature. (272) In addition, the non-covalent interaction between them is facile and does not require extensive reaction time making it ideally suited for this application. As avidin possesses four binding sites for biotin, three remain available for conjugation to the biotinylated payloads **5** or **8** to produce MB-PTX-RB or MB-PTX-Dox.

3.2.4.1. Characterisation of MB-PTX-Dox and MB-PTX-RB

The loading of **5** and **8** on the two MB formulations was determined using UV-Vis spectrophotometry. A UV-Vis calibration curve was constructed for **5** and **8** using standards of known concentrations (Figure 3.20 and Figure 3.21). Good linearity was observed for both **5** and **8** over the concentration ranges tested with R^2 values of 0.9999 and 0.9957 respectively.
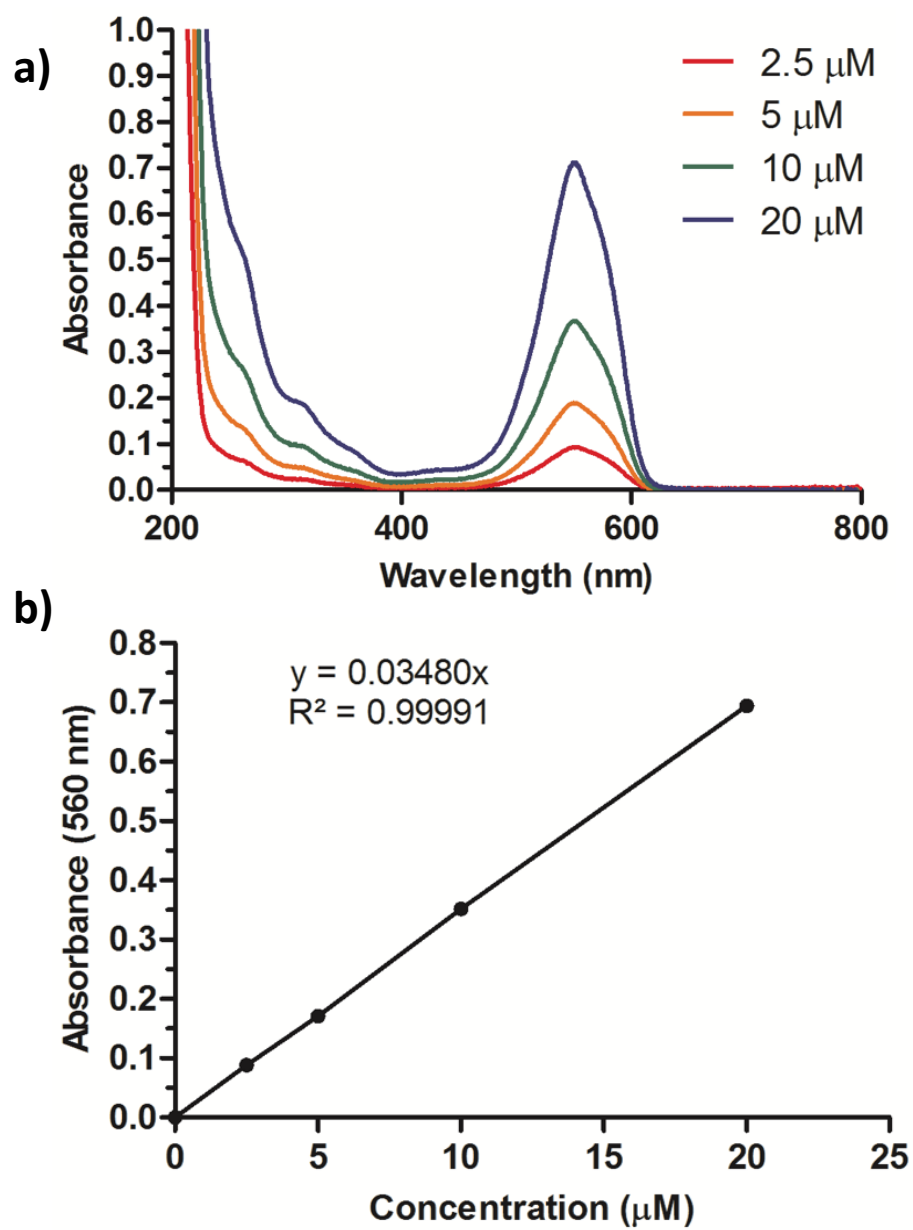
Figure 3.20. a) UV-Vis spectra for 8 at concentrations ranging from 2.5 – 20 µM and b) Plot of absorbances of 8 against concentration.
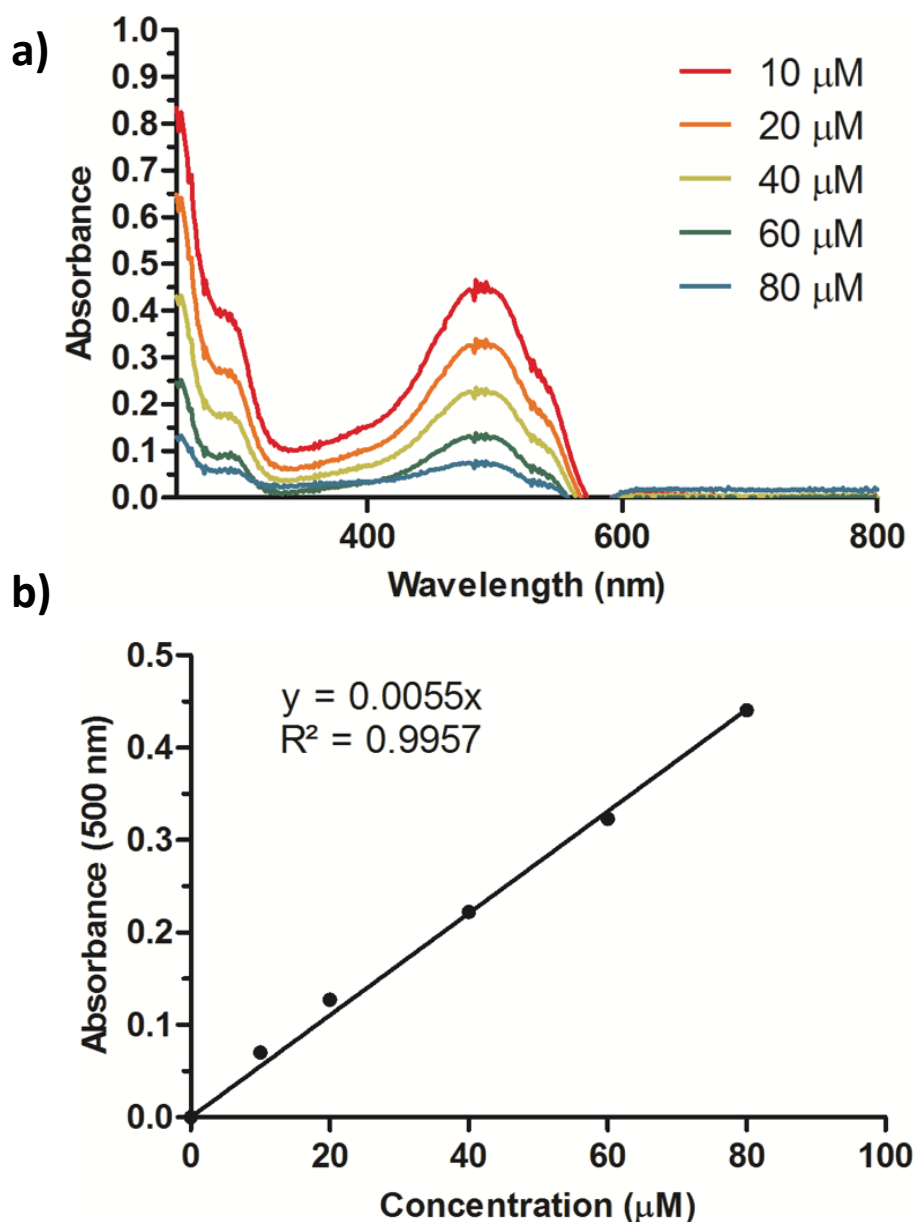
Figure 3.21. a) UV-Vis spectra for 5 at concentrations ranging from 10 – 80 μM and b) Plot of absorbances of 5 against concentration.

Analysis of optical microscope images (Figure 3.22) confirmed the presence of spherical MB-PTX-Dox and MB-PTX-RB with mean particle diameters of 2.82 ± 0.05 and 2.61 ± 0.02 μm respectively and mean microbubble concentrations of 1.20×10^9 and 1.35×10^9 MB / mL respectively. Both MB-PTX-Dox and MB-PTX-RB also exhibited bright red fluorescent shells when analysed using fluorescent microscopy consistent with the successful attachment of the inherently fluorescent Dox and RB respectively (Figure 3.22).
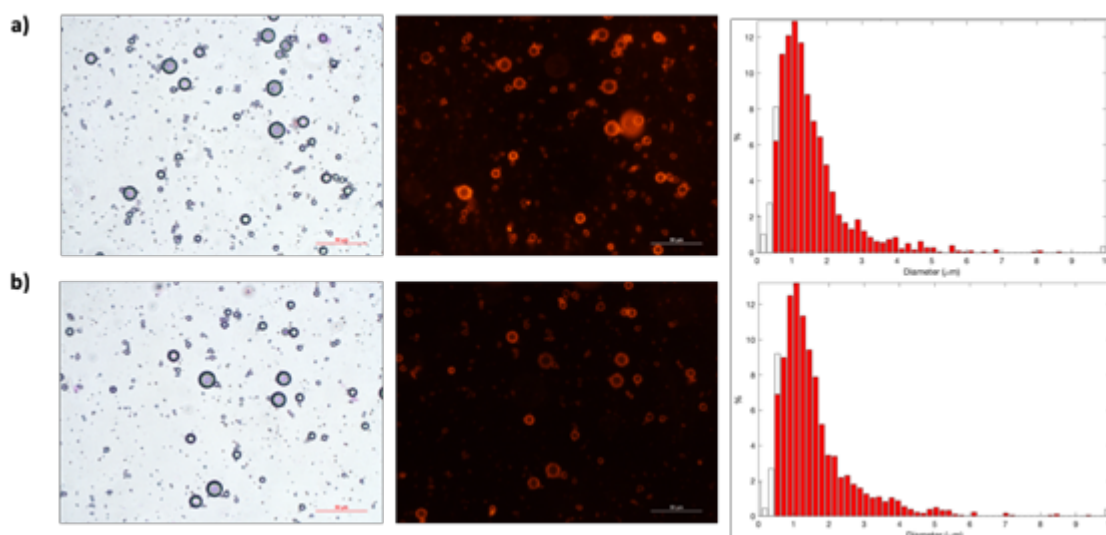
Figure 3.22. Representative bright field (left panel) and fluorescence (middle panel) micrographs and corresponding size distribution analyses (right panel) of (a) PTX-RB MB and (b) PTX-Dox MB (n=20 images). Scale bar represents 50 μm.

The mean loading of PTX, Dox and RB in the final MB preparation was determined to be 51.8 ± 8.3 μg / 10^8 MBs, 41.3 ± 2.6 μg / 10^8 MBs and 140.0 ± 23.4 μg /10^8 MBs respectively. It is unclear as to why the loading for RB was significantly greater than Dox despite being similar in size but may be due to some non-specific binding of RB to the MB surface (i.e. not bound through avidin-biotin linkage). The loading for PTX compares favourably with previous studies where PTX was loaded hydrophobically within the MB shell. (206,265)

Indeed, the loadings achieved for both PTX and DOX using the approach adopted in this chapter suggest it would be possible to deliver clinically relevant doses of both agents PTX (175 mg/m²) (273) and DOX (25 mg/m²) (274) as a part of the MB platform whilst remaining within the maximum tolerated MB dose, which was determined to be 1 x10^{13} MB for MRX-115 contrast agent in primates (i.e. 3.31 x 10^{11} MBs to deliver 175 mg/m² PTX and 6.09 x 10^{10} MBs to deliver 25 mg/m² DOX). (275,276) Off course, targeted delivery using UTMD means it should be possible to use much lower concentrations of these toxic chemotherapy drugs while maintaining an effective therapeutic outcome.

3.2.4.2. Effect of PTX on the loading capability of biotinylated payloads.

One potential complication of loading PTX in the MB shell is that it could compromise the subsequent loading of biotinylated payloads to the MB surface. To investigate any potential effect on MB loading, batches of MBs with or without 5 mg of PTX added into the lipid film prior to MB synthesis were prepared and the ability of each batch to attach **8** to the surface determined. Compound **8** was chosen for this experiment as its synthesis is more trivial and less expensive than that of **5**. Consequently, if there was any effect on the loading capacity for **8** we could assume that the same would be true for **5**. The results are shown in Figure 3.23 and reveal no significant change in the loading of **8** in the absence or presence of PTX.
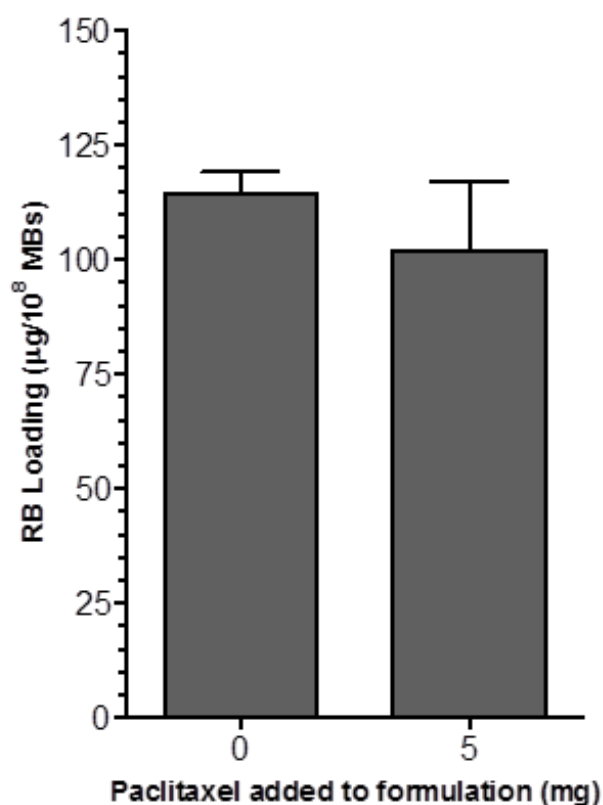
Figure 3.23. Plot of loading of 8 (normalized to 10^8 MBs) in the absence (0 mg) and presence (5 mg) of PTX incorporated within the lipid layer during MB formulation (final PTX loading = 51.8 ± 8.3 µg/10^8 MB) (n = 4).

3.2.5. Efficacy of MB-PTX-DOX and MB-PTX-RB in MCF-7 spheroids

Having successfully prepared and characterised the MB-PTX-Dox and MB-PTX-RB conjugates, the next step was to determine their efficacy in a three-dimensional (3D) spheroid model of breast cancer. Standard two-dimensional (2D) cell culture lacks the necessary cell to cell and cell to extracellular matrix interactions required to bridge the gap between in vitro cell experimentation and in vivo animal models of cancer. 3D cell models of cancer, particularly spheroids, incorporate many important characteristics associated with the *in vivo* cellular environment such as tumour morphology and heterogeneity, growth kinetics, gene expression and response to anticancer agents into a high throughput and cost-effective *in vitro* setting and thus is a valuable tool in the screening of new drugs and drug delivery systems. (277,278)

Spheroids were prepared by growing MCF-7 cells in ultra-low attachment 96 well plates which have a rounded bottom causing cells to migrate towards the middle of each well where they can aggregate together. Cells were seeded at a density of 8000 cells per well and incubated for three days to allow spheroid formation to take place. Once formed, spheroids were treated with MB only (i.e. no drugs attached), PTX / Dox only (i.e. not MB bound) and the MB-PTX-Dox / MB-PTX-RB conjugates in the presence and absence of US (1 MHz, 3.0 W/cm², duty cycle = 50% PRF = 100 Hz) which was placed below each well (Figure 3.24). Untreated spheroids and spheroids treated with US only were also included for comparative purposes. Following treatment, the spheroids were trypsinised to break up cell aggregates before the extent of cell viability was determined using an MTT assay. In a separate experiment, intact spheroids were stained with propidium iodide (P.I.) following treatment and imaged using fluorescence microscopy according to the protocol outlined in Section 2.19.
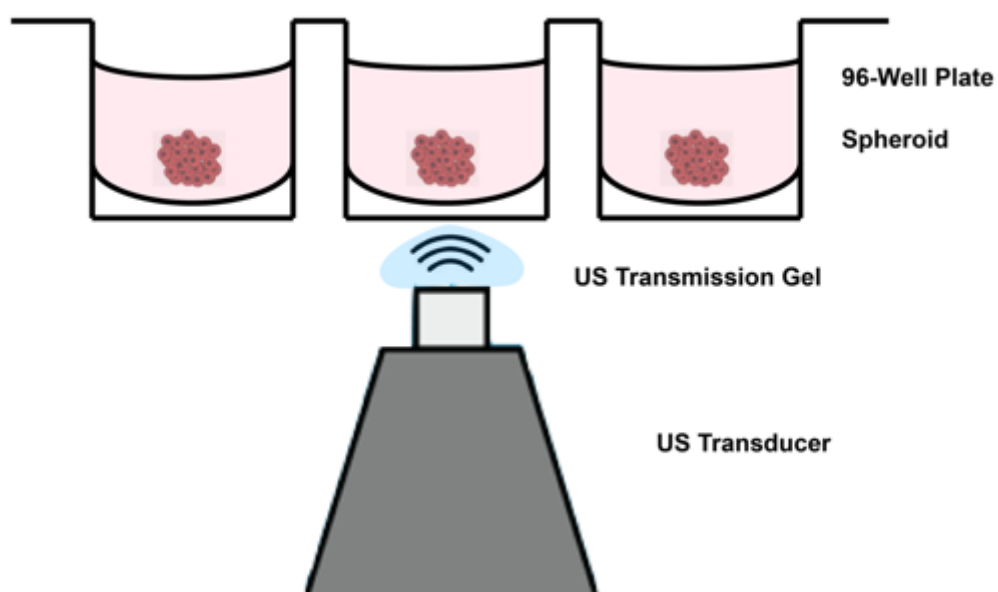
Figure 3.24. Diagram illustrating the set-up used for all in vitro cell experiments (not to scale).

Results from the MTT assay are shown in Figure 3.25 and reveal a moderate reduction in the viability of cells following exposure to US alone (28.03%, $p < 0.05$), which was similar to the reduction observed for the MB + US treatment (29.40 %). Treatment with PTX / Dox alone reduced viability by 21.98% ($p < 0.05$) relative to untreated spheroids, which was broadly unchanged in the presence of US (23.67%). However, when spheroids were treated with the MB-PTX-Dox / MB-PTX-RB conjugates and US, the cell viability decreased by 72.6% which was significantly greater than treatment with the MB-PTX-Dox / MB-PTX-RB conjugates in the absence of US (8.2%) or the other groups. This improved cytotoxicity is most likely due to both SDT and the ability of MB induced cavitation to enhance dispersion of the drugs within the spheroid matrix. (279–281) Indeed, MB cavitation is known to create associated microstreaming and microjetting events that have been attributed to improved tumour uptake and efficacy of chemotherapy drugs in several pre-clinical and clinical studies (Section 1.3.3.1.2). (218,227,282,283)
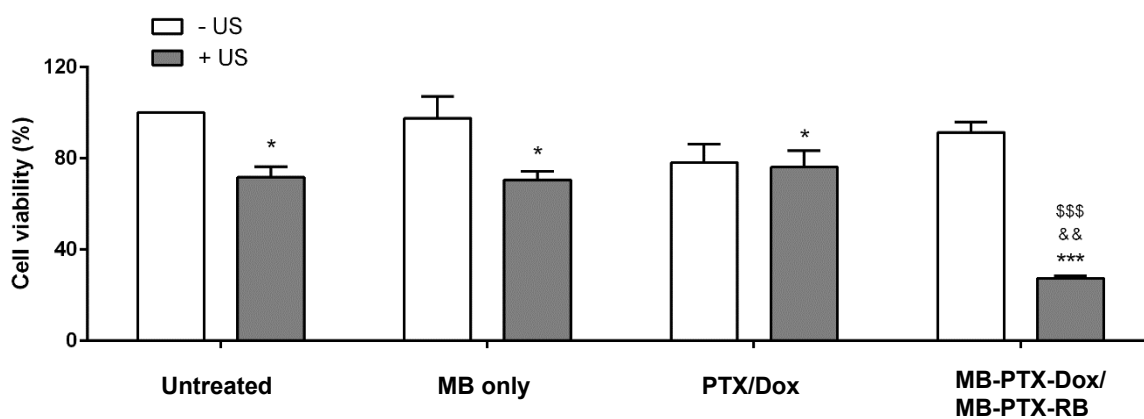
Figure 3.25. Plot of cell viability for 3D MCF-7 spheroids following exposure to (i) no treatment (ii) MB only (no drugs), (iii) PTX/Dox only (i.e. no MBs) or (iv) MB-PTX-Dox/MB-PTX-RB in the presence or absence of US: $^*p < 0.05$, $^{***}p < 0.001$ for treatment groups compared to untreated group. $^{\&\&}p < 0.01$ for MB-PTX-Dox/MB-PTX-RB + US v PTX/Dox + US. $^{\$\$\$}p < 0.001$ for MB-PTX-Dox/MB-PTX-RB + US v MB-PTX-Dox/MB-PTX-RB – US. Error bars represent ± standard error of mean (n = 3).

Results from the P.I staining experiments revealed a slightly different trend from those obtained using the MTT assay. P.I is a DNA-selective permeable dye that passes freely through compromised plasma membranes of dead cells and does not permeate the membrane of living cells. (284) In contrast to the MTT assay experiments, where a single cell suspension of cells derived from spheroids was analysed post-treatment, intact spheroids were examined following treatment using P.I staining. This means that cell damage can only be detected on the outer cell surface of the spheroid structure. The brightfield and fluorescent images from each treatment group are shown in Figure 3.26a with the fluorescence intensities quantified and plotted in Figure 3.26b. Bright red P.I fluorescence was observed for spheroids treated with the MB-PTX-Dox / MB-PTX-RB + US group which was visibly more intense than any of the other groups. It was also observed that the mean volume of spheroids treated with MB-PTX-Dox / MB-PTX-RB + US was significantly smaller than in any of the other groups including those spheroids treated with MB-PTX-Dox / MB-PTX-RB in the absence of US. To account for this reduction in size, the P.I fluorescence was normalised according to the size of each individual spheroid. This particular study was limited in that there was no control for the scattering of the unfocused US signal from the plastic surface of the well plate. This could have been improved through the use of an acoustically transparent cell culture container.

Nevertheless, when combined, the intense P.I fluorescence and size reduction observed for spheroids treated with MB mediated chemo-sonodynamic therapy, in addition to the reduced cell viability observed from the MTT assay experiments, highlight the effectiveness of this treatment in this particular model of breast cancer.
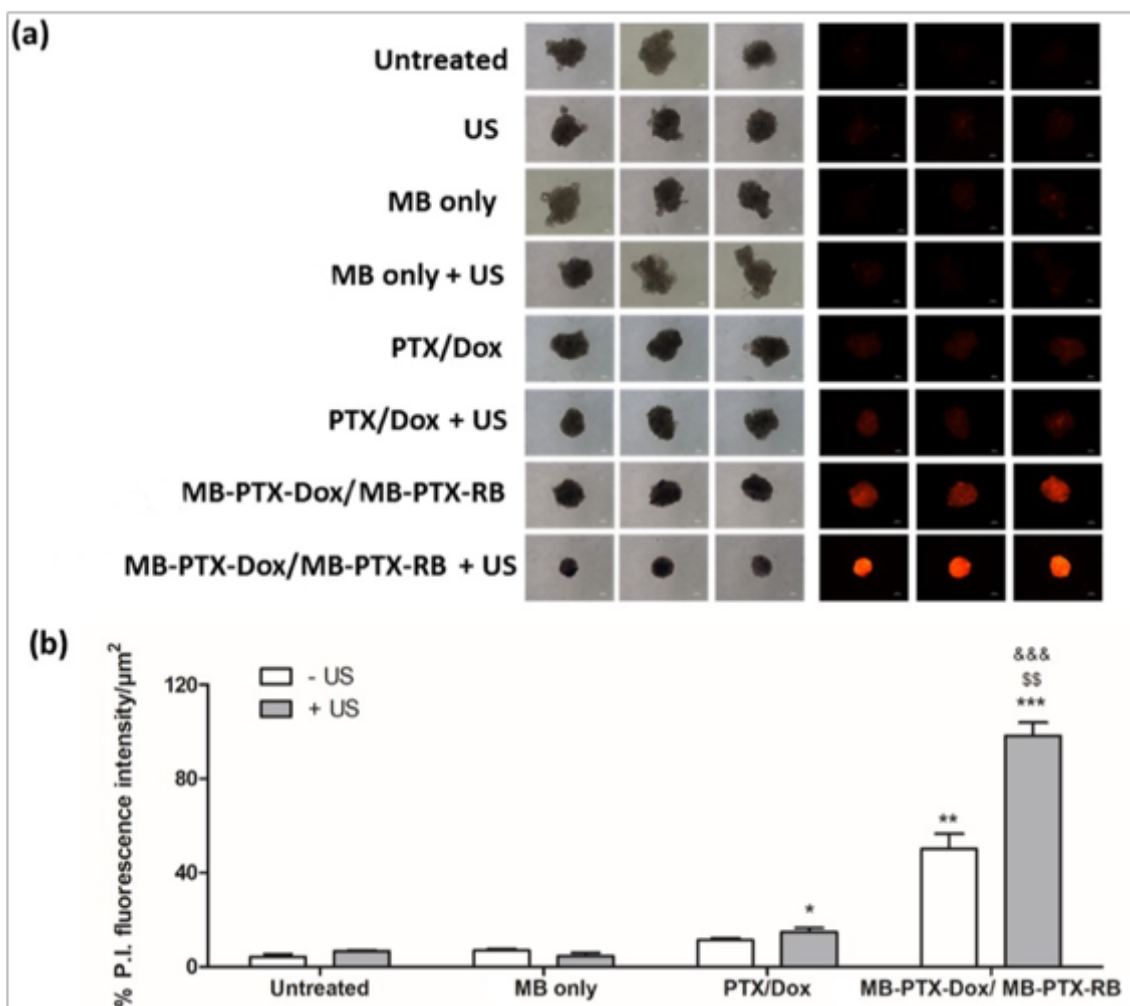
Figure 3.26. Optical (left panel) and fluorescence (right panel) micrographs of MCF-7 spheroids exposed to: (i) no treatment, (ii) US only (iii) MB only, (iv) MB + US (v) PTX/Dox only ([PTX] = 0.34 μM, [Dox] = 1 μM), (vi) PTX / Dox + US (vii) MB-PTX-Dox / MB-PTX-RB ([Dox] = 1 μM, [RB] = 10 μM) and (viii) MB-PTX-Dox / MB-PTX-RB + US. Spheroids were stained with P.I. following treatment. (b) plot of P.I. intensity per μm^2 for each of the groups shown in (a) (normalized to 100% by comparison with MB-PTX-Dox / MB-PTX-RB + US group). *p < 0.05, **p < 0.01, ***p < 0.001 significance for treatment groups relative to untreated group. $^{\$\$}$p < 0.01 significance for MB-PTX-Dox / MB-PTX-RB + US v MB-PTX-Dox / MB-PTX-RB / PTX/Dox + US. $^{\&\&\&}$p < 0.001 significance for MB-PTX-Dox / MB-PTX-RB + US v PTX/Dox + US. Error bars represent $\pm$ the standard error (n = 3).

3.2.6. In vivo efficacy of O$_2$MB-PTX-DOX and O$_2$MB-PTX-RB in ectopic MCF-7 tumour bearing mice

While encouraged by the results obtained from the 3D spheroid experiments discussed above, the full utility of O$_2$MBs as a delivery vehicle can only be determined *in vivo*. To this end, subcutaneous MCF-7 tumours were established in recipient mice and once tumours reached a mean volume of 150 mm^3, a mixed suspension of the O$_2$MB-PTX-Dox/O$_2$MB-PTX-RB formulations was administered to animals by IV injection through the tail vein. During injection, US was positioned at the tumour to disrupt the O$_2$MB, releasing the anticancer payloads and activating the sonosensitiser, where appropriate (Figure 3.27). To evaluate the effectiveness of the O$_2$MB delivered treatments, a group of animals were also treated with a combination of free PTX / Dox (i.e. not O$_2$MB attached). PTX was delivered using Cremophor EL as a solubilising agent which is commonly used clinically for the delivery non-albumin based PTX formulations.
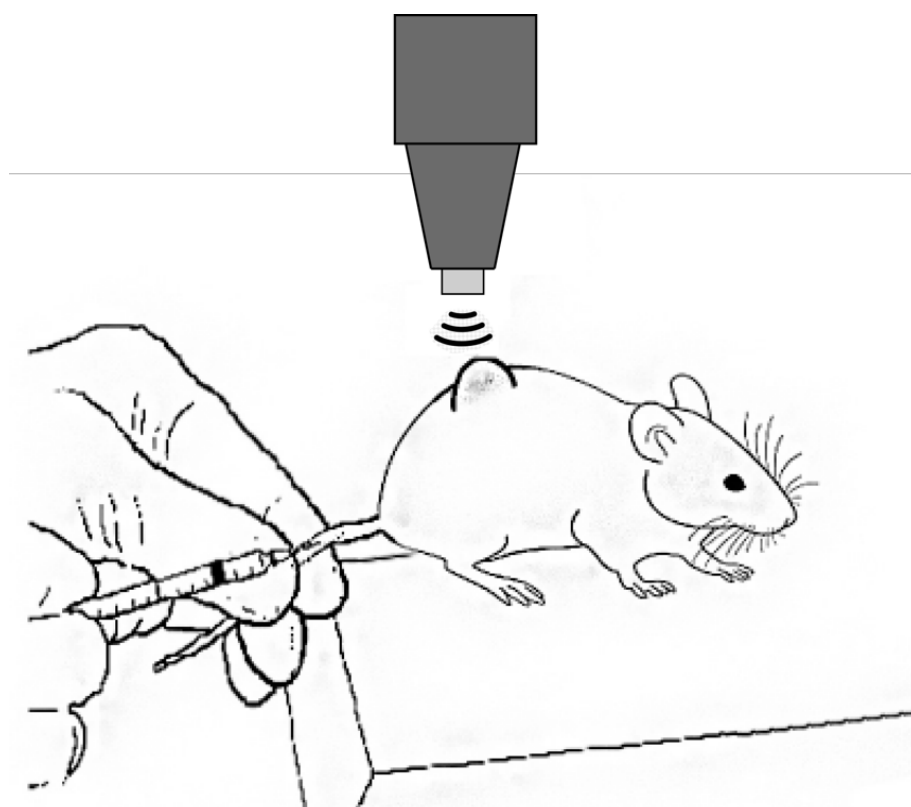
Figure 3.27. Diagram illustrating of the set-up used for all in vivo experiments (not to scale).

The tumour growth delay plot is shown in Figure 3.28a and reveals a significant reduction in tumour volume for animals treated with O_2MB-PTX-Dox / O_2MB-PTX-RB + US (p<0.001), with tumours still 6.96% smaller than the pre-treatment size 25 days after the initial treatment. In contrast, tumours in animals treated with the same O_2MB-PTX-Dox / O_2MB-PTX-RB formulation in the absence of US increased in volume by 43.15% over the same time period. Indeed, the effect of O_2MB-PTX-Dox / O_2MB-PTX-RB + US was also significantly better than that observed following treatment using the free PTX / Dox combination which increased in volume by 24.77% at day 25, despite receiving a 16.8% and 98.4% increased dose of PTX and Dox respectively. Combined, these results corroborate the in vitro efficacy results and highlight the effectiveness of O_2MB delivered chemo-sonodynamic therapy as a targeted treatment for breast cancer. In addition to the improved efficacy offered by this approach, the treatment was also well tolerated with the body weight of animals in the O_2MB treated groups mapping closely to that of untreated animals (Figure 3.28b). In contrast, there was a 12.1% drop in body weight for animals treated with free PTX / Dox over the course of the experiment. This reduction in body weight most likely as a result of toxicity exhibited by the free drugs or the Cremophor EL vehicle required to deliver PTX. Cremophor EL is known to produce undesirable side-effects and while poorly tolerated, (285,286) is necessary to enable the dispersion of hydrophobic PTX in aqueous solution. Therefore, the ability to avoid the use of such a toxic vehicle by incorporating PTX within the O_2MB shell is an added advantage of the MB-based drug delivery system.
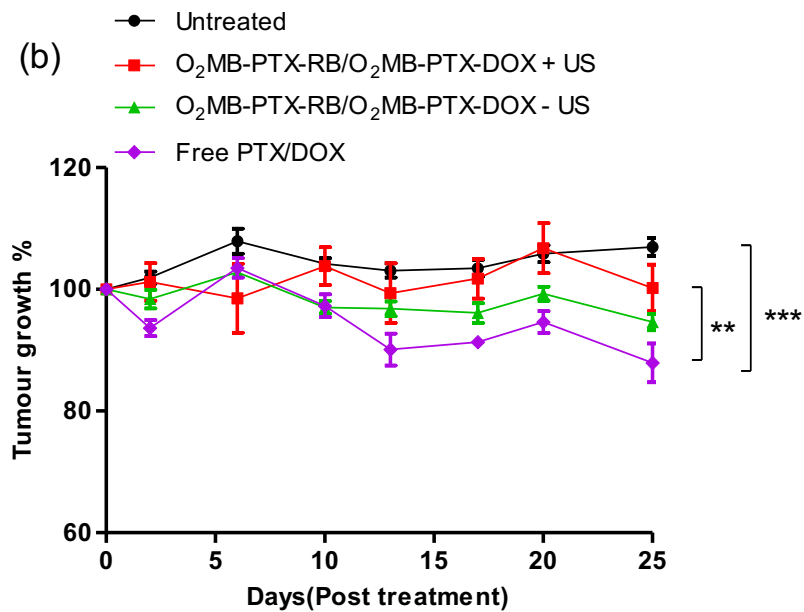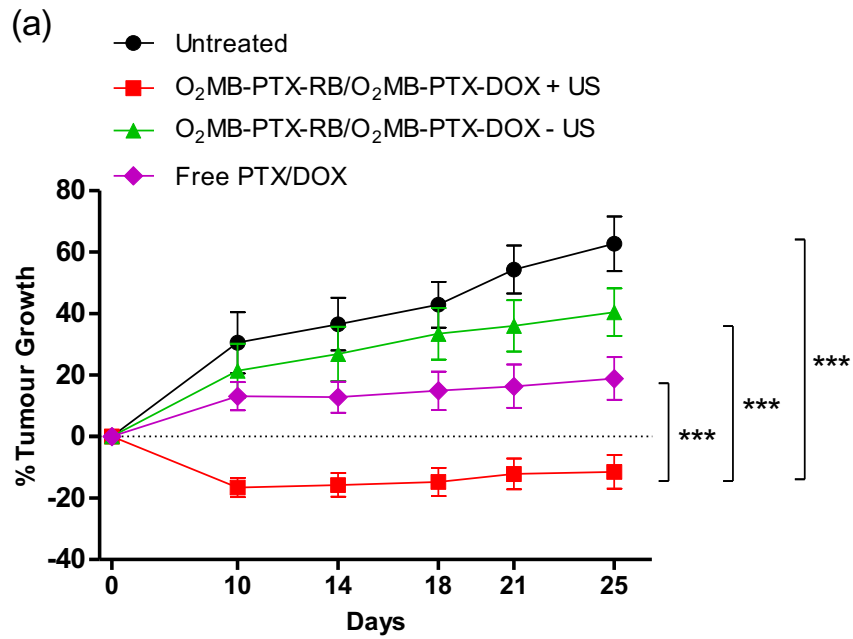
Figure 3.28. (a) Tumour growth delay plot for mice bearing MCF-7 xenograft tumours. Control animals received no treatment. Groups were treated with a mixed suspension (50 μL) of O$_2$MB-PTX-RB and O$_2$MB-PTX-Dox (6.18x10^7 MB, [PTX] = 1.13 $\pm$ 0.16 mg/kg, [RB] = 2.63 $\pm$ 0.35 mg/kg, [Dox] = 0.97 $\pm$ 0.15 mg/kg) delivered by IV in the presence and absence of US.. A group was also treated with Cremophor EL solution containing free PTX and Dox ([PTX] = 4.7 mg / kg, [Dox] = 2.5 mg / kg) **(b)** Plot of animal weights recorded over the course of the experiment for each group. For plot (a) and (b) **p < 0.01, ***p < 0.001. Error bars represent $\pm$ SEM (n = 5).

3.3. Conclusions

In summary, MBs containing the hydrophobic anticancer drug PTX, loaded into the lipid shell, were successfully synthesised. In addition, biotinylated derivatives of Dox and RB were synthesised and successfully attached to the surface of avidin functionalised PTX-loaded MBs. In in vitro experiments, spheroids treated with MBs containing a combination of PTX, Dox and RB showed an improved response when compared to cells treated with either free drug or MB-PTX-RB and MB-PTX-Dox administered separately.

A similar trend was observed during in vivo experiments where a significant reduction in tumour volume in mice treated with the combination of O_2MB-PTX-RB and O_2MB-PTX-Dox was observed when compared to each of the MB conjugates alone and with each of the anticancer drugs delivered systemically. Furthermore, mice treated with systemic clinical dose of PTX/Dox displayed a significant drop in body weight over the course of the 25-day experiment when compared to mice treated with MB delivered PTX / Dox.

The improved efficacy of O_2MB delivered chemo-sonodynamic therapy, when compared to standard PTX / Dox treatment demonstrates its potential as a neo-adjuvant therapy to downstage tumours in advance of surgery, or, as a treatment for locally recurrent chest wall disease. An added advantage of this approach is that each component of the treatment (i.e. the MBs, PTX, Dox, RB and US) has been safely used in humans previously thus providing the opportunity for rapid clinical translation. Furthermore, using O_2MB as a delivery vehicle allows for the use of much lower doses of toxic chemotherapy thereby causing fewer undesirable side effects. MB mediated delivery of Dox has been achieved through its loading into the shell of polymeric MBs through hydrophobic interactions. (287) However, in this study a low loading of Dox was achieved (6 μg drug/mg of MB). As a consequence, dangerously high concentrations of MBs would therefore be needed to achieve a therapeutic dose of the payload drug. In comparison, the work described herein describes the first single MB formulation capable of delivering both PTX and Dox at therapeutically relevant doses of these agents while remaining within a safe concentration of MBs. While the results presented in this chapter were encouraging, it was limited in that two separate batches of MBs had to be prepared and mixed in equal ratio which reduced the

effective dose of each agent. It would therefore be beneficial to incorporate multiple payloads on a single MB.

Chapter 4

Targeted Delivery of Paclitaxel, Gemcitabine and Rose Bengal to Pancreatic Tumours Using a Multifunctional Microbubble Delivery Platform

Chapter 4 – Targeted delivery of Paclitaxel, Gemcitabine and Rose Bengal to Pancreatic Tumours Using a Multifunctional Microbubble Delivery Platform

4.0. Introduction

There is a growing trend within oncology for the use of a combination of chemotherapy drugs in an effort to produce a synergistic response leading to improved patient outcome. One such combination which has been successful in the treatment of PDAC is Gem plus nabPTX. This particular regimen is currently a standard of care, alongside FOLFRINOX, for patients with advanced or metastatic pancreatic cancer and has also shown promise in several clinical studies as an effective neo-adjuvant treatment. (288–292)

Despite their widespread use in the treatment of PDAC, their non-targeted nature means large quantities of these cytotoxic agents must be administered to the patient to achieve a therapeutic response (Gem = 1000 mg/m^2 nabPTX = 125 mg/m^2. (105) This often leads to a host of unpleasant side effects such as fatigue, alopecia, and nausea. (105) This problem is further compounded when considering the average age of pancreatic cancer patients is approximately 70 years old. (293) If treatment of patients with neoadjuvant chemotherapy is to be successful in making more patients eligible for life saving surgery, then it is important that these patients are healthy enough to undergo the surgical procedure.

As described in chapter 3, the MB-mediated delivery of PTX along with the anthracycline anticancer drug Dox and the sonosensitiser RB showed promise for the treatment of MCF-7 tumours. However, the technique was limited as two separate MB formulations had to be prepared separately and mixed prior to use which made controlling the delivery of each drug to the target site more challenging. The synergistic activity of combination therapy requires confidence that both drugs are being simultaneously delivered in known, controlled quantities to the target site. In addition, the use of a single formulation is also more attractive from a manufacturing, regulatory and clinical translation perspective.

In this chapter, a single tripodal ligand was synthesised which incorporated the antimetabolite drug Gem and the sonosenistiser, RB, together

with a biotin anchor which enabled attachment to the MB shell. This ligand was then conjugated to the surface of avidin-functionalised MB-PTX, prepared as described in Section 3.2.2.1. The in vitro efficacy of the MB-PTX-Gem-RB was established in two common pancreatic cancer cell lines using both 2D and 3D cell culture techniques and the in vivo efficacy was determined in two ectopic mouse models of PDAC. In addition, a safety study was undertaken to examine the toxicity of the MB conjugate in healthy non-tumour-bearing mice.

4.1. Hypothesis and specific objectives

The hypothesis of the work undertaken in this chapter was that a UTMD mediated chemo-SDT using a single MB formulation carrying PTX, Gem and RB is more effective and better tolerated than the systemic delivery of PTX/Gem in *in vitro* and *in vivo* models of pancreatic cancer.

The specific objectives were to:

1. synthesise and fully characterise a novel tripodal ligand containing biotin, RB and PTX within its structure.

2. determine the efficacy of this compound when compared to commercially available Gem in BxPC-3 and MIA-PaCa-2 cell lines.

3. prepare and characterise MBs loaded with the tripodal ligand and also carrying PTX in the lipid shell (i.e. MB-PTX-RB-Gem).

4. determine the efficacy of this MB conjugate when compared to MB-PTX and MB-RB-Gem in 3D Panc-1 spheroids.

5. determine the in vivo effectiveness of O_2MB-PTX-RB-Gem when compared to commercial Gem and PTX controls.

6. examine the effect of O_2MB-PTX-RB-Gem on key blood biochemical markers in healthy non-tumour bearing mice.

4.2. Results and discussion

4.2.1. Synthesis of biotin-Gem-RB (12)

Compound **12** was designed as a target molecule containing both RB and Gem with biotin also present to permit attachment to the surface of avidin coated MBs (Figure 4.1).   The first step in this scheme involved reacting the N-hydroxysuccinimde ester of biotin (**3**) with tris(2-aminoethyl)amine (**9**) in a 1:1 molar reaction to encourage only one of the primary amines of biotin (**1**) to form an amide bond with **9**. This product was characterised by ESI-MS and ^{1}H NMR and these are presented in Figure A1 and A2 (appendices). Both the mass and ^{1}H resonances were consistent with the structure of **10**. The product (**10**) was then reacted with disuccinimidyl suberate in a 1:2 molar ratio forming amide bonds with the two remaining amine residues of **10** yielding compound **11** which also contained two pendant active esters.
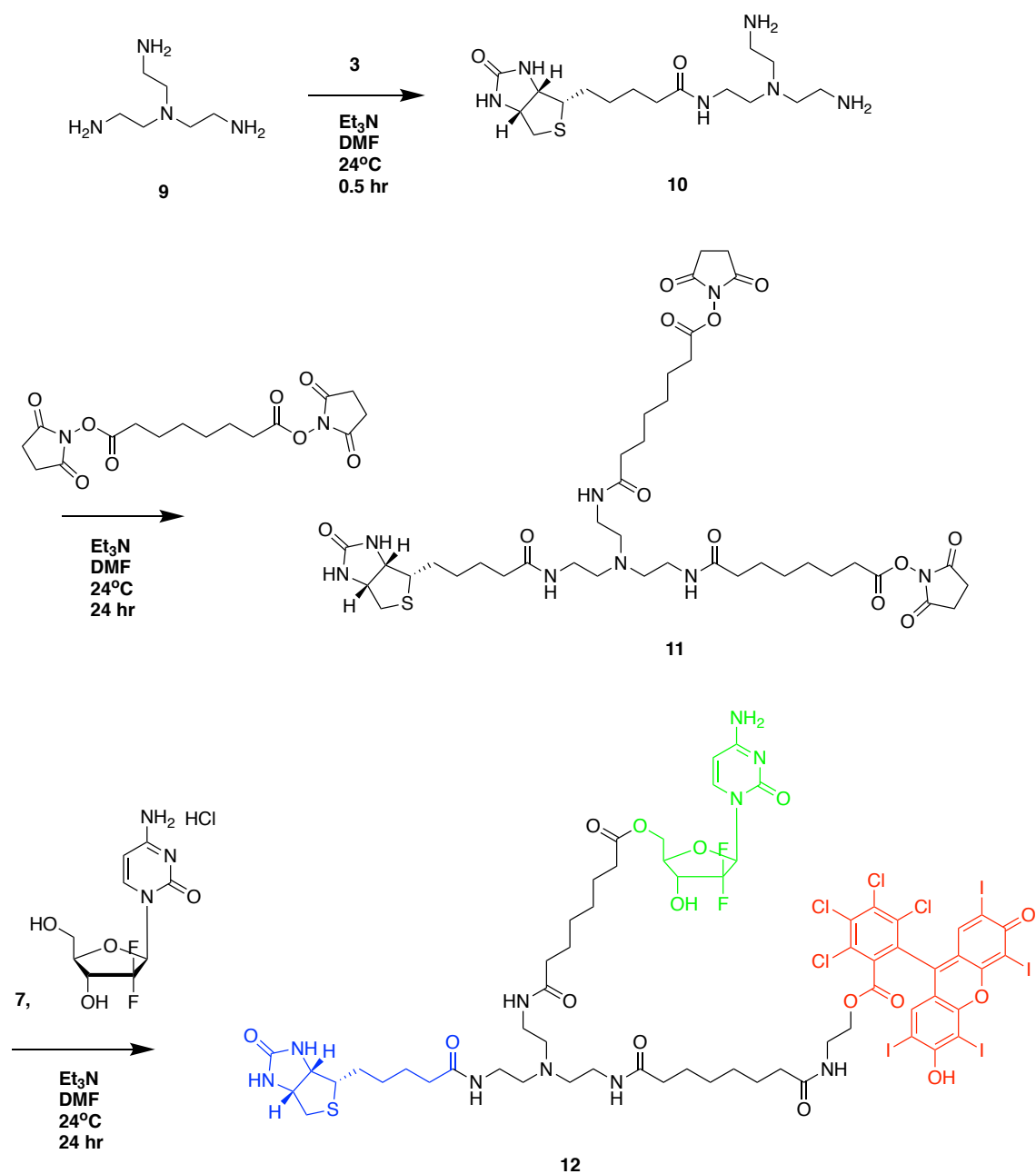
Figure 4.1. Scheme for the synthesis of biotin-Gem-RB. The biotin, Gem and RB moieties are highlighted in blue, green and red respectively.

The ESI-MS spectrum of **11** is shown in Figure A4 (appendices) and reveals a base peak of 901.3 which corresponds to the [M+Na]$^+$ ion. The ^{1}H NMR spectrum is shown in the stacked plot in Figure 4.2c and shows resonances associated with the carbamide protons (6.35 and 6.41 ppm) and the two protons of the fused rings of biotin (4.12 and 4.30 ppm) in addition to characteristic succinimide methylene protons appearing at 2.73 ppm. The active esters of **11** were then reacted in turn with gemcitabine hydrochloride and amine functionalised Rose Bengal (**7**) which was prepared as described in Section 2.3.1, generating ester and amide linkages respectively with **11** to form target compound (**12**). Compound **12** was subsequently characterised using ESI-MS, ^{1}H NMR and ^{13}C NMR shown in Figure 4.3 – 4.5. The ESI-MS spectrum shown in Figure 4.3 reveals a base peak of 1925.9 consistent with the [M+H]$^+$ ion. To aid in the identification of resonances associated with Gem, a previously synthesised derivative of Gem harbouring a ester linkage was used for comparative purposes and is shown in the stacked plot in Figure 4.2b along with compound **7**, **11** and **12**. While the ^{1}H NMR spectrum of **12** is complex, the stacked plot reveals that the two equivalent sets of methylene protons belonging to the pendant succinimide functionalities of **11** at 2.73 ppm are no longer visible in the spectra of **12** indicating the absence of the succinimide groups in **12** and suggesting that Gem and **7** reacted at this position. Furthermore, a newly formed amide proton from the reaction of **7** and one of the activated carboxylic acids was observed at 7.37 ppm, just downfield of the two aromatic RB protons. The ^{1}H NMR spectrum shown in Figure 4.4 also reveals a group of resonances in the upfield region corresponding to methylene protons on the aliphatic chain of biotin as well as on the two tripodal aliphatic arms of the appearing between 1.10 and 2.36 ppm. The methine protons attached to the sp^2 hybridised carbons on the cytosine moiety of Gem appeared as to distinct resonances at 5.78 and 7.68 ppm while the ring amine appeared furthest downfield at 7.95 ppm. The ^{13}C NMR spectrum shown in Figure 4.5 revealed resonances between 162 and 165 ppm corresponding to the 5 newly formed amide carbonyl carbons. The sp^2 hybridised carbons of RB appeared as a group of resonances between 95 and 171 ppm. The two characteristic aromatic carbons of the cytosine moiety of Gem appeared at 95 and 145 ppm. Resonances corresponding to 3 carbons from the aliphatic chain of biotin appeared between 25 and 28 ppm while the remaining carbon closest to the amide carbonyl group appeared at 35 ppm. The two adjacent chiral carbons

of the biotin ring appeared at 59 and 61 ppm respectively while the remaining chiral carbon next to the sulfur atom appeared further upfield at 55 ppm. The remaining resonances have been assigned as shown in Figure 4.4 and 4.5.
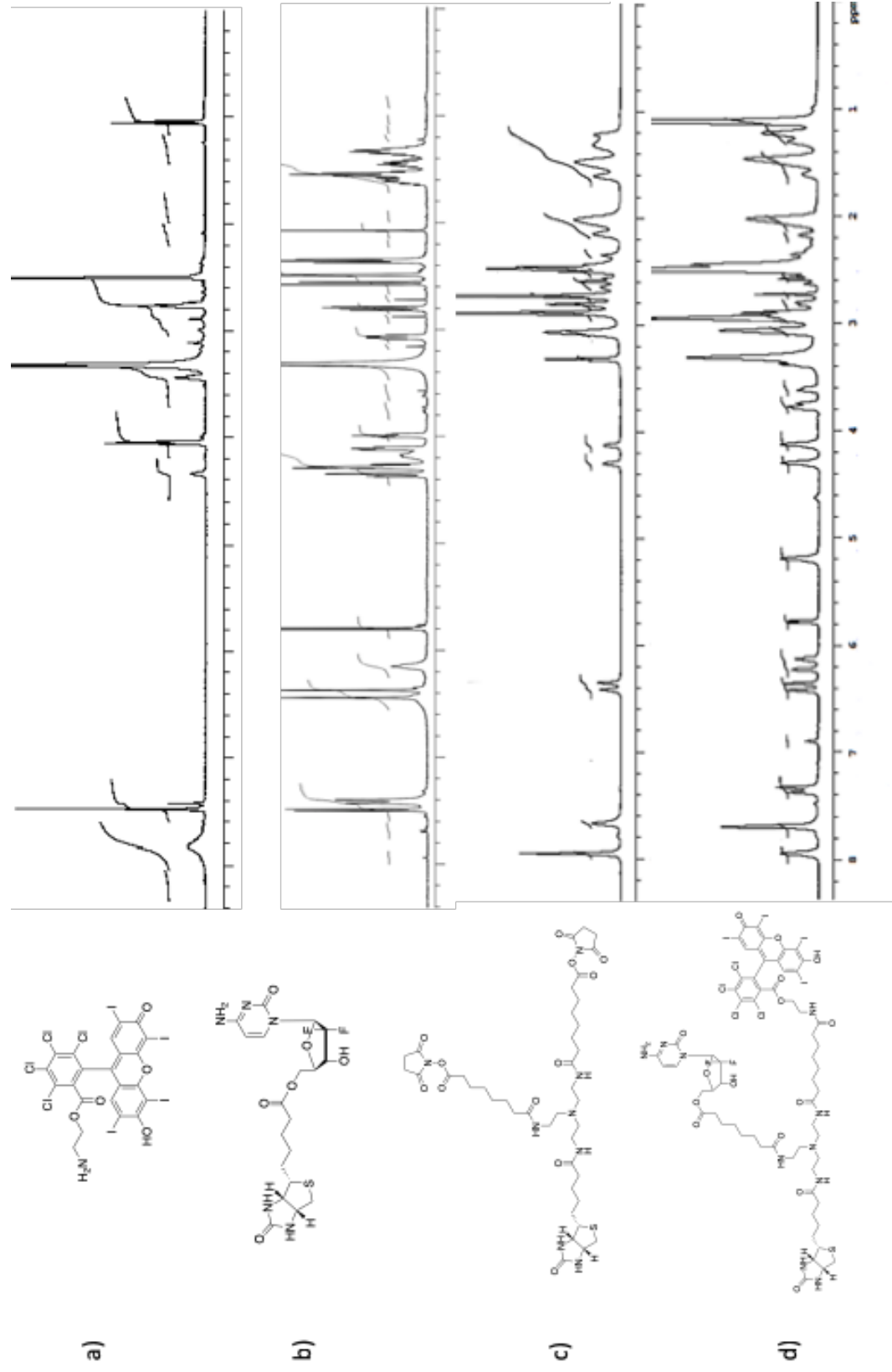
Figure 4.2. Stacked ¹H NMR spectra of a) 7 b) Gem ester derivative c) 11 and d) 12 all recorded in DMSO-*d6*.

119
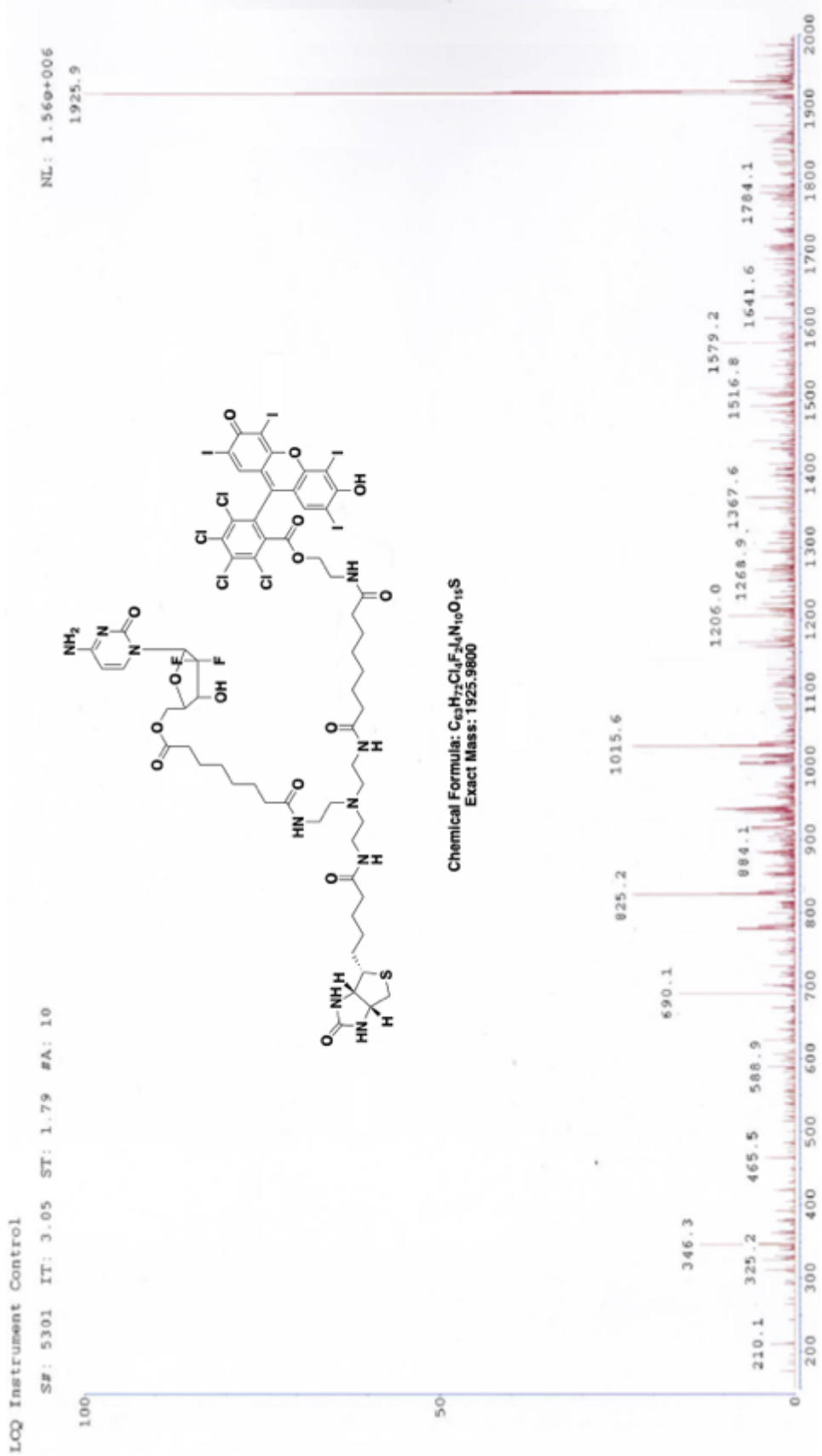
Figure 4.3. ESI-MS spectrum (positive mode) of 12 recorded in methanol.

Chemical Formula: $C_{69}H_{72}Cl_4F_{14}N_{10}O_{19}S$
Exact Mass: 1925.9800
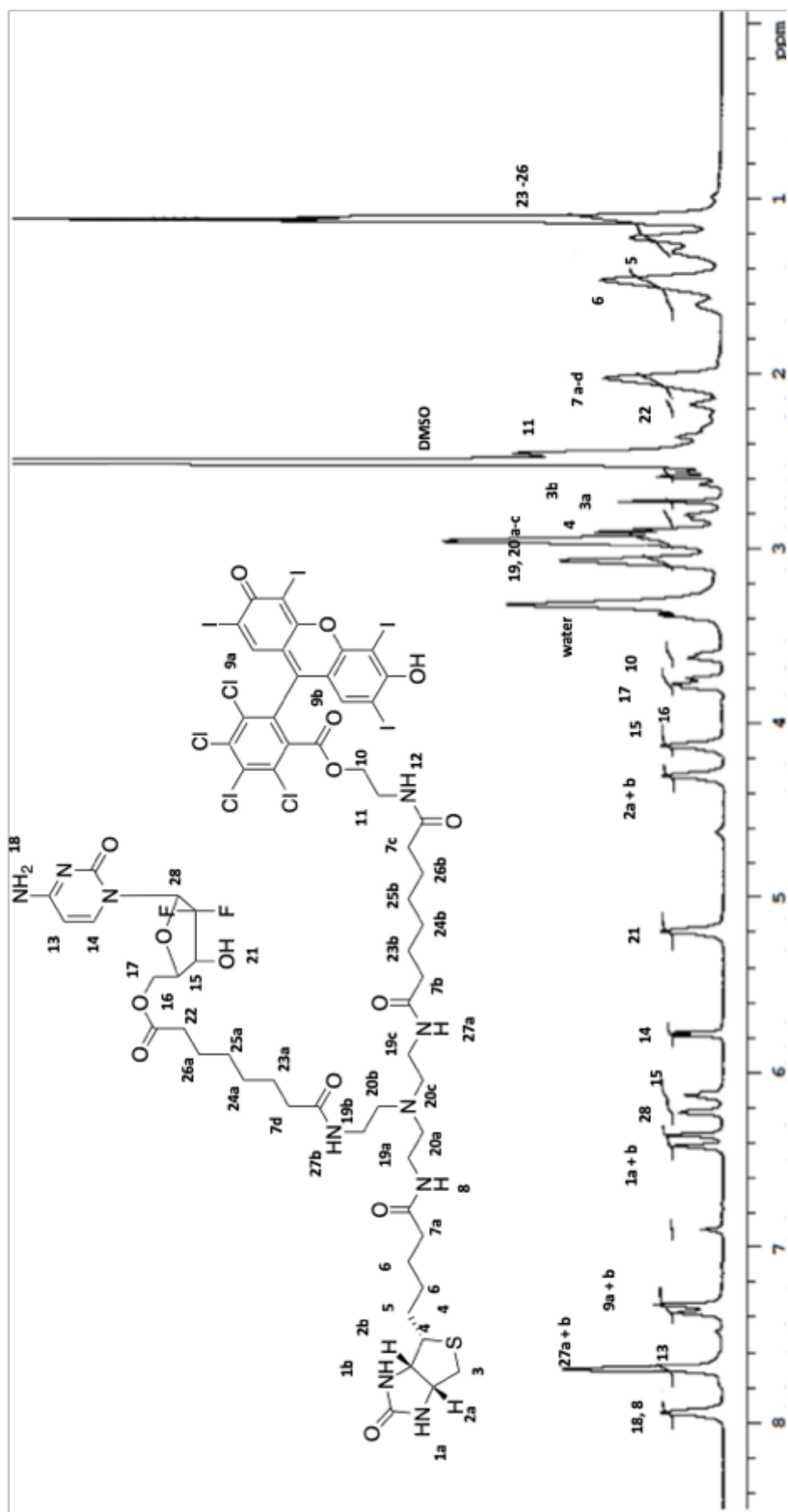
Figure 4.4. ¹H NMR spectrum of 12 recorded in DMSO-*d6*.
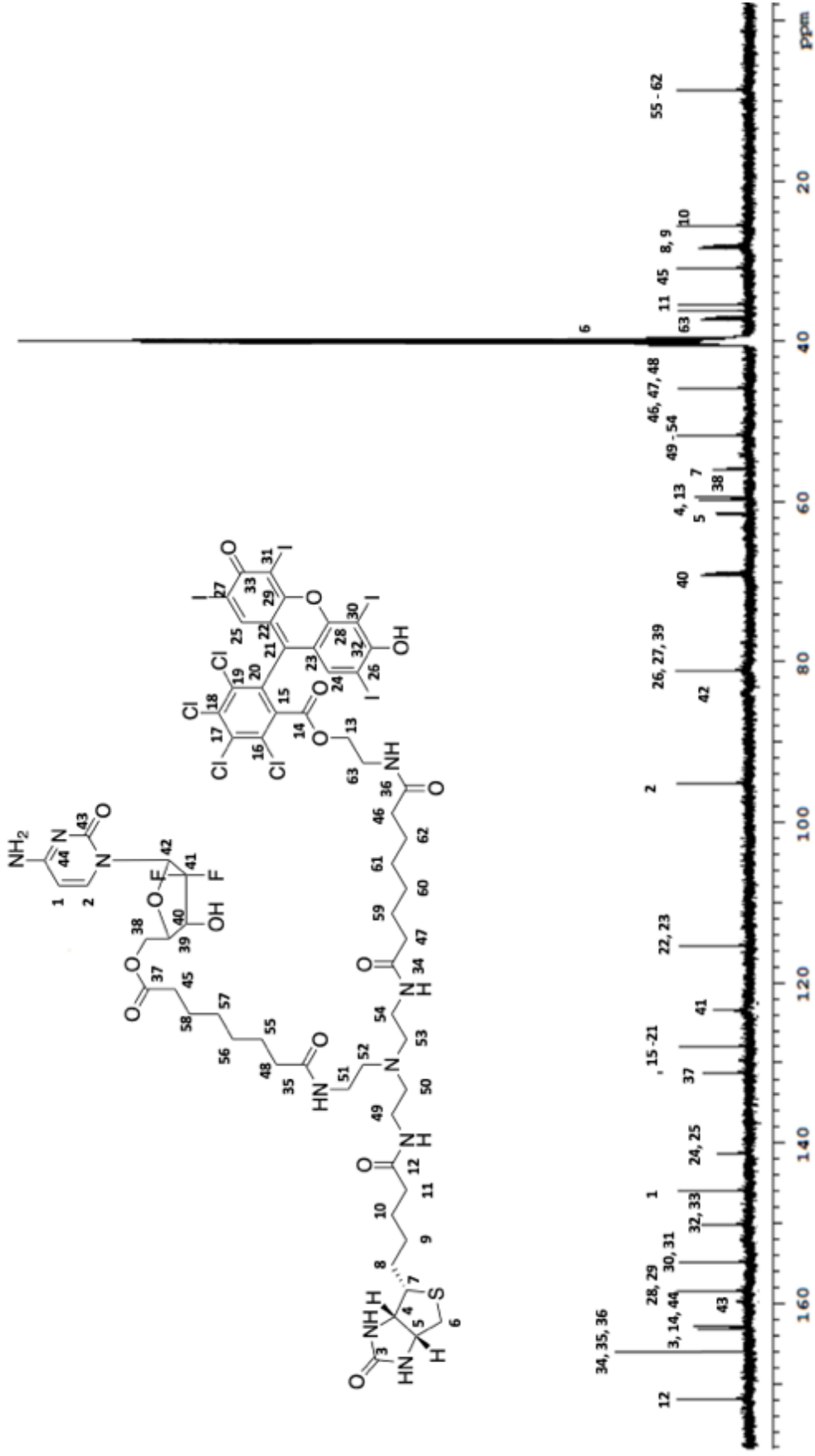
Figure 4.5. ^{13}C NMR spectrum of 12 recorded in DMSO-*d6*

122

4.2.2. In vitro efficacy of 12 in BxPC-3 and MIA-PaCa-2 cell lines

Following the preparation and characterisation of compound **12**, the next step was to determine its efficacy in two pancreatic cancer cell lines, to ensure that derivatising Gem for incorporation within **12** did not impair its efficacy. BxPC-3 and MiaPaCa-2 cells were incubated with **12** at a range of concentrations from 0.001 μM to 100 μM in the absence of light to ensure that there was limited activation of RB. Cell viability was determined 48 hours later using an MTT assay. As a comparison, cells were also treated with the same concentrations of commercial Gem HCl.
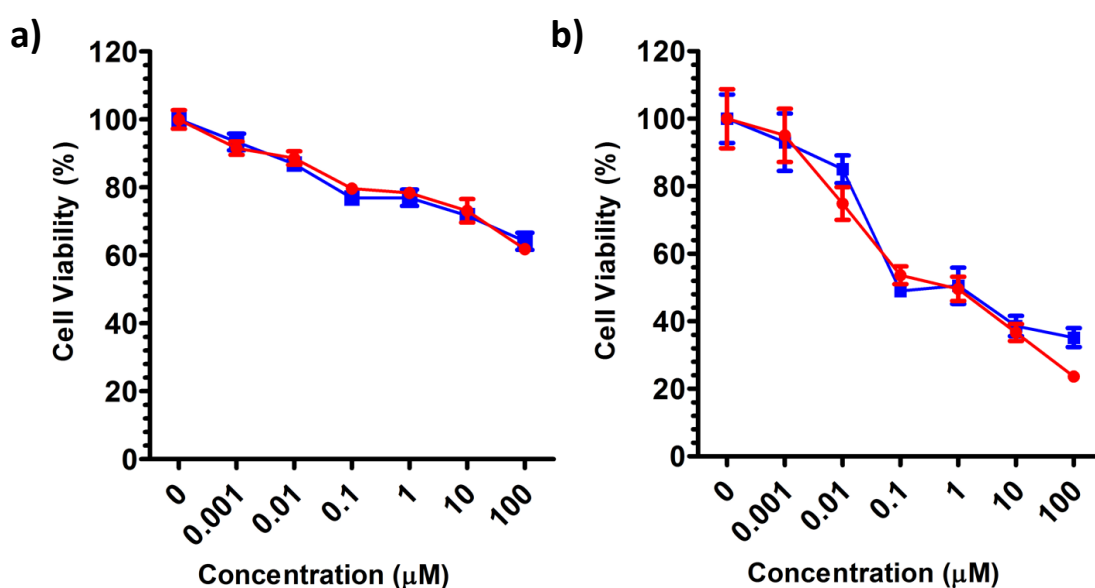
Figure 4.6. MTT assay comparing the efficacy of 12 (red circles) and Gem HCl (blue squares) in (a) BxPC-3 and (b) Mia-PaCa-2 cell lines (n=6).

The results are shown in Figure 4.6 and reveal very similar toxicity profiles between **12** and Gem in both cell lines with the median lethal dose (LD$_{50}$) values determined as 0.71 $\pm$ 0.16 μM and 0.74 $\pm$ 0.19 μM in MiaPaCa-2 and 362.30 $\pm$ 0.12 μM and 474.40 $\pm$ 0.13 μM in BxPC-3 cells respectively. These results suggest that the ester bond connecting Gem in **12** is rapidly hydrolysed by endogenous esterase enzymes to liberate free Gem. It has been shown that many PDAC cell lines express markedly high levels of carboxylesterase 2. (294) Carboxylesterases are ubiquitous enzymes responsible for the hydrolysis of numerous clinically useful drugs including the commonly used PDAC drug, irinotecan. (295)

Furthermore, while it is important for cellular cleavage of Gem to enable its activation by deoxycytidine kinase mediated phosphorylation, rapid cleavage of RB from **12** is less important, as the mechanism of action for SDT does not require the sensitiser to bind to a receptor or be metabolised for ROS to be generated.

In an effort to verify whether any additional contribution to the cytotoxicity of **12** by RB was occurring in the absence of light or US stimulation, BxPC-3 cells were treated with increasing concentrations of **8** which was prepared as described in Section 2.2 with no light or US stimulus applied. The results are shown in Figure 4.7 and reveal no decrease in cell viability between 0 and 10 µM, with a modest 15% decrease in viability observed when the concentration was increased to 100 µM. This suggests that the small decrease in viability for **12** at 100 µM compared to Gem HCl, was likely caused by RB.
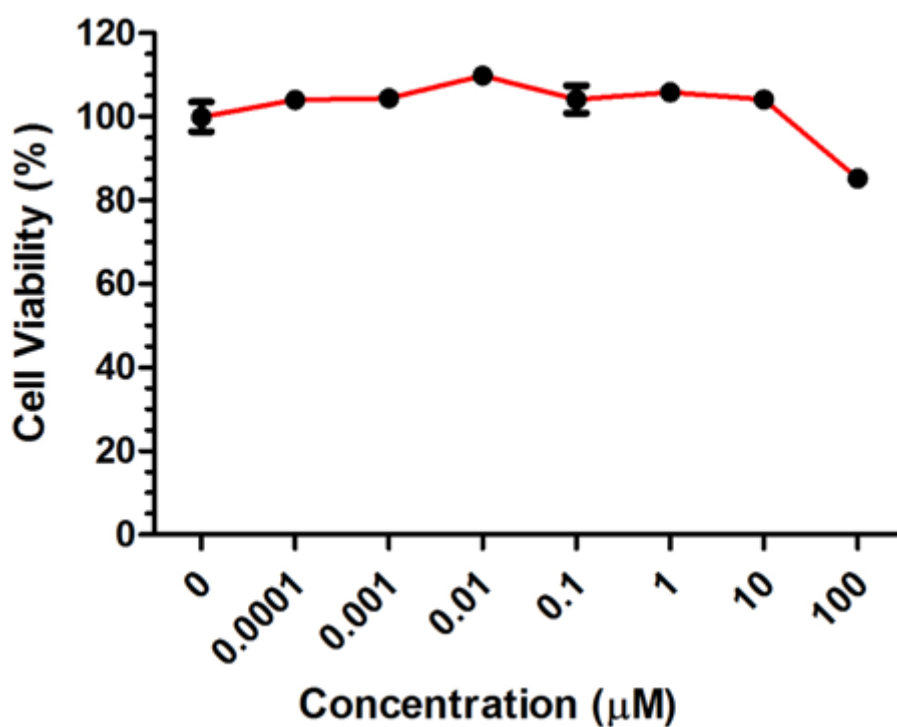
Figure 4.7. MTT assay to determine the toxicity of 8 (0 – 100 µM) in BxPC-3 cells.

4.2.3. Synthesis and characterisation of MB-PTX-Gem-RB

Having established the activity of **12** relative to Gem HCl, the next step was to incorporate the ligand onto the surface of PTX-loaded MBs (Figure 4.8).
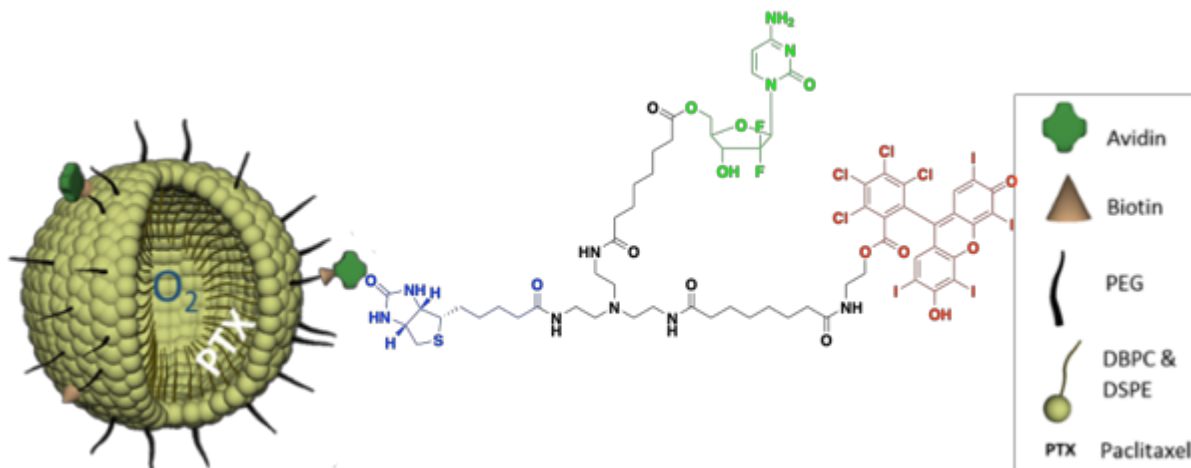
Figure 4.8. Schematic representation of O_2MB-PTX-Gem-RB.

The preparation of avidin-functionalised MB-PTX has been described in Chapter 3. MB-PTX was then subsequently mixed with **12** to generate the MB-PTX-Gem-RB. The resulting MB size and concentration was determined through analysis of optical images taken of MBs in a haemocytometer chamber as described in Section 2.9. A representative analysis is shown in Figure 4.9 and reveals the mean concentration of MB-PTX-RB-Gem to be $1.14 \times 10^9 \pm 1.34 \times 10^8$ MB/mL and a mean particle diameter of 1.47 ± 1.09 μm which is comparable with previous data presented in Section 3.2.4 in which RB and Dox were loaded onto PTX-MB. As **12** contains the RB fluorophore in its structure, its successful loading onto the surface of PTX-MB-Gem-RB could be visualised using fluorescence microscopy, as was the case for PTX-MB-Dox and PTX-MB-RB in chapter 3. A representative image is shown in Figure 4.9a and again shows bright red fluorescence on the MB surface indicating the successful attachment of **12** to the MB shell.
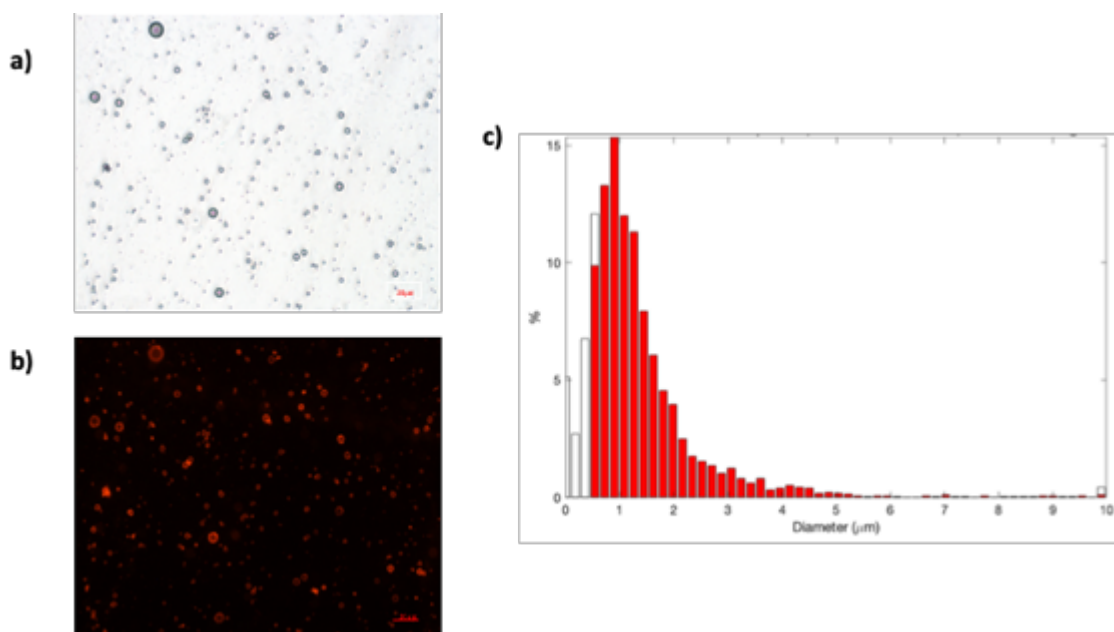
Figure 4.9. a) Optical and b) brightfield images of MB-PTX-Gem-RB taken with 40x objective lens (1:25 dilution in PBS); c) image size distribution analysis produced using a custom MATLAB algorithm (n=20 images).

RB and Gem exist in a 1:1 ratio within **12** making it possible to determine the concentration of both agents in a suspension of PTX-MB-Gem-RB using UV-Vis spectroscopy. A UV-Vis calibration curve was constructed for **12** using standards of known concentrations (Figure 4.10a). Good linearity was observed over the concentration range tested (2.5 – 40 μM) with an R^2 value of 0.9998 Following the preparation of MB-PTX-RB-Gem, a small sample was taken, and the absorbance compared to the calibration curve. Additionally, the loading of PTX was determined using HPLC, as described in Section 2.10. The mean loading of PTX and of **12** was determined to be 58.38 ± 6.74 μg/10^8 MB and 191.34 ± 20.43 μg/10^8 MB respectively. This compares favourably with previous studies where both RB and Gem were separately loaded onto the surface of MBs. (240) However, as MB-PTX-Gem-RB has both Gem and RB attached to a single MB, the loading of each ligand per MB is effectively doubled as no dilution is required to deliver both agents. This clearly demonstrates the effectiveness of combining multiple payloads on a single MB, as there is a limit to the quantity of MB that can be injected at any one time (6.4×10^{10} MB /kg based on preclinical studies of MRX-115 contrast agent in primates) (276).
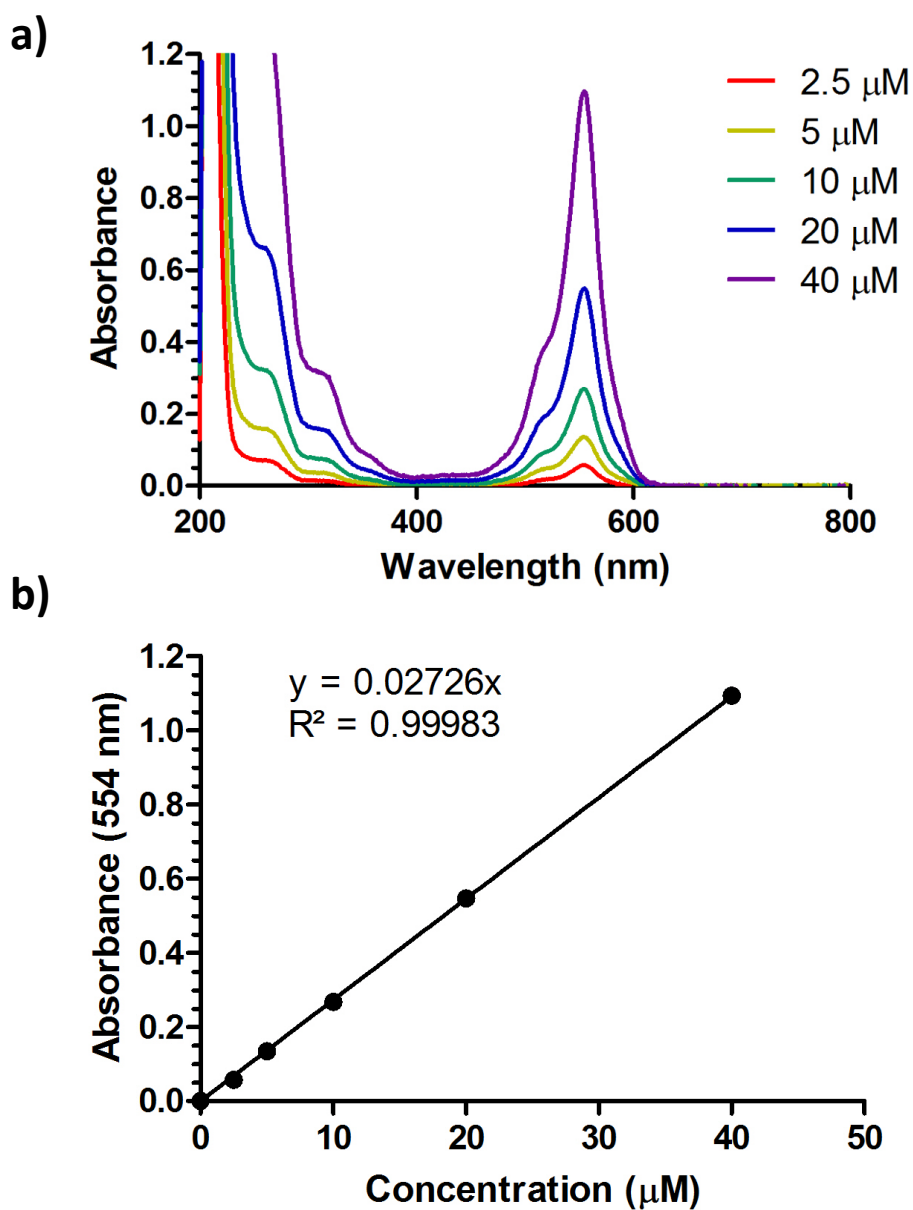
Figure 4.10. UV-Vis spectra for **12** at concentrations ranging from 2.5 – 40 µM and b) Plot of absorbances of **12** against concentration (n=3).

4.2.4. Efficacy of MB-PTX-RB-Gem in Panc-1 spheroids

Following the preparation of MB-PTX-RB-Gem, the next step was to determine the effectiveness of this formulation in a 3D Panc-1 spheroid model. As discussed in Section 3.2.5, the use of 3D spheroid models provides significant advantages over traditional 2D cell models including tumour-mimicking morphology and response to chemotherapy. 96-well plates were coated with 60 µL of 1.5% agarose solution to create a non-adherent meniscus coating at the bottom of each well which induced spheroid formation through aggregation of cells in the middle of each well. Panc-1 cells were subsequently seeded at a density of 2000 cells per well and incubated for 4 days to allow spheroids form. Once formed, spheroids were treated with either a suspension of MB-RB-Gem (i.e. no PTX), MB-PTX or MB-PTX-RB-Gem in the presence and absence of US. The US conditions and experimental set-up adopted for this study were the same as described in Section 3.2.5. Following treatment, cell viability was determined using either an MTT assay or P.I stain.
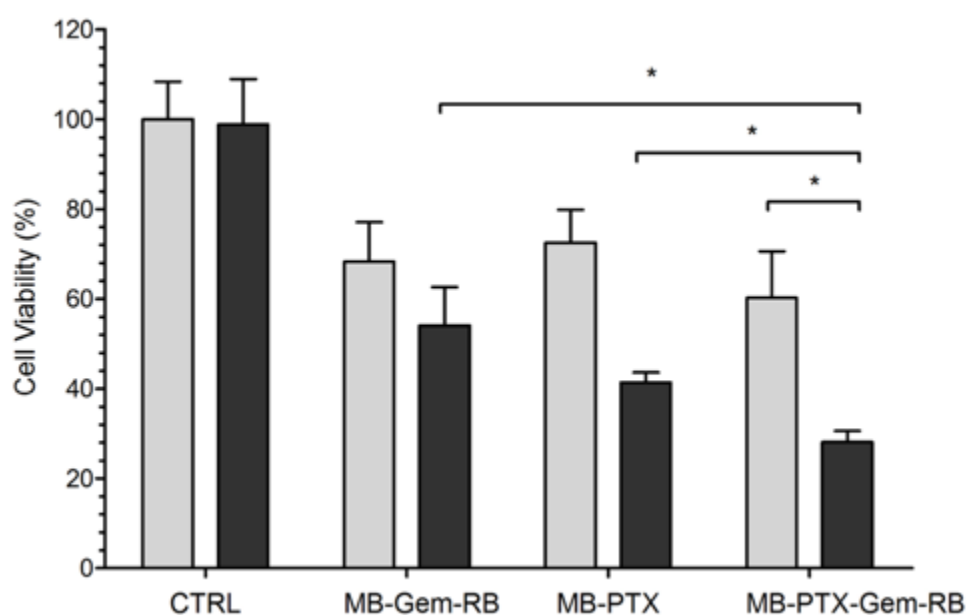
Figure 4.11. MTT assay comparing the cell viability of Panc-1 spheroids treated with of MB-Gem-RB ([Gem/RB] = 5 μM), MB-PTX ([PTX] = 6.6 μM) and MB-PTX-Gem-RB ([PTX] = 6.6 μM, [Gem/RB] = 5 μM) in Panc-1 spheroids with (grey) and without (black) US exposure. . *p < 0.05, **p < 0.01, ***p < 0.001. Error bars represent ± SEM (n = 5).

Results from the MTT assay are shown in Figure 4.11 and reveal no statistically significant reduction in cell viability for spheroids treated with US alone. This was surprising as in previous studies using MCF-7 spheroids, US alone caused a 28.03% reduction in cell viability. This difference may be due to stronger cell-cell interactions in Panc-1 spheroids compared to MCF-7 spheroids. All three MB formulations showed modest reductions in viability in the absence of US with values of 68%, 72% and 60% for MB-Gem-RB, MB-PTX and MB-PTX-Gem-RB respectively. In the presence of US activation, this increased to 54%, 41% and 28% for the same groups respectively. This improvement in cytotoxicity upon US activation is most likely attributed to the physical effects that accompany MB destruction such as micro-jetting and microstreaming. Indeed, representative optical microscope images of the spheroids from each group are shown in Figure 4.12 and reveal visible changes in morphology for spheroids that were treated with MBs + US, with no change observed for spheroids treated with US alone. Spheroids treated with the MBs + US were less densely packed and appeared shredded when compared to untreated or US only treated spheroids. This loss of structural integrity may be due to cell death throughout the body of the spheroid structure resulting from the enhanced drug penetration achieved using US. Combined with sonoporation effects, the reduction in spheroid integrity following MB cavitation most likely further enhances cellular uptake of the PTX, Gem and RB resulting in improved efficacy. Furthermore, the reduction in cell viability observed for the MB-PTX-Gem-RB + US group was also significantly better than both the MB-Gem-RB + US (p ≤0.05) and MB-PTX + US groups (p ≤ 0.05). This suggests that MB mediated PTX treatment compliments Gem/SDT treatment resulting in a potent combination treatment.
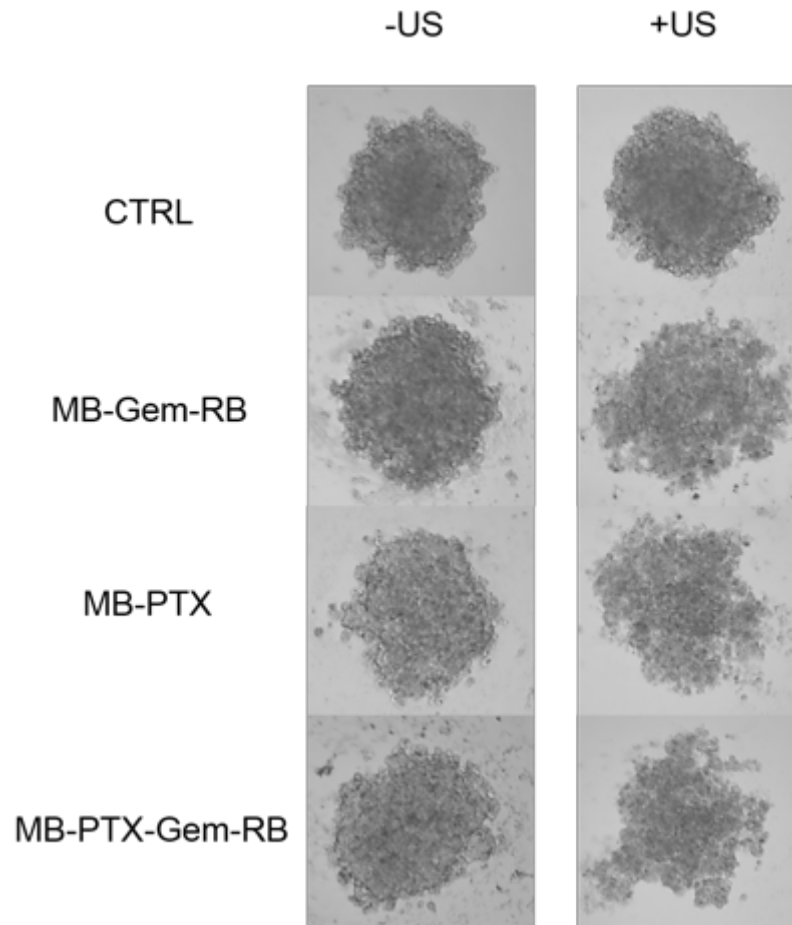
Figure 4.12. Representative images of Panc-1 spheroids treated with of MB-Gem-RB ([Gem/RB] = 5 μM), MB-PTX ([PTX] = 6.6 μM) and MB-PTX-Gem-RB ([PTX] = 6.6 μM, [Gem/RB] = 5 μM) in panc-1 spheroids with (right) and without (left) US exposure.

When the spheroids were stained with PI following treatment and subsequently imaging using fluorescence spectroscopy, a slightly different pattern of results was observed when compared to the MTT experiment (Figure 4.13). Most noticeable was the lack of PI fluorescence observed for MB-PTX + US group with a minor 3% enhancement in intensity relative to the control group. However, the MB-Gem-RB + US group did produce a substantial enhancement in P.I fluorescence which was significant when compared to the same treatment in the absence of US ($p \leq 0.05$) or US alone ($p \leq 0.001$). Again, the most potent treatment was MB-PTX-Gem-RB + US which was also significantly better than both the MB-Gem-RB + US ($p \leq 0.05$) and MB-PTX +US ($p \leq 0.01$) groups as well as the MB-PTX-Gem-RB (i.e without US) ($p \leq 0.01$).
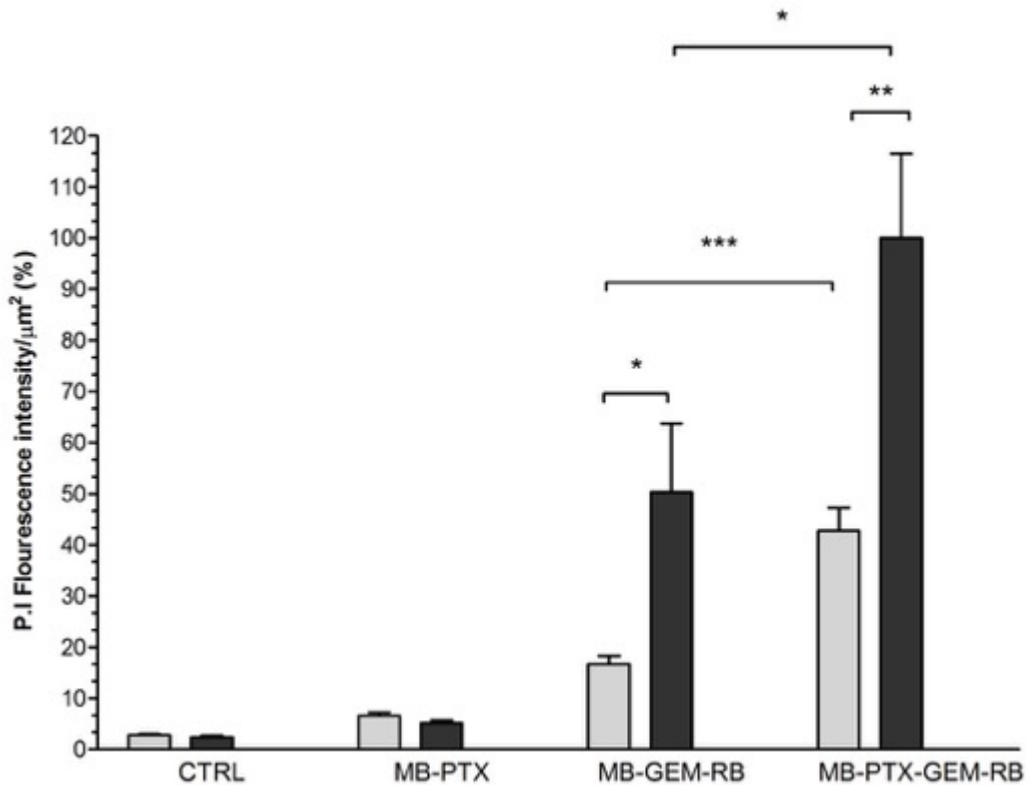
Figure 4.13. Propidium Iodide (P.I) assay comparing the cell viability of Panc-1 spheroids following treatment with MB-Gem-RB ([Gem/RB] = 6.8 μM), MB-PTX ([PTX] = 5 μM) and MB-PTX-Gem-RB ([PTX] - 5 μM, [Gem/RB] = 6.8 μM) with (grey) and without (black) US exposure. *p < 0.05, **p < 0.01, ***p < 0.001. Error bars represent ± the standard error (n=5)

Indeed, images of the spheroids following treatment with MB-PTX-Gem-RB + US were intensely red and visibly brighter than any of the other groups (Figure 4.14). The lack of spheroid shredding which was observed in previous spheroid experiments (Figure 4.12) was due to the fact that spheroids were washed to remove excess drug and P.I which likely also removed any cell debris around the spheroid. The lack of effect observed for MB-PTX + US from the P.I experiment is difficult to explain but it must be remembered that P.I staining of intact spheroids can only detect cell death on the surface of the spheroid structure whereas MTT staining of a cell suspension, derived from treated spheroids, is capable of detecting cell viability of the entire spheroid. Furthermore, MTT and P.I staining detect cell death through distinctly separate mechanisms, with MTT being primarily an indicator of metabolic function and P.I being an indicator of cell membrane permeability. (296,297) Nonetheless, it is clear from both the MTT

and P.I experiments that the best performing treatment was MB-PTX-Gem-RB + US.
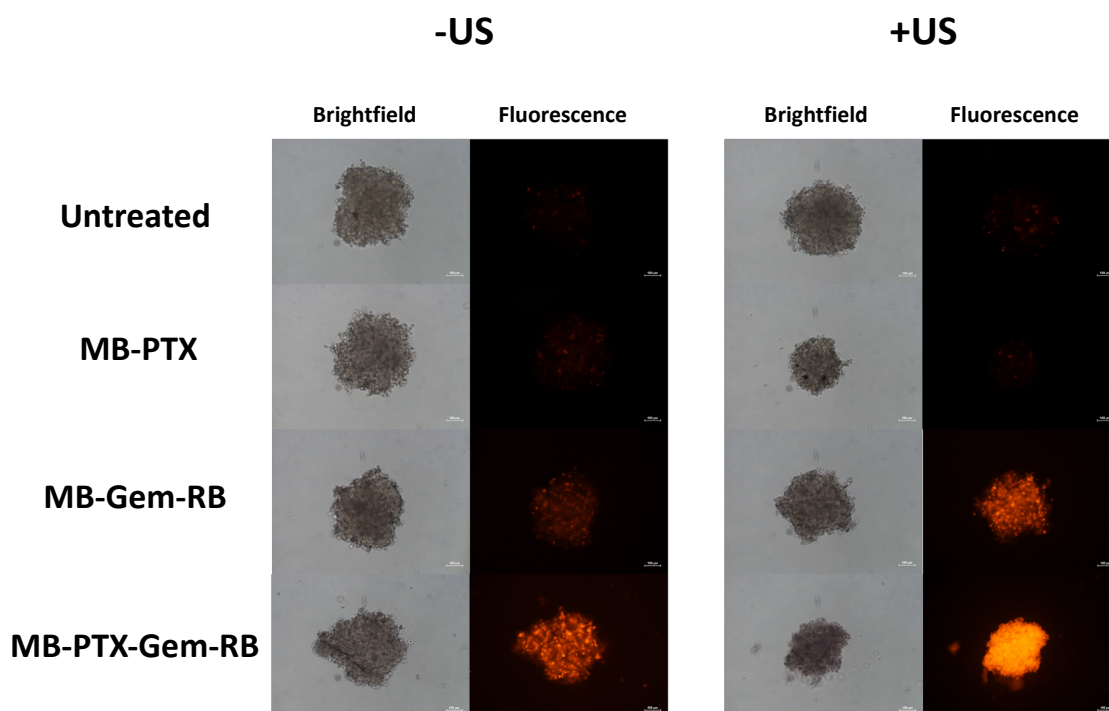
Figure 4.14. Representative images of Panc-1 spheroids following treatment with MB-Gem-RB ([Gem/RB] = 6.8 μM), MB-PTX ([PTX] = 5 μM) and MB-PTX-Gem-RB ([PTX] - 5 μM, [Gem/RB] = 6.8 μM) with (right) and without (left) US exposure.

4.2.5. Efficacy of O_2MB-PTX-Gem-RB in vivo

Encouraged by the efficacy of MB-PTX-Gem-RB in vitro, the next step was to determine the efficacy of O_2MB-PTX-Gem-RB in an in vivo model of pancreatic cancer. To this end BxPC-3 tumours were established in the rear dorsum of SCID mice. Once tumours reached an average volume of 230 ± 104 mm^3 a suspension of O_2MB-PTX-Gem-RB ($6.86 \times 10^7 \pm 1.99 \times 10^6$ MB, [PTX] = 2.44 ± 0.37 mg/kg, [Gem] = 0.5 ± 0.04 mg/kg, [RB] = 1.85 ± 0.14 mg/kg) was administered via a tail vein injection. US (Frequency = 1 MHz, power density = 3.5 W/cm^2, duty cycle = 30%, PNP = 0.4 MPa, 3.5 min) was then applied to the tumour immediately after injection to facilitate MB destruction and delivery of O_2 and drug payloads to the tumour region. A further dose of US, using the same parameters, was applied 30 min later in order to activate the sonosensitiser within the tumour

tissue. For control purposes, two separate groups of animals were either left untreated or administered with a clinical dose of Gem (120 mg/kg) via intraperitoneal injection (I.P). To determine tolerability of the treatments, mouse body weight was also recorded. Previous studies have indicated that administration of drug loaded MBs without any US stimulus provided no significant benefit compared to untreated controls. For this reason and to reduce the number of animals used, US only controls were excluded from these experiments. (238)

The BxPC-3 tumour growth delay curve is shown in Figure 4.15a and reveals a significant regression of 12% ($p < 0.005$) in tumour volume 3 days after the initial treatment for animals treated with O_2MB-PTX-Gem-RB + US. Indeed, the tumours remained below their pre-treatment size for a total of 9 days. In contrast, animals treated with the scaled clinical dose of Gem increased by 53% by day 10 and at no stage did the tumours fall below their pre-treatment volume. It was also of interest to determine how well tolerated the MB mediated treatment was in comparison to the clinically scaled Gem dose. These results are shown in Figure 4.15b and reveal no significant difference in the weight of animals treated with O_2MB-PTX-Gem-RB +US compared to the control group. However, animals treated with the clinically scaled Gem dose displayed a significant 11.70% reduction ($p < 0.05$) in body weight 5 days after the initial treatment indicating acute toxic effects. Combined, these results illustrate that chemo-SDT treatment using the O_2MB-PTX-Gem-RB formulation is both effective and well tolerated when used to treat this particular model of pancreatic cancer.
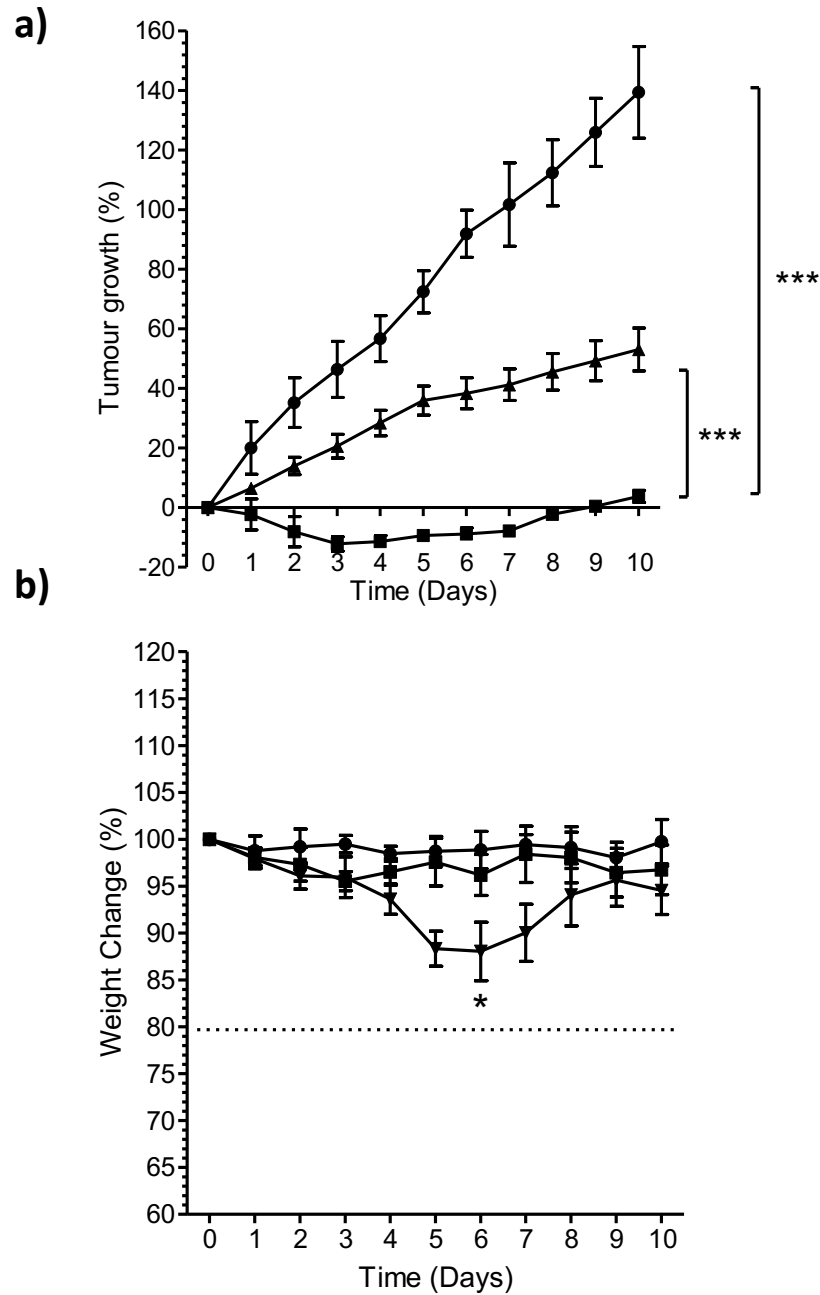
Figure 4.15. Plot of (a) % change in tumour volume and (b) average body weight for BxPC-3 tumour bearing mice treated with (i) no treatment (circles) (ii) O₂MB-PTX-Gem-RB (squares) (iii) gemcitabine (triangles). The MB suspension (6.86 x10⁷ ± 1.99 x 10⁶ MB) was delivered as a 100 μL I.V injection ([PTX] = 2.44 ± 0.37 mg/kg, [Gem] = 0.5 ± 0.04 mg/kg, [RB] = 1.85 ±0.14 mg/kg). Gemcitabine hydrochloride was dissolved in sterile PBS and administered as a 100 μL I.P injection (120 mg/kg). US treatment was delivered for 3.5 mins at frequency of 1 MHz, an US power density of 3.5 W/cm² and a duty cycle of 30% immediately after injection and 30 minutes following. *p < 0.05, **p < 0.01, ***p < 0.001. Error bars represent ± the standard error (n=5).

To determine the robustness of these results the experiments were repeated in a second murine model of pancreatic cancer. In this particular experiment, an additional group was including involving treatment using O_2MB-PTX in an attempt to differentiate any difference between the MB mediated PTX treatment and MB mediated PTX/Gem/SDT treatment. Mia-PaCa-2 cells were implanted in the rear flank of SCID mice and when the average tumour volume reached 150 ± 47 mm^3 the animals were randomly allocated to 4 groups. Group 1 contained untreated animals, group 2 animals treated with O_2MB-PTX-Gem-RB + US, group 3 animals treated with O_2MB-PTX + US while group 4 involved animals treated with a clinically scaled dose of Gem / PTX respectively (i.e. non-MB bound). As was the case in the BxPC-3 model, the O_2MB-PTX-Gem-RB + US treatment had the most potent effect on tumour growth with a 105% increase, 22 days following the initial treatment (Figure 4.16). Again, a regression of 12.9% in tumour was observed for this group 3 days after the initial treatment which was not observed in any of the other groups. The effect on tumour growth delay for this group was significantly better ($p \leq 0.05$) than for the animals treated with O_2MB-PTX (group 3) which grew by 218% at day 22, and also significantly better ($p \leq 0.001$) than the untreated animals that grew by 533% over the same time period. Unfortunately, it was not possible to compare between the O_2MB-PTX-Gem-RB + US and clinically scaled Gem/PTX groups for the entirety of the experiment for toxicity reasons, with animals in this group displaying significant weight loss by day 12 that required them to be removed from the study for ethical reasons. Nonetheless, up until this point, there was no significant difference in tumour growth between these groups. Encouragingly, no significant change in body weight was observed for those animals treated with the MB formulations (groups 2 & 3) again suggesting the treatment was well tolerated. These results very powerfully reflect the toxicity of systemic non-targeted Gem/PTX treatment and how UTMD mediated chemo-SDT can produce superior results in terms of tumour growth control while at the same time causing no significant acute toxic effects.
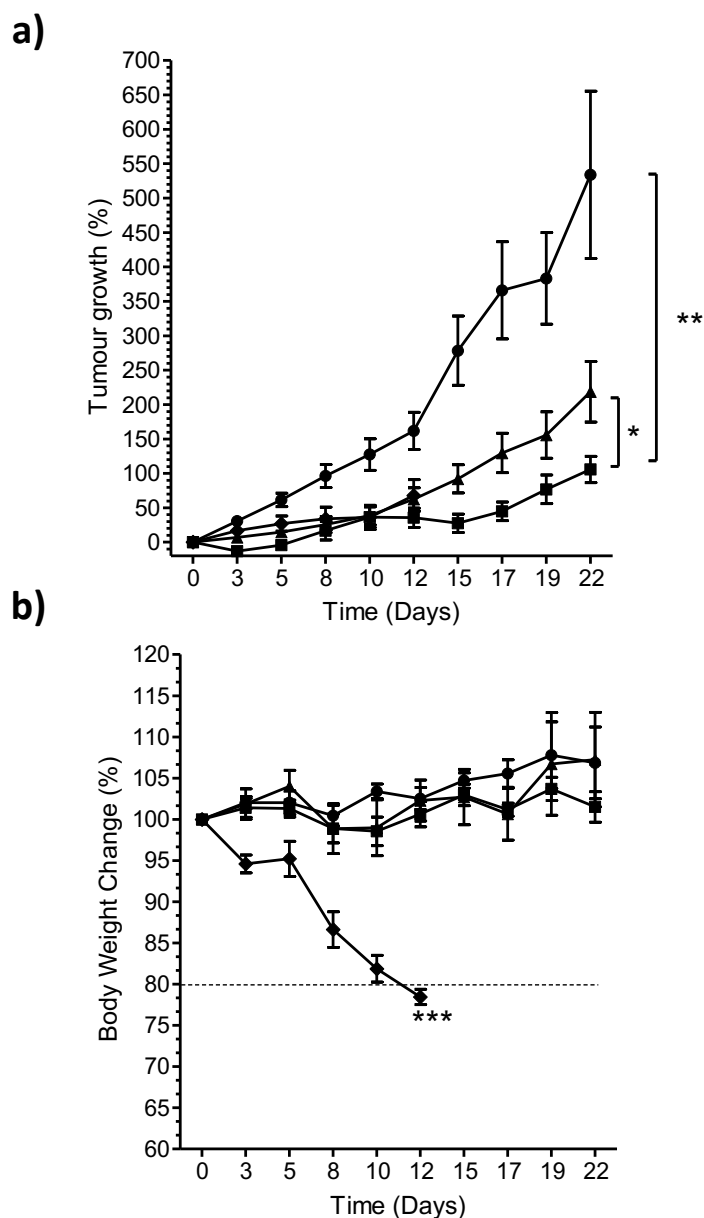
Figure 4.16. Plot of (a) % change in tumour volume and (b) average body weight for MIA-PaCa-2 tumour bearing mice treated with (i) no treatment (circles) (ii) O₂MB-PTX-Gem-RB (squares) (iii) O₂MB-PTX (↑triangles) (v) Gem HCl + PTX in cremophor EL (diamonds). The MB suspensions (O₂MB-PTX-Gem-RB – $6.47 \times 10^7 \pm 1.86 \times 10^6$ MBs, O₂MB-PTX – $7.01 \times 107 \pm 1.5 \times 10^6$ MBs) were delivered as a 100 μL I.V injection (O₂MB-PTX-Gem-RB – [PTX] = 3.38 ± 0.21 mg/kg [Gem] = 0.82 ± 0.06 mg/kg [RB] = 3.02 ± 0.24 mg/kg, O₂MB-PTX – [PTX] = 4.69 ± 0.75 mg/kg). Gem HCl was dissolved in sterile PBS and administered as a 100 μL I.P injection (120 mg/kg). PTX was dissolved in 1 mL of ethanol, 1 mL of Cremophor and 8 mL of sterile PBS and administered as a 100 μL I.V injection. US treatment was delivered for 3.5 minutes at frequency of 1 MHz, an US power density of 3.5 W/cm² and a duty cycle of 30% immediately after injection and 30 minutes following. Error bars represent ± standard error of the mean (n=4).

4.2.6. Determination of toxicity associated with O_2MB-PTX-Gem-RB in healthy, non-tumour bearing mice

The results of combined systemic Gem/PTX treatment in the BxPC-3 model described in the preceding section clearly illustrate the acute toxic effects exhibited this treatment. Nonetheless, these drugs are clinically approved for use in humans. The targeted nature of UTMD as a delivery platform also ensures that lower doses of chemotherapy can be administered to achieve the desired therapeutic response. Following consultation with the UK medicines regulator (MHRA) regarding future translation of this technology to the clinic, a small single species safety study was requested to ensure no deleterious effects were observed by combining the O_2MB platform with the active payloads. To this end, healthy non-tumour-bearing mice were separated into four treatment groups as detailed in Table 1.

Table 4.1. Safety study treatment groups. (n=10 animals per group)

Group	Treatment
1	Untreated
2	US only at abdomen
3	PTX + RB I.V plus Gem HCl I.P
4	O_2MB-PTX-Gem-RB conjugate

Group 1 included untreated animals while group 2 included US treatment only (frequency = 1 MHz, power density = 3.5 W/cm^2, duty cycle = 30%, PNP 0.4 MPa, 3.5 min). As these animals were non-tumour bearing, the US was directed to the pancreas as would be the case in orthotopic tumour treatment. Group 3 included animals treated with Gem, PTX and RB. PTX and RB were delivered by I.V injection with PTX pre-formulated in a Cremophor EL vehicle while Gem was administered by IP injection ([Gem] = 120 mg/kg, [PTX] = 15 mg/kg, [RB] = 6 mg/kg). Group 4 involved treatment with O_2MB-PTX-Gem-RB again delivered by I.V injection ($6.58 \times 10^7 \pm 1.25 \times 10^6$ MB, [PTX] = 2.03 ± 0.19 mg/kg [Gem] = 0.72 ± 0.07 mg/kg, [RB] = 2.66 ± 0.27 mg/kg). The body weights of the animals in each group were recorded daily and 14 days following treatment, blood samples were removed and analysed for several key biochemical and haematological

markers in both whole blood and serum. The body weight measurements are plotted in Figure 4.17 and reveal no significant difference between any of the treatment groups indicating that all treatments were well tolerated with no acute adverse effects. This is in contrast to previous results where the clinical standard dose of PTX and Gem showed high levels of toxicity. However, in those experiments, animals were treated twice weekly for a total of 4 treatments whereas in the current study animals were only treated once weekly for a total of two treatments. This would have given animals enough time to recover between treatments. Additionally, animals used for the current safety study were healthy non-tumour bearing mice whereas in the efficacy study immunodeficient mice were used which may be a contributing factor. Results from the blood biochemistry analysis are plotted in Figure 4.18. Two key biochemical markers involved in blood analysis are urea and alanine aminotransferase (ALT) with increased levels of these markers suggesting damage to the kidneys and liver respectively. The results reveal no significant difference in levels of urea or ALT for any of the treatment groups when compared to untreated animals. Similarly, all the other biochemical markers remained largely unchanged between the four groups. These results corroborate a previous pre-clinical safety study where a similar O_2MB delivery platform was used to deliver both RB and Gem. In this study, further histological analysis of liver and kidney sections harvested from treated animals also revealed no evidence of toxicity, with only a minor increase liver steatosis caused by the MB groups and an increase in glomerular cellular for animals treated with free Gem. (240) While further histological analysis would be required to confirm the safety of O_2MB-PTX-Gem-RB treatment, the blood biochemistry results, and the lack of acute weight loss would support the tolerability of this treatment.
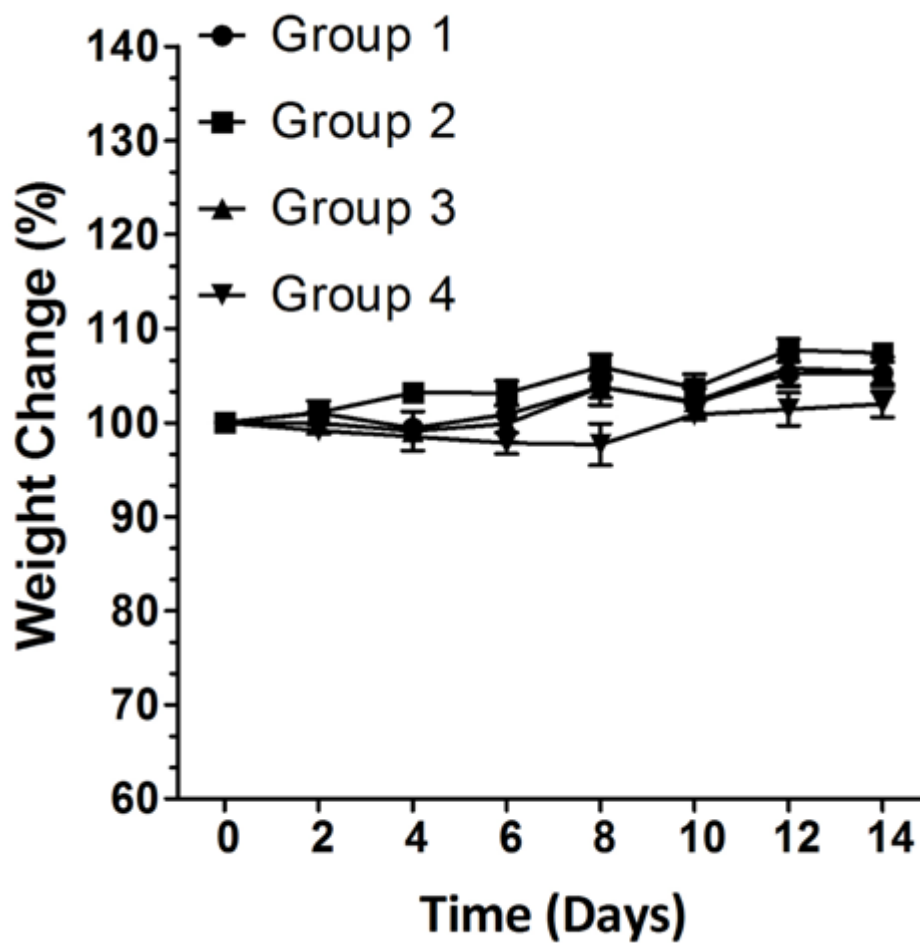
Figure 4.17. Plot of % change in body weight against time during treatment. Mice were separated into 4 groups; untreated, US only, I.V injection of RB and PTX and I.P injection of Gem, and I.V injection of a suspension of O$_2$MB-PTX-Gem-RB (n=10).
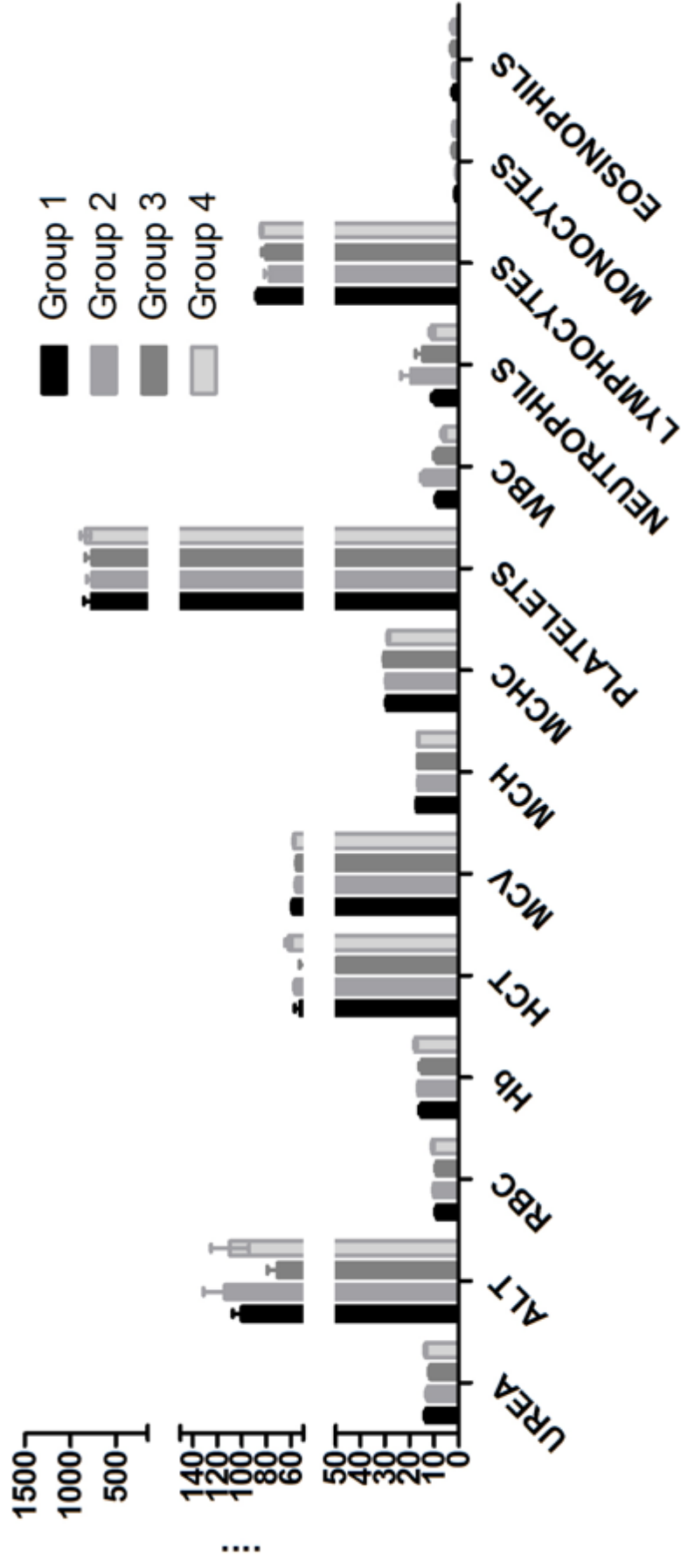
Figure 4.18. Whole blood and serum biochemical marker analysis from healthy non-tumour- bearing mice treated as described in Table 4.1.

4.3. Conclusion

In summary, a novel tripodal ligand was synthesised comprising RB and Gem connected to a biotin anchor to facilitate conjugation of both payloads to the MB shell. The ligand was then added to the surface of MB-PTX, which were prepared as described in chapter 3. Cell viability studies confirmed that modification of Gem at the 5′ hydroxyl position in **12** did not compromise its toxicity with similar LD_{50} values observed when compared to unmodified Gem in both Mia-PaCa-2 and BxPC-3 cell lines. The ligand was also successfully attached to the surface of MB-PTX with drug loading which compared favourably with that of MB-PTX-RB prepared in chapter 3. The resulting MB-PTX-Gem-RB caused a significant change in the morphology of Panc-1 spheroids following US treatment with the cells also displaying intensely red PI fluorescence indicating a large quantity of non-viable cells. This conclusion was supported when the same cellular suspension was analysed using an MTT assay. The effectiveness of MB mediated chemo-SDT treatment using the O_2MB-PTX-Gem-RB formulation was also demonstrated in two murine models of pancreatic cancer with improved efficacy and better tolerability when compared to clinically scaled doses of the free (i.e non-MB bound) chemotherapies. It should be noted however, that this improved efficacy for the MB mediated treatment was obtained using substantially lower doses of chemotherapy when compared to normal systemic doses with 155-fold lower Gem and 8-fold lower PTX respectively. In addition, no deleterious effects on key blood biochemistry markers or acute changes to bodyweight were observed when the O_2MB-PTX-Gem-RB were administered to healthy non-tumour bearing mice, also confirming the tolerability of the treatment.

The ability of O_2MB to deliver chemo-SDT for the treatment of pancreatic tumours has been established in the literature. (214,238,240,242) However, to the best of our knowledge, a single O_2MB formulation to deliver chemo-SDT and PTX/Gem chemotherapy has not yet been described in the published literature. Previous attempts at using UTMD mediated delivery to pancreatic tumours involved the use of a mixed MB suspension meaning that simultaneous delivery of both drug to the target site could not be guaranteed. The fact that all three drugs used in this study were delivered in a single MB formulation offers a significant advantage to previous methods as it is well established that for multiple payload drugs to act synergistically, they must be simultaneously

delivered to the target site. (298) The results outlined from the in vivo studies also demonstrate the potential of the chemo-SDT using the O_2MB-PTX-Gem-RB formulation to cause an initial regression in tumour volume that may be of benefit when considering use in a neo-adjuvant setting.

Collectively, the results described in this chapter make a positive step-forward in the development of single MB formulations for the delivery of multiple payloads. While the context of the work in this chapter was focussed on pancreatic cancer, a similar strategy could also be adopted for other indications using alternative drug combinations.

Chapter 5

Magnetic Microbubble Mediated Chemo-Sonodynamic Therapy using a Combined Magnetic-Acoustic Device

Chapter 5 – Magnetic Microbubble Mediated Chemo-Sonodynamic Therapy using a Combined Magnetic-Acoustic Device

5.0. Introduction

As has been described in previous chapters, drug-loaded MB can be targeted to the tumour site using an external US stimulus, enabling the deposition of drug payloads into the surrounding tissue. Several targeting techniques have also been developed to further increase the localised concentration of drug loaded MBs. For example, MBs have been functionalised through the attachment of targeting ligands such as peptides and antibodies, enabling receptor binding and subsequent accumulation of MBs within the tumour endothelium. (299,300) However, the short half-life of MBs (< 5 min in circulation) has limited the application of this method. Acoustic radiation force has also been used alongside targeted MBs in an effort to remotely control the flow of MBs in circulation and encourage accumulation of targeted MBs at the endothelial lining, thereby increasing their binding to target sites. (299,301)

A more recent approach has been to incorporate magnetic particles into MBs. This strategy enables the capture and retention of MBs in the target region using an external magnetic field. (302) This often involves the incorporation of iron oxide nanoparticles (IONPs) into the formulation. IONPs have the capacity for functionalisation with various coatings such as polymers, carbohydrates and phospholipids. (303) Phospholipid coated IONPs, due to their amphiphilic nature, are capable of embedding within the hydrophobic fatty acid chains of MB. There are several methods for accomplishing this. IONPs can be incorporated into an oil phase which can be subsequently formulated into acoustically active liposheres (AALs). Although this method has the advantage of excellent IONP loading, it suffers from low magnetic retention as a result of a poor half-life under flow. In addition, it has also been shown that the thick oil shell renders the AALs more stable to US meaning that higher mechanical indices are required to induce drug release. Alternatively, IONPs can be functionalized with biotin enabling the use of avidin-biotin binding chemistry to allow conjugation to the outer surface of the MB. Much like the AALs, this approach has the advantage of excellent IONP loading, and, in contrast, has a high magnetic retention. However, as this approach uses surface functionalisation, it is likely that there would be limited

binding sites available for drug loading onto the exterior of the MB using an avidin-biotin bridge. Another approach is to incorporate IONPs into the phospholipid shell. While this method provides a relatively low magnetic response, it may provide a more favourable compromise between targeting efficiency, stability, acoustic response and surface loading potential for hydrophilic drugs. (304) The latter approach was used in a 2017 study in which magnetically responsive O_2MBs (MagO$_2$MBs) in combination with the antimetabolite drug 5-FU and the sonosensitiser, RB, were delivered to pancreatic tumours. (247)
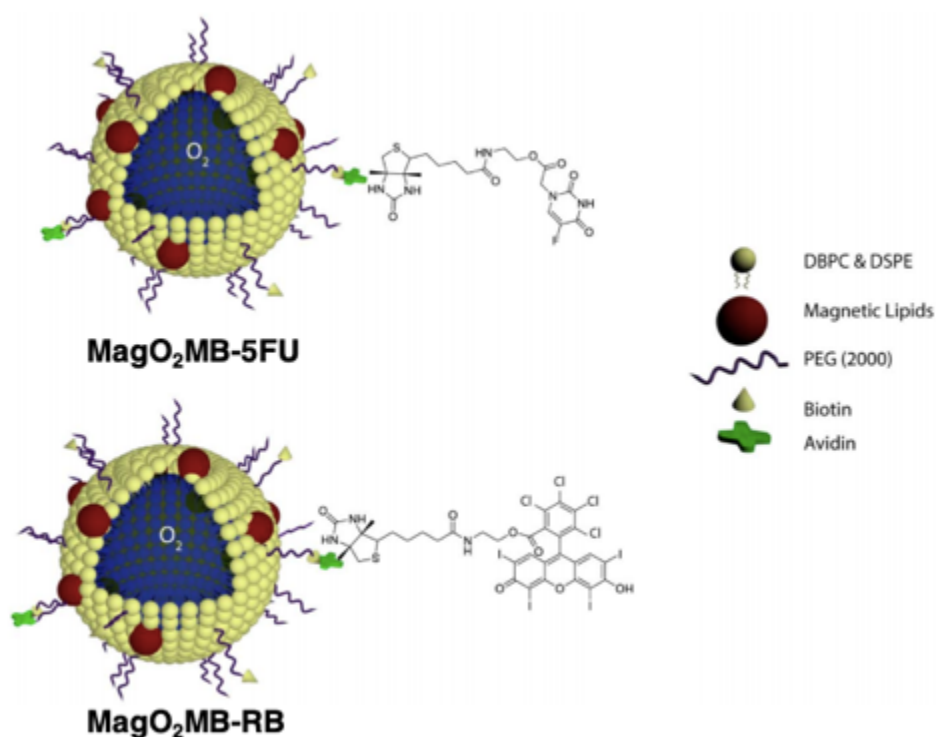
Figure 5.1. Schematic representation of the MagO$_2$MB-5FU and MagO$_2$MB-RB conjugates. Taken from (247)**.**

In this study, two separate MagO$_2$MB formulations were prepared, each bearing either 5-FU or RB, attached to the surface of the MB through the use of an avidin-biotin bridge. In vitro retention studies using a flow chamber with physiologically relevant flow rates showed a significantly increased retention in MagO$_2$MB when a magnetic field was applied to the flow chamber compared to when no magnetic field was applied. When tested in a panel of pancreatic cancer

cell lines, a significant improvement in cytotoxicity was observed in cells treated with $MagO_2MB$-5FU plus $MagO_2MB$-RB, in the presence of US, indicating that the presence of IONPs in the MB shell did not hamper their efficacy. This effect was also apparent in vivo, when studies using an orthotopic BxPC-3 model in SCID mice, treated with the mixed $MagO_2MB$-5-FU / $MagO_2MB$-5-RB formulation in the presence of US and an external magnetic field, displayed a significant 48.3% reduction in tumour growth ($p \leq 0.05$) compared to untreated animals. In contrast, tumours in animals treated with the mixed $MagO_2MB$-5-FU / $MagO_2MB$-5-RB formulation and US in the absence of a magnetic field reduced by 27.9%

While the combination of magnetic and US fields demonstrated an improved tumour growth delay and increased apoptotic cell signalling compared to treatment with US only, this study had two important shortcomings. First, the simultaneous application and alignment of magnetic and US fields represented a significant practical challenge in vivo. This problem is particularly acute in small animal models due to space constraints and may greatly limit the potential synergistic benefits of magnetic-acoustic targeting. Second, it was necessary to use a mixture of MBs: (i) with 5-FU and (ii) with RB bound to the surface. This meant that upon injection it was impossible to control the delivery of each individual agent to the target site.

In the present chapter, the first shortcoming was addressed by using a prototype probe enabling co-aligned US and magnetic fields to be applied simultaneously. (245) The second was addressed through the ligand discussed in chapter 4, wherein both the SDT and chemotherapy drugs were linked to a single biotin moiety, thereby enabling the attachment of both drugs to a single O_2MB.

5.1. Hypothesis and specific objectives

The hypothesis for the work undertaken in this chapter is that a magnetically responsive O_2MB formulation, carrying both Gem and RB, can be targeted and activated using a combination of externally applied magnetic and US fields, delivered via a combined acoustic-magnetic device (MAD). The work presented in this chapter is currently under review for publication at the time of writing. The specific objectives were to:

1. prepare and fully characterise magnetically responsive MB functionalised with ligand **12.**

2. determine the singlet oxygen production and acoustic emission characteristics of $MagO_2MB$-RB.

3. determine the effectiveness of the MAD device at enabling the delivery of $MagO_2MB$-RB in agar phantom models.

4. determine the effectiveness of the MAD device at enabling the delivery of $MagO_2MB$-Gem-RB in ectopic BxPC-3 xenografts.

5.2. Results and discussion

5.2.1. Preparation and characterisation of MagO₂MB-RB and MagO₂MB-Gem-RB

Avidin-functionalised magnetically responsive MBs (MagMB) were prepared as previously described. (247) However, in the current work, 1,2-dibehenoyl-sn-glycero-3-phosphocholine coated IONPs were used (3.75 mg iron) instead of FluidMAG-Lipid nanoparticles, in order to use the same lipid as the one comprising the MB coating. First, a liposomal suspension was prepared as described in Section 2.8. DBPC-IONPs were then added and the suspension was further sonicated using a probe sonicator to fully disperse the lipids and IONPs. The headspace of the vial was then filled with PFB gas and the liquid-gas interface was sonicated to produce MagMB. Following preparation of MagMB, either **8** or **12** was attached to the surface of the MB using an avidin-biotin bridge as previously described in section 4.2.3. In an effort to preserve the limited stock of **12**, and given its relatively complicated synthesis, for all in vitro experimentation including in vitro activation and drug delivery in agar phantoms, **8** was used as a surrogate drug as it is significantly more straightforward to prepare.
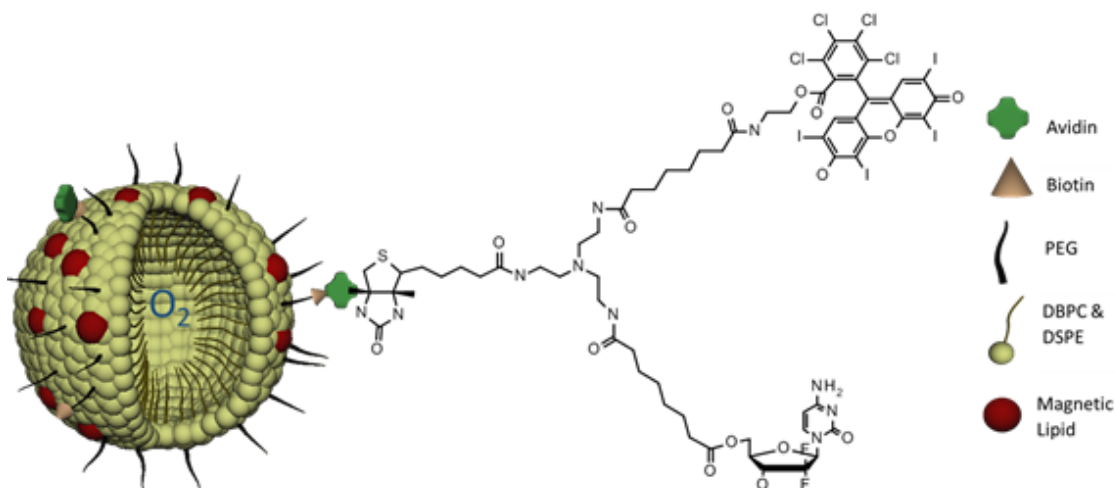
Figure 5.2. Schematic of MagO₂MB-Gem-RB.

5.2.2 Characterisation of MagMB-RB and MagMB-Gem-RB

Following preparation, MB were characterised in terms of size, concentration and drug loading as described previously in Sections 2.9 and 2.11 as well as IONP loading. The mean MB concentration was determined to be $2.1 \pm 0.3 \times 10^9$ MB/mL

with a mean diameter of 1.6 μm. Purification of MBs through centrifugation decreased the MB concentration to an average of 7.2 ± 2.0 x 10^8 MB/mL, with a mean diameter of 1.8 μm. A comparison of the size distributions from before and following conjugation with **12** suggest that the loading and subsequent washing mostly removes the smallest MBs (Figure 5.3). However, MBs with a diameter between 1 and 8 μm appeared stable during this process. The drug loading for **8** and **12** after washing was determined using UV-Vis as described in Section 2.11 and was determined to be 82.87 ± 62.15 μg/10^8 MB and 139.10 ± 48.15 μg/10^8 MB for **8** and **12** respectively. These loadings are slightly lower than in previous chapters where **8** and **12** were loaded onto PTX-MB and may be as a result of the relatively large IONPs within the lipid monolayer inhibiting the avidin-biotin interaction.
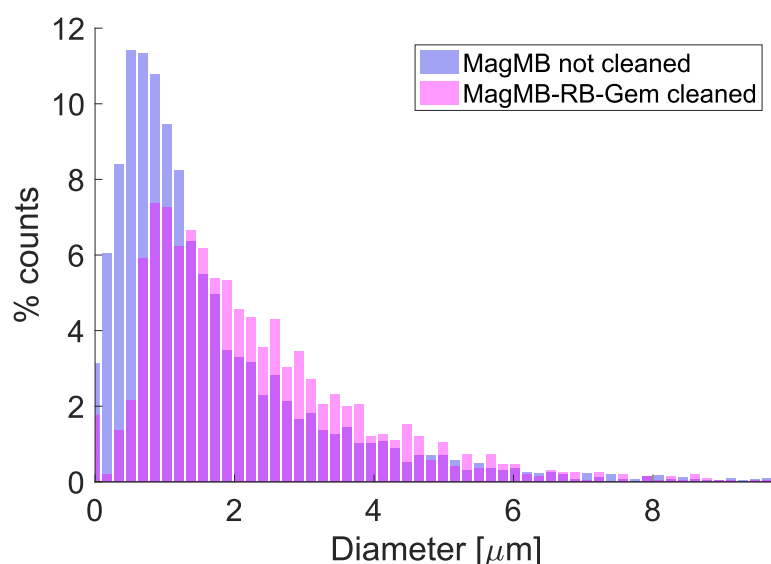
Figure 5.3. Size distribution of MagMBs before and after loading of 12 obtained from analysis of optical microscope images for each batch. The concentration of MagMB-RB-Gem after 3x centrifugation cleaning was on average 7.2 ± 2.0 x10^8 MB/mL. (n = 20 images).

5.2.3 Determination of iron content of MagMB-Gem-RB

As the iron content of MagMB is generally proportional to the magnetic responsiveness and hence targeting ability of the MB, it was crucial to determine the loading of IONPs within the formulation. (304) This was done indirectly through the determination of the iron loading. Iron content was determined using inductively coupled plasma-optical emission spectrometry (ICP-OES) measurements of samples diluted in 2% nitric acid at a wavelength of 238 nm. A calibration curve was produced using standards containing known concentrations of iron (Figure 5.4). Good linearity was observed over the concentration range tested (0-1 mg/L) with a R^2 value of 0.9997. Using the calibration curve and the emission intensity of the unknown samples the mean iron loading was determined to be 0.07 ρg/MB. This compares favourably with a previous study where DBPC-IONPs were loaded into MB in which a loading of 0.04 ρg/MB was achieved. The reason for the increase is not fully understood but could be partly due to due to the variation in the centrifugal washing steps used in their preparation. (304)
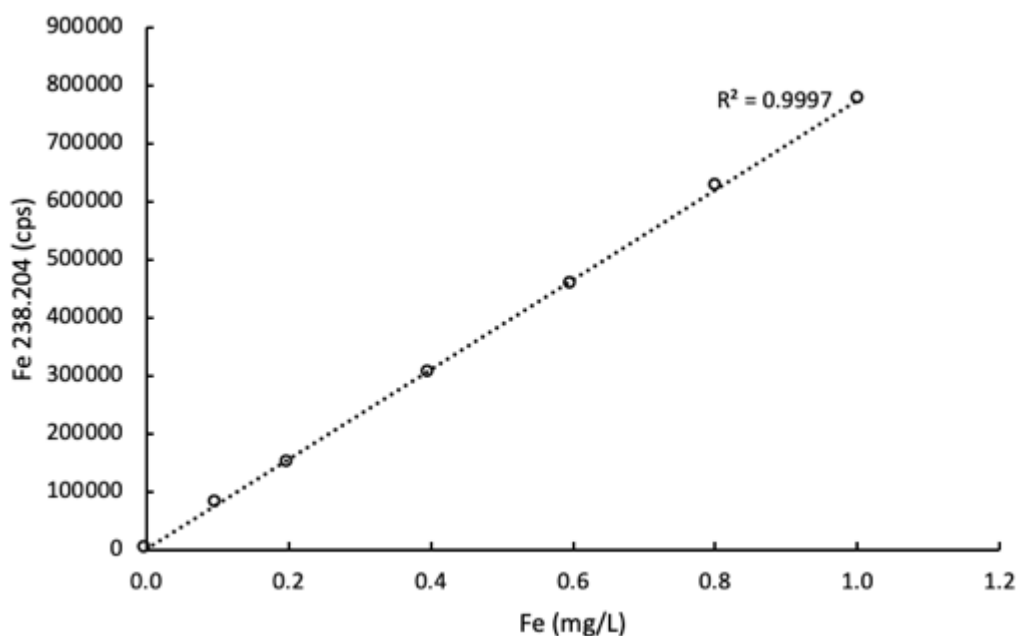
Figure 5.4. Inductively coupled plasma-optical emission spectrometry (ICP-OES) calibration curve of Fe measured at 238 nm in 2% nitric acid.

5.2.4. Combined magneto-acoustic device (MAD)

The MAD was designed as described by Barnsley *et al.* and assembled as shown in Figure 5.5. (245) The main magnetic body consisted of a N52 grade neodymium permanent magnet (NdFeB) with geometry which was optimized to have a maximum magnetic field strength of 0.2 T at a distance of 10 mm from the body's leading edge. An integrated ultrasonic element with a focal distance also of 10 mm provided a pressure field that spatially overlapped with the magnetic field peak, with sufficient amplitude to cause inertial cavitation of MBs used in this study. This was key as it meant that $MagO_2MB$-Gem-RB could be both optimally retained and destroyed at the same focal depth. An aluminium-bodied copy of the MAD (aMAD) was produced to provide an US-only control for in vitro and in vivo experimentation.

(A)   (B)
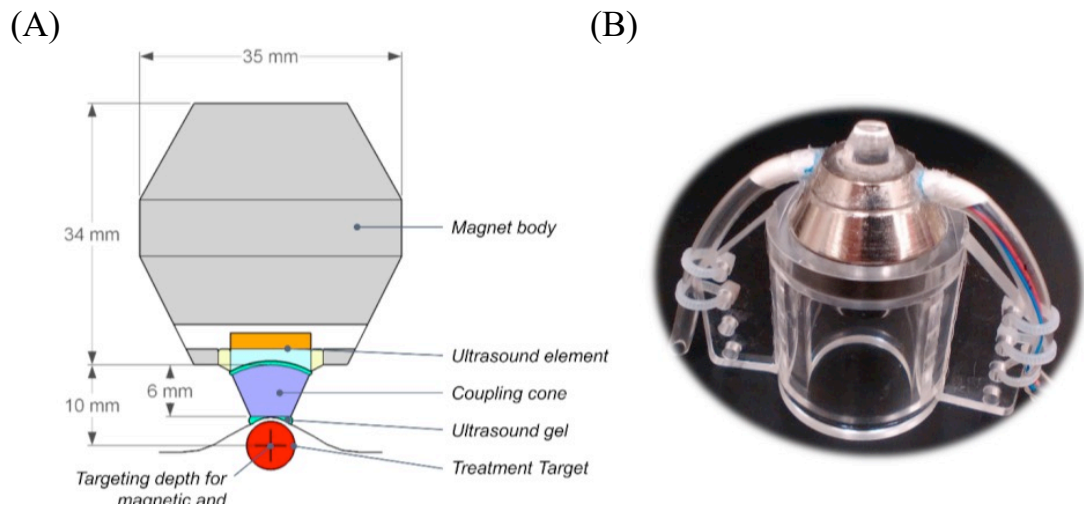
Figure 5.5. (A) MAD configuration illustration and (B) photograph as tested, with Perspex holder.

An important constituent of any type of therapeutic/diagnostic US device is the mechanism for coupling the acoustic beam into the tissue. The efficient transfer of US energy from the transducer to the treatment site is reliant on good acoustic coupling. The ideal acoustic coupler needs to be a homogeneous material with low attenuation and acoustic impedance similar to that of the tissue being treated. For this reason, a coupling cone (Figure 5.5), cast from paraffin wax, was secured onto the leading edge of the US element with US gel. The cone

material was chosen for its ease of casting and minimal transmission loss in the 1 MHz frequency range.

5.2.5. In vitro activation and delivery

Before further work could be done with MagO$_2$MB-Gem-RB it was deemed prudent to evaluate the ability of MagO$_2$MB in combination with **8** to produce singlet oxygen (^{1}O$_2$), as Fe(II) is redox active and could potentially participate in electron transfer reactions with the excited sensitiser. This was done using singlet oxygen sensor green (SOSG) which is a commercially available fluorescent probe selective for ^{1}O$_2$. SOSG comprises a fluorescein fluorophore connected to an anthracene quencher. Under normal conditions the anthracene moiety quenches the fluorescein emission through a photoinduced electron transfer (PET) process as shown in Figure 5.6. However, in the presence of ^{1}O$_2$, the anthracene unit is oxidised to the corresponding endoperoxide (SOSG-EP), increasing its oxidation potential and cancelling the PET process. Thus, the interaction of SOSG with ^{1}O$_2$ generates a strong fluorescein emission at 530 nm following excitation at 490 nm, the intensity of which is dependent on the amount of ^{1}O$_2$ present.
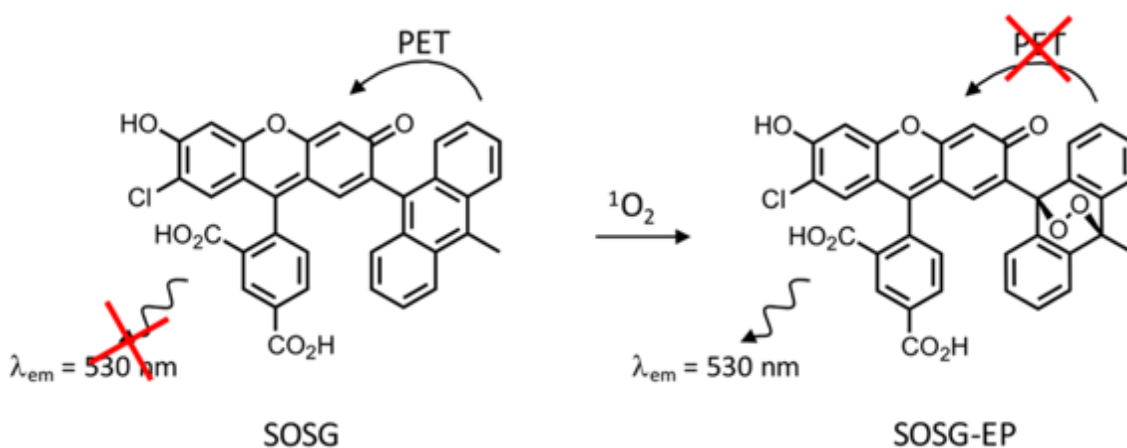
Figure 5.6. Schematic showing the chemical structure of SOSG and the formation of SOSG-EP upon reaction with singlet oxygen to produce fluorescence. Taken from (305)**.**

For the singlet oxygen generation experiments, a sample of degassed PBS containing either MagO$_2$MB (5x10^7 MB/mL), MagO$_2$MB-RB (5x10^7 MB/mL, 541 µM) or **8** (541 µM) and SOSG (1.25 µM) was exposed to US (1.17 MHz, PNP =

0.70 MPa, duty cycle = 30%, PRP = 100 Hz, 3.5 min). The fluorescence intensity of SOSG at 520 nm was measured for each sample with and without US exposure. In addition to measuring $^1O_2$ generation, the characterisation of MB acoustic emissions during US exposure were recorded using a passive cavitation detector (PCD) focused on the top of the sample chamber. The results are shown in Figure 5.7 and reveals that the generation of cytotoxic $^1O_2$ was significantly enhanced when $MagO_2MB$-RB were exposed to US, compared to $MagO_2MBs$ or **8** alone (p < 0.01), thereby indicating a more effective activation of the sensitiser. This is likely as a result of O_2MB providing the oxygen substrate needed to facilitate the generation of $^1O_2$ by RB in the otherwise degassed medium. Further, the presence of exogenous MBs has been shown to facilitate sonoluminescence thereby activating the sensitiser. (174) **8**. A similar result was observed in the ultraharmonic energy of MB emissions recorded from the PCD, but the emissions from the two types of MB and **8** alone were all significantly different (p < 0.01). The reason for the increased cavitation activity of $MagO_2MB$-RB compared to $MagO_2MBs$ is not fully understood but could be explained by an enhanced stabilisation of $MagO_2MB$-RB due to the surface functionalisation of **8** that prevents bubble dissolution in the degassed medium akin to that of Pickering stabilisation. (306)
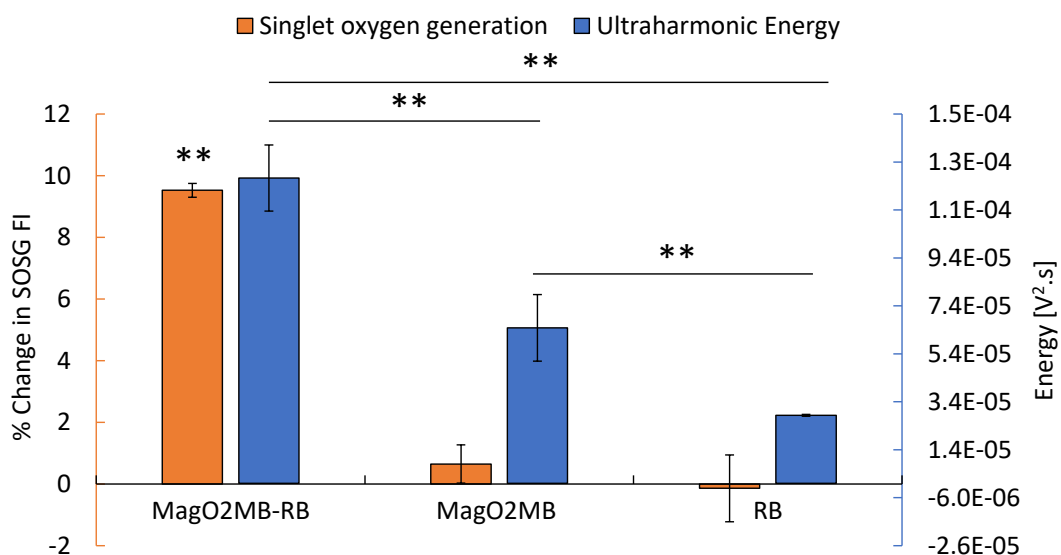
Figure 5.7. Singlet oxygen production (orange, n=3) from activation of 8 after US exposure, with associated ultraharmonic emissions from MBs (blue) undergoing nonlinear oscillations. ** = p < 0.01 determined through a 1-way ANOVA with Tukey's post hoc test. A sample was prepared with ± 5x10^7 MB/mL, ± 541 μM biotin-RB, and 1.25 μM SOSG in degassed PBS. US parameters were 1.17 MHz, 0.7 MPa PNP, 30% duty cycle, 100 Hz PRF for 3.5 minutes.

5.2.6 Drug delivery comparison in agar between devices

The performance of the MAD compared to the use of separate magnetic / US devices and the contributions of US and of the magnetic fields individually were assessed in an agar phantom model. Ultrasonic phantoms are often used to mimic the US properties of biological tissues such as US propagation, velocity, density, attenuation and acoustic impedance allowing the study of its interactions with US. In soft tissue like that of the pancreas, the values corresponding to these properties are very similar to that of agarose and so this was the ideal material for the tissue mimicking phantom. The phantom body was made up of 1.25% agarose with a straight, 1.2 mm diameter channel running through it. Into this channel was injected either MagMB-RB ([MB] = (1.74±0.62) x 10^8 MB/mL or free **8** ([**8**] = 506±53 μM) at a flow rate of 0.2 mL/min. The top of the agar phantom was then treated according to Table 1 using both the MAD device and a separate device with only magnetic functionality (aMAD) (US: 1.17 MHz, 30% duty cycle, peak negative pressure 0.7 MPa, 3.5 minutes, magnet strength: 0.2 T at 10 mm). The combination of MAD and aMAD was used to

mimic previous studies where US and magnetic fields were applied separately. (247)
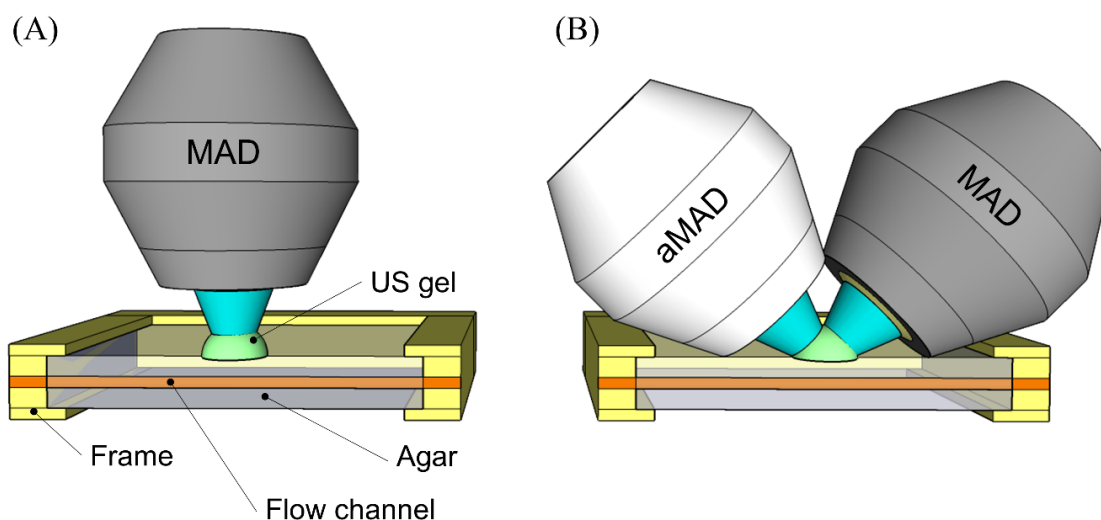
Figure 5.8. *In vitro* **flow phantom set-up for (A) the MAD with co-aligned fields compared to (B) the separate but simultaneous application of magnetic (MAD with US element turned off) and US (aMAD) fields. Phantom is shown cutaway to visualize the 1.2 mm diameter channel through which MMBs were flown. The underlying water bath is not shown.**

Table 5.1. Treatment groups for drug delivery comparison in agar between devices.

Group Name	Water	MagMB-RB*	US**	Magnet***
Untreated	X			
MB		X		
US		X	X (aMAD)	
Mag		X		X (MAD)
US + Mag		X	X (aMAD)	X (MAD)
MAD		X	X (MAD)	X (MAD)

MagMB-RB: MB = (1.7±0.6) x10^8 MB/mL and [8] = 500±50 μM

*** US: 1.17 MHz, 30% duty cycle, peak negative pressure 0.7 MPa, 3.5 minutes*

**** Magnet: 0.2 T at 10 mm*

Following treatment, the channel was rinsed with deionised water and the agar channel was immediately cut out. The concentration of **8** delivered was then determined based on the absorbance of a set volume of agar gel surrounding a channel after flowing 100 µL of MagMB-RB through it while exposed to one of the device configurations. Figure 5.9 shows the concentration of **8** delivered for the various groups tested, and when US was used, the associated cavitation activity is provided. A significantly higher quantity of **8** was delivered ($p < 0.01$) using the MAD compared to all other groups; more specifically a 1.6 and 1.4-fold increase in **8** was measured compared to the US only and US + Mag groups respectively. Moreover, a comparison between the MAD and US only groups indicate a significant increase in delivery ($p < 0.01$) from the addition of magnetic targeting, but the minimal enhancement observed for the US + Mag group compared to US highlights the difficulty in optimally aligning devices when two separate units are used. The delivery recorded for MagO$_2$MB-RB alone (i.e no magnet or US) could be associated with residual **8** (i.e. non-MB bound) in the suspension diffusing across pores in the agar gel (307) and was found to be significant compared to the untreated group ($p < 0.01$). Individually, US and Mag fields enhanced delivery to a similar degree, in agreement with previous results from Stride *et al* (235) where combined US and magnetic fields enhanced the transfection of DNA into Chinese hamster ovary cells.
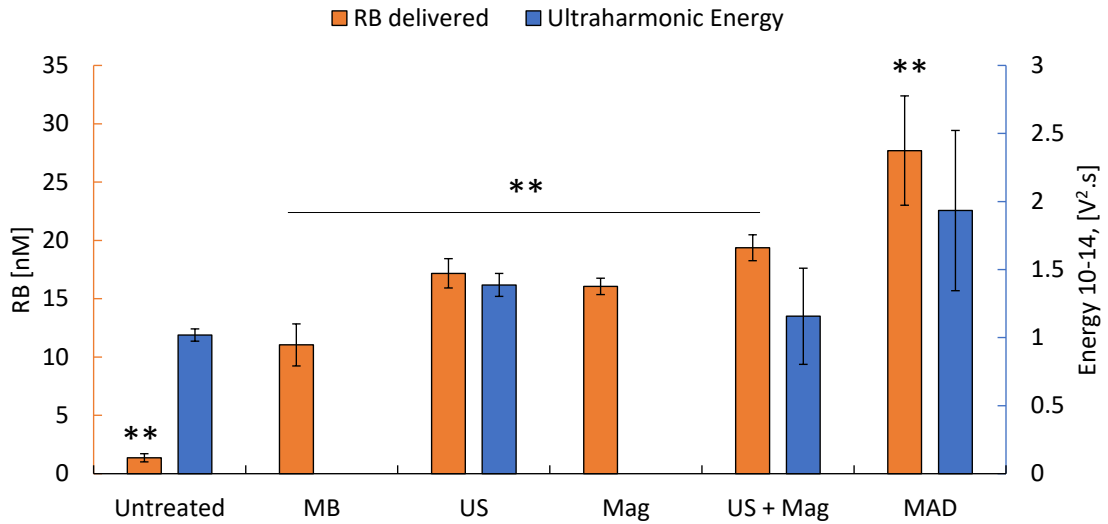
Figure 5.9. Delivery of 8 (orange, n=3) in a volume of 0.7 mL agar (1.25% w/w) with different US and magnetic device configurations as listed in Table 5.1. ** = $p < 0.01$ determined through a 1-way ANOVA with Tukey's post hoc test. The corresponding ultraharmonic emissions of MBs (blue) are shown. For the treatment-receiving groups, 100 μL of MagMB-RB ([MB] = $(1.74\pm0.62) \times 10^8$ MB/mL, [8] = 506±53 μM) were administered and flown at 0.2 mL/min. When a magnet was used, a 0.2 T magnetic field from the MAD was applied at the US focus. When US was applied (MAD or aMAD), the parameters were: 1.17 MHz, 0.7 MPa PNP, 30% duty cycle (DC), 100 Hz PRF for 3.5 minutes. The ultraharmonic emissions plotted for the untreated group reflect the background noise recorded with water flowing in the agar channel.

5.2.7. In vivo efficacy in BxPC-3 xenografts

To fully assess the utility of the MAD as a platform for the delivery of combined magnetic and US fields in vivo, 25 SCID mice were implanted with ectopic human pancreatic BxPC-3 tumours and randomly distributed into 4 groups for treatment as described in Table 5.2.

Table 5.2. In vivo drug delivery experiment groups.

Group Name	No treatment	MagO$_2$MB-RB-Gem*	US**	Magnet***
Untreated	X			
MB		X		
US + Mag		X	X (aMAD)	X (MAD)
MAD		X	X (MAD)	X (MAD)

** MagO$_2$MB-RB-Gem: [MB] = (1.3±0.4) x 10^9 MB/mL, [**12**] = 520±80 μM*

** US: 1.17 MHz, 30% duty cycle, peak negative pressure 0.7 MPa, 3.5 minutes

*** Magnet: 0.2 T at 10 mm

The results in Figure 5.10 reveal a 37% reduction in tumour volume relative to the pre-treatment volume 4 days after the initial treatment for animals treated with MagO$_2$MB-RB-Gem and the MAD, compared to a 9% reduction when combined magnetic and US fields were simultaneously delivered using separate probes (US + Mag). This difference was maintained for four days, and 12 days following the initial treatment, tumours treated with MagO$_2$MB-RB-Gem and the MAD were still 9% smaller than their pre-treatment volume and 54% smaller than tumours treated with MagO$_2$MB-RB-Gem and separate probes. Compared to the untreated group, the MAD enabled a more significant reduction in tumour volume sustained to day 12 with a p-value of 0.0028, while the US + Mag group produced a p-value of 0.0346. In addition, while tumours treated with MagO$_2$MB-RB-Gem in the absence of magnetic or US fields (MB) were smaller than untreated animals, the difference was not significant. It is important to note that BxPC-3 tumours treated with a clinically relevant dose of Gem (120 mg/kg) showed no significance at controlling the tumour volume compared to the untreated control. The combined treatment was not only effective at reducing

tumour burden but was also well tolerated, as the animals remained healthy and exhibited no weight loss over the duration of the study (Figure 5.11). Furthermore, the clinical standard Gem group lost an average of 7.29% on Day 8, indicating toxicological stress.

The observed differences between treatments performed with the MAD, and physically separate but simultaneous magnetic and ultrasonic field generating devices, illustrate the importance of field alignment. When co-aligned as in the MAD, the tendency of bubbles to be pushed away from the US focus by radiation force is counteracted by the pulling force of the magnet. This effect, which helps maintain a population of bubbles in the US beam, is weaker and potentially becomes detrimental to MB availability in the US focus when the ultrasonic and magnetic fields are separated by a large angle, as with the separate device tests.
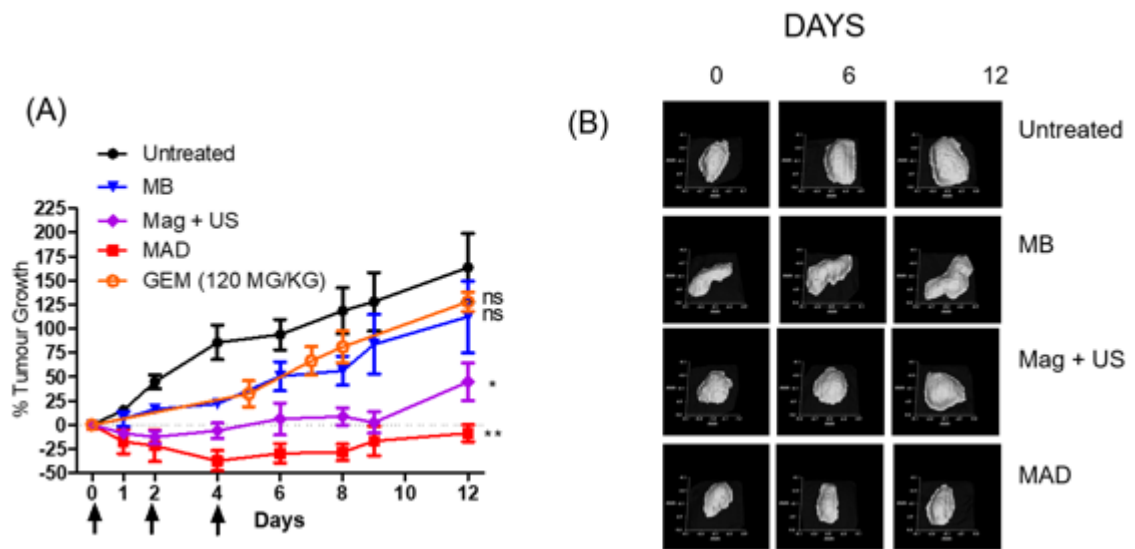
Figure 5.10. In vivo results with (A) % tumour growth over time relative to day 0. Arrows indicate treatment days. * p<0.05, ** p<0.01 compared to the untreated group determined with a 1-way ANOVA followed by Sidak's post hoc test on the tumour volume data (n = 5 for untreated and n = 4 for MAD, MB, and US + Mag) from day 12. (B) Images of xenograft ectopic BxPC-3 tumours on day 0, 6, and 12 from the start of treatment.
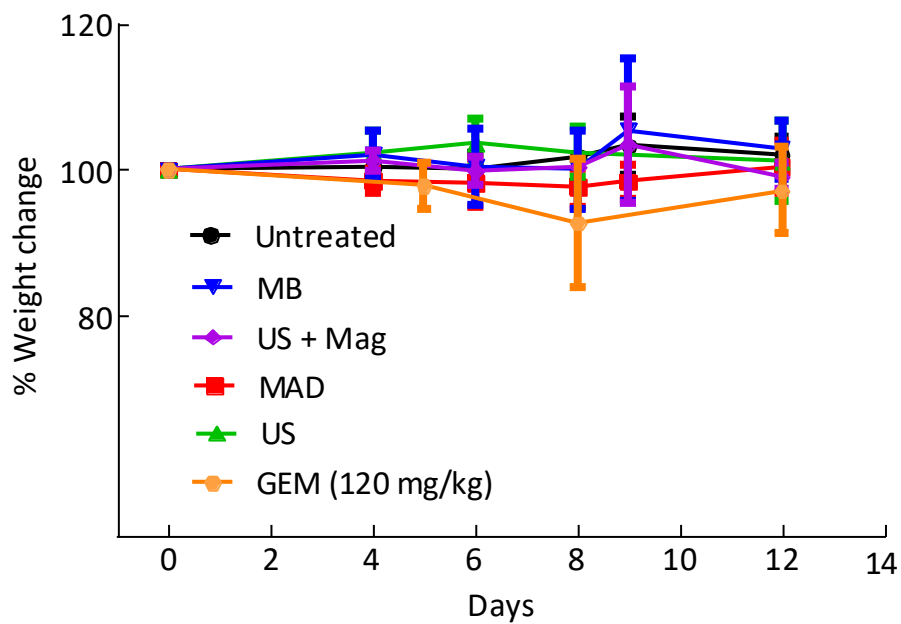
Figure 5.11. Group-average body weight of mice bearing xenograft ectopic BxPC-3 tumours (n=5).

Taken together, these results demonstrate an improved therapeutic effect obtained from the co-aligned application of magnetic and acoustic fields using a single device compared to the use of two separate devices. Additionally, the chemo-sonodynamic therapy delivered using the MAD provided a rapid, substantial and stable reduction in tumour volume, suggesting that this approach may be ideal as a neo-adjuvant treatment to downstage pancreatic tumours in advance of surgery.

5.3 Conclusions

Use of the MAD device in combination with $MagO_2MB$-RB-Gem demonstrated enhanced efficacy in a pre-clinical animal model of pancreatic cancer when compared to activation using separate devices delivering US and magnetic fields. The use of ligand **12** also enabled both Gem and RB to be delivered as a single MB formulation.

The ability of sensitizer loaded $MagO_2MB$, to produce $^1O_2$ was clearly demonstrated using the SOSG assay indicating the presence of the IONPs do not hinder ROS generation. In addition, the use of MAD significantly increased the delivery of attached payloads by 1.6- fold in an agar flow phantom ($p < 0.01$) compared to the use of two separate devices, and an increase in the energy of MB ultraharmonic emissions was also observed. These results indicate that the MAD enabled a more precise application of both targeting and activation fields to promote drug delivery. The advantages of the combined MAD were further demonstrated in vivo and showed a significant decrease in tumour size after 12 days of treatment ($p < 0.05$) compared to the use of two separate devices. In addition, a substantial decrease in tumour size of 37% after 4 days of treatment was observed for animals treated using the MAD when compared to pre-treatment values. Furthermore, previous studies performed with the MAD have demonstrated that this technology can be adapted for the larger length scales relevant for human applications. (245)

The work presented in this chapter demonstrates a clear progression from work undertaken in chapters 3 and 4 with the addition of an extra layer of targeting, enabling the delivery of significant quantities of cytotoxic agents to the tumour and clearly highlights the potential of this approach as an ideal neo-adjuvant therapy to downstage tumours prior to surgery.

Chapter 6

Microbubble Mediated Delivery of a Novel Gemcitabine Phospholipid-Prodrug and Paclitaxel

Chapter 6 – Microbubble mediated delivery of a Novel Gemcitabine Phospholipid-Prodrug and Paclitaxel.

6.0. Introduction

In chapters 3-5, the active drugs Dox, RB and Gem were modified with biotin to enable attachment to pre-formed MBs using the biotin-avidin interaction. Despite the utility of this conjugation technique for preliminary preclinical evaluations it has two main shortcomings. First, several synthetic steps are required following MB preparation to first add avidin and then the biotinylated payload. This not only increases the overall complexity and cost of the synthetic process, but also reduces the yield of loaded MB, as a washing step is required following each conjugation procedure. Second, as the loading capability of a particular ligand is dependent upon its physiochemical characteristics such as aqueous solubility, this strategy also provides a limited degree of control over loading levels of the therapeutic agent onto the MBs. Therefore, an alternative method for the preparation of drug loaded MBs for use in targeted anti-cancer therapy would be highly beneficial. More specifically, there is a need for methods which minimise the need to manipulate the MBs once formed and/or which permit greater control over the loading levels of the therapeutic agent.

There are a number of techniques described in the literature to facilitate drug loading onto the surface of MBs (Figure 6.1). One method is the use of a covalent bonding between the therapeutic agent and the MB. This can be achieved in a number of ways including the use of carbodiimide chemistry, maleimide-thiol chemistry and click-chemistry. Carbodiimide chemistry involves the use of a carboxyl functionalised lipid within the MB. (209,237,308,309) The carboxyl functionality is then often activated using the water soluble 1-ethyl-3-(3′-dimethylaminopropyl)carbodiimide (EDC) in the presence of N-Hydroxysulfosuccinimide (sulfo-NHS) to produce the N-hydroxysulfosuccinimide ester which is highly reactive to primary amines. However, the efficiency of this method is often limited by multiple competing side reactions. Firstly, the unstable O-acylisourea is capable of undergoing isomerisation to the stable N-acylisourea, essentially preventing further binding. In an effort to prevent this, the N-hydroxysulfosuccinimide ester is formed using

sulfo-NHS. (310) This reactive intermediate can also be rapidly hydrolysed in basic conditions (i.e. PBS) back to the relatively unreactive carboxyl functionality. These side reactions therefore severely limit the practicality and loading capability of the MBs. Alternatively, ligands bearing a thiol functionality can be covalently bound to MB using thiol-maleimide chemistry. (311–315) This method has the advantage of improved aqueous stability and high coupling yields. However, residual maleimide groups, are capable of reacting with cysteine residues found on serum proteins, leading to a loss of targeting, premature clearance, and hypersensitivity reactions. (316)

More recently there has been a growing interest in the use of click-chemistry such as strain-promoted [3+2] azide-alkyne cycloaddition (SPAAC) to enable covalent binding to the surface of the MB. (316–318) However, this technique, much like the beforementioned strategies, is undertaken following MB preparation. This complicates the synthetic process and limits the potential for rapid clinical translation.
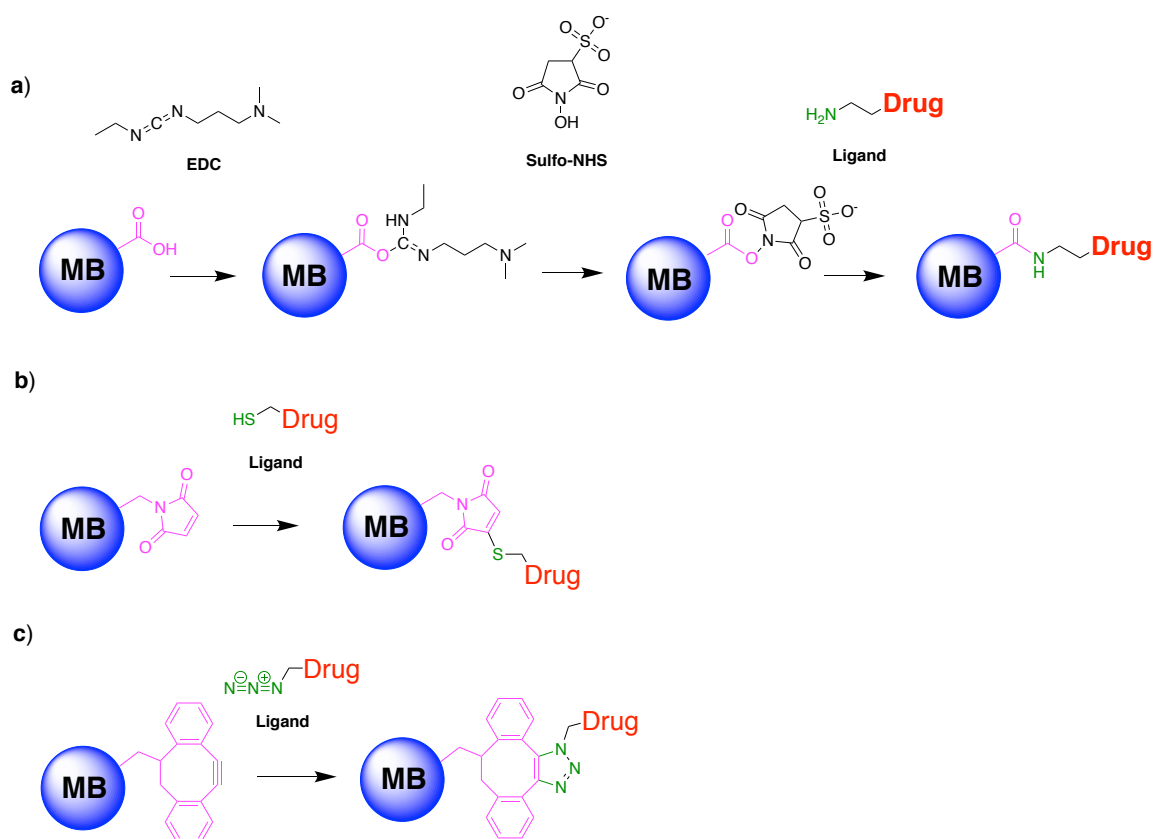
Figure 6.1. Schematic illustrating techniques used to covalently conjugate ligands to the surface of MBs. a) Reaction of EDC with carboxylic acid functionalised MB to produce unstable O-acylisourea intermediate followed by reaction with sulfo-NHS to produce highly reactive sulfo-NHS derivative which subsequently reacts with a ligand bearing a primary amine functional group b) Reaction of a thiol functionalised ligand with a MB bearing a maleimide group (e.g. DSPE-PEG-2000-maleimide) to produce thioester linkage c) Reaction of azide functionalised ligand with MB bearing a dibenzocyclooctyne (DBCO) functionality (e.g. DOPE-N-DBCO).

In this chapter, the shortcomings described above have been addressed through the preparation of MBs using pre-functionalised precursor phospholipids. More specifically, a novel phospholipid conjugate of Gem (LipidGem) was synthesised using an enzyme catalysed transphosphatidylation reaction. This conjugate was then formulated into MBs with / without the anticancer drug PTX, which was incorporated into the acyl chain layer of the MB.

6.1. Hypothesis and specific aims

The overarching hypothesis of this study was that a phospholipid bearing a choline polar head group could be modified to include the anticancer drug Gem in a single step enzymatic reaction and that this novel phospholipid-conjugate could be formulated into an US-responsive MB formulation. A secondary aim was to further load this preparation with PTX in the hydrophobic layer of the MB shell and test the effectiveness of this formulation in 3D spheroid and murine models of pancreatic cancer. The specific aims were to:

1. synthesise, purify and fully characterise a novel phospholipid conjugate of Gem (Lipid-Gem) using a single step enzymatic transphosphatidylation reaction.

2. generate MBs prepared from Lipid-Gem with / without PTX hydrophobically incorporated into the lipid shell and fully characterise the resulting formulations.

3. assess the stability of the MB formulations at 37°C compared to unmodified MBs.

4. determine the efficacy of the MB formulations in Panc-1 spheroids.

5. determine the efficacy of the MB formulations in a BxPC-3 ectopic xenograft model of pancreatic cancer.

6.2. Results and Discussion

6.2.1. Enzyme catalysed Synthesis and Characterisation of LipidGem

Chemical manipulation of Gem is often troublesome due to the multiple potential reactive sites identified in Figure 6.2. This is particularly problematic when an amide/ester coupling strategy is proposed given the different sites capable of this reaction. The presence of hydroxyl moieties at the 3' and 5' positions make it difficult to construct ester bonds with these groups in a regiospecific manner. The presence of the primary amine moiety also provides the possibility of amide formation with carboxylic acids or reactive derivatives. This means that any attempt to couple Gem with another compound using this strategy will inevitably lead to a mixture of compounds which need to be separated through laborious chromatography. This lack of selectivity often results in a very low yield of the desired compound and is therefore unsuitable for scale up and clinical translation.
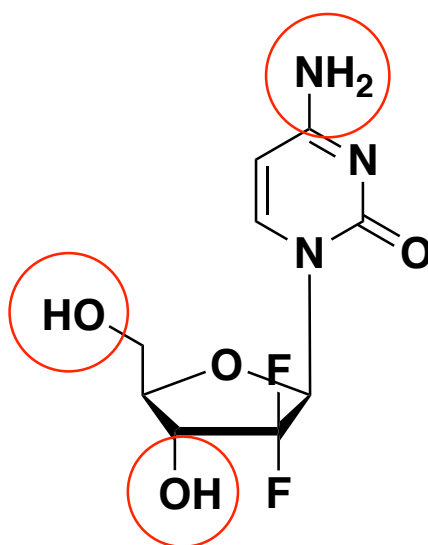
Figure 6.2. Chemical structure of Gem with the 3' hydroxyl, 5' hydroxyl and cytosine amine highlighted in red.

Shuto et al developed a simple, one-step enzymatic reaction, to selectively synthesise 5'-phosphatidyl nucleosides. (319–322) This reaction was achieved through the use of the enzyme, phospholipase D from Streptomyces *sp* in a reaction known as a transphosphatidylation. This reaction is carried out in a biphasic reaction mixture composed of an aqueous buffer layer containing the

acceptor alcohol (Gem) and the enzyme, and an organic layer containing the donor phospholipid - a phosphatidylcholine. Under these conditions, phospholipase D is selective for primary alcohols and therefore is capable of catalysing the coupling of the 5′ hydroxyl group of Gem with the phosphatidyl group of any phosphatidylcholine in a single step without the need of protecting group chemistry.

The exact mechanism for this reaction is not fully understood. However, it has been theorised that the reaction proceeds as shown in Figure 6.3. The first step is thought to involve the formation of a phospholipid-enzyme intermediate through a nucleophilic attack on the phosphorus atom of the lipid by a histidine (His-1) residue on the enzyme and protonation of the leaving group by a second His residue (His-2). The next step involves the deprotonation of a water molecule by His-2 and another nucleophilic attack on the phosphorus atom by the resultant hydroxide. From this hypothetical mechanism, it can be assumed that the acceptor alcohol (i.e. Gem) will compete with surrounding water molecules in the reaction mixture, for the phosphatidyl group. (323) For this reason, it is important that the concentration of the acceptor alcohol in the reaction mixture remains as high as possible to reduce enzymatic hydrolysis of the phosphatidylcholine to the undesirable phosphatidic acid side product.
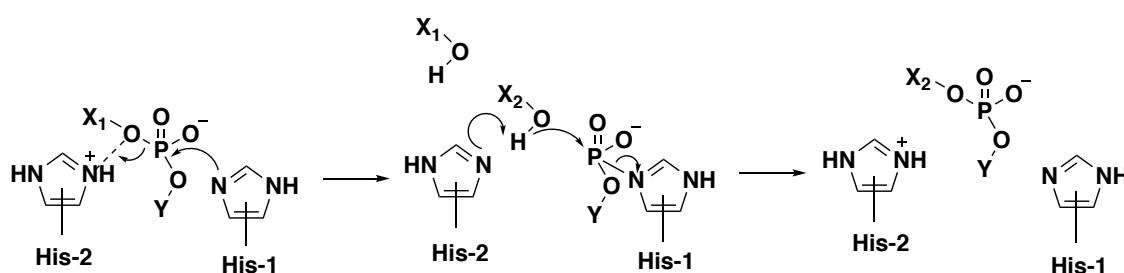
Figure 6.3. Hypothesised mechanism for the transphosphatidylation reaction. X_1 = choline, X_2 = Gem and Y = diacyl glycerol moiety. Reproduced from (323).

In an effort to be consistent with work presented in previous chapters (Chapter 3-5), DBPC was chosen as the phosphatidylcholine donor compound. The scheme for the reaction of Gem with DBPC is shown in Figure 6.4. Gem is first dissolved in a buffer of sodium acetate and acetic acid at pH 4.5 and Phospholipase D added as a lyophilised powder. This aqueous phase is then added to a solution of DBPC in chloroform at 45°C and this mixture is stirred vigorously to emulsify the biphasic mixture. Vigorous stirring was essential as the reaction takes place at the interface between the organic and aqueous phases.
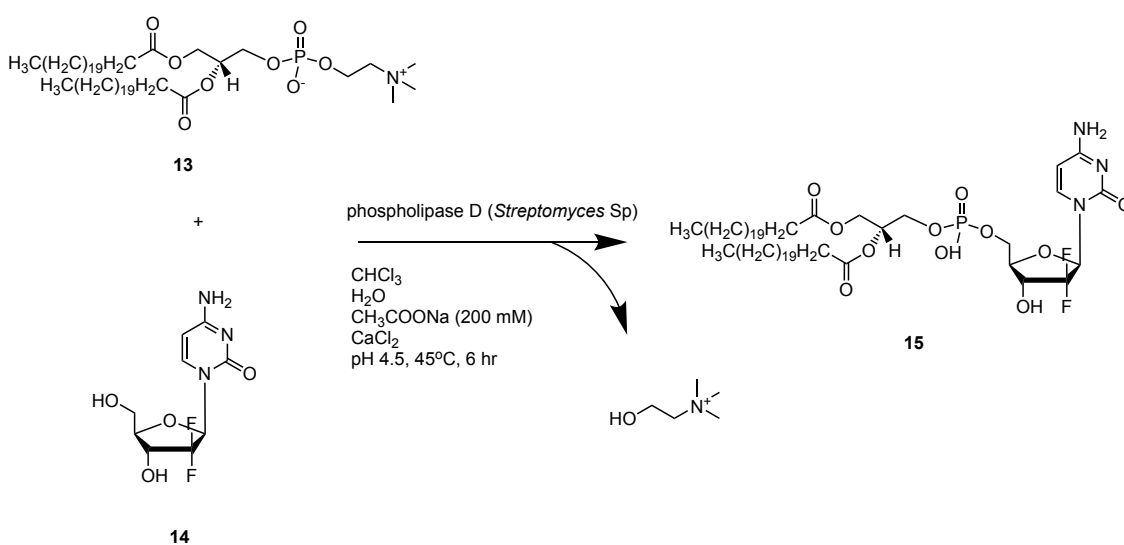
Figure 6.4. Synthetic scheme for the synthesis of LipidGem.

Following completion of the reaction, the organic layer was removed and concentrated to dryness. The crude solid was then washed with water to remove excess Gem and purified using PTLC as described in Section 2.5. The success of the separation and estimation of purity was determined using analytical TLC. As Gem contains a chromophore within the cytosine moiety, the purified conjugate could be easily visualised under UV irradiation. As an added control, TLC plates were sprayed with Dittmer-Lester reagent which selectively stains phosphate groups blue. As the starting material or side product (DBPC or DBPA) are not UV active, the presence of a dark spot under UV along with a blue spot once stained with Dittmer-Lester reagent, strongly indicates the presence of the target compound (Figure 6.5).
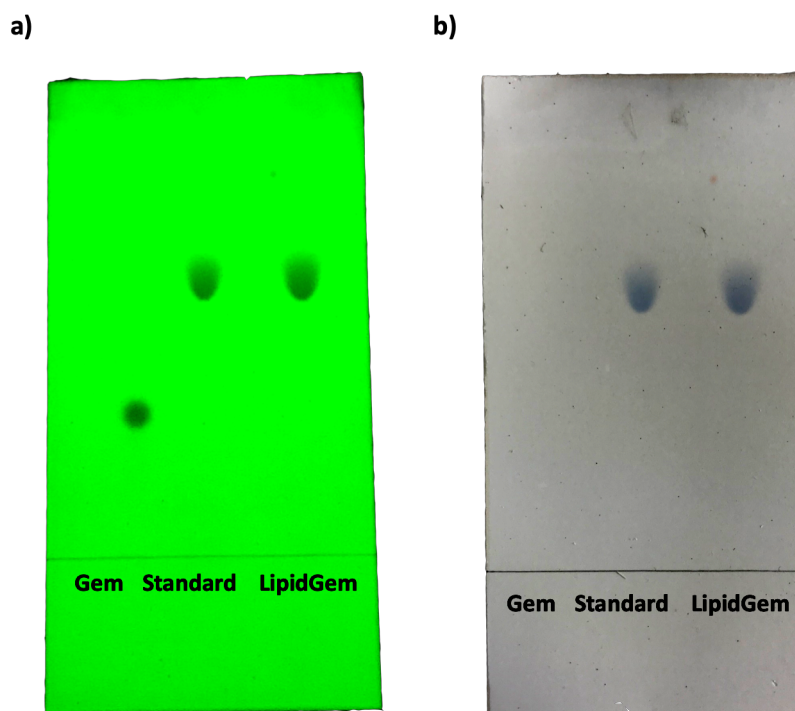
Figure 6.5. Images of a TLC plate after a) irradiation under UV light and b) stained with Dittmer-Lester reagent (left spot – Gem free base standard, middle spot – 15 standard prepared previously, right spot – purified 15).

The purified **15** was characterised by MALDI-TOF-MS, ^{1}H NMR and ^{13}C NMR. The MALDI-TOF-MS spectrum is shown in Figure 6.6 and reveals three main peaks at 1084.7758 (base peak), 1062.7800 and 1106.7753 corresponding to the $[M+Na]^+$, $[M+H]^+$ and $[M+2Na-H]^+$ ions respectively. The assigned ^{1}H NMR spectrum is shown in Figure 6.7 and reveals the characteristic resonances associated with the terminal methyl groups of the lipid chains appearing at 0.8 ppm, the main block of lipid methylene protons between 1.0 and 1.4 ppm and the lipid methylene protons in the alpha and beta positions to the carbonyl group appearing at 2.3 and 1.5 ppm respectively. A cluster of resonances associated with diastereotopic glycerol/Gem methylene protons in addition to methine protons from the Gem furanose ring appeared between 3.9 and 4.5 ppm. The methine proton attached the chiral glycerol moiety appeared downfield at 5.2 ppm while the methine proton of the furanose ring on the carbon directly bonded to the cytosine ring nitrogen atom of Gem appeared at 6.2 ppm. Finally, the cytosine ring methine protons attached appeared separately as two distinct resonances at 6.0 and 7.8 ppm.

To further illustrate the differences between **15** and the starting materials, a stacked spectra of 1,2-dibehenoyl-sn-glycero-3-phosphocholine standard (top), Gem standard (middle) and **15** (bottom) is presented in Figure 6.8 and clearly shows that the resonances corresponding to the choline methyl groups (3.15 ppm) and methylene protons (3.6 and 4.0 ppm) protons present in the spectrum of DBPC are absent in the spectrum of **15**, confirming this unit has been cleaved during the reaction as described in Figure 6.4. In addition, the resonance corresponding to the Gem furanose methylene protons appearing at 3.75 ppm in Gem shifted downfield to 4.15 ppm in **15**, reflecting their new environment adjacent to phosphoester bond. In addition, other resonances associated with Gem, such as the two cytosine ring methine protons at 5.9 and 7.8 ppm respectively which were not present in the spectrum of DBPC, are clearly visible in the spectrum corresponding to **15**. The structure of **15** was further confirmed using ^{13}C NMR (Figure 6.9) with the carbons of the lipid chains appearing between 10 and 35 ppm. The methylene carbons of the glycerol moiety, as well as the Gem furanose methine carbon and adjacent methylene carbon, appeared as a small cluster of resonances between 50 and 70 ppm. The Gem cytosine ring carbons appeared at 85 and 141 ppm while the neighbouring carbonyl carbon appeared at 156 ppm. The two carbonyl carbons from the acyl chain groups of the phospholipid appeared furthest downfield at 174 ppm. When combined these analyses confirmed the formation of **15**.
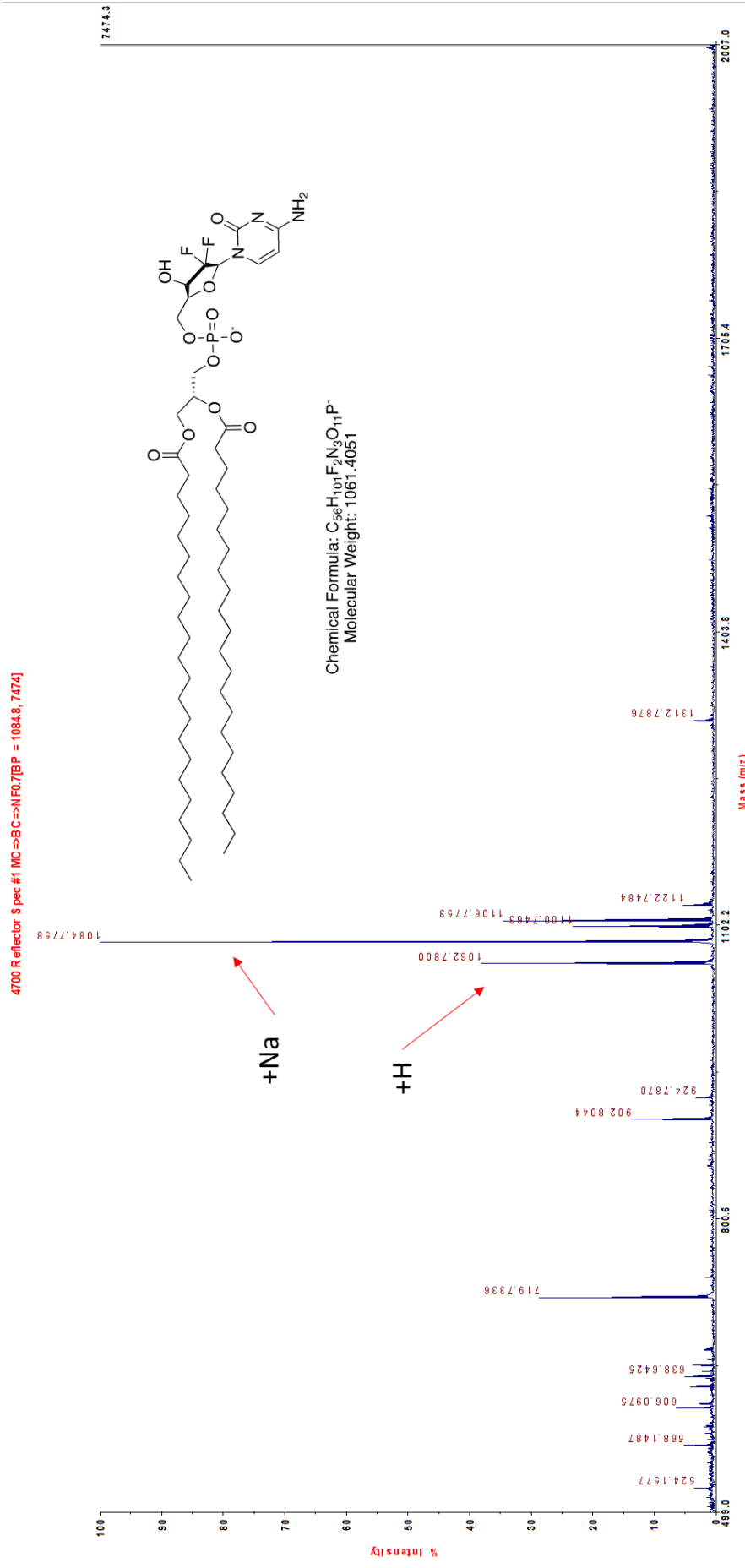
Figure 6.6. MALDI-TOF-MS spectrum of 15 (m/z 500–2000) recorded in CHCl₃:MeOH (2:1).

172
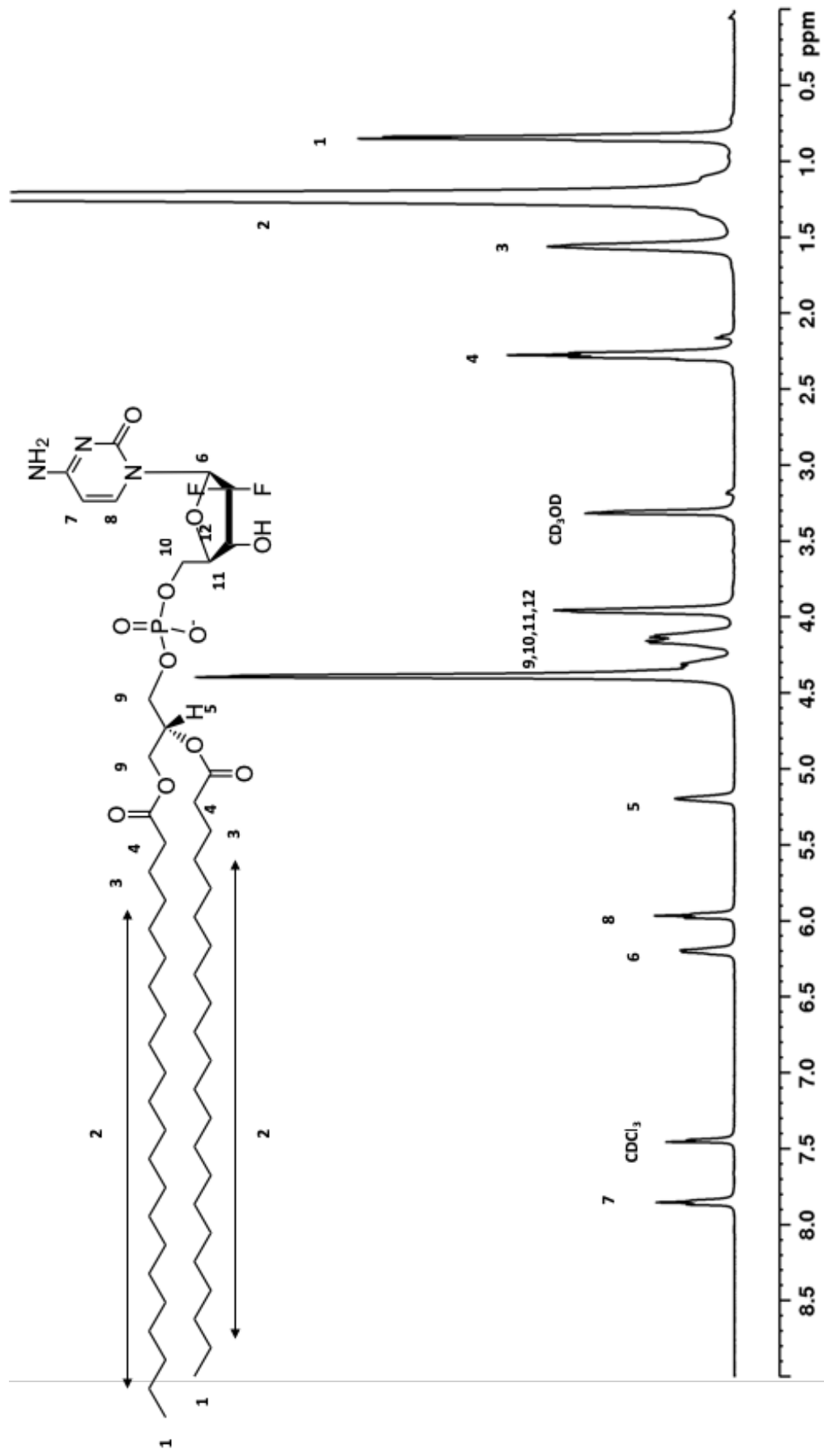
Figure 6.7. ^{1}H NMR spectrum of 15 recorded in CDCl$_3$:CD$_3$OD (2:1).

173
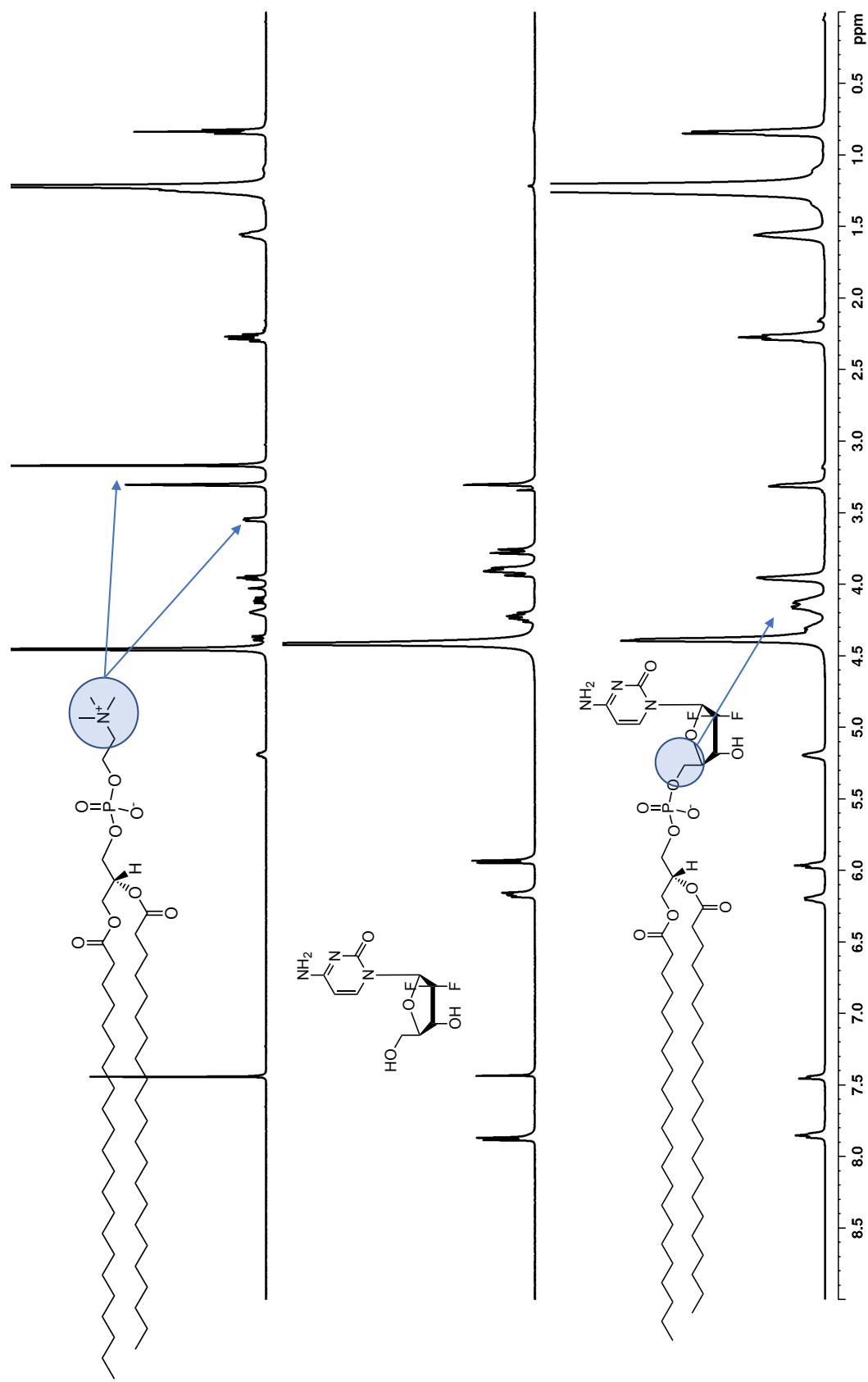
Figure 6.8. Stacked ^{1}H NMR spectra of DBPC standard (top), Gem (middle) and 15 (bottom) recorded in CDCl$_3$:CD$_3$OD (2:1 v/v).

174
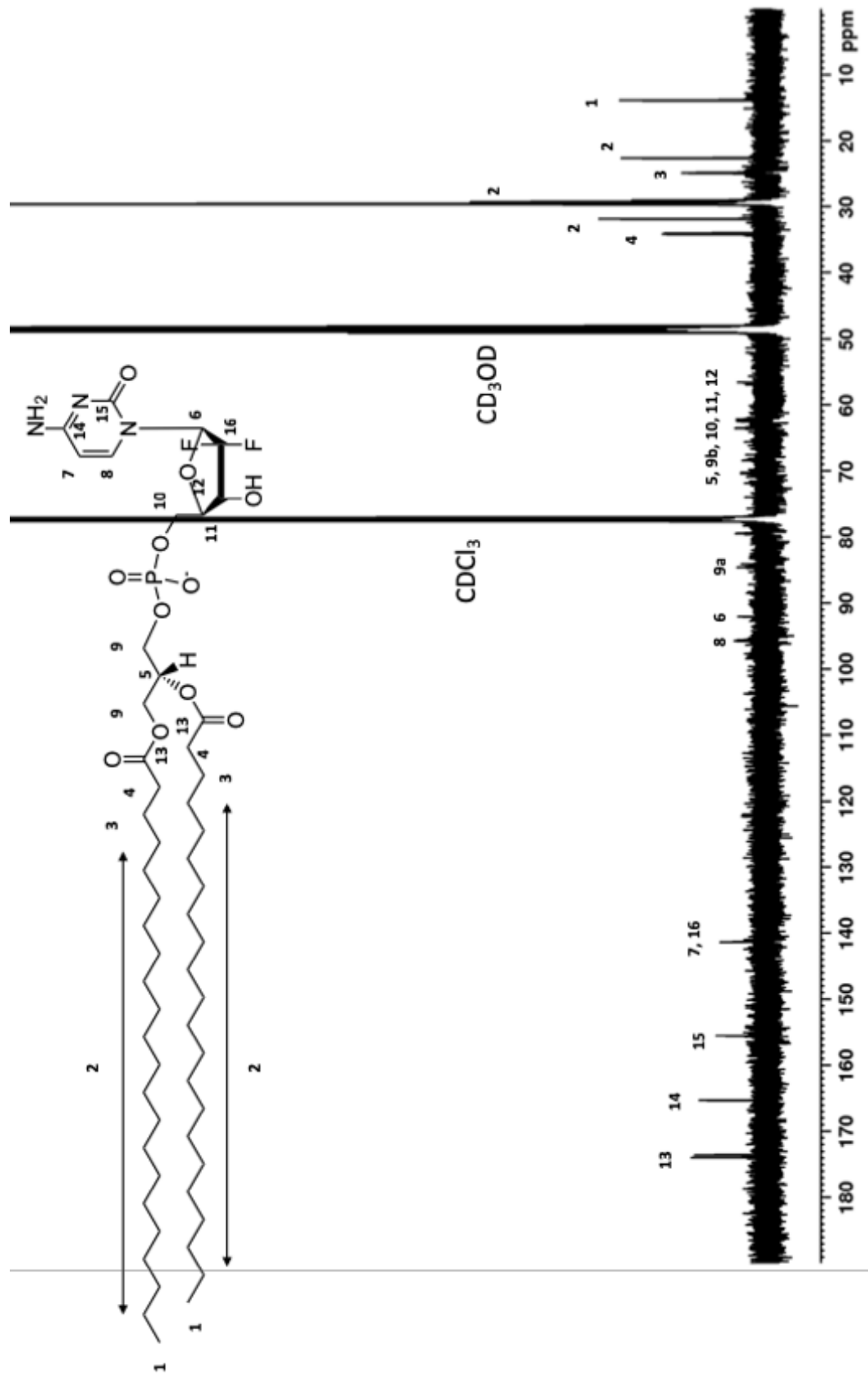
Figure 6.9. ¹³C NMR spectrum of **15** recorded in CDCl₃:CD₃OD (2:1 v/v)

175

6.2.2. Synthesis and characterisation of MB-LipidGem and MB-LipidGem-PTX

Following the successful synthesis of **15**, the next step was to investigate whether the lipid was capable of producing stable MBs. MB-LipidGem were prepared using the same protocol discussed in previous chapter. MBs prepared using only LipidGem were unstable and rapidly dissolved after synthesis. This was likely due to a combination of (i) poorer lipid packing when compared to phosphatidylcholine MBs due to the bulkier Gem head group and (ii) coalescence of MBs through an Ostwald ripening-type process. In an effort to improve stability by reducing MB coalescence, the polymeric phospholipid, DSPE-PEG (2000), was introduced into the formulation. Both **15** and DSPE-PEG (2000) were dissolved in a mixture of chloroform and methanol. The solvents were removed to from a thin film which was hydrated in a solution of glycerol and propylene glycol in PBS. As the phase transition temperature of **15** was not known, the solution was heated to 10°C above the phase transition temperature of the precursor lipid (DBPC). The MB-LipidGem were then formed as described previously by sonication at 22% to form a colloidal suspension followed by sonication at 90% in a PFB headspace to form a milky white suspension of MB.

Following the preparation of MB-LipidGem, the MBs were characterised in terms of mean size, mean concentration and drug loading as described in previous chapters. A representative microscope image of the MB suspension along with the corresponding size distribution is shown in Figure 6.10. The mean diameter of MB-LipidGem was determined to be 1.84 $\pm$ 1.57 μm with a mean concentration of 1.8 x10^9 $\pm$ 1.5 x10^8 MB/mL. These are comparable with MBs prepared using the commercially sourced phospholipids described in previous chapters.
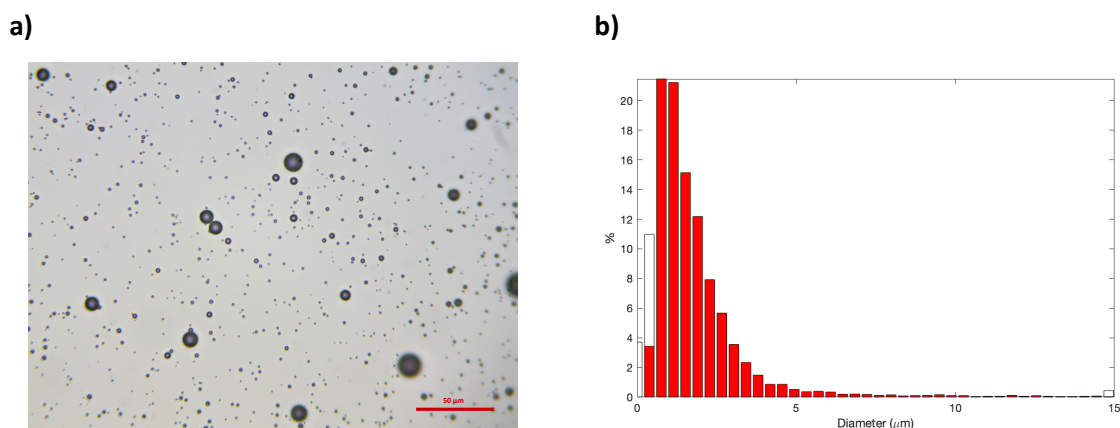
Figure 6.10. a) a representative optical micrograph of MB-LipidGem (x40 magnification) (n=20) b) representative size distribution analysis of images of MB-LipidGem (n=20 images). Scale bar represents 50 μm.

As the cysteine moiety of **15** contains a chromophore, the extent to which **15** was incorporated into the MB was evaluated by UV-Vis spectroscopy. A UV-Vis calibration curve was constructed for **15** using standards of known concentrations (Figure 6.11b). Good linearity was observed over the concentration range tested (0 – 100 μM) with an R^2 value of 0.9974. The mean loading of **15** within the MB shell was 68.49 ± 6.99 μg/ 10^8 MB. This represents a loading of 24.7% of the total amount of lipid used to form the film.
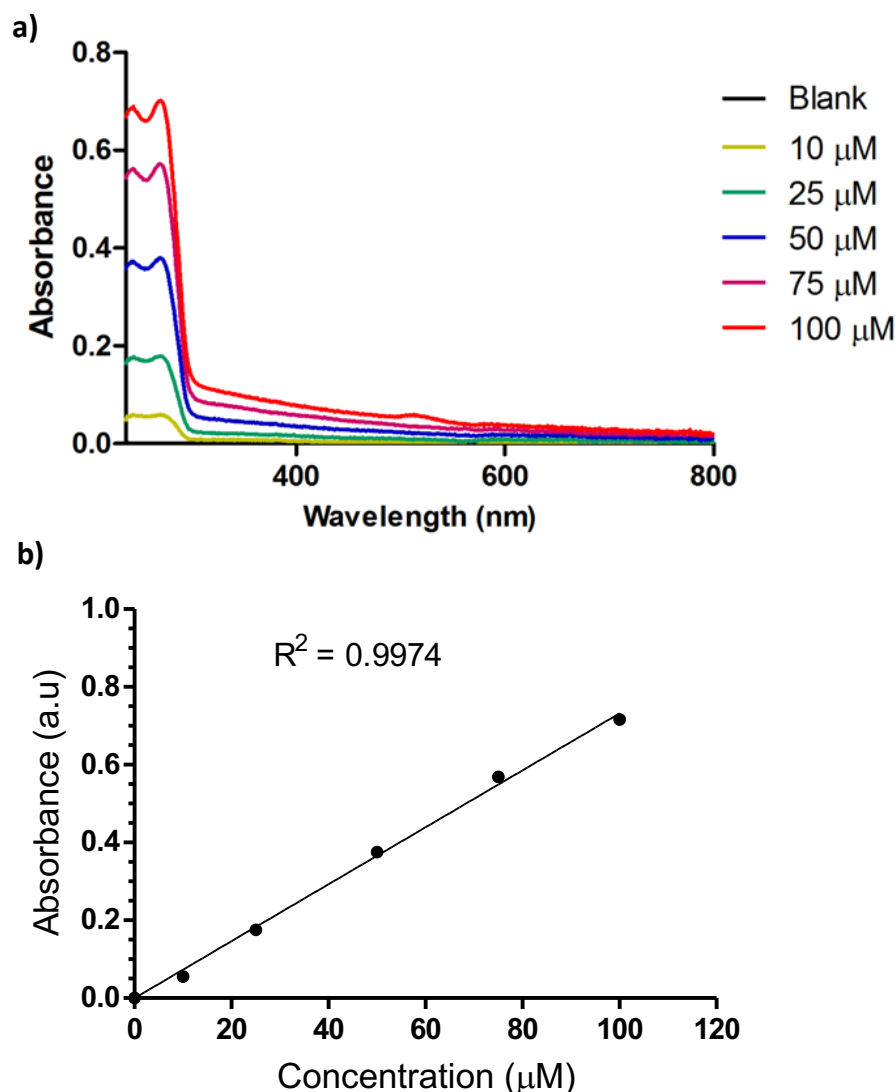
Figure 6.11. a) UV-Vis spectra for 15 at concentrations ranging from 0 – 100 μM and b) Plot of absorbances of 12 against concentration (n=3).

The next step was assessing whether PTX could be hydrophobically incorporated into the acyl chain layer of the MB shell. As the acyl chain length of **15** is the same as that of DBPC which was used in previous chapters, it should also be possible to incorporate PTX within the shell of MB made from **15**. This was achieved using the protocol outlined in Chapter 3. As before, these MB were characterised in terms of mean concentration, mean diameter and mean drug concentration. A representative microscope image of the MB suspension along with the corresponding size distribution is shown in Figure 6.12. The mean diameter of MB-LipidGem was determined to be 1.86 ± 1.62 μm with a mean concentration of $1.7 \times 10^9 \pm 1.1 \times 10^8$ MB/mL. This indicated that the addition of PTX into the shell had little effect on the MB forming ability of **15**. The loading of

15 within these MB was determined to be 79.97 ± 10.36 µg/10^8 MBs which is comparable with MBs containing no PTX. The loading of PTX within these MB was determined using an HPLC method described in Section 2.10. The PTX loading within these MB was determined to be 48.57 ± 5.13 µg/10^8 MB. This represents a loading of 16.6% which is comparable with previous studies (Chapter 3-4).

a)

b)
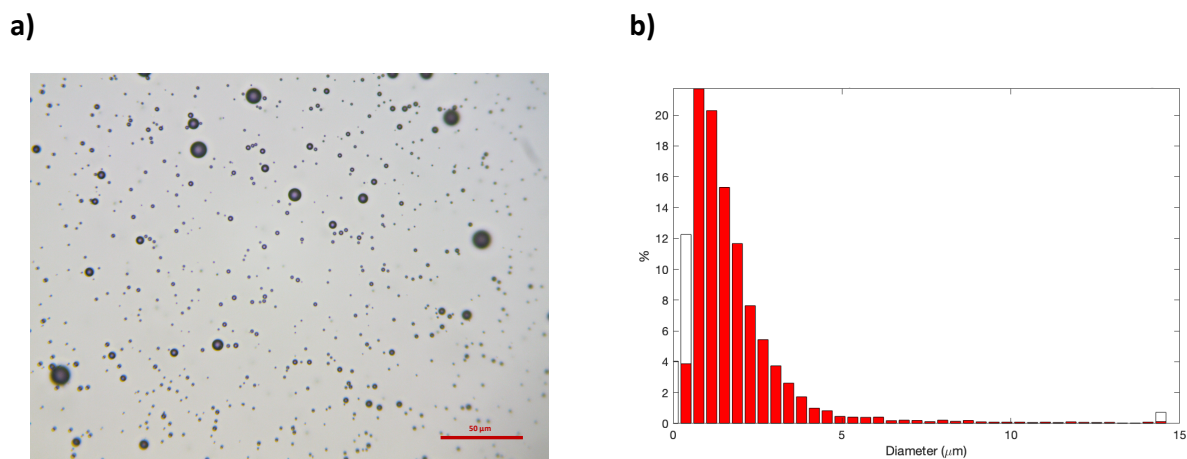
Figure 6.12. a) representative optical micrograph of MB-LipidGem-PTX (1:25 dilution, x40 magnification) b) representative size distribution analysis of images of MB-LipidGem-PTX (n=20 images). Scale bar represents 50 µm.

Following the preparing of MB-LipidGem-PTX, it was important to determine the relative stability when compared to MB-LipidGem containing and unmodified MBs (i.e carrying no payloads). This was achieved by counting the MB number immediately after preparation and then placing the MB suspensions in an incubator at 37°C. The MB number was then measured every 15 minutes for a total of 1 hour. The results are shown in Figure 6.13 and reveal a small yet insignificant decrease in relative MB number for MB-LipidGem and MB-LipidGem-PTX compared to the unmodified MBs. However, there was no significant decrease in MB number observed between either MB-LipidGem or MB-LipidGem-PTX over the time investigated. These results suggest that **15** is capable of producing MBs with stability comparable with that of standard DBPC MBs and that have the capacity to load hydrophobic drugs into the shell at comparable quantities.
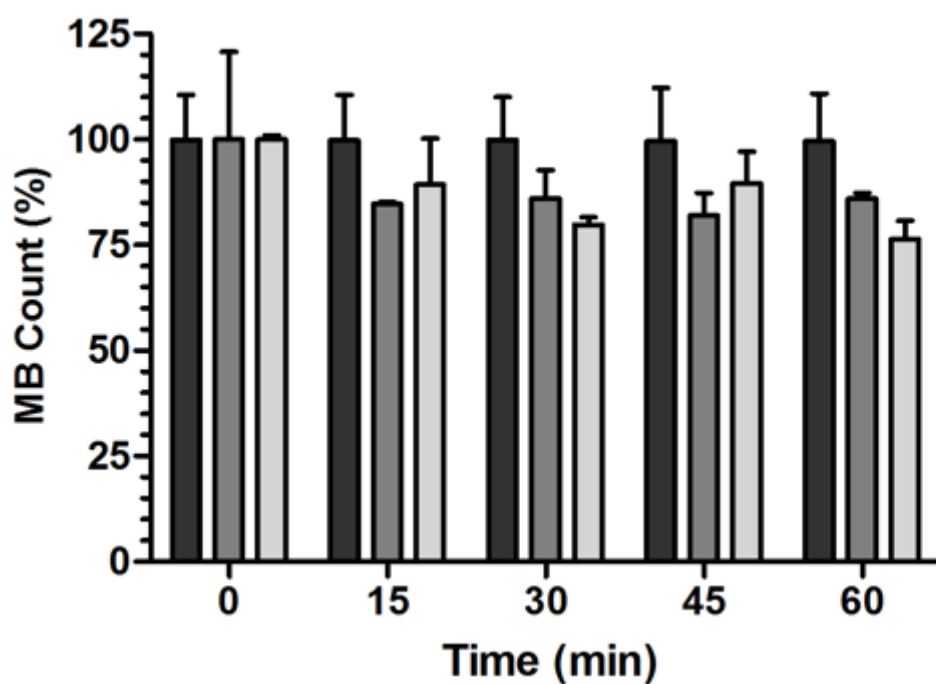
Figure 6.13. Plot showing % MB count of plain DBPC MB (8.81 x10^8 MB/mL) (left), MB-LipidGem ([LipidGem] – 55.55 ± 5.72 μg/10^8 MB, 9.97 x10^8 MB/mL) (middle) or MB-LipidGem-PTX ([LipidGem] – 73.26 ± 3.12 μg/10^8, [PTX] - 45.96 ± 4.95 μg/10^8 MB, 8.6 x10^8 MB/mL) (right) (n=4).

6.2.3. In vitro efficacy of MB-LipidGem and MB-LipidGem-PTX in Panc-1 spheroids.

Following the preparation of MB-LipidGem and MB-LipidGem-PTX, the next step was to determine efficacy in a 3D panc-1 spheroid model. Spheroids were prepared as described in Section 2.18. Once formed, spheroids were treated with either a suspension of MB-LipidGem or MB-LipidGem-PTX in the presence and absence of US. The US conditions and experimental set-up adopted for this study were the same as described in Section 3.2.5 (30 s, frequency - 1 MHz, US power density - 3.0 W/cm², duty cycle - 40%). Following treatment, cell viability was determined using an MTT assay.

Optical images of the treated and untreated spheroids are shown in Figure 6.14 and reveal no visually apparent effects on spheroid morphology for those treated with US in the absence of MBs. Similarly, spheroids treated with MB-Lipid-Gem in the absence of US also appeared visually intact. However, spheroids treated with MB-LipidGem and US appeared less cohesive in structure than those treated with MB-LipidGem alone (i.e. no US). This effect was amplified for spheroids treated with MB-LipidGem-PTX + US where a significant disruption in spheroid morphology was apparent with small areas of cellular debris evident around the perimeter of the spheroid corona. Indeed, changes in morphology were also evident in spheroids treated with MB-LipidGem-PTX alone (i.e. no US) indicating that the addition of PTX to the MB-LipidGem induces significantly more spheroid damage even in the absence of US. When spheroid viability was determined using a MTT assay (Figure 6.15), the proportion of viable cells remaining following treatment with MB-LipidGem + US or MB-LipidGem-PTX + US were significantly reduced relative to untreated spheroids or spheroids treated with US alone or with the respective MB formulation alone (i.e no US). Indeed, while the reduction in viability for spheroids treated with MB-LipidGem + US was 38.13%, this reduced further to 69.70% for MB-LipidGem-PTX + US, consistent with the visual effects apparent from the optical images shown below in Figure 6.14.
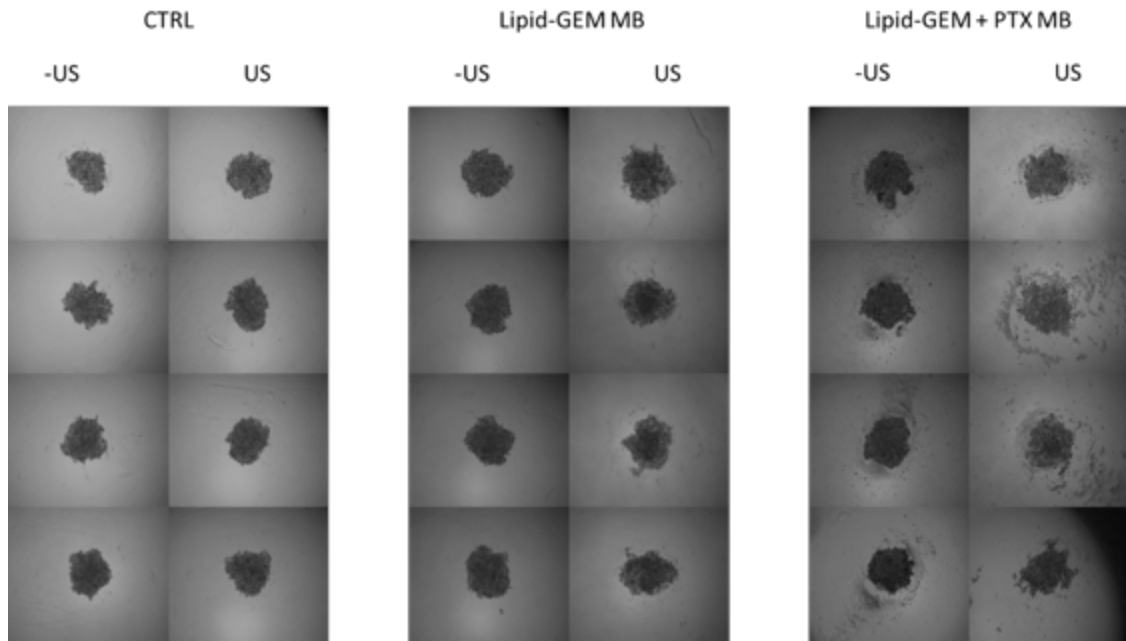
Figure 6.14. Representative images of human pancreas ductal adenocarcinoma cell line (Panc-1) spheroids treated with a) no drug ± US b) MB-LipidGem ([LipidGem] = 10 μM, 3.40 x10^7 MB) ± US c) MB-LipidGem-PTX ([LipidGem] = 10 μM, [PTX] = 6.2 μM, 2.61 x10^7 MB) ± US. (US parameters - frequency - 1 MHz, US power density - 3.0 W/cm^2, duty cycle - 40%, time- 30 sec).
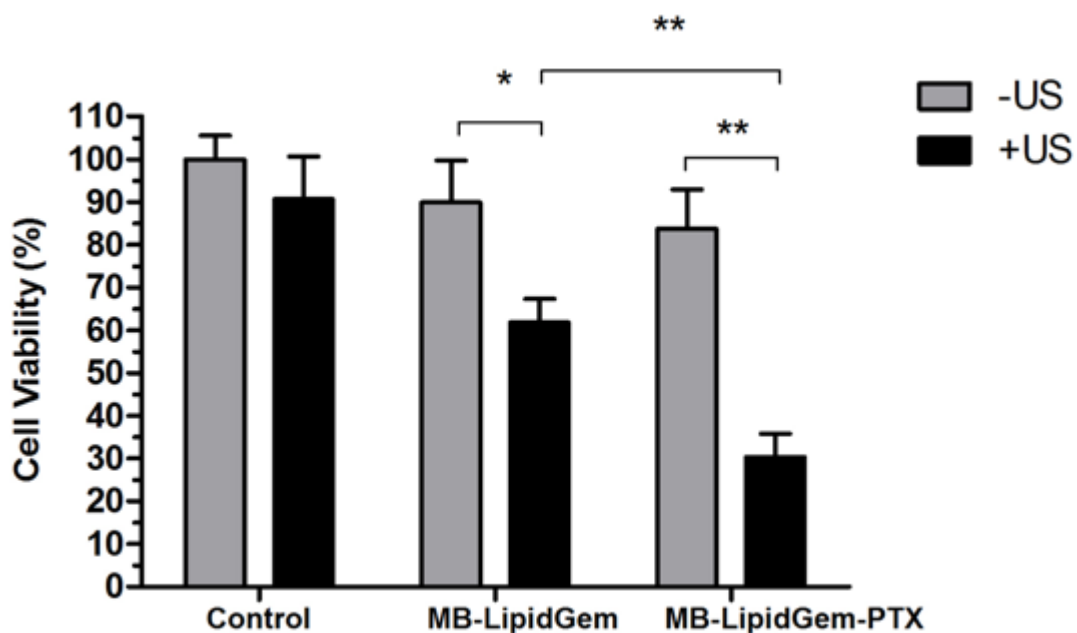
Figure 6.15. Plot of cell viability of spheroids treated with a) human pancreas ductal adenocarcinoma cell line (Panc-1) spheroids treated with a) no drug ± US b) MB-LipidGem ([LipidGem] = 10 μM, 3.40 x10^7 MB) ± US c) MB-LipidGem-PTX ([LipidGem] = 10 μM, [PTX] = 6.2 μM, 2.61 x10^7 MB) ± US. (US parameters - frequency - 1 MHz, US power density - 3.0 W/cm^2, duty cycle - 40%, time- 30 sec) (n=4).

Shuto *et al* attributed the apparent effectiveness of phospholipid-nucleoside prodrugs to two main mechanisms. First, due to the hydrophobic nature of the molecule, it may be transported into the cell more readily through passive diffusion through the phospholipid bilayer. This effect may be further improved through the application of US mediated sonoporation. Second, once inside the cancer cell, a phospholipid-nucleoside prodrug must undergo metabolic activation to either unmodified Gem or to the active metabolite Gem-monophosphate. This could theoretically be achieved via multiple possible activation mechanisms outlined in Figure 6.16. The prodrug could be directly transformed into Gem-monophosphate via cleavage of the diacyl glycerol moiety by phospholipase C or into Gem via cleavage at the 5′ hydroxyl position. Gem can then be further metabolised by a kinase enzyme into the active Gem monophosphate. Alternatively, Gem and Gem-monophopshate can be indirectly produced through a series of enzymatic manipulations by phospholipase A, phosphodiesterase and lysophospholipase. Of course, further work is needed to clarify the intracellular activation of LipidGem. (320)

a) phospholipase C
b) phospholipase D
c) phospholipase A
d) phosphodiesterase
e) lysophospholipase
f) phosphatase, 5'-nucleotidase
g) adenosine kinase
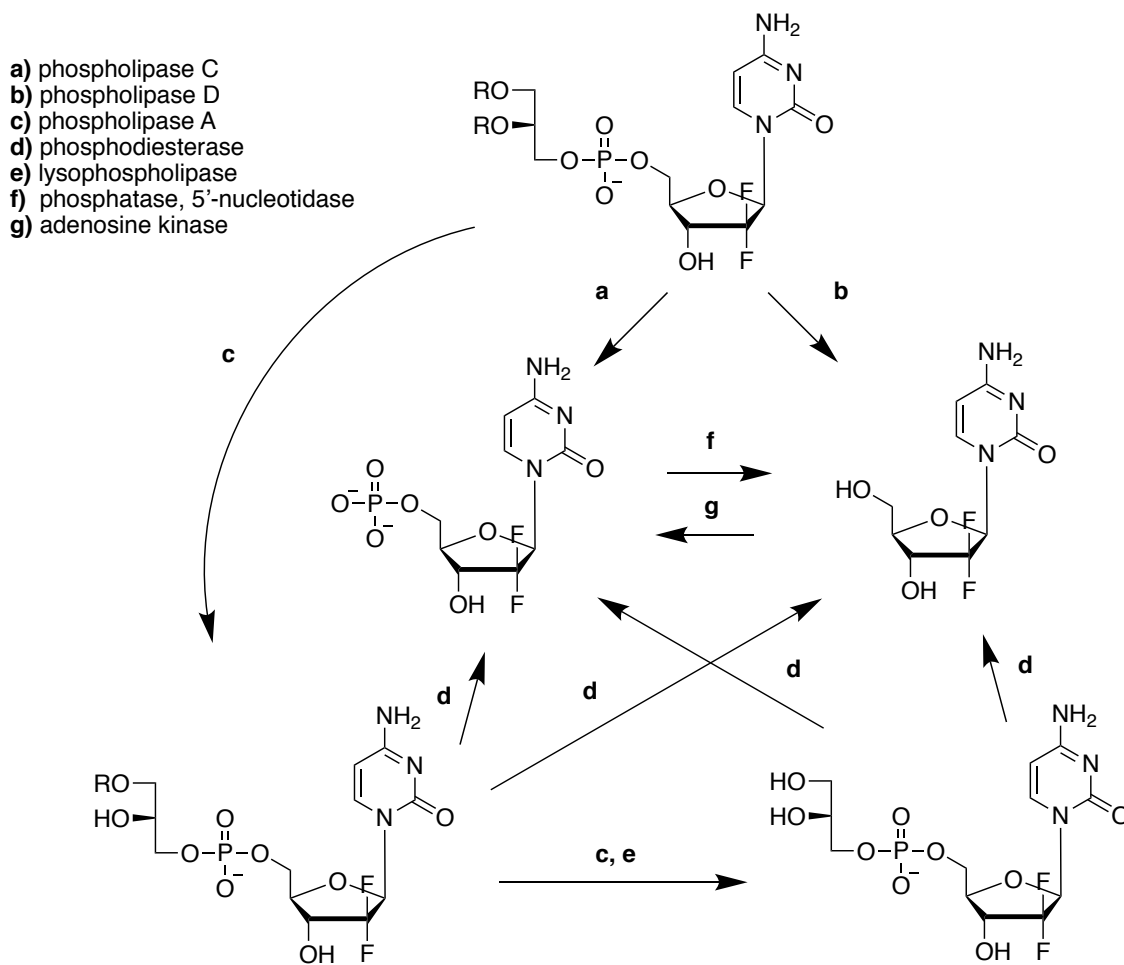
Figure 6.16. Scheme showing hypothetical, intracellular, enzyme-mediated activation pathways for 15. Reproduced from (320).

6.2.4. Efficacy of MB-LipidGem-PTX in mice bearing BxPC-3 tumours.

Having established the efficacy MB-LipidGem-PTX in vitro, the next step was to determine its efficacy in an in vivo model of pancreatic cancer. To this end BxPC-3 tumours were established in the rear dorsum of SCID mice as described in previous chapters. Once the tumours had reached an average volume of 150 mm^3 animals were randomly assigned into treatment groups. Animals were anaesthetised using isoflurane with medical grade oxygen as the carrier gas. Animals were treated with a 100 μL I.V. injection of either MB-LipidGem ([LipidGem] = 70.1 μg/10^8 MB) or MB-LipidGem-PTX([LipidGem] = 75.1 μg/10^8 MB, [PTX] = 48.57 μg/10^8 MB). As control groups, animals were treated with a 100 μL I.P injection Gem (120 mg/kg). As is described in Section 4.2.5, the combination of Gem and PTX at clinically relevant concentrations resulted in severe toxicity. Therefore, for ethical reasons, animals were not treated with this combination. Immediately following injection, US (Frequency = 1 MHz, power density = 3.5 W/cm^2, duty cycle = 30%, PNP 0.4 MPa, duration 3.5 min) was then applied to the tumour to facilitate MB destruction and delivery drug payloads to the tumour region.

The tumour growth plot in Figure 6.17a reveals, unsurprisingly, that the scaled clinical dose of Gem HCl significantly controls tumour growth progression. MB-LipidGem without PTX showed a significant improvement in tumour growth control compared to free Gem (p< 0.05). The greatly enhanced tumour inhibitory effect delivered by treatment with the MB-LipidGem clearly demonstrates one of the advantages of UTMD since the amount of Gem in this formulation is some 120-fold lower than that administered to the group treated with the clinical dose of Gem (i.e. Gem HCl). There was a further small but non-significant decrease in tumour growth progression for mice treated with MB-LipidGem-PTX compared to animals treated with non-PTX containing MB. The plot in Figure 6.17b of % change in body weight against time during treatment shows that no significant reduction in body weight was observed in any animal from any of the treatment groups. This was in contrast to previous findings that showed that the clinical dose of Gem caused a significant drop in body weight (Figure 4.15 and 4.16). These results again clearly demonstrate the advantage of UTMD mediated chemotherapy, producing superior tumour growth control while at the same time causing no significant acute toxic effects.
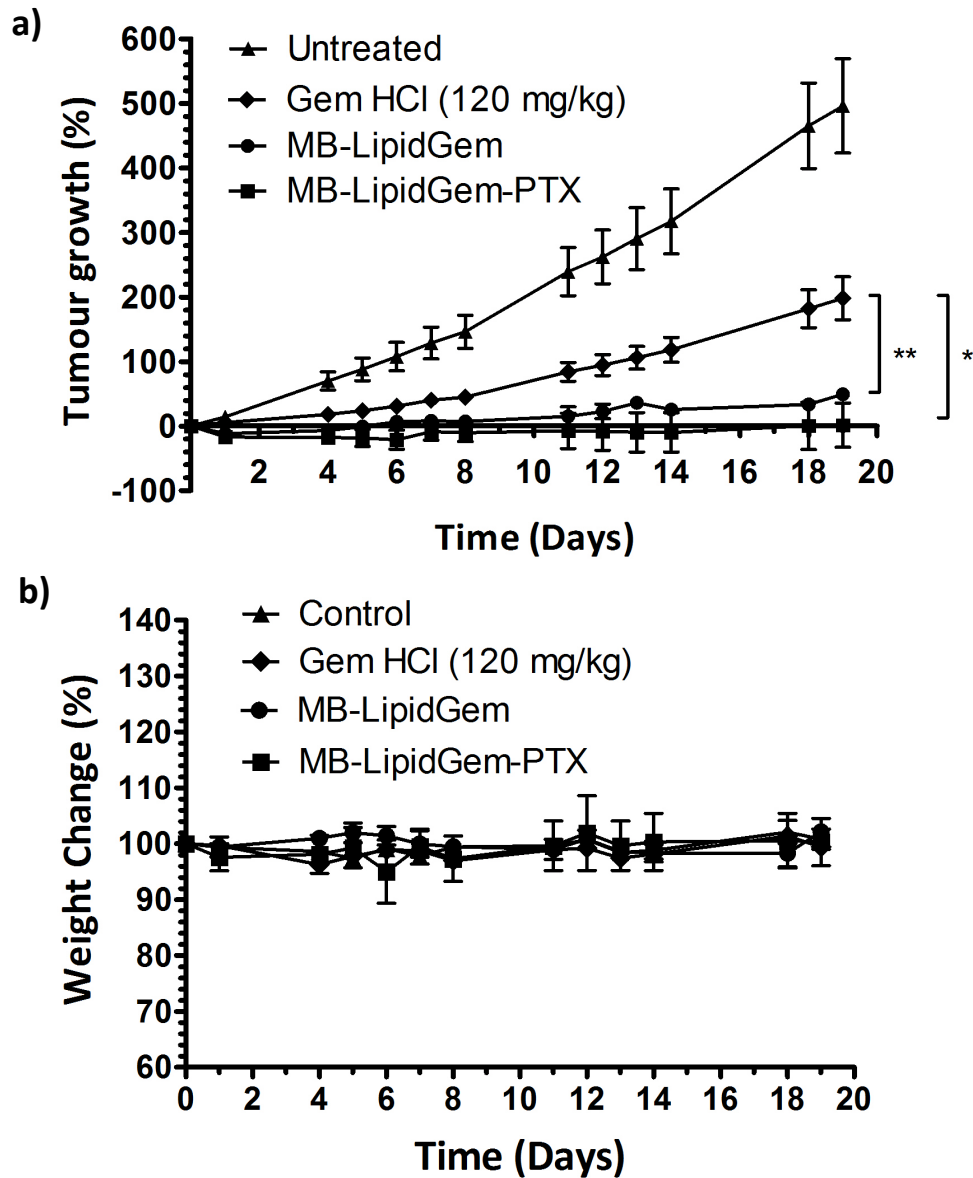
Figure 6.17. Plot of (a) % change in tumour volume and (b) average body weight for BxPC-3 tumour bearing mice treated with (i) no treatment (triangle) (ii) MB-LipidGem (circle) (iii) MB-LipidGem-PTX (square) (v) Gem HCl (diamond). The MB suspensions (MB-LipidGem - 9.97 x10^8 MB/mL, MB-LipidGem-PTX - 8.6 x10^8) were delivered as a 100 µL I.V injection (MB-LipidGem – [LipidGem] = 2.77 mg/kg, MB-LipidGem-PTX – [LipidGem] = 3.15 mg/kg, [PTX] = 1.98 mg/kg). Gem HCl was dissolved in sterile PBS and administered as a 100 µL I.P injection (120 mg/kg). US treatment was delivered for 3.5 min at frequency of 1 MHz, an US power density of 3.5 W/cm^2 and a duty cycle of 30% immediately after injection. Error bars represent ± standard error of the mean. For plot (a) and (b) *p < 0.05 **p < 0.01, ***p < 0.001. Error bars represent ± SEM where n = 4.

6.3. Conclusion

The phospholipid-based prodrug strategy is an emerging field for overcoming a number of biopharmaceutical and drug delivery challenges. Owing to their structure, phospholipid-based prodrugs are capable of participating in endogenous phospholipid metabolic pathways therefore leading to improved pharmacokinetic and pharmacodynamic properties of the drug. Additional advantages include drug targeting by enzyme-mediated drug release and overcoming drug resistance. Phospholipid prodrugs are also ideally suited to formulation into both liposomes and MBs. The work undertaken in this chapter demonstrates the effectiveness of the co-delivery of a phospholipid-Gem prodrug and PTX using UTMD. (324,325)

In summary a novel phospholipid derivative of Gem has been successfully synthesised through a single step enzymatically catalysed transphosphatidylation reaction. This novel compound was shown to form MB using common MB forming methods and was capable of loading significant quantities of PTX within the acyl chain layer of the MB. Importantly, this did not require any post MB manipulation. MB-LipidGem and MB-LipidGem-PTX displayed comparable stability at 37°C to plain unloaded MBs. In vitro testing using Panc-1 spheroids showed that MB-LipidGem and MB-LipidGem-PTX had little effect on cell viability in the absence of US stimulation, but upon US application, showed significant levels of cell death with MB-LipidGem-PTX having the greatest effect. The in vivo effectiveness of the MB conjugate was determined in an ectopic BxPC-3 murine model and showed that the combination of LipidGem and PTX was significantly more effective at controlling tumour growth compared with untreated controls and mice treated with a scaled clinical dose of Gem at significantly lower doses (120-fold). This once again highlights the advantage of UTMD, in that lower concentrations of cytotoxic agent are required to achieve an improve therapeutic response. As described in Section 6.1, a variety of techniques for conjugating drugs to shell of MBs have been described in the published literature. However, to the best of our knowledge, pre-conjugation of an anticancer drug to the precursor phospholipids prior to MB formation has not yet been communicated in the literature. The work described in this chapter allows provides means of tighter control of drug loading onto the MB leading to reduced batch to batch variability.

This coupled with improved ease of preparation, make this strategy more amenable to scale up and clinical translation.

Collectively, the results described in this chapter make another positive step-forward in the development of single MB formulations for the delivery of multiple payloads. Given the simplistic nature of the synthesis discussed herein, this strategy can be applied to a wide variety of other clinically approved drug candidates.

Chapter 7

General Conclusions and Future Outlook

Chapter 7 - General Conclusions and Future Outlook

The work described in this thesis explored novel techniques for the synthesis and subsequent drug loading of novel US-responsive MB delivery platforms and their application for UTMD in the treatment of solid tumours with particular focus on PDAC, which is one of the deadliest forms of cancer.

Work conducted in chapter 3 explored the potential of loading MBs with multiple payloads and was based upon previous research conducted in the area of combined chemo-SDT delivered using O_2MBs. The hydrophobic anticancer drug PTX was successfully loaded into the hydrophobic region of the MB monolayer. This enabled the subsequent unhindered surface functionalisation of the MB with either RB of Dox through avidin-biotin conjugation chemistry. In vitro models of breast cancer (MCF-7) the combination of MB-PTX-Dox and MB-PTX-RB performed significantly better than either of the MB conjugates alone and free dug groups at the same concentration with the combination of MBs reducing cell viability by 72.6% in the presence of US as determined by an MTT assay. This translated into a significant regression in tumour growth (6.96%) in an in vivo model of the same cell line while being comparatively well tolerated by the animals in contrast to animals treated with the free drug combination. The primary limitations with this study were that two separate MB formulations had to be prepared and mixed prior to treatment. This not only made the preparation more laborious but also limited the dose which could be administered. Due to the limited treatment options, besides surgical resection and large doses of systemic chemotherapy, triple negative breast cancer still remains one of the main challenges in the treatment of breast cancer. Further work in this area should build upon results presented in this chapter and focus on in vitro/ in vivo models of triple negative breast cancer as this subgroup of patients could benefit greatly from a delivery system which can improve drug uptake and efficacy while remaining non-toxic to the patient.

As previously mentioned, the main limitation why work conducted in chapter 3 was that only two agents could be loaded on a single MB meaning that multiple formulations had to be prepared separately and mixed prior to use. Work conducted in chapter 4 aimed to address these shortcomings through the

preparation of MB-PTX, surface functionalised with a novel tripodal ligand composed of Gem and RB with a biotin anchor facilitating the loading of three components onto the MB. This approach allowed for the simultaneous delivery of all three active agents on a single MB therefore increasing the control of drug deposition into the tumour. Prepared MBs showed high loadings of all three active agents and in vitro experiments in Panc-1 spheroids revealed a synergistic affect between the three active agents contained within MB-PTX-Gem-RB with a reduction in cell viability of 72%. In vivo experiments in both BxPC-3 and MIA-PaCa-2 xenografts revealed a significant reduction in tumour growth when compared to clinically relevant doses of free Gem and PTX. In spite of the encouraging in vitro/ in vivo results described in chapter 4, the utility of **15** as a MB surface ligand in a clinical setting could be limited due to its complex chemical structure and difficult synthetic route. Future work in this area should focus on developing an efficient and scalable synthetic procedure for **15.** This could also be extended to include other clinically relevant drug combinations for the use in a variety of other cancers. Stemming from the prevalence of metastatic disease in the pancreatic cancer patient pool, there is a particular interest in the use of MB mediated delivery of chemo-SDT in combination with immunotherapy aimed at reducing primary tumour burden while also tackling systemic disease.

Chapter 5 progressed the work from previous chapters through the addition of an extra layer of targeting by incorporating magnetically responsive nanoparticles into the hydrophobic region of the MB shell, in combination with a prototype magneto-acoustic device enabling simultaneous coalignment of magnetic and acoustic fields. In vitro phantom experiments showed 1.6-fold increase in uptake of RB with the MAD device when compared to magnetic and acoustic filed applied separately. In *in vivo* models the MagMBs loaded with **15**, described in chapter 4, showed an enhanced reduction in tumour growth (37%) when treated with the MAD device when compared to animals treated with the MB conjugate with acoustic and magnetic fields applied separately (9%). However, the in vivo study was limited by the low number of animals used (n=4) per treatment group which lowered the statistical power of the study. Additionally, it would also be highly beneficial to include cavitation monitoring in future iterations of the MAD device as this would provide significant feedback as to the effectiveness of the treatment. Further work could involve the

examination of the MAD device in a setting representative of human length scales.

Finally, chapter 6 described the synthesis of a novel prodrug of Gem capable of assembling into stable MBs using techniques common in the literature for MB preparation. The novel MBs were further powered through the addition of PTX into the hydrophobic shell. This MB conjugate showed improved efficacy in in vitro Panc-1 spheroids with a reduction in cell viability of 69.7%. In vivo experiments revealed significant reduction in tumour growth when compared to untreated controls. The distinct advantage of this method of production is that the drug is preloaded onto the lipid prior to MB formation. Not only does this shorten the process of MB synthesis, but also allows for tighter control of drug loading on the MB. There may also be scope to further enhance the stability of the MB conjugate through the addition of various other lipids such as phosphatidylcholines. This study had several limitations worth discussing. Firstly, there remains the question of scalability and regulatory alignment of the synthetic approach adopted in the chapter, given the bacterial source of phospholipase D. Future work will endeavour to rationally design and develop a classical synthetic approach to a Gem-phospholipid conjugate. Secondly, there remains uncertainty regarding the precise mechanism of intracellular activation of LipidGem. This could be addressed by attaching Gem to the phospholipid using enzymatically labile ester or amide bonds as this would result in a more predictable activation pathway. The utility of the approach used in this chapter could also be extended to a wide variety of other drug candidates and/or targeting ligands for a wide variety of solid malignancies.

While the use of MBs for the targeted drug delivery has been shown to be highly effective in many cancers as well as numerous other diseases, there still remains the challenge of clinical translation. One of the main challenges is the shelf life and long-term storage of MB preparations. Lessons can certainly be learned from current clinically approved contrast agents such as SonoVue and Definity. SonoVue MBs are prepared at the bedside by reconstituting a lyophilised liposomal suspension under a headspace of SF_6 while Definity MBs are also prepared at the bedside and require activation of a stable liposomal suspension with a PFB headspace using a high-speed vial shaking device. Compound **15**, which was designed and synthesised in chapter 6, along with

other similar phospholipid-drug conjugates would be ideally suited to formulation into MBs produced by either of these two methods which could help to address one of the main barriers to clinical translation of therapeutic MBs. A further avenue for future research could involve the development of nanoscale particles which could enable improved tumour penetration and drug delivery.

Appendices

8.0. Appendices

LCQ Instrument Control
SH: 3868 IT: 0.39 ST: 0.54 #A: 10
NL: 2.42e+008
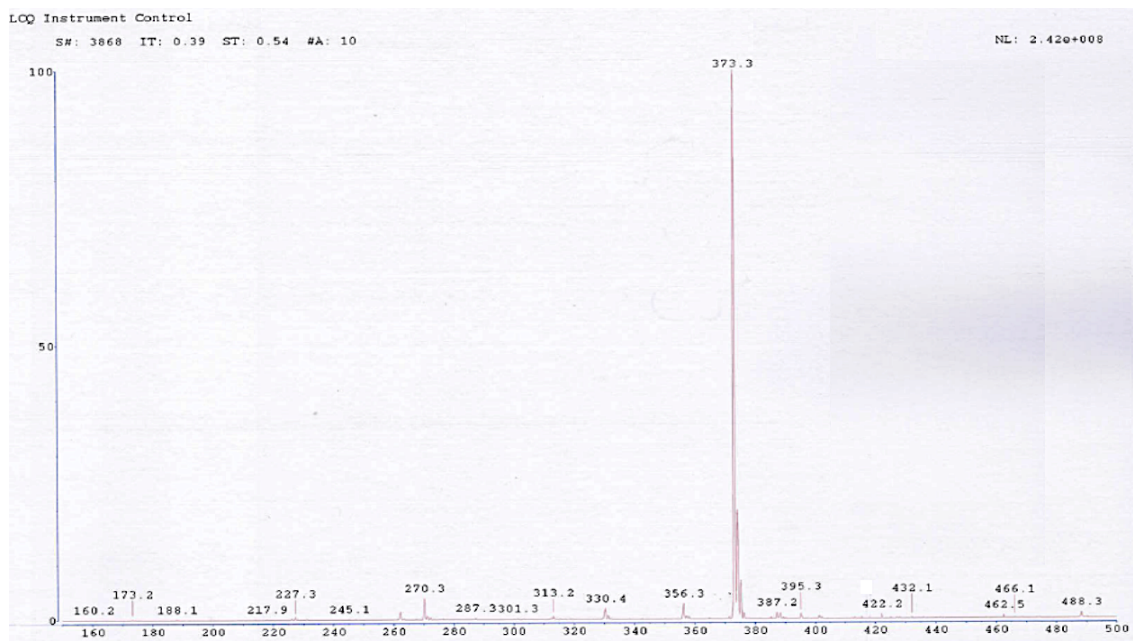
Figure A1. ESI-MS spectrum of 10. Recorded in methanol.
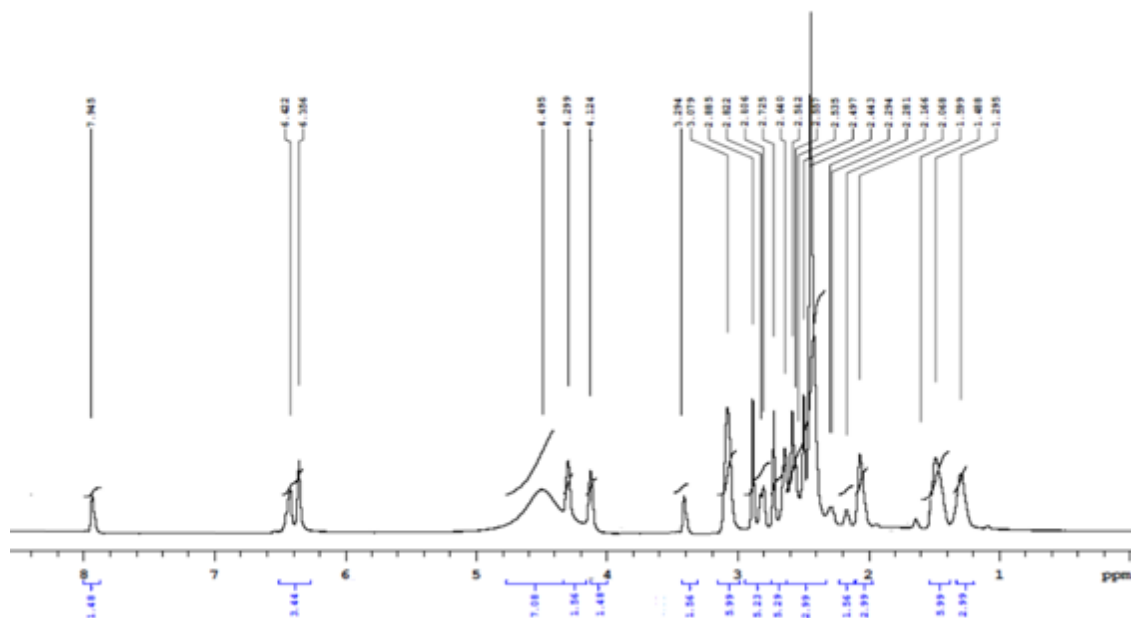
Figure A2. ¹H NMR spectrum of 10. Recorded in DMSO-*d*₆.
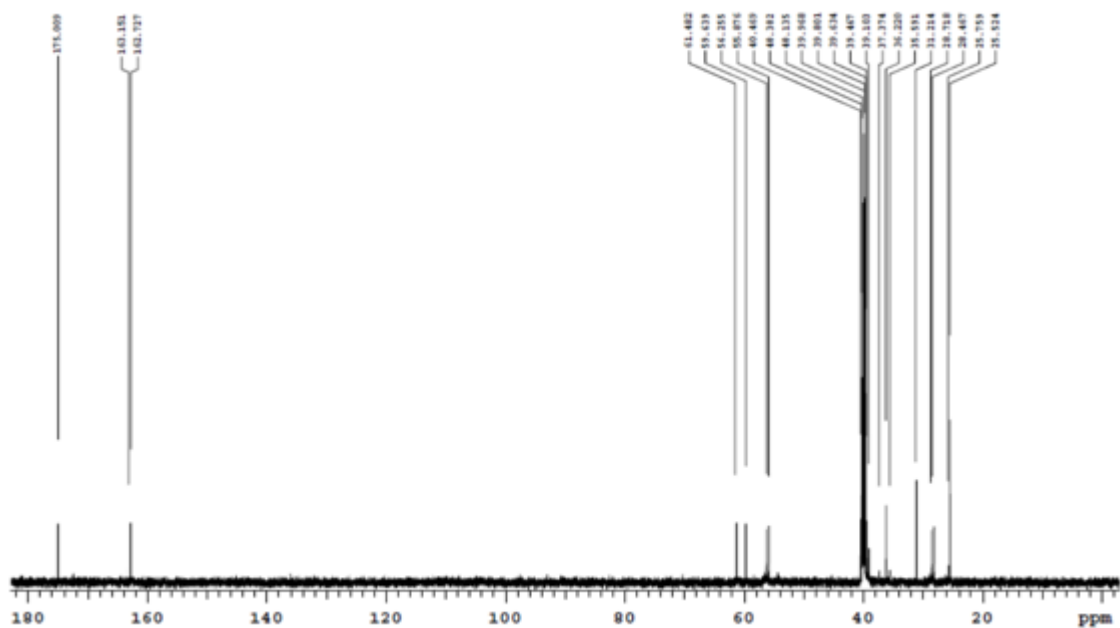
Figure A3. ^{13}C NMR spectrum of 10. Recorded in DMSO-d_6.
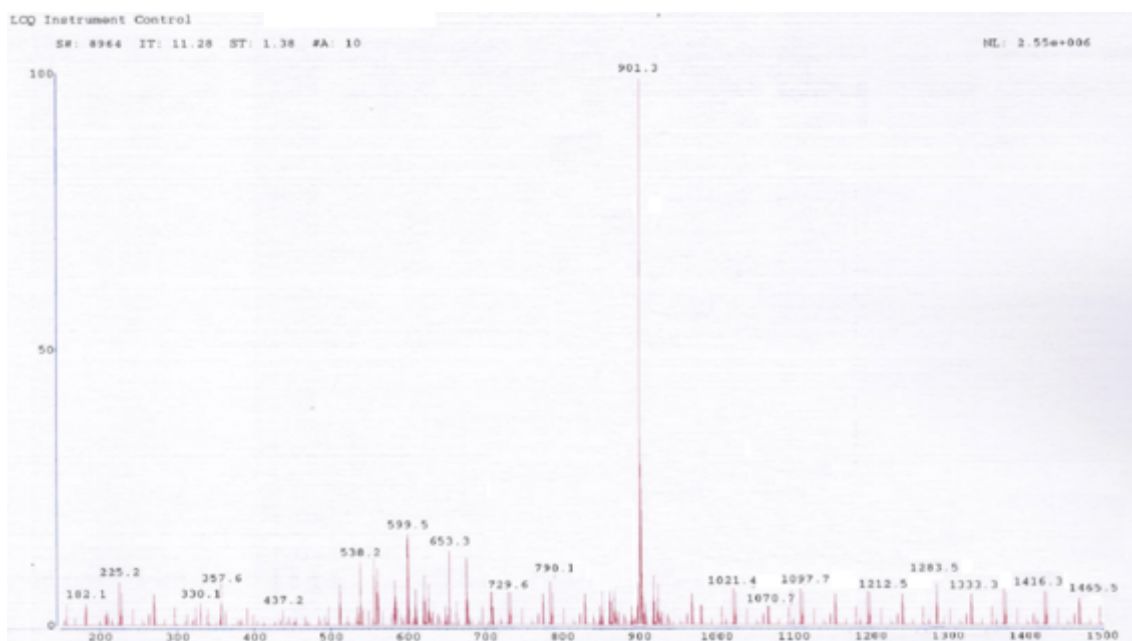
Figure A4. ESI-MS spectrum of 11. Recorded in methanol.
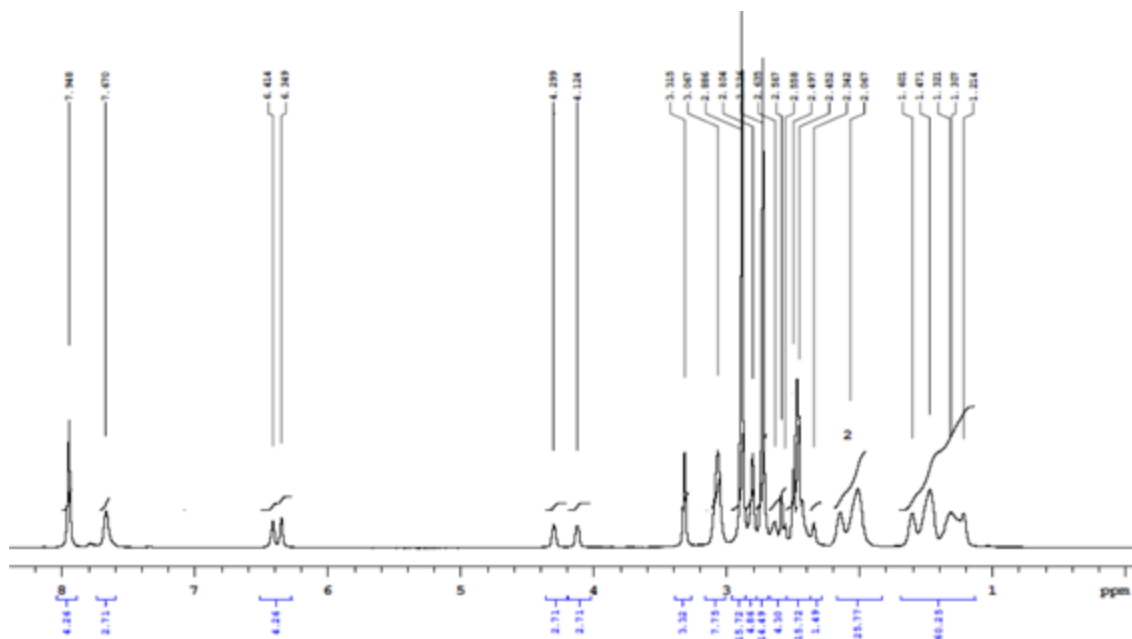
Figure A5. ¹H NMR spectrum of **11**. Recorded in DMSO-*d*₆.
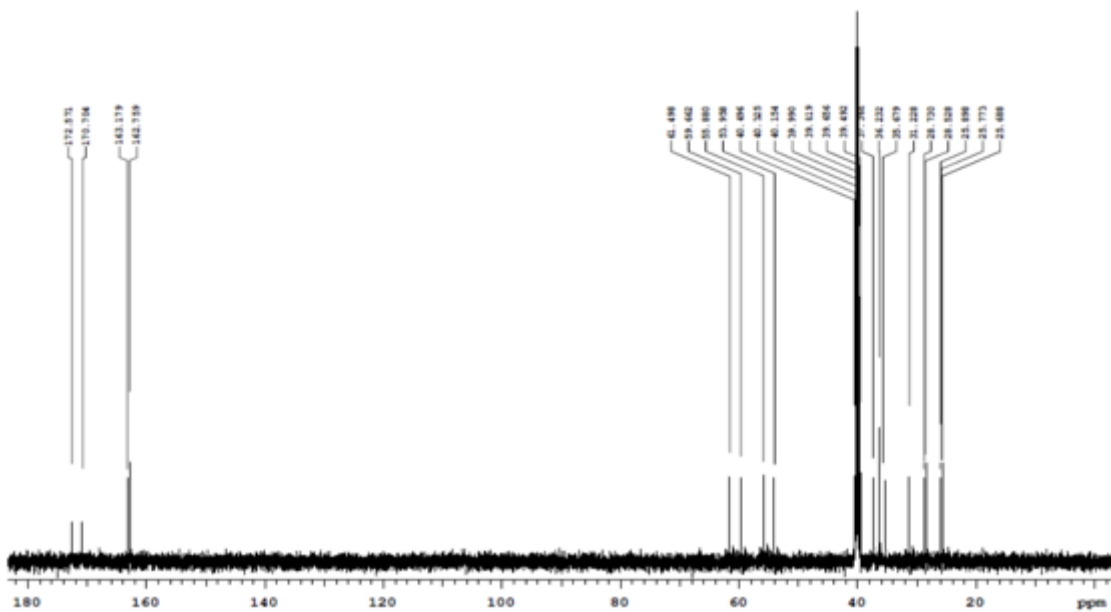
Figure A6. ¹³C NMR spectrum of **11**. Recorded in DMSO-*d*₆
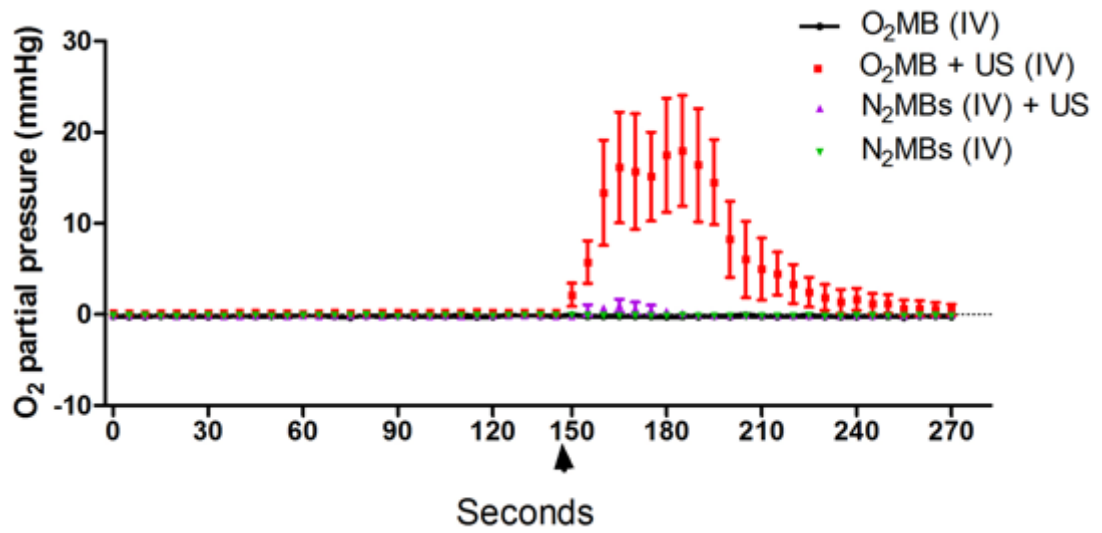
Figure A7. Plot of tumour oxygen partial pressure over time of ectopic BxPC-3 tumour bearing mice following a 100 uL I.V injection of O_2MB (1 x10^9 MB/mL) or N_2MB (1 x 10^9 MB) in the presence and absence of US. Arrow indicates the point of I.V injection. Error bars indicate SEM (n=3).

9.0. References

1. Bray F, Ferlay J, Soerjomataram I, Siegel RL, Torre LA, Jemal A. Global cancer statistics 2018: GLOBOCAN estimates of incidence and mortality worldwide for 36 cancers in 185 countries. CA Cancer J Clin. 2018 Nov;68(6):394–424.

2. Hanahan D, Weinberg RA. Hallmarks of cancer: The next generation. Vol. 144, Cell. 2011. p. 646–74.

3. Blick SKA, Scott LJ. Cetuximab. Drugs. 2007;67(17):2585–607.

4. Brand TM, Dunn EF, Iida M, Myers RA, Kostopoulos KT, Li C, et al. Erlotinib is a viable treatment for tumors with acquired resistance to cetuximab. Cancer Biol Ther. 2011 Sep 1;12(5):436–46.

5. Banys-Paluchowski M, Krawczyk N, Paluchowski P. Cyclin-dependent kinase 4/6 inhibitors: what have we learnt across studies, therapy situations and substances. Curr Opin Obstet Gynecol. 2019 Feb 1;31(1):56–66.

6. Callahan MK, Wolchok JD, Allison JP. AntiCTLA-4 antibody therapy: Immune monitoring during clinical development of a novel immunotherapy. Semin Oncol. 2010;37(5):473–84.

7. Orr RM. Technology evaluation: fomivirsen, Isis Pharmaceuticals Inc/CIBA vision. Curr Opin Mol Ther. 2001 Jun;3(3):288–94.

8. Chiappori AA, Kolevska T, Spigel DR, Hager S, Rarick M, Gadgeel S, et al. A randomized phase II study of the telomerase inhibitor imetelstat as maintenance therapy for advanced non-small-cell lung cancer. Ann Oncol. 2015 Feb 1;26(2):354–62.

9. Harris RE, Chlebowski RT, Jackson RD, Frid DJ, Ascenseo JL, Anderson G, et al. Breast cancer and nonsteroidal anti-inflammatory drugs: prospective results from the Women's Health Initiative. Cancer Res. 2003 Sep 15;63(18):6096–101.

10. Casanova I, Parreño M, Farré L, Guerrero S, Céspedes MV, Pavon MA, et

al. Celecoxib induces anoikis in human colon carcinoma cells associated with the deregulation of focal adhesions and nuclear translocation of p130Cas. Int J Cancer. 2006 May 15;118(10):2381–9.

11. Daud A, Kluger HM, Kurzrock R, Schimmoller F, Weitzman AL, Samuel TA, et al. Phase II randomised discontinuation trial of the MET/VEGF receptor inhibitor cabozantinib in metastatic melanoma. Br J Cancer. 2017 Feb 14;116(4):432–40.

12. Chen RL, Zhao J, Zhang XC, Lou NN, Chen HJ, Yang X, et al. Crizotinib in advanced non-small-cell lung cancer with concomitant ALK rearrangement and c-Met overexpression. BMC Cancer. 2018 Nov 26;18(1).

13. Van Cutsem E, Lambrechts D, Prenen H, Jain RK, Carmeliet P. Lessons from the adjuvant bevacizumab trial on colon cancer: What next? Journal of Clinical Oncology. 2011 Jan 1;29(1):1–4.

14. Wang TF, Lockhart AC. Aflibercept in the treatment of metastatic colorectal cancer. Vol. 6, Clinical Medicine Insights: Oncology. Libertas Academica Ltd.; 2012. p. 19–30.

15. Fong PC, Boss DS, Yap TA, Tutt A, Wu P, Mergui-Roelvink M, et al. Inhibition of poly(ADP-ribose) polymerase in tumors from BRCA mutation carriers. N Engl J Med. 2009 Jul 9;361(2):123–34.

16. Brown JS, Kaye SB, Yap TA. PARP inhibitors: the race is on. Br J Cancer. 2016 Mar 29;114(7):713–5.

17. Anderson MA, Deng J, Seymour JF, Tam C, Kim SY, Fein J, et al. The BCL2 selective inhibitor venetoclax induces rapid onset apoptosis of CLL cells in patients via a TP53-independent mechanism. Blood. 2016 Jun 23;127(25):3215–24.

18. Tolcher AW, LoRusso P, Arzt J, Busman TA, Lian G, Rudersdorf NS, et al. Safety, efficacy, and pharmacokinetics of navitoclax (ABT-263) in combination with irinotecan: results of an open-label, phase 1 study. Cancer Chemother Pharmacol. 2015 Nov;76(5):1041–9.

19. Gründker C, Wokoun U, Hellriegel M, Emons G. Inhibition of aerobic glycolysis enhances the anti-tumor efficacy of Zoptarelin Doxorubicin in

triple-negative breast cancer cells. J Obstet Gynaecol Res. 2019 Jul 1;45(7):1334–42.

20. Pichla M, Sroka J, Pienkowska N, Piwowarczyk K, Madeja Z, Bartosz G, et al. Metastatic prostate cancer cells are highly sensitive to 3-bromopyruvic acid. Life Sci. 2019 Jun 15;227:212–23.

21. Bianco R, Troiani T, Tortora G, Ciardiello F. Intrinsic and acquired resistance to EGFR inhibitors in human cancer therapy. Endocr Relat Cancer. 2005 Jul;12 Suppl 1:S159-71.

22. Torre LA, Bray F, Siegel RL, Ferlay J, Lortet-Tieulent J, Jemal A. Global cancer statistics, 2012. CA Cancer J Clin. 2015 Mar;65(2):87–108.

23. Oluwasanmi A, Al-Shakarchi W, Manzur A, Aldebasi MH, Elsini RS, Albusair MK, et al. Diels Alder-mediated release of gemcitabine from hybrid nanoparticles for enhanced pancreatic cancer therapy. J Control Release. 2017 Nov 28;266:355–64.

24. Tas F, Sen F, Odabas H, Kilic L, Keskin S, Yildiz I. Performance status of patients is the major prognostic factor at all stages of pancreatic cancer. Int J Clin Oncol. 2013 Oct;18(5):839–46.

25. Longnecker D. Anatomy and Histology of the Pancreas. Pancreapedia Exocrine Pancreas Knowl Base. 2014;1–26.

26. Ryan DP, Hong TS, Bardeesy N. Pancreatic Adenocarcinoma. N Engl J Med. 2014 Sep 11;371(11):1039–49.

27. Lau MK, Davila JA, Shaib YH. Incidence and survival of pancreatic head and body and tail cancers: A population-based study in the United States. Pancreas. 2010 May;39(4):458–62.

28. Watanabe I, Sasaki S, Konishi M, Nakagohri T, Inoue K, Oda T, et al. Onset symptoms and tumor locations as prognostic factors of pancreatic cancer. Pancreas. 2004 Mar;28(2):160–5.

29. Artinyan A, Soriano PA, Prendergast C, Low T, Ellenhorn JDI, Kim J. The anatomic location of pancreatic cancer is a prognostic factor for survival. In: HPB. Taylor and Francis Ltd.; 2008. p. 371–6.

30. Tomasello G, Ghidini M, Costanzo A, Ghidini A, Russo A, Barni S, et al. Outcome of head compared to body and tail pancreatic cancer: a systematic review and meta-analysis of 93 studies. J Gastrointest Oncol. 2019 Apr;10(2):259–69.

31. Rahib L, Smith BD, Aizenberg R, Rosenzweig AB, Fleshman JM, Matrisian LM. Projecting cancer incidence and deaths to 2030: The unexpected burden of thyroid, liver, and pancreas cancers in the united states. Vol. 74, Cancer Research. American Association for Cancer Research Inc.; 2014. p. 2913–21.

32. Yadav D, Lowenfels AB. The epidemiology of pancreatitis and pancreatic cancer. Gastroenterology. 2013 Jun;144(6):1252–61.

33. Klein AP, Brune KA, Petersen GM, Goggins M, Tersmette AC, Offerhaus GJA, et al. Prospective risk of pancreatic cancer in familial pancreatic cancer kindreds. Cancer Res. 2004 Apr 1;64(7):2634–8.

34. Ghiorzo P. Genetic predisposition to pancreatic cancer. World J Gastroenterol. 2014 Aug 21;20(31):10778–89.

35. Kuzmickiene I, Everatt R, Virviciute D, Tamosiunas A, Radisauskas R, Reklaitiene R, et al. Smoking and other risk factors for pancreatic cancer: a cohort study in men in Lithuania. Cancer Epidemiol. 2013 Apr;37(2):133–9.

36. Mizuno S, Nakai Y, Isayama H, Kawahata S, Saito T, Takagi K, et al. Smoking, family history of cancer, and diabetes mellitus are associated with the age of onset of pancreatic cancer in Japanese patients. Pancreas. 2014 Oct;43(7):1014–7.

37. Pelucchi C, Galeone C, Polesel J, Manzari M, Zucchetto A, Talamini R, et al. Smoking and body mass index and survival in pancreatic cancer patients. Pancreas. 2014 Jan;43(1):47–52.

38. Calle EE, Rodriguez C, Walker-Thurmond K, Thun MJ. Overweight, obesity, and mortality from cancer in a prospectively studied cohort of U.S. adults. N Engl J Med. 2003 Apr 24;348(17):1625–38.

39. Rawla P, Sunkara T, Gaduputi V. Epidemiology of Pancreatic Cancer: Global Trends, Etiology and Risk Factors. World J Oncol. 2019

Feb;10(1):10–27.

40. Hruban RH, Adsay NV, Albores-Saavedra J, Compton C, Garrett ES, Goodman SN, et al. Pancreatic intraepithelial neoplasia: A new nomenclature and classification system for pancreatic duct lesions. Am J Surg Pathol. 2001;25(5):579–86.

41. Tanaka M. Intraductal Papillary Mucinous Neoplasm as the Focus for Early Detection of Pancreatic Cancer. Gastroenterology. 2018;154(3):475–8.

42. Zavoral M, Minarikova P, Zavada F, Salek C, Minarik M. Molecular biology of pancreatic cancer. World J Gastroenterol. 2011 Jun 28;17(24):2897–908.

43. Khan MA, Azim S, Zubair H, Bhardwaj A, Patel GK, Khushman M, et al. Molecular drivers of pancreatic cancer pathogenesis: Looking inward to move forward. Vol. 18, International Journal of Molecular Sciences. MDPI AG; 2017.

44. Sohn TA, Yeo CJ. The molecular genetics of pancreatic ductal carcinoma: a review. Surg Oncol. 2000 Nov;9(3):95–101.

45. Caldas C, Hahn SA, da Costa LT, Redston MS, Schutte M, Seymour AB, et al. Frequent somatic mutations and homozygous deletions of the p16 (MTS1) gene in pancreatic adenocarcinoma. Nat Genet. 1994 Sep;8(1):27–32.

46. Kamisawa T, Isawa T, Koike M, Tsuruta K, Okamoto A. Hematogenous metastases of pancreatic ductal carcinoma. Pancreas. 1995 Nov;11(4):345–9.

47. Griffin JF, Poruk KE, Wolfgang CL. Pancreatic cancer surgery: Past, present, and future. Vol. 27, Chinese Journal of Cancer Research. AME Publishing Company; 2015. p. 332–48.

48. Gillen S, Schuster T, Meyer Zum Büschenfelde C, Friess H, Kleeff J. Preoperative/neoadjuvant therapy in pancreatic cancer: a systematic review and meta-analysis of response and resection percentages. PLoS Med. 2010 Apr 20;7(4):e1000267.

49. Raufi AG, Manji GA, Chabot JA, Bates SE. Neoadjuvant Treatment for Pancreatic Cancer. Semin Oncol. 2019 Feb;46(1):19–27.

50. M. Y, T. C, J.F. S, S. G, A. H, D. M-M, et al. An open phase I study assessing the feasibility of the triple combination: Oxaliplatin plus irinotecan plus leucovorin/5-fluorouracil every 2 weeks in patients with advanced solid tumors. Ann Oncol. 2003 Mar;14(3):481–9.

51. Longley DB, Harkin DP, Johnston PG. 5-fluorouracil: mechanisms of action and clinical strategies. Nat Rev Cancer. 2003 May;3(5):330–8.

52. Noordhuis P, Holwerda U, Van der Wilt CL, Van Groeningen CJ, Smid K, Meijer S, et al. 5-Fluorouracil incorporation into RNA and DNA in relation to thymidylate synthase inhibition of human colorectal cancers. Ann Oncol Off J Eur Soc Med Oncol. 2004 Jul;15(7):1025–32.

53. Piedbois P, Buyse M, Rustum Y, Machover D, Erlichman C, Carlson RW, et al. Modulation of fluorouracil by leucovorin in patients with advanced colorectal cancer: Evidence in terms of response rate by the advanced colorectal cancer meta-analysis project. J Clin Oncol. 1992;10(6):896–903.

54. DeLap RJ. The effect of leucovorin on the therapeutic index of fluorouracil in cancer patients. Yale J Biol Med. 1988;61(1):23–34.

55. Gerrits CJ, Jonge MJ de, Schellens JH, Stoter G, Verweij J. Topoisomerase I inhibitors: the relevance of prolonged exposure for present clinical development. Br J Cancer. 1997;76(7):952.

56. Jonsson E, Dhar S, Jonsson B, Nygren P, Graf W, Larsson R. Differential activity of topotecan, irinotecan and SN-38 in fresh human tumour cells but not in cell lines. Eur J Cancer. 2000;36(16):2120–7.

57. Glassman DC, Palmaira RL, Covington CM, Desai AM, Ku GY, Li J, et al. Nanoliposomal irinotecan with fluorouracil for the treatment of advanced pancreatic cancer, a single institution experience. BMC Cancer. 2018 Jun 27;18(1):693.

58. Alcindor T, Beauger N. Oxaliplatin: A review in the era of molecularly targeted therapy. Curr Oncol. 2011;18(1):18–25.

59. Di Francesco AM, Ruggiero A, Riccardi R. Cellular and molecular aspects of drugs of the future: oxaliplatin. Cell Mol Life Sci. 2002 Nov;59(11):1914–27.

60. Raymond E, Faivre S, Woynarowski JM, Chaney SG. Oxaliplatin: mechanism of action and antineoplastic activity. Semin Oncol. 1998 Apr;25(2 Suppl 5):4–12.

61. Graham J, Muhsin M, Kirkpatrick P. Fresh from the pipeline: Oxaliplatin. Nat Rev Drug Discov. 2004;3(1):11–2.

62. Hertel LW. Difluoro antivirals and intermediate therefor. 480,861,4, 1983.

63. Nagourney RA, Flam M, Link J, Hager S, Blitzer J, Lyons W, et al. Carboplatin plus gemcitabine repeating doublet therapy in recurrent breast cancer. Clin Breast Cancer. 2008 Oct;8(5):432–5.

64. Lopez-Chavez A, Thomas A, Rajan A, Raffeld M, Morrow B, Kelly R, et al. Molecular profiling and targeted therapy for advanced thoracic malignancies a biomarker-derived, multiarm, multihistology phase ii basket trial. J Clin Oncol. 2015 Mar 20;33(9):1000–7.

65. S. Gesto D, M.F.S.A. Cerqueira N, A. Fernandes P, J. Ramos M. Gemcitabine: A Critical Nucleoside for Cancer Therapy. Curr Med Chem. 2012 Oct 16;19(7):1076–87.

66. Bouffard DY, Laliberté J, Momparler RL. Kinetic studies on 2',2'-difluorodeoxycytidine (Gemcitabine) with purified human deoxycytidine kinase and cytidine deaminase. Biochem Pharmacol. 1993 May 5;45(9):1857–61.

67. Gandhi V, Legha J, Chen F, Hertel LW, Plunkett W. Excision of 2',2'-difluorodeoxycytidine (gemcitabine) monophosphate residues from DNA. Cancer Res. 1996 Oct 1;56(19):4453–9.

68. De Sousa Cavalcante L, Monteiro G. Gemcitabine: Metabolism and molecular mechanisms of action, sensitivity and chemoresistance in pancreatic cancer. Vol. 741, European Journal of Pharmacology. Elsevier; 2014. p. 8–16.

69. Zhou BS, Tsai P, Ker R, Tsai J, Ho R, Yu J, et al. Overexpression of transfected human ribonucleotide reductase M2 subunit in human cancer cells enhances their invasive potential. Clin Exp Metastasis. 1998 Jan;16(1):43–9.

70. Zhou J, Oliveira P, Li X, Chen Z, Bepler G. Modulation of the ribonucleotide reductase-antimetabolite drug interaction in cancer cell lines. J Nucleic Acids. 2010 Sep 28;2010:597098.

71. Jia Y, Xie J. Promising molecular mechanisms responsible for gemcitabine resistance in cancer. Vol. 2, Genes and Diseases. Chongqing yi ke da xue, di 2 lin chuang xue yuan Bing du xing gan yan yan jiu suo; 2015. p. 299–306.

72. Gilbert JA, Salavaggione OE, Ji Y, Pelleymounter LL, Eckloff BW, Wieben ED, et al. Gemcitabine pharmacogenomics: Cytidine deaminase and deoxycytidylate deaminase gene resequencing and functional genomics. Clin Cancer Res. 2006 Mar 15;12(6):1794–803.

73. Greenhalf W, Ghaneh P, Neoptolemos JP, Palmer DH, Cox TF, Lamb RF, et al. Pancreatic cancer hENT1 expression and survival from gemcitabine in patients from the ESPAC-3 trial. J Natl Cancer Inst. 2014 Jan;106(1):djt347.

74. Mini E, Nobili S, Caciagli B, Landini I, Mazzei T. Cellular pharmacology of gemcitabine. Ann Oncol. 2006 May;17(SUPPL. 5).

75. Kroep JR, Loves WJP, van der Wilt CL, Alvarez E, Talianidis I, Boven E, et al. Pretreatment deoxycytidine kinase levels predict in vivo gemcitabine sensitivity. Mol Cancer Ther. 2002 Apr;1(6):371–6.

76. Beumer JH, Eiseman JL, Parise RA, Joseph E, Covey JM, Egorin MJ. Modulation of gemcitabine (2′,2′-Difluoro-2′- Deoxycytidine) pharmacokinetics, metabolism, and bioavailability in mice by 3,4,5,6-tetrahydrouridine. Clin Cancer Res. 2008 Jun 1;14(11):3529–35.

77. Mackey JR, Mani RS, Selner M, Mowles D, Young JD, Belt JA, et al. Functional Nucleoside Transporters Are Required for Gemcitabine Influx and Manifestation of Toxicity in Cancer Cell Lines. Cancer Res. 1998;58(19).

78. Moysan E, Bastiat G, Benoit JP. Gemcitabine versus modified gemcitabine:

A review of several promising chemical modifications. Vol. 10, Molecular Pharmaceutics. 2013. p. 430–44.

79. Alexander RL, Greene BT, Torti S V., Kucera GL. A novel phospholipid gemcitabine conjugate is able to bypass three drug-resistance mechanisms. Cancer Chemother Pharmacol. 2005 Jul;56(1):15–21.

80. Wang Y, Fan W, Dai X, Katragadda U, Mckinley D, Teng Q, et al. Enhanced tumor delivery of gemcitabine via PEG-DSPE/TPGS mixed micelles. Mol Pharm. 2014 Apr 7;11(4):1140–50.

81. Lewis WH, Elvin-Lewis MPF. Medical botany : plants affecting human health. J. Wiley; 2003. 812 p.

82. Weaver BA. How Taxol/paclitaxel kills cancer cells. Mol Biol Cell. 2014 Sep 15;25(18):2677–81.

83. Fang W-S, Liang X-T. Recent progress in structure activity relationship and mechanistic studies of taxol analogues. Mini Rev Med Chem. 2005 Jan;5(1):1–12.

84. Kingston DGI. The shape of things to come: Structural and synthetic studies of taxol and related compounds. Vol. 68, Phytochemistry. 2007. p. 1844–54.

85. Kingston DGI. Recent advances in the chemistry of taxol. Vol. 63, Journal of Natural Products. 2000. p. 726–34.

86. Schiff PB, Horwitz SB. Taxol stabilizes microtubules in mouse fibroblast cells. Proc Natl Acad Sci U S A. 1980 Mar;77(3):1561–5.

87. Konno T, Watanabe J, Ishihara K. Enhanced solubility of paclitaxel using water-soluble and biocompatible 2-methacryloyloxyethyl phosphorylcholine polymers. J Biomed Mater Res A. 2003 May 1;65(2):209–14.

88. Singla AK, Garg A, Aggarwal D. Paclitaxel and its formulations. Int J Pharm. 2002 Mar 20;235(1–2):179–92.

89. Dorr RT. Pharmacology and toxicology of Cremophor EL diluent. Ann

Pharmacother. 1994 May;28(5 Suppl):S11-4.

90.   Gelderblom H, Verweij J, Nooter K, Sparreboom A. Cremophor EL: The drawbacks and advantages of vehicle selection for drug formulation. Eur J Cancer. 2001;37(13):1590–8.

91.   Weiss RB. Hypersensitivity reactions from taxol. J Clin Oncol. 1990;8(7):1263–8.

92.   Green MR, Manikhas GM, Orlov S, Afanasyev B, Makhson AM, Bhar P, et al. Abraxane®, a novel Cremophor®-free, albumin-bound particle form of paclitaxel for the treatment of advanced non-small-cell lung cancer. Ann Oncol. 2006 Aug;17(8):1263–8.

93.   Desai N. Nanoparticle albumin-bound paclitaxel (Abraxane®). In: Albumin in Medicine: Pathological and Clinical Applications. Springer Singapore; 2016. p. 101–19.

94.   Yardley DA. Nab-Paclitaxel mechanisms of action and delivery. Vol. 170, Journal of Controlled Release. Elsevier B.V.; 2013. p. 365–72.

95.   Gardner ER, Dahut WL, Scripture CD, Jones J, Aragon-Ching JB, Desai N, et al. Randomized crossover pharmacokinetic study of solvent-based paclitaxel and nab-paclitaxel. Clin Cancer Res. 2008 Jul 1;14(13):4200–5.

96.   Haley B, Frenkel E. Nanoparticles for drug delivery in cancer treatment. Vol. 26, Urologic Oncology: Seminars and Original Investigations. 2008. p. 57–64.

97.   Maeda H, Matsumura Y. A new concept for macromolecular therapeutics in cancer chemotherapy: mechanism of tumoritropic accumulation of proteins and the antitumor agent smancs. Cancer Res. 1986;46(12 Pt 1):6387–92.

98.   Maeda H, Sawa T, Konno T. Mechanism of tumor-targeted delivery of macromolecular drugs, including the EPR effect in solid tumor and clinical overview of the prototype polymeric drug SMANCS. In: Journal of Controlled Release. 2001. p. 47–61.

99.   Infante JR, Matsubayashi H, Sato N, Tonascia J, Klein AP, Riall TA, et al.

Peritumoral fibroblast SPARC expression and patient outcome with resectable pancreatic adenocarcinoma. J Clin Oncol. 2007 Jan 20;25(3):319–25.

100. Podhajcer OL, Benedetti L, Girotti MR, Prada F, Salvatierra E, Llera AS. The role of the matricellular protein SPARC in the dynamic interaction between the tumor and the host. Cancer Metastasis Rev. 2008 Sep 6;27(3):523–37.

101. Von Hoff DD, Ramanathan RK, Borad MJ, Laheru DA, Smith LS, Wood TE, et al. Gemcitabine plus nab-paclitaxel is an active regimen in patients with advanced pancreatic cancer: A phase I/II trial. J Clin Oncol. 2011 Dec 1;29(34):4548–54.

102. Yardley DA, Daniel BR, Inhorn RC, Vazquez ER, Trieu VN, Motamed K, et al. SPARC microenvironment signature (SMS) analysis of a phase II trial of neoadjuvant gemcitabine (G), epirubicin (E), and nab -paclitaxel (nab - P) in locally advanced breast cancer (LABC). . J Clin Oncol. 2010 May 20;28(15_suppl):10574–10574.

103. Hamilton EP, Kimmick GG, Desai N, Singh S, Hopkins JO, Marcom PK, et al. Use of SPARC, EGFR, and VEGFR expression to predict response to nab-paclitaxel (nabP)/carboplatin (C)/bevacizumab (B) chemotherapy in triple-negative metastatic breast cancer (TNMBC). J Clin Oncol. 2010 May 20;28(15_suppl):1109–1109.

104. Frese KK, Neesse A, Cook N, Bapiro TE, Lolkema MP, Jodrell DI, et al. Nab-paclitaxel potentiates gemcitabine activity by reducing cytidine deaminase levels in a mouse model of pancreatic cancer. Cancer Discov. 2012 Mar;2(3):260–9.

105. Von Hoff DD, Ervin T, Arena FP, Chiorean EG, Infante J, Moore M, et al. Increased survival in pancreatic cancer with nab-paclitaxel plus gemcitabine. N Engl J Med. 2013 Oct 31;369(18):1691–703.

106. Hammel P, Lacy J, Portales F, Sobrero AF, Pazo Cid RA, Manzano Mozo JL, et al. Phase II LAPACT trial of nab -paclitaxel (nab -P) plus gemcitabine (G) for patients with locally advanced pancreatic cancer (LAPC). . J Clin Oncol. 2018 Feb;36(4_suppl):204–204.

107. Conroy T, Desseigne F, Ychou M, Bouché O, Guimbaud R, Bécouarn Y, et al. FOLFIRINOX versus gemcitabine for metastatic pancreatic cancer. N Engl J Med. 2011 May 12;364(19):1817–25.

108. Frykberg ER. Lobular Carcinoma In Situ of the Breast. Breast J. 1999 Sep 5;5(5):296–303.

109. Cancer CG on HF in B. Menarche, menopause, and breast cancer risk: individual participant meta-analysis, including 118 964 women with breast cancer from 117 epidemiological studies. Lancet Oncol. 2012 Nov;13(11):1141–51.

110. Calle EE, Heath CW, Miracle-McMahill HL, Coates RJ, Liff JM, Franceschi S, et al. Breast cancer and hormonal contraceptives: Collaborative reanalysis of individual data on 53 297 women with breast cancer and 100 239 women without breast cancer from 54 epidemiological studies. Vol. 347, Lancet. Lancet Publishing Group; 1996. p. 1713–27.

111. Chlebowski RT, Manson JE, Anderson GL, Cauley JA, Aragaki AK, Stefanick ML, et al. Estrogen plus progestin and breast cancer incidence and mortality in the Women's Health Initiative Observational Study. J Natl Cancer Inst. 2013 Apr 17;105(8):526–35.

112. Thun MJ, Linet MS, Cerhan JR, Haiman C, Schottenfeld D. Schottenfeld and fraumeni Cancer epidemiology and prevention, fourth edition. Schottenfeld and Fraumeni Cancer Epidemiology and Prevention, Fourth Edition. Oxford University Press; 2017. 1–1308 p.

113. Sinn HP, Kreipe H. A brief overview of the WHO classification of breast tumors, 4th edition, focusing on issues and updates from the 3rd edition. Vol. 8, Breast Care. S. Karger AG; 2013. p. 149–54.

114. Breast Anatomy and How Cancer Starts | About Breast Cancer [Internet]. [cited 2019 Sep 12]. Available from: https://nbcf.org.au/about-national-breast-cancer-foundation/about-breast-cancer/what-you-need-to-know/breast-anatomy-cancer-starts/

115. Weigelt B, Geyer FC, Reis-Filho JS. Histological types of breast cancer: How special are they? Vol. 4, Molecular Oncology. John Wiley and Sons Ltd;

2010. p. 192–208.

116. Waks AG, Winer EP. Breast Cancer Treatment: A Review. Vol. 321, JAMA - Journal of the American Medical Association. American Medical Association; 2019. p. 288–300.

117. Piccart-Gebhart MJ, Procter M, Leyland-Jones B, Goldhirsch A, Untch M, Smith I, et al. Trastuzumab after adjuvant chemotherapy in HER2-positive breast cancer. N Engl J Med. 2005 Oct 20;353(16):1659–72.

118. Wolmark N, Wang J, Mamounas E, Bryant J, Fisher B. Preoperative chemotherapy in patients with operable breast cancer: nine-year results from National Surgical Adjuvant Breast and Bowel Project B-18. J Natl Cancer Inst Monogr. 2001;(30):96–102.

119. Van der Hage JA, Van de Velde CJH, Julien JP, Tubiana-Hulin M, Vandervelden C, Duchateau L. Preoperative chemotherapy in primary operable breast cancer: Results from the European Organization for Research and Treatment of Cancer Trial 10902. J Clin Oncol. 2001 Nov 15;19(22):4224–37.

120. Bear HD, Anderson S, Smith RE, Geyer CE, Mamounas EP, Fisher B, et al. Sequential preoperative or postoperative docetaxel added to preoperative doxorubicin plus cyclophosphamide for operable breast cancer: National surgical adjuvant breast and bowel project protocol B-27. J Clin Oncol. 2006 May 1;24(13):2019–27.

121. Gianni L, Baselga J, Eiermann W, Porta VG, Semiglazov V, Lluch A, et al. Phase III trial evaluating the addition of paclitaxel to doxorubicin followed by cyclophosphamide, methotrexate, and fluorouracil, as adjuvant or primary systemic therapy: European cooperative trial in operable breast cancer. J Clin Oncol. 2009 May 20;27(15):2474–81.

122. Rastogi P, Anderson SJ, Bear HD, Geyer CE, Kahlenberg MS, Robidoux A, et al. Preoperative chemotherapy: Updates of national surgical adjuvant breast and bowel project protocols B-18 and B-27. Vol. 26, Journal of Clinical Oncology. 2008. p. 778–85.

123. Kuerer HM, Newman LA, Smith TL, Ames FC, Hunt KK, Dhingra K, et al.

Clinical Course of Breast Cancer Patients With Complete Pathologic Primary Tumor and Axillary Lymph Node Response to Doxorubicin-Based Neoadjuvant Chemotherapy. J Clin Oncol. 1999 Feb;17(2):460–460.

124. De Laurentiis M, Cancello G, D'Agostino D, Giuliano M, Giordano A, Montagna E, et al. Taxane-based combinations as adjuvant chemotherapy of early breast cancer: A meta-analysis of randomized trials. J Clin Oncol. 2008 Jan 1;26(1):44–53.

125. Thorn CF, Oshiro C, Marsh S, Hernandez-Boussard T, McLeod H, Klein TE, et al. Doxorubicin pathways: pharmacodynamics and adverse effects. Pharmacogenet Genomics. 2011 Jul;21(7):440–6.

126. Arcamone F, Cassinelli G, Franceschi G, Penco S, Pol C, Redaelli S, et al. Structure and Physicochemical Properties of Adriamycin (Doxorubicin). In: International Symposium on Adriamycin. Springer Berlin Heidelberg; 1972. p. 9–22.

127. Tacar O, Sriamornsak P, Dass CR. Doxorubicin: An update on anticancer molecular action, toxicity and novel drug delivery systems. Vol. 65, Journal of Pharmacy and Pharmacology. 2013. p. 157–70.

128. Doroshow JH. Role of hydrogen peroxide and hydroxyl radical formation in the killing of Ehrlich tumor cells by anticancer quinones. Proc Natl Acad Sci U S A. 1986;83(12):4514–8.

129. von Hoff DD, Layard MW, Basa P, Davis HL, Von Hoff AL, Rozencweig M, et al. Risk factors for doxorubicin-induced congestive heart failure. Ann Intern Med. 1979;91(5):710–7.

130. Lotrionte M, Biondi-Zoccai G, Abbate A, Lanzetta G, D'Ascenzo F, Malavasi V, et al. Review and meta-analysis of incidence and clinical predictors of anthracycline cardiotoxicity. Vol. 112, American Journal of Cardiology. 2013. p. 1980–4.

131. Volkova M, Russell R. Anthracycline Cardiotoxicity: Prevalence, Pathogenesis and Treatment. Curr Cardiol Rev. 2012 Mar 26;7(4):214–20.

132. Alfarouk KO, Verduzco D, Rauch C, Muddathir AK, Bashir AHH, Elhassan GO, et al. Glycolysis, tumor metabolism, cancer growth and

dissemination. A new pH-based etiopathogenic perspective and therapeutic approach to an old cancer question. Oncoscience. 2014;1(12):777–802.

133. Buchanan CL, Dorn PL, Fey J, Giron G, Naik A, Mendez J, et al. Locoregional recurrence after mastectomy: incidence and outcomes. J Am Coll Surg. 2006 Oct;203(4):469–74.

134. Abe O, Abe R, Enomoto K, Kikuchi K, Koyama H, Masuda H, et al. Effects of radiotherapy and of differences in the extent of surgery for early breast cancer on local recurrence and 15-year survival: An overview of the randomised trials. Lancet. 2005 Dec 17;366(9503):2087–106.

135. Wapnir IL, Aebi S, Geyer CE, Zahrieh D, Gelber RD, Anderson SJ, et al. A randomized clinical trial of adjuvant chemotherapy for radically resected locoregional relapse of breast cancer: IBCSG 27-02, BIG 1-02, and NSABP B-37. Clin Breast Cancer. 2008;8(3):287–92.

136. Wakeam E, Acuna SA, Keshavjee S. Chest Wall Resection for Recurrent Breast Cancer in the Modern Era. Vol. 267, Annals of Surgery. Lippincott Williams and Wilkins; 2018. p. 646–55.

137. Aebi S, Gelber S, Anderson SJ, Láng I, Robidoux A, Martín M, et al. Chemotherapy for isolated locoregional recurrence of breast cancer (CALOR): a randomised trial. Lancet Oncol. 2014 Feb;15(2):156–63.

138. Russell J, Pillarsetty N, Kramer RM, Romesser PB, Desai P, Haimovitz-Friedman A, et al. In Vitro and In Vivo Comparison of Gemcitabine and the Gemcitabine Analog 1-(2′-deoxy-2′-fluoroarabinofuranosyl) Cytosine (FAC) in Human Orthotopic and Genetically Modified Mouse Pancreatic Cancer Models. Mol Imaging Biol. 2017 Dec 1;19(6):885–92.

139. MacDonald IJ, Dougherty TJ. Basic principles of photodynamic therapy. In: Journal of Porphyrins and Phthalocyanines. John Wiley and Sons Ltd; 2001. p. 105–29.

140. Ito T. CELLULAR AND SUBCELLULAR MECHANISMS OF PHOTODYNAMIC ACTION: THE O2 HYPOTHESIS AS A DRIVING FORCE IN RECENT RESEARCH. Photochem Photobiol. 1978;28(4–5):493–

506.

141. Weishaupt KR, Gomer CJ, Dougherty TJ. Identification of singlet oxygen as the cytotoxic agent in photoinactivation of a murine tumor. Cancer Res. 1976 Jul;36(7 PT 1):2326–9.

142. Kwiatkowski S, Knap B, Przystupski D, Saczko J, Kędzierska E, Knap-Czop K, et al. Photodynamic therapy – mechanisms, photosensitizers and combinations. Vol. 106, Biomedicine and Pharmacotherapy. Elsevier Masson SAS; 2018. p. 1098–107.

143. Reginato E, Wolf P, Hamblin MR. Immune response after photodynamic therapy increases anti-cancer and anti-bacterial effects. World J Immunol. 2014 Mar 27;4(1):1–11.

144. Craig RA, McCoy CP, Gorman SP, Jones DS. Photosensitisers-the progression from photodynamic therapy to anti-infective surfaces. Vol. 12, Expert Opinion on Drug Delivery. Informa Healthcare; 2015. p. 85–101.

145. Kübler AC. Photodynamic therapy. Med Laser Appl. 2005 May;20(1):37–45.

146. Baskaran R, Lee J, Yang S-G. Clinical development of photodynamic agents and therapeutic applications. Biomater Res. 2018 Dec;22(1).

147. Abrahamse H, Hamblin MR. New photosensitizers for photodynamic therapy. Vol. 473, Biochemical Journal. Portland Press Ltd; 2016. p. 347–64.

148. Paczkowski J, Lamberts JJ, Paczkowska B, Neckers DC. Photophysical properties of rose bengal and its derivatives (XII). J Free Radic Biol Med. 1985;1(5–6):341–51.

149. Gollnick K, Schenck GO. Mechanism and Stereoselectivity of Photosensitized Oxygen Transfer Reactions. Pure Appl Chem. 1964;9(4):507–26.

150. Gorman A, Killoran J, O'Shea C, Kenna T, Gallagher WM, O'Shea DF. In vitro demonstration of the heavy-atom effect for photodynamic therapy. J Am Chem Soc. 2004 Sep 1;126(34):10619–31.

151. Houba-Herin N, Calberg-Bacq CM, Piette J, Van de Vorst A. MECHANISMS FOR DYE-MEDIATED PHOTODYNAMIC ACTION: SINGLET OXYGEN PRODUCTION, DEOXYGUANOSINE OXIDATION AND PHAGE INACTIVATING EFFICIENCIES. Photochem Photobiol. 1982;36(3):297–306.

152. Costa ACBP, Rasteiro VMC, Pereira CA, Rossoni RD, Junqueira JC, Jorge AOC. The effects of rose bengal- and erythrosine-mediated photodynamic therapy on Candida albicans. Mycoses. 2012 Jan;55(1):56–63.

153. Panzarini E, Inguscio V, Fimia GM, Dini L. Rose Bengal Acetate PhotoDynamic Therapy (RBAc-PDT) induces exposure and release of Damage-Associated Molecular Patterns (DAMPs) in human HeLa cells. PLoS One. 2014 Aug 20;9(8).

154. Ash C, Dubec M, Donne K, Bashford T. Effect of wavelength and beam width on penetration in light-tissue interaction using computational methods. Lasers Med Sci. 2017 Nov 1;32(8):1909–18.

155. Pan X, Wang H, Wang S, Sun X, Wang L, Wang W, et al. Sonodynamic therapy (SDT): a novel strategy for cancer nanotheranostics. Sci China Life Sci. 2018;61(4):415–26.

156. Franklin DL, Schlegel W, Rushmer RF. Blood flow measured by Doppler frequency shift of back-scattered ultrasound. Science (80-). 1961;134(3478):564–5.

157. Rösch T, Lorenz R, Braig C, Feuerbach S, Rudiger Siewert J, Schusdziarra V, et al. Endoscopic ultrasound in pancreatic tumor diagnosis. Gastrointest Endosc. 1991;37(3):347–52.

158. Shung KK. Diagnostic ultrasound : imaging and blood flow measurements. 262 p.

159. Feleppa EJ. Basic physics of diagnostic ultrasound. In: Prostate Ultrasound: Current Practice and Future Directions. Springer New York; 2015. p. 31–56.

160. McHale AP, Callan JF, Nomikou N, Fowley C, Callan B. Sonodynamic therapy: Concept, mechanism and application to cancer treatment. Vol. 880,

Advances in Experimental Medicine and Biology. Springer New York LLC; 2016. p. 429–50.

161. Begui ZE. Acoustic Properties of the Refractive Media of the Eye. J Acoust Soc Am. 1954;26(3):365–8.

162. Johnston RL, Dunn F, Goss SA. Compilation of empirical ultrasonic properties of mammalian tissues. ll. J Acoust Soc Am. 1980;68(1):93–108.

163. Berger G, Laugier P, Perrin J, Thalabard JC. Global Breast Attenuation: Control Group and Benign Breast Diseases. Ultrason Imaging. 1990;12(1):47–57.

164. Wu F. Heat-based Tumor ablation: Role of the immune response. Adv Exp Med Biol. 2016 Jan 1;880:131–53.

165. Chaussy C, Thüroff S, Rebillard X, Gelet A. Technology insight: High-intensity focused ultrasound for urologic cancers. Vol. 2, Nature Clinical Practice Urology. Nature Publishing Group; 2005. p. 191–8.

166. Leighton TG, Apfel RE. The Acoustic Bubble . J Acoust Soc Am. 1994 Oct;96(4):2616–2616.

167. MIŠÍK V, RIESZ P. Free Radical Intermediates in Sonodynamic Therapy. Ann N Y Acad Sci. 2006 Jan 25;899(1):335–48.

168. Umemura S -i, Yumita N, Nishigaki R, Umemura K. Mechanism of Cell Damage by Ultrasound in Combination with Hematoporphyrin. Japanese J Cancer Res. 1990;81(9):962–6.

169. Giuntini F, Foglietta F, Marucco AM, Troia A, Dezhkunov N V., Pozzoli A, et al. Insight into ultrasound-mediated reactive oxygen species generation by various metal-porphyrin complexes. Free Radic Biol Med. 2018 Jun 1;121:190–201.

170. Miyoshi N, Igarashi T, Riesz P. Evidence against singlet oxygen formation by sonolysis of aqueous oxygen-saturated solutions of Hematoporphyrin and rose bengal. The mechanism of sonodynamic therapy. Ultrason Sonochem. 2000 Jul;7(3):121–4.

171. Marinesco, N. and Trillat JJ. Actions des ultrasons sur les plaques photographiques. Proc R Acad Sci. 1933;196:858-860.

172. Byun K-T, Kim KY, Kwak H-Y. Sonoluminescence Characteristics from Micron and Submicron Bubbles. Vol. 47, Journal of the Korean Physical Society. 2005.

173. Suslick KS, Doktycz SJ, Flint EB. On the origin of sonoluminescence and sonochemistry. Ultrasonics. 1990;28(5):280–90.

174. Beguin E, Shrivastava S, Dezhkunov N V., Mchale AP, Callan JF, Stride E. Direct Evidence of Multibubble Sonoluminescence Using Therapeutic Ultrasound and Microbubbles. ACS Appl Mater Interfaces. 2019 Jun 5;11(22):19913–9.

175. Yumita N, Nishigaki R, Umemura K, Umemura S -i. Hematoporphyrin as a Sensitizer of Cell-damaging Effect of Ultrasound. Japanese J Cancer Res. 1989;80(3):219–22.

176. Umemura S, Kawabata K, Yumita N, Nishigaki R, Umemura K. Sonodynamic approach to tumor treatment. In: Proceedings - IEEE Ultrasonics Symposium. Institute of Electrical and Electronics Engineers Inc.; 1992. p. 1231–40.

177. Yumita N, Sasaki K, Umemura SI, Yukawa A, Nishigaki R. Sonodynamically induced antitumor effect of gallium-porphyrin complex by focused ultrasound on experimental kidney tumor. Cancer Lett. 1997 Jan 15;112(1):79–86.

178. Ohmura T, Fukushima T, Shibaguchi H, Yoshizawa S, Inoue T, Kuroki M, et al. Sonodynamic therapy with 5-aminolevulinic acid and focused ultrasound for deep-seated intracranial glioma in rat. Anticancer Res. 2011 Jul;31(7):2527–33.

179. Wan GY, Liu Y, Chen BW, Liu YY, Wang YS, Zhang N. Recent advances of sonodynamic therapy in cancer treatment. Vol. 13, Cancer Biology and Medicine. Cancer Biology and Medicine; 2016. p. 325–38.

180. Costley D, Mc Ewan C, Fowley C, McHale AP, Atchison J, Nomikou N, et

al. Treating cancer with sonodynamic therapy: A review. Vol. 31, International Journal of Hyperthermia. Informa Healthcare; 2015. p. 107–17.

181. Erkan M, Kurtoglu M, Kleeff J. The role of hypoxia in pancreatic cancer: A potential therapeutic target? Vol. 10, Expert Review of Gastroenterology and Hepatology. Taylor and Francis Ltd; 2016. p. 301–16.

182. Milani M, Harris AL. Targeting tumour hypoxia in breast cancer. Eur J Cancer. 2008 Dec;44(18):2766–73.

183. Koong AC, Mehta VK, Le QT, Fisher GA, Terris DJ, Brown JM, et al. Pancreatic tumors show high levels of hypoxia. Int J Radiat Oncol Biol Phys. 2000 Nov 1;48(4):919–22.

184. Graffman S, Björk P, Ederoth P, Ihse I. Polarographic pO2 measurements of intra-abdominal adenocarcinoma in connection with intraoperative radiotherapy before and after change of oxygen concentration of anaesthetic gases. Vol. 40, Acta Oncologica. 2001. p. 105–7.

185. DeWitt JM, Sandrasegaran K, O'Neil B, House MG, Zyromski NJ, Sehdev A, et al. Phase 1 study of EUS-guided photodynamic therapy for locally advanced pancreatic cancer. Gastrointest Endosc. 2019 Feb 1;89(2):390–8.

186. Couture O, Foley J, Kassell NF, Larrat B, Aubry J-F. Review of ultrasound mediated drug delivery for cancer treatment: updates from pre-clinical studies. Transl Cancer Res. 2014;3(5):494–511.

187. Huber PE, Jenne JW, Rastert R, Simiantonakis I, Sinn HP, Strittmatter HJ, et al. A new noninvasive approach in breast cancer therapy using magnetic resonance imaging-guided focused ultrasound surgery. Cancer Res. 2001 Dec 1;61(23):8441–7.

188. Kennedy JE, Ter Haar GR, Cranston D. High intensity focused ultrasound: surgery of the future? Br J Radiol. 2003 Sep;76(909):590–9.

189. Tacker JR, Anderson RU. Delivery of antitumor drug to bladder cancer by use of phase transition liposomes and hyperthermia. J Urol. 1982;127(6):1211–4.

190. Mills JK, Needham D. Lysolipid incorporation in dipalmitoylphosphatidylcholine bilayer membranes enhances the ion permeability and drug release rates at the membrane phase transition. Biochim Biophys Acta - Biomembr. 2005 Oct 15;1716(2):77–96.

191. Wang S, Shin IS, Hancock H, Jang BS, Kim HS, Lee SM, et al. Pulsed high intensity focused ultrasound increases penetration and therapeutic efficacy of monoclonal antibodies in murine xenograft tumors. J Control Release. 2012 Aug 20;162(1):218–24.

192. Barnett SB, Ter Haar GR, Ziskin MC, Nyborg WL, Maeda K, Bang J. Current status of research on biophysical effects of ultrasound. Vol. 20, Ultrasound in Medicine and Biology. 1994. p. 205–18.

193. Stride E, Edirisinghe M. Novel microbubble preparation technologies. Soft Matter. 2008;4(12):2350–9.

194. Wheatley MA, Schrope B, Shen P. Contrast agents for diagnostic ultrasound: development and evaluation of polymer-coated microbubbles. Biomaterials. 1990;11(9):713–7.

195. Christiansen C, Kryvi H, Sontum P, Skotland T. Physical and biochemical characterization of Albunex, a new ultrasound contrast agent consisting of air-filled albumin microspheres suspended in a solution of human albumin. Biotechnol Appl Biochem. 1994;19(3):307–20.

196. Ferrara K, Pollard R, Borden M. Ultrasound Microbubble Contrast Agents: Fundamentals and Application to Gene and Drug Delivery. Annu Rev Biomed Eng. 2007 Aug 15;9(1):415–47.

197. Lee M, Lee EY, Lee D, Park BJ. Stabilization and fabrication of microbubbles: applications for medical purposes and functional materials. Soft Matter. 2015 Mar 21;11(11):2067–79.

198. Lindner JR. Microbubbles in medical imaging: current applications and future directions. Nat Rev Drug Discov. 2004 Jun;3(6):527–33.

199. Borden MA, Song KH. Reverse engineering the ultrasound contrast agent. Vol. 262, Advances in Colloid and Interface Science. Elsevier B.V.; 2018. p.

39–49.

200. Sirsi SR, Borden MA. Microbubble compositions, properties and biomedical applications. Vol. 1, Bubble Science, Engineering and Technology. 2009. p. 3–17.

201. Feshitan JA, Chen CC, Kwan JJ, Borden MA. Microbubble size isolation by differential centrifugation. J Colloid Interface Sci. 2009 Jan 15;329(2):316–24.

202. DIJKMANS P, JUFFERMANS L, MUSTERS R, VANWAMEL A, TENCATE F, VANGILST W, et al. Microbubbles and ultrasound: from diagnosis to therapy. Eur J Echocardiogr. 2004 Aug;5(4):245–56.

203. De Jong N, Bouakaz A, Frinking P. Basic acoustic properties of microbubbles. Vol. 19, Echocardiography. Futura Publishing Company Inc.; 2002. p. 229–40.

204. Weissleder R. Molecular imaging : principles and practice. People's Medical Pub. House--USA; 2010. 135 p.

205. Unger EC, McCreery TP, Sweitzer RH, Caldwell VE, Wu Y. Acoustically active liposheres containing paclitaxel: A new therapeutic ultrasound contrast agent. Invest Radiol. 1998 Dec;33(12):886–92.

206. Xing W, Gang WZ, Yong Z, Yi ZY, Shan XC, Tao RH. Treatment of Xenografted Ovarian Carcinoma Using Paclitaxel-loaded Ultrasound Microbubbles. Acad Radiol. 2008 Dec;15(12):1574–9.

207. Wang DS, Panje C, Pysz MA, Paulmurugan R, Rosenberg J, Gambhir SS, et al. Cationic versus neutral microbubbles for ultrasound-mediated gene delivery in cancer. Radiology. 2012 Sep;264(3):721–32.

208. Rychak JJ, Klibanov AL. Nucleic acid delivery with microbubbles and ultrasound. Vol. 72, Advanced Drug Delivery Reviews. Elsevier; 2014. p. 82–93.

209. Nomikou N, Fowley C, Byrne NM, McCaughan B, McHale AP, Callan JF. Microbubble-sonosensitiser conjugates as therapeutics in sonodynamic therapy. Chem Commun. 2012 Aug 28;48(67):8332–4.

210. Bettinger T, Tranquart F. Design of microbubbles for gene/drug delivery. Adv Exp Med Biol. 2016 Jan 1;880:191–204.

211. Lentacker I, De Smedt SC, Demeester J, Van Marck V, Bracke M, Sanders NN. Lipoplex-loaded microbubbles for gene delivery: A trojan horse controlled by ultrasound. Adv Funct Mater. 2007 Aug 13;17(12):1910–6.

212. Kheirolomoom A, Dayton PA, Lum AFH, Little E, Paoli EE, Zheng H, et al. Acoustically-active microbubbles conjugated to liposomes: Characterization of a proposed drug delivery vehicle. J Control Release. 2007 Apr 23;118(3):275–84.

213. Lentacker I, De Smedt SC, Sanders NN. Drug loaded microbubble design for ultrasound triggered delivery. Soft Matter. 2009;5(11):2161–70.

214. McEwan C, Owen J, Stride E, Fowley C, Nesbitt H, Cochrane D, et al. Oxygen carrying microbubbles for enhanced sonodynamic therapy of hypoxic tumours. J Control Release. 2015 Apr 10;203:51–6.

215. Liu H, Chang S, Sun J, Zhu S, Pu C, Zhu Y, et al. Ultrasound-mediated destruction of LHRHa-targeted and paclitaxel-loaded lipid microbubbles induces proliferation inhibition and apoptosis in ovarian cancer cells. Mol Pharm. 2014 Jan 6;11(1):40–8.

216. Luan Y, Faez T, Gelderblom E, Skachkov I, Geers B, Lentacker I, et al. Acoustical Properties of Individual Liposome-Loaded Microbubbles. Ultrasound Med Biol. 2012 Dec;38(12):2174–85.

217. Ibsen S, Benchimol M, Simberg D, Schutt C, Steiner J, Esener S. A novel nested liposome drug delivery vehicle capable of ultrasound triggered release of its payload. J Control Release. 2011 Nov 7;155(3):358–66.

218. Kotopoulis S, Dimcevski G, Helge Gilja O, Hoem D, Postema M. Treatment of human pancreatic cancer using combined ultrasound, microbubbles, and gemcitabine: A clinical case study. Med Phys. 2013;40(7).

219. Marmottant P, Hilgenfeldt S. Controlled vesicle deformation and lysis by single oscillating bubbles. Nature. 2003 May 8;423(6936):153–6.

220. Wu J. Shear stress in cells generated by ultrasound. Vol. 93, Progress in

Biophysics and Molecular Biology. 2007. p. 363–73.

221. Wu J. Theoretical study on shear stress generated by microstreaming surrounding contrast agents attached to living cells. Ultrasound Med Biol. 2002;28(1):125–9.

222. Invited Editorial – Sonoporation: Why Microbubbles Create Pores. Ultraschall der Medizin - Eur J Ultrasound. 2012 Feb 14;33(01):97–8.

223. Skyba DM, Price RJ, Linka AZ, Skalak TC, Kaul S. Direct in vivo visualization of intravascular destruction of microbubbles by ultrasound and its local effects on tissue. Circulation. 1998 Jul 28;98(4):290–3.

224. Zhang Q, Jin H, Chen L, Chen Q, He Y, Yang Y, et al. Effect of Ultrasound Combined With Microbubble Therapy on Interstitial Fluid Pressure and VX2 Tumor Structure in Rabbit. Front Pharmacol. 2019 Jun 26;10.

225. Nande R, Claudio PP, Howard C. Ultrasound-mediated oncolytic virus delivery and uptake for increased therapeutic efficacy: state of art. Oncolytic Virotherapy. 2015 Nov;193.

226. Kotopoulis S, Delalande A, Popa M, Mamaeva V, Dimcevski G, Gilja OH, et al. Sonoporation-enhanced chemotherapy significantly reduces primary tumour burden in an orthotopic pancreatic cancer xenograft. Mol Imaging Biol. 2014 Feb;16(1):53–62.

227. Dimcevski G, Kotopoulis S, Bjånes T, Hoem D, Schjøt J, Gjertsen BT, et al. A human clinical trial using ultrasound and microbubbles to enhance gemcitabine treatment of inoperable pancreatic cancer. J Control Release. 2016 Dec 10;243:172–81.

228. Lee HJ, Yoon Y Il, Bae YJ. Theragnostic ultrasound using microbubbles in the treatment of prostate cancer. Vol. 35, Ultrasonography. Korean Society of Ultrasound in Medicine; 2016. p. 309–17.

229. Pysz MA, Foygel K, Rosenberg J, Gambhir SS, Schneider M, Willmann JK. Antiangiogenic cancer therapy: Monitoring with molecular US and a clinically translatable contrast agent (BR55). Radiology. 2010;256(2):519–27.

230. Giatromanolaki A, Koukourakis MI, Sivridis E, Chlouverakis G,

Vourvouhaki E, Turley H, et al. Activated VEGFR2/KDR pathway in tumour cells and tumour associated vessels of colorectal cancer. Eur J Clin Invest. 2007 Nov;37(11):878–86.

231. Ferrara N, Hillan KJ, Gerber HP, Novotny W. Discovery and development of bevacizumab, an anti-VEGF antibody for treating cancer. Vol. 3, Nature Reviews Drug Discovery. Nature Publishing Group; 2004. p. 391–400.

232. Bruns CJ, Liu W, Davis DW, Shaheen RM, McConkey DJ, Wilson MR, et al. Vascular endothelial growth factor is an in vivo survival factor for tumor endothelium in a murine model of colorectal carcinoma liver metastases. Cancer. 2000 Aug 1;89(3):488–99.

233. Ellis LM. Vascular Endothelial Growth Factor in Human Colon Cancer: Biology and Therapeutic Implications. Oncologist. 2000 Apr 1;5(90001):11–5.

234. Villanueva FS, Jankowski RJ, Klibanov S, Pina ML, Alber SM, Watkins SC, et al. Microbubbles targeted to intercellular adhesion molecule-1 bind to activated coronary artery endothelial cells. Circulation. 1998 Jul 7;98(1):1–5.

235. Stride E, Porter C, Prieto AG, Pankhurst Q. Enhancement of Microbubble Mediated Gene Delivery by Simultaneous Exposure to Ultrasonic and Magnetic Fields. Ultrasound Med Biol. 2009 May;35(5):861–8.

236. Mulvana H, Eckersley RJ, Browning R, Hajnal J V., Stride E, Barrack T, et al. Enhanced gene transfection in vivo using magnetic localisation ofultrasound contrast agents: Preliminary results. In: Proceedings - IEEE Ultrasonics Symposium. 2010. p. 670–3.

237. McEwan C, Fowley C, Nomikou N, McCaughan B, McHale AP, Callan JF. Polymeric microbubbles as delivery vehicles for sensitizers in sonodynamic therapy. Langmuir. 2014;30(49):14926–30.

238. McEwan C, Kamila S, Owen J, Nesbitt H, Callan B, Borden M, et al. Combined sonodynamic and antimetabolite therapy for the improved treatment of pancreatic cancer using oxygen loaded microbubbles as a delivery vehicle. Biomaterials. 2016 Feb;80:20–32.

239. Borden MA, Longo ML. Dissolution behavior of lipid monolayer-coated, air-filled microbubbles: Effect of lipid hydrophobic chain length. Langmuir. 2002 Nov 26;18(24):9225–33.

240. Nesbitt H, Sheng Y, Kamila S, Logan K, Thomas K, Callan B, et al. Gemcitabine loaded microbubbles for targeted chemo-sonodynamic therapy of pancreatic cancer. J Control Release. 2018 Jun 10;279:8–16.

241. Neoptolemos JP, Stocken DD, Bassi C, Ghaneh P, Cunningham D, Goldstein D, et al. Adjuvant chemotherapy with fluorouracil plus folinic acid vs gemcitabine following pancreatic cancer resection: A randomized controlled trial. JAMA - J Am Med Assoc. 2010 Sep 8;304(10):1073–81.

242. Logan K, Foglietta F, Nesbitt H, Sheng Y, McKaig T, Kamila S, et al. Targeted chemo-sonodynamic therapy treatment of breast tumours using ultrasound responsive microbubbles loaded with paclitaxel, doxorubicin and Rose Bengal. Eur J Pharm Biopharm. 2019 Jun 1;139:224–31.

243. Susumu K, Uyeda HT, Medintz IL, Pons T, Delehanty JB, Mattoussi H. Enhancing the Stability and Biological Functionalities of Quantum Dots via Compact Multifunctional Ligands. J Am Chem Soc. 2007 Nov;129(45):13987–96.

244. Sennoga CA, Mahue V, Loughran J, Casey J, Seddon JM, Tang M, et al. On sizing and counting of microbubbles using optical microscopy. Ultrasound Med Biol. 2010 Dec;36(12):2093–6.

245. Barnsley LC, Gray MD, Beguin E, Carugo D, Stride E. A Combined Magnetic-Acoustic Device for Simultaneous, Coaligned Application of Magnetic and Ultrasonic Fields. Adv Mater Technol. 2018 Jul 1;3(7).

246. Holtz J. Peripheral Circulation: Fundamental Concepts, Comparative Aspects of Control in Specific Vascular Sections, and Lymph Flow. In: Comprehensive Human Physiology. Springer Berlin Heidelberg; 1996. p. 1865–915.

247. Sheng Y, Beguin E, Nesbitt H, Kamila S, Owen J, Barnsley LC, et al. Magnetically responsive microbubbles as delivery vehicles for targeted sonodynamic and antimetabolite therapy of pancreatic cancer. J Control

Release. 2017 Sep 28;262:192–200.

248. Breast cancer statistics | Cancer Research UK [Internet]. [cited 2019 Sep 13]. Available from: https://www.cancerresearchuk.org/health-professional/cancer-statistics/statistics-by-cancer-type/breast-cancer

249. The Second All Breast Cancer Report - Association of Breast Surgery [Internet]. [cited 2019 Sep 13]. Available from: https://associationofbreastsurgery.org.uk/news/2011/june/the-second-all-breast-cancer-report/

250. M. Ali A, A.K. Ansari J, M. Abd El-Aziz N, N. Abozeed W, M. Abdel Warith A, Alsaleh K, et al. Triple Negative Breast Cancer: A Tale of Two Decades. Anticancer Agents Med Chem. 2016 Jul 27;17(4):491–9.

251. Steenbruggen TG, van Ramshorst MS, Kok M, Linn SC, Smorenburg CH, Sonke GS. Neoadjuvant Therapy for Breast Cancer: Established Concepts and Emerging Strategies. Drugs. 2017 Aug;77(12):1313–36.

252. Mieog JSD, Van Der Hage JA, Van De Velde CJH. Preoperative chemotherapy for women with operable breast cancer. Cochrane Database of Systematic Reviews. John Wiley and Sons Ltd; 2007.

253. Mieog JSD, Van Der Hage JA, Van De Velde CJH. Neoadjuvant chemotherapy for operable breast cancer. Br J Surg. 2007 Oct;94(10):1189–200.

254. Kiebert GM, De Haes JCJM, Van De Velde CJH. The impact of breast-conserving treatment and mastectomy on the quality of life of early-stage breast cancer patients: A review. J Clin Oncol. 1991;9(6):1059–70.

255. Asselain B, Barlow W, Bartlett J, Bergh J, Bergsten-Nordström E, Bliss J, et al. Long-term outcomes for neoadjuvant versus adjuvant chemotherapy in early breast cancer: meta-analysis of individual patient data from ten randomised trials. Lancet Oncol. 2018 Jan 1;19(1):27–39.

256. Perez EA. Doxorubicin and paclitaxel in the treatment of advanced breast cancer: Efficacy and cardiac considerations. Vol. 19, Cancer Investigation. 2001. p. 155–64.

257. Fisher B, Anderson S, Bryant J, Margolese RG, Deutsch M, Fisher ER, et al. Twenty-year follow-up of a randomized trial comparing total mastectomy, lumpectomy, and lumpectomy plus irradiation for the treatment of invasive breast cancer. N Engl J Med. 2002 Oct 17;347(16):1233–41.

258. Wapnir IL, Anderson SJ, Mamounas EP, Geyer CE, Jeong JH, Tan-Chiu E, et al. Prognosis after ipsilateral breast tumor recurrence and locoregional recurrences in five national surgical adjuvant breast and bowel project node-positive adjuvant breast cancer trials. J Clin Oncol. 2006 May 1;24(13):2028–37.

259. Elkhuizen PHM, Van De Vijver MJ, Hermans J, Zonderland HM, Van De Velde CJH, Leer JWH. Local recurrence after breast-conserving therapy for invasive breast cancer: High incidence in young patients and association with poor survival. Int J Radiat Oncol Biol Phys. 1998 Mar 1;40(4):859–67.

260. Schiff PB, Fant J, Horwitz SB. Promotion of microtubule assembly in vitro by taxol. Vol. 277, Nature. 1979. p. 665–7.

261. Haldar S, Chintapalli J, Croce CM. Taxol induces bcl-2 phosphorylation and death of prostate cancer cells. Cancer Res. 1996 Mar 15;56(6):1253–5.

262. Zhang J, Wang S, Deng Z, Li L, Tan G, Liu X, et al. Ultrasound-triggered drug delivery for breast tumor therapy through iRGD-targeted paclitaxel-loaded liposome-microbubble complexes. J Biomed Nanotechnol. 2018 Aug 1;14(8):1384–95.

263. Shen Y, Pi Z, Yan F, Yeh CK, Zeng X, Diao X, et al. Enhanced delivery of paclitaxel liposomes using focused ultrasound with microbubbles for treating nude mice bearing intracranial glioblastoma xenografts. Int J Nanomedicine. 2017 Aug 9;12:5613–29.

264. Zhou L, Luo W. Vascular endothelial growth factor–targeted paclitaxel-loaded liposome microbubbles and inhibition of human epidermoid-2 cell proliferation. Head Neck. 2017 Apr 1;39(4):656–61.

265. Luo T, Wang Z, He J, Hao L, Xiao L, Zhu Y, et al. Ultrasound-mediated destruction of oxygen and paclitaxel loaded dual-targeting microbubbles for intraperitoneal treatment of ovarian cancer xenografts. Cancer Lett.

2017 Apr 10;391:1–11.

266. Zhu X, Guo J, He C, Geng H, Yu G, Li J, et al. Ultrasound triggered image-guided drug delivery to inhibit vascular reconstruction via paclitaxel-loaded microbubbles. Sci Rep. 2016 Feb 22;6.

267. Sun J, Yin M, Zhu S, Liu L, Zhu Y, Wang Z, et al. Ultrasound-mediated destruction of oxygen and paclitaxel loaded lipid microbubbles for combination therapy in hypoxic ovarian cancer cells. Ultrason Sonochem. 2016 Jan 27;28:319–26.

268. Ibrahim NK, Desai N, Legha S, Formulation N, Soon-shiong P, Theriault RL, et al. Phase I and Pharmacokinetic Study of ABI-007 , a of Paclitaxel Phase I and Pharmacokinetic Study of ABI-007 , a Cremophor-free ,. Clin Cancer Res. 2002;8(May):1038–44.

269. Liu L, Chang S, Sun J, Zhu S, Yin M, Zhu Y, et al. Ultrasound-mediated destruction of paclitaxel and oxygen loaded lipid microbubbles for combination therapy in ovarian cancer xenografts. Cancer Lett. 2015 May 28;361(1):147–54.

270. SCHNEIDER M. Characteristics of SonoVue™. Echocardiography. 1999 Oct;16(s1):743–6.

271. Siewert B, Langerman M, Pannwitz A, Bonnet S. Synthesis and Avidin Binding of Ruthenium Complexes Functionalized with a Light-Cleavable Free Biotin Moiety. Eur J Inorg Chem. 2018 Oct 9;2018(37):4117–24.

272. Lesch HP, Kaikkonen MU, Pikkarainen JT, Ylä-Herttuala S. Avidin-biotin technology in targeted therapy. Vol. 7, Expert Opinion on Drug Delivery. Informa Healthcare; 2010. p. 551–64.

273. Taxol (paclitaxel) dosing, indications, interactions, adverse effects, and more [Internet]. [cited 2019 Sep 13]. Available from: https://reference.medscape.com/drug/taxol-paclitaxel-342187

274. (doxorubicin) dosing, indications, interactions, adverse effects, and more [Internet]. [cited 2019 Sep 13]. Available from: https://reference.medscape.com/drug/doxorubicin-342120

275. Lentacker I, Geers B, Demeester J, De Smedt SC, Sanders NN. Design and evaluation of doxorubicin-containing microbubbles for ultrasound-triggered doxorubicin delivery: Cytotoxicity and mechanisms involved. Mol Ther. 2010 Jan;18(1):101–8.

276. Fritz T, McKeon M, Unger E. Preclinical studies of MRX-115: Safety evaluations of a myocardial perfusion agent. Acad Radiol. 1996 Aug;3:S185–7.

277. Burdett E, Kasper FK, Mikos AG, Ludwig JA. Engineering tumors: a tissue engineering perspective in cancer biology. Tissue Eng Part B Rev. 2010 Jun;16(3):351–9.

278. Do Amaral JB, Rezende-Teixeira P, Freitas VM, MacHado-Santelli GM. MCF-7 cells as a three-dimensional model for the study of human breast cancer. Tissue Eng - Part C Methods. 2011 Nov 1;17(11):1097–107.

279. Yang F, Gu N, Chen D, Xi X, Zhang D, Li Y, et al. Experimental study on cell self-sealing during sonoporation. J Control Release. 2008 Nov 12;131(3):205–10.

280. Park J, Fan Z, Deng CX. Effects of shear stress cultivation on cell membrane disruption and intracellular calcium concentration in sonoporation of endothelial cells. J Biomech. 2011 Jan 4;44(1):164–9.

281. Karshafian R, Bevan PD, Williams R, Samac S, Burns PN. Sonoporation by Ultrasound-Activated Microbubble Contrast Agents: Effect of Acoustic Exposure Parameters on Cell Membrane Permeability and Cell Viability. Ultrasound Med Biol. 2009 May;35(5):847–60.

282. Postema M, Van Wamel A, Lancée CT, De Jong N. Ultrasound-induced encapsulated microbubble phenomena. Ultrasound Med Biol. 2004 Jun;30(6):827–40.

283. van Wamel A, Kooiman K, Emmer M, ten Cate FJ, Versluis M, de Jong N. Ultrasound microbubble induced endothelial cell permeability. J Control Release. 2006 Nov;116(2):e100–2.

284. Suzuki T, Fujikura K, Higashiyama T, Takata K. DNA staining for fluorescence and laser confocal microscopy. J Histochem Cytochem.

1997;45(1):49–53.

285. Gelderblom H, Verweij J, van Zomeren DM, Buijs D, Ouwens L, Nooter K, et al. Influence of Cremophor El on the bioavailability of intraperitoneal paclitaxel. Clin Cancer Res. 2002 Apr;8(4):1237–41.

286. Liebmann J, Cook JA, Mitchell JB. Cremophor EL, solvent for paclitaxel, and toxicity. Vol. 342, The Lancet. 1993. p. 1428.

287. Cochran MC, Eisenbrey J, Ouma RO, Soulen M, Wheatley MA. Doxorubicin and paclitaxel loaded microbubbles for ultrasound triggered drug delivery. Int J Pharm. 2011 Jul 29;414(1–2):161–70.

288. Alvarez R, Musteanu M, Garcia-Garcia E, Lopez-Casas PP, Megias D, Guerra C, et al. Stromal disrupting effects of nab-paclitaxel in pancreatic cancer. Br J Cancer. 2013 Aug 20;109(4):926–33.

289. Giordano G, Vaccaro V, Lucchini E, Bertocchi P, Bergamo F, Musettini G, et al. Analysis of prognostic factors in advanced pancreatic cancer (APDAC) patients (pts) undergoing to first-line nab-paclitaxel (Nab-P) and gemcitabine (G) treatment. J Clin Oncol. 2015 Jan 20;33(3_suppl):412–412.

290. S M, H Z, L.E M, T.D S, N B, T.E G, et al. A pilot phase II multicenter study of nab-paclitaxel (Nab-P) and gemcitabine (G) as preoperative therapy for potentially resectable pancreatic cancer (PC). J Clin Oncol. 2013;

291. Sliesoraitis S, Desai NV, Trevino JG, Hughes SJ, Zlotecki R, Lightsey JL, et al. Final results for gemcitabine with nab-paclitaxel in neoadjuvant treatment of resectable pancreatic adenocarcinoma: GAIN-1 study. J Clin Oncol. 2014 May 20;32(15_suppl):e15201–e15201.

292. Ielpo B, Duran H, Diaz E, Fabra I, Caruso R, Ferri V, et al. Preoperative treatment with gemcitabine plus nab-paclitaxel is a safe and effective chemotherapy for pancreatic adenocarcinoma. Eur J Surg Oncol. 2016 Sep 1;42(9):1394–400.

293. Age as risk factor · Pancreatic Cancer Action [Internet]. [cited 2019 Sep 13]. Available from: https://pancreaticcanceraction.org/about-pancreatic-cancer/causes-pancreatic-cancer/age-risk-factor/

294. Capello M, Lee M, Wang H, Babel I, Katz MH, Fleming JB, et al. Carboxylesterase 2 as a Determinant of Response to Irinotecan and Neoadjuvant FOLFIRINOX Therapy in Pancreatic Ductal Adenocarcinoma. J Natl Cancer Inst. 2015 Aug 1;107(8).

295. Hatfield JM, Wierdl M, Wadkins RM, Potter PM. Modifications of human carboxylesterase for improved prodrug activation. Vol. 4, Expert Opinion on Drug Metabolism and Toxicology. 2008. p. 1153–65.

296. Stockert JC, Horobin RW, Colombo LL, Blázquez-Castro A. Tetrazolium salts and formazan products in Cell Biology: Viability assessment, fluorescence imaging, and labeling perspectives. Vol. 120, Acta Histochemica. Elsevier GmbH; 2018. p. 159–67.

297. Crowley LC, Scott AP, Marfell BJ, Boughaba JA, Chojnowski G, Waterhouse NJ. Measuring cell death by propidium iodide uptake and flow cytometry. Cold Spring Harb Protoc. 2016 Jul 1;2016(7):647–51.

298. Cao J, Chen Z, Chi J, Sun Y, Sun Y. Recent progress in synergistic chemotherapy and phototherapy by targeted drug delivery systems for cancer treatment. Vol. 46, Artificial Cells, Nanomedicine and Biotechnology. Taylor and Francis Ltd.; 2018. p. 817–30.

299. Borden MA, Sarantos MR, Stieger SM, Simon SI, Ferrara KW, Dayton PA. Ultrasound Radiation Force Modulates Ligand Availability on Targeted Contrast Agents. Mol Imaging. 2006 Jul;5(3):7290.2006.00016.

300. Pochon S, Tardy I, Bussat P, Bettinger T, Brochot J, Von Wronski M, et al. BR55: A lipopeptide-based VEGFR2-targeted ultrasound contrast agent for molecular imaging of angiogenesis. Invest Radiol. 2010 Feb;45(2):89–95.

301. Dayton P, Klibanov A, Brandenburger G, Ferrara K. Acoustic radiation force in vivo: A mechanism to assist targeting of microbubbles. Ultrasound Med Biol. 1999 Oct;25(8):1195–201.

302. Owen J, Pankhurst Q, Stride E. Magnetic targeting and ultrasound mediated drug delivery: Benefits, limitations and combination. Int J Hyperth. 2012 Jun;28(4):362–73.

303. Zhu N, Ji H, Yu P, Niu J, Farooq MU, Akram MW, et al. Surface

modification of magnetic iron oxide nanoparticles. Vol. 8, Nanomaterials. MDPI AG; 2018.

304. Beguin E, Bau L, Shrivastava S, Stride E. Comparing Strategies for Magnetic Functionalization of Microbubbles. ACS Appl Mater Interfaces. 2019 Jan 16;11(2):1829–40.

305. Liu H, Carter PJH, Laan AC, Eelkema R, Denkova AG. Singlet Oxygen Sensor Green is not a Suitable Probe for 1O2 in the Presence of Ionizing Radiation. Sci Rep. 2019 Dec 1;9(1).

306. Chevalier Y, Bolzinger MA. Emulsions stabilized with solid nanoparticles: Pickering emulsions. Colloids Surfaces A Physicochem Eng Asp. 2013 Dec 20;439:23–34.

307. Narayanan J, Xiong JY, Liu XY. Determination of agarose gel pore size: Absorbance measurements vis a vis other techniques. J Phys Conf Ser. 2006 Jan 1;28(1):83–6.

308. Shen J, Zhuo N, Xu S, Song Z, Hu Z, Hao J, et al. Resveratrol delivery by ultrasound-mediated nanobubbles targeting nucleus pulposus cells. Nanomedicine. 2018 Jun 1;13(12):1433–46.

309. Wu M, Zhao H, Guo L, Wang Y, Song J, Zhao X, et al. Ultrasound-mediated nanobubble destruction (UMND) facilitates the delivery of A10-3.2 aptamer targeted and siRNA-loaded cationic nanobubbles for therapy of prostate cancer. Drug Deliv. 2018 Jan 9;25(1):226–40.

310. Klibanov AL. Ligand-carrying gas-filled microbubbles: Ultrasound contrast agents for targeted molecular imaging. In: Bioconjugate Chemistry. 2005. p. 9–17.

311. Zhu L, Wang L, Liu Y, Xu D, Fang K, Guo Y. CAIX aptamer-functionalized targeted nanobubbles for ultrasound molecular imaging of various tumors. Int J Nanomedicine. 2018;13:6481–95.

312. Yeh JSM, Sennoga CA, McConnell E, Eckersley R, Tang MX, Nourshargh S, et al. A targeting microbubble for ultrasound molecular imaging. PLoS One. 2015 Jul 10;10(7).

313. Yan F, Xu X, Chen Y, Deng Z, Liu H, Xu J, et al. A Lipopeptide-Based $\alpha\text{v}\beta$ 3 Integrin-Targeted Ultrasound Contrast Agent for Molecular Imaging of Tumor Angiogenesis. Ultrasound Med Biol. 2015;41(10):2765–73.

314. Wu W, Wang Y, Shen S, Wu J, Guo S, Su L, et al. In vivo ultrasound molecular imaging of inflammatory thrombosis in arteries with cyclic Arg-Gly-Asp-modified microbubbles targeted to glycoprotein IIb/IIIa. Invest Radiol. 2013 Nov;48(11):803–12.

315. Sirsi SR, Hernandez SL, Zielinski L, Blomback H, Koubaa A, Synder M, et al. Polyplex-microbubble hybrids for ultrasound-guided plasmid DNA delivery to solid tumors. J Control Release. 2012 Jan 30;157(2):224–34.

316. Slagle CJ, Thamm DH, Randall EK, Borden MA. Click Conjugation of Cloaked Peptide Ligands to Microbubbles. Bioconjug Chem. 2018 May 16;29(5):1534–43.

317. Liu X, Gong P, Song P, Xie F, Miller AL, Chen S, et al. Rapid conjugation of nanoparticles, proteins and siRNAs to microbubbles by strain-promoted click chemistry for ultrasound imaging and drug delivery. Polym Chem. 2019 Feb 14;10(6):705–17.

318. Liu X, Gong P, Song P, Xie F, Miller AL, Chen S, et al. Fast functionalization of ultrasound microbubbles using strain promoted click chemistry. Biomater Sci. 2018 Mar 1;6(3):623–32.

319. Shuto S, Ueda S, Imamura S, Fukukawa K, Matsuda A, Ueda T. A facile one-step synthesis of 5′-phosphatidylnucleosides by an enzymatic two-phase reaction. Tetrahedron Lett. 1987;28(2):199–202.

320. Matsuda A, Ueda T, Obara T, Nakagami K, Yaso M, Yaginuma S, et al. New neplanocin analogues II. Enzymatic one-step synthesis and antitumor activity of 6′-(3-sn-phosphatidyl)neplanocin a derivatives. Nucleosides and Nucleotides. 1992 Feb 1;11(2–4):437–46.

321. Shuto S, Itoh H, Sakai A, Nakagami K, Imamura S, Matsuda A. Nucleosides and nucleotides-CXXXVII. Antitumor phospholipids with 5-fluorouridine as a cytotoxic polar-head: Synthesis of 5′-phosphatidyl-5-fluorouridines by phospholipase d-catalyzed transphosphatidylation. Bioorganic Med Chem.

1995;3(3):235–43.

322. Shuto S, Awano H, Shimazaki N, Hanaoka K, Matsuda A. Nucleosides and nucleotides. 150. Enzymatic synthesis of 5′-phosphatidyl derivatives of 1-(2-C-cyano-2-deoxy-β-D-Arabino-pentofuranosyl)cytosine (CNDAC) and their notable antitumor effects in mice. Bioorganic Med Chem Lett. 1996 May 7;6(9):1021–4.

323. Ulbrich-Hofmann R. Enzyme-catalysed transphosphatidylation. Vol. 105, European Journal of Lipid Science and Technology. 2003. p. 305–8.

324. Arouri A, Hansen AH, Rasmussen TE, Mouritsen OG. Lipases, liposomes and lipid-prodrugs. Vol. 18, Current Opinion in Colloid and Interface Science. 2013. p. 419–31.

325. Irby D, Du C, Li F. Lipid-Drug Conjugate for Enhancing Drug Delivery. Mol Pharm. 2017 May 1;14(5):1325–38.